Fraunhofer ISE

FRAUNHOFER INSTITUTE FOR SOLAR ENERGY SYSTEMS ISE

SOLAR ENERGY AND SYSTEMS RESEARCH

Mathias List

ADVANCED ELECTRICAL AND OPTICAL CHARACTERIZATION OF RECOMBINATION IN ORGANIC SOLAR CELLS

FRAUNHOFER VERLAG

Fraunhofer Institute for Solar Energy Systems ISE

SOLARE ENERGIE- UND SYSTEMFORSCHUNG /
SOLAR ENERGY AND SYSTEMS RESEARCH

Advanced Electrical and Optical Characterization of Recombination in Organic Solar Cells

Mathias List

FRAUNHOFER VERLAG

Kontakt:
Fraunhofer-Institut für Solare Energiesysteme ISE
Heidenhofstraße 2
79110 Freiburg
Telefon +49 761/4588-5150
Fax +49 761/4588-9342
E-Mail info@ise.fraunhofer.de
URL www.ise.fraunhofer.de

Bibliografische Information der Deutschen Nationalbibliothek
Die Deutsche Nationalbibliothek verzeichnet diese Publikation in der Deutschen Nationalbibliografie; detaillierte bibliografische Daten sind im Internet über www.dnb.de abrufbar.
ISSN: 2512-3629
ISBN (Print): 978-3-8396-1468-6

Reihe: »Solare Energie- und Systemforschung / Solar Energy and Systems Research«

D 25

Zugl.: Freiburg/Br., Univ., Diss., 2019

Druck: Fraunhofer Verlag Mediendienstleistung

Für den Druck des Buches wurde chlor- und säurefreies Papier verwendet.

Fraunhofer-Informationszentrum Raum und Bau IRB
Postfach 80 04 69, 70504 Stuttgart
Nobelstraße 12, 70569 Stuttgart
Telefon 07 11 9 70-25 00
Telefax 07 11 9 70-25 08
E-Mail verlag@fraunhofer.de
URL http://verlag.fraunhofer.de

Advanced Electrical and Optical Characterization of Recombination in Organic Solar Cells

vorgelegt von

Mathias List

aus Engen

· März 2019 ·

Dissertation zur Erlangung des Doktorgrades
der
Fakultät für Mathematik und Physik
der
Albert-Ludwigs-Universität Freiburg im Breisgau

durchgeführt am
Freiburger Materialforschungszentrum
in Zusammenarbeit mit dem
Fraunhofer-Institut für Solare Energiesysteme, Freiburg

Dekan:	Prof. Dr. Gregor Herten
Referent:	Prof. Dr. Eicke R. Weber
Korreferent:	Prof. Dr. Marc Schumann
Datum der mündlichen Prüfung:	11.03.2019

Gefördert durch das Promotionsstipendienprogramm der Dr. Ruth Heerdt-Stiftung

Wir blasen unsere Kohleminen in die Luft. ... Es wäre leicht möglich, dass diese Veränderung den Planeten derart aufheizt, dass es jenseits aller menschlichen Erfahrung läge.

Svante Arrhenius, schwedischer Chemiker, 1896

Contents

Chapter I

Introduction

In 2016, the annual global energy demand was about 160 PWh corresponding to a continuously consumed power of 18 TW which is predicted to rise to about 45 TW in 2060 [1, 2]. The catastrophes in Chernobyl and Fukushima and the progressive climate change show the social and environmental risks of conventional energy production from fossil fuels and nuclear energy. Furthermore, the objective of a CO_2-free global economy to the end of this century was formulated on the G7 summit in 2015 [3]. To reach this goal diversified development and installation of renewable energy technologies using biomass, geothermal heat, wind, water, or solar energy are indispensable.
Photovoltaics (PV) have huge potential to cover a substantial part of the global energy demand in the energy mix of the future. The total solar irradiance on the surface of our planet is about 120 000 TW. This exceeds the current global energy demand by a factor > 6500. The prices for utility-scale PV systems dropped from 4.5 to 1.0 USD per Watt in the last eight years and the installed power increased from 40 GW in 2010 to over 415 GW in 2017 reaching a share of 1.7 % of the global electric power production [4, 5]. Regardless of these promising developments of PV, there is still a demand for research on the improvement of the efficiency, the lifetime, the reduction of costs of established technologies and for the development of novel concepts.

Organic Photovoltaics

This work focuses on organic photovoltaics (OPV). In OPV, solar energy is converted to electrical energy using carbon-based organic semiconductors. This technology is based on the discoveries of conductive polymers by Heeger, MacDiarmid and Shirakawa in 1977 which was honored with the Nobel Prize in chemistry in 2000 [6]. The first organic solar cells with a considerable power conversion efficiency (PCE) of 1 % were reported by Tang et al. in 1986 [7]. The properties of the materials commonly utilized in OPV enable a variety of interesting module designs. They allow the manufacturing of light-weight, flexible and semitransparent modules using low-cost large-area production techniques like roll-to-roll processing, making OPV a promising candidate for future applications. Organic solar cells consist of a photoactive layer commonly sandwiched between a transparent and a reflective electrode. In contrast to solar cells using crystalline materials, the absorber layer in OPV is a mixture of at least two materials. This is mandatory since an electron-hole pair is strongly bound after photogeneration. The splitting of this bound pairs takes place at the interface of the two materials, where the electron is transferred from the so-called donor material to the acceptor material while the hole remains in the donor phase. The separated charge carriers can be extracted at their respective electrodes. An interpenetrating network of the mixed materials is referred to as bulk-heterojunction. Figure 0.1 illustrates schematically a typical bulk-heterojunction organic solar cell. The PCE of such cells was recently improved to 12.1 % for a single junction cell [8] and to 17.3 % for a tandem cell [9]. These advances have been achieved by improved chemical synthesis of donor and acceptor materials with higher absorption

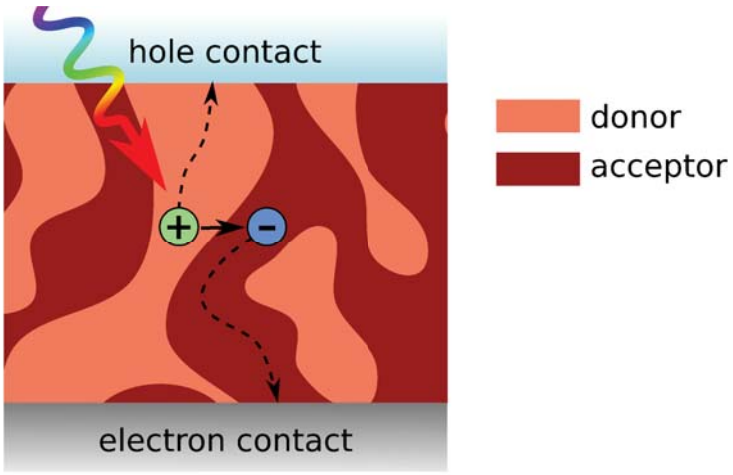

Figure 0.1: Schematic illustration of a bulk-heterojunction organic solar cell.

coefficients and beneficial band gap engineering as well as by the development of novel interfacial materials to increase selectivity. In addition, promising long time stability with cell lifetimes > 10 years from accelerated aging under standard conditions has been reported [10–13] and a large scale application was demonstrated when organic PV has been integrated into the rooftop of the German pavilion at the world expo in 2015 [14]. However, the achieved PCE is so far not competitive to commercially available technologies like e.g. crystalline silicon solar cells. Hence, its improvement is still a key challenge in OPV research and development.

Motivation and Scope of this Thesis

The photovoltaic power conversion efficiency η of solar cells is determined by

$$\eta = \frac{J_{\mathrm{SC}} V_{\mathrm{OC}} FF}{P_{\mathrm{in}}}$$

where J_{SC} is the short-circuit current density, V_{OC} is the open-circuit voltage, FF is the fill factor, and P_{in} is the incident power density. Efficiencies for the extraction of an electron-hole pair for each absorbed photon of 70 % to nearly 100 % are commonly observed for organic solar cells [15–17]. Therefore, the J_{SC} is usually good for a given absorption spectrum in OPV. The latter holds true for the fill factor, for which good values of $FF > 0.8$ are no exception. In contrast, typically observed voltages under open-circuit conditions of $(0.6 - 1.0)$ V are about $(0.7 - 1.4)$ eV lower than the optical band gap [18]. This implies that more than half of the energy of an absorbed photon is commonly lost. It gets obvious that the rather low V_{OC} for the comparably high absorption band edge is the main limiting factor for the PCE in OPV. In order to improve V_{OC} it is essential to develop a thorough understanding of mechanisms and material properties that contribute to the V_{OC} of organic solar cells. This covers energy losses from recombination of electrons and holes and the knowledge about the energy of the relevant states in the donor-acceptor systems. This work aims to contribute to a better understanding of significant effects and material properties through detailed characterization of recombination processes and their effects on V_{OC} in organic solar cells.
The thesis is structured in five chapters. This introduction is followed by chapter II, where the necessary theoretical background is introduced and fundamentals of semiconductor physics, general photovoltaics, organic semiconductors and donor-acceptor systems of bulk-heterojunction solar cells are explained. Chapter III deals with the

used materials, sample preparation, the measurement setups and the numerical and experimental methods applied in this work. Those introductory parts are followed by the experimental results and their discussion in chapter IV. This chapter comprises of four thematic blocks. The first study focuses on charge extraction from organic solar cells and examines the capacitance of organic solar cells and its impact on transient electrical characterization. After these considerations the recombination of free charge carriers in the absorber layer is determined. The second study examines additional recombination losses, due to poor selectivity of contacts in organic semiconductors with rather poor transport properties. The gained insights are transferred and expanded in the third study about the temperature dependence of V_{OC}. In the last study the energetic states, involved in recombination of electrons and holes, are investigated by luminescence spectroscopy and the results are compared to the previously obtained values and to literature. Finally, a summary of all results is given in chapter V.

Chapter II

Fundamentals

In this chapter the essential fundamentals of semiconductor physics, needed to understand the presented experimental results are introduced, mainly based on the books of P. Würfel [19], J. Nelson [20] and C. Kittel [21]. Further the relevant processes within organic semiconductors and working principle of organic solar cells are discussed. Most of the relevant theory about organic materils can be found in the textbooks of M. Schwörer [22] and U. Würfel, M. Thorwart and E. Weber [23].

1 Physics of Semiconductors

The efficient conversion of light to electric power in the field of photovoltaics is realized using semiconducting materials. If two atoms are brought in close proximity the energy levels of individual atoms split up, due to a partial overlap of atomic wave functions of electrons. For N atoms, N slightly shifted energetic levels form. For the quasi infinite number of atoms in a solid materials, the energy difference between the single levels gets so small that a quasi continuum is formed. This continuous density of states (DOS) is called a band. Dependent on the energy of the band, the states can be occupied and contribute to the chemical bonding of the material. The band lowest in energy, which is fully occupied at a temperature (T) of 0 K is called valence band (VB), while the lowest unoccupied band is called conduction band (CB). The energetic distribution and thus occupation of these bands depends on the atomic structure and composition of the solid. In a metal, the VB is only partially filled or overlaps with the CB which is

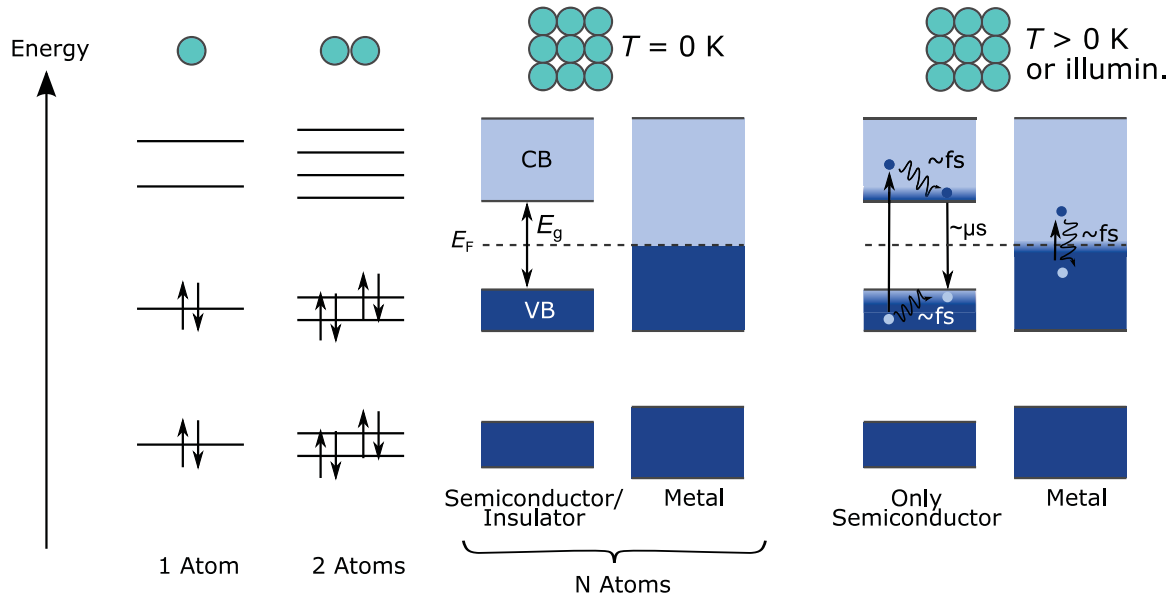

Figure 1.1: Schematic illustration of the energy of electronic states for different numbers of atoms (indicated in light green) from states of single atoms all the way to the formation of energetic bands (blue) for a large number of interacting atoms (N). In case of bands the occupied states are indicated in dark blue, while empty states are colored in light blue. In addition the Fermi energy E_F, giving the energy of the state with an occupation probability of 1/2. Furthermore the characteristic lifetimes of thermalization and excited electrons are indicated. Modified from [18] after [20].

depicted in figure 1.1. In a metal electrons can be easily excited into the continuum of higher energetic, unoccupied states. At the same time, excited electrons can rapidly relax back to their relaxed state on a femtosecond time scale called thermalization. There the excitation energy is dissipated into lattice vibrations i.e. phonons. The very fast thermalization processes make an extraction of excited charges in metals challenging and a technology featuring hot charge carrier extraction with reasonable efficiency has thus far not been developed. In case of semiconductors the VB is fully occupied at 0 K while the CB is unoccupied. At the same time these materials have a distinct energetic gap, called band gap E_g, between VB and CB illustrated in figure 1.1. When electrons are excited into the CB the band gap acts as a barrier for thermalization. As a result the lifetime of electrons in the CB is strongly enhanced to the µs to ms range. This enables the utilization of semiconductors for photovoltaic energy conversion. In the case of excitation of the semiconductor with photons of frequency ν, their energy has to exceed the gap energy ($h\nu \geq E_g$, with h being the Planck constant).

1.1 Semiconductor in the Dark

Electrons are fermions, since they feature a quantum mechanical spin of $\frac{1}{2}$. Thereby they obey the Pauli exclusion principle, i.e. every unique state can only be occupied by one electron at the same time. Thus, at a temperature of 0 K, the electrons will occupy the lowest available energetic states of the DOS up to a certain energy. For higher energies all states are empty. At a non zero temperature the electrons possess an average kinetic energy of $\frac{3}{2}k_\mathrm{B}T$ (k_B is the Boltzmann constant), resulting in the occupation of higher energetic states. In that case the DOS will be occupied in the way that the Helmholtz free energy F is minimized.

$$F = E_\mathrm{e} - TS \tag{1.1}$$

Here E_e is the energy of the electrons and S the entropy. The depicted Fermi energy E_F in figure 1.1 is a statistical quantity, giving the energy of the state which is occupied with a probability of $\frac{1}{2}$ while states lower in energy are occupied with a higher probability and higher energetic states are less likely filled. Since E_F is a statistical number an actual state with precisely this energy does not necessarily exist. At thermodynamic equilibrium, with no currents flowing inside the material, the occupation probability of the DOS for fermionic electrons is described by Fermi-Dirac statistics and is given by the temperature dependent Fermi function $f_\mathrm{F}(E)$.

$$f_\mathrm{F}(E) = \frac{1}{\exp\left(\frac{E-E_\mathrm{F}}{k_\mathrm{B}T}\right)+1} \tag{1.2}$$

For an Energy $E = E_\mathrm{F}$ the Fermi function gives an occupation probability of $\frac{1}{2}$ in accordance to the definition of the Fermi energy. For an intrinsic semiconductor in the dark the Fermi energy is located in the middle of the band gap. It is depicted for different temperatures in figure 1.2. The density of electrons n_e in the conduction band can be calculated by integration of the product of the density of states for electrons $D(E_\mathrm{e})$ and the occupation number given by the Fermi function:

$$n_\mathrm{e} = \int_{E_\mathrm{CB}}^{\infty} D(E_\mathrm{e}) f_\mathrm{F}(E_\mathrm{e}) dE_\mathrm{e} \tag{1.3}$$

E_CB is the lower energetic edge of the CB. The upper integration boarder is set to infinity here. This is valid in this case since the Fermi distribution converges exponentially to zero for rising energies, while the used DOS just rises with the square root of the electron energy as discussed in the following. In case of free electrons described by Bloch waves

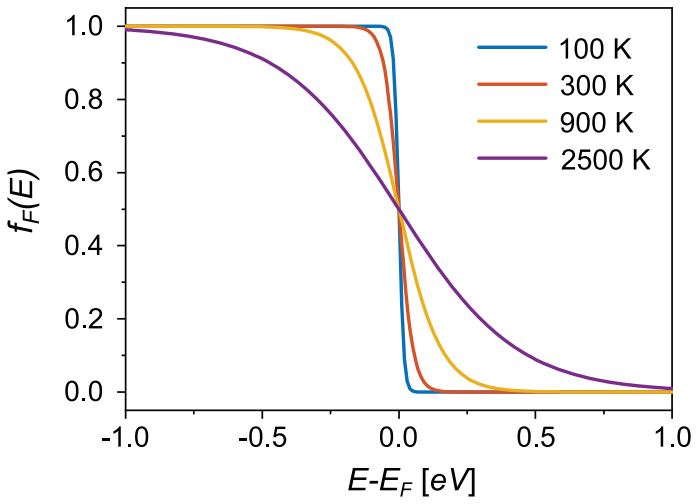

Figure 1.2: Fermi distribution for different temperatures. $f_{\mathrm{F}}(E)$ gives the occupation probability of a state with energy E.

with a wave vector $\vec{k}$, $D(E_{\mathrm{e}})$ is proportional to the square root of E_{e}. A detailed derivation from the Heisenberg's uncertainty relation for position and momentum and the dispersion relation for electron energy $E_{\mathrm{e}}(\vec{k})$ is given in [19] and can be expressed as:

$$D(E_{\mathrm{e}}) = 4\pi\left(\frac{2m_{\mathrm{e}}^*}{h^2}\right)^{\frac{3}{2}}(E_{\mathrm{e}} - E_{\mathrm{CB}})^{\frac{1}{2}} \tag{1.4}$$

Here m_{e}^* is the effective mass, that an electron seems to possess when moving through the periodic lattice, which differs from the electrons mass m_{e} measured in vacuum. For this DOS the solution of equation (1.3) including the Fermi-Dirac integral ($F_{1/2}$) of order $\frac{1}{2}$ which can not be solved analytically. However the Fermi function converges to zero for energies higher than E_{F} as can be seen from figure 1.2. For $E_{\mathrm{F}} - E_{\mathrm{e}} >> 3k_{\mathrm{B}}T$ it can be approximated by the Boltzmann distribution [20, 24]. This can be described figuratively by the fact, that for the low occupation probabilities at this energies electrons always find a free state within the DOS. Thus we do not have to account for the Pauli exclusion principle and Boltzmann statistics can be used. Since in an intrinsic semiconductor at thermodynamic equilibrium the Fermi energy is located in the middle of the band gap (assuming identical effective masses for electrons and holes), $E_{\mathrm{F}} - E_{\mathrm{e}} \geq \frac{E_{\mathrm{g}}}{2} >> 3k_{\mathrm{B}}T$ is reasonable and we can write equation (1.3) using (1.4) as:

$$n_{\mathrm{e}}^0 = 2\left(\frac{2\pi m_{\mathrm{e}}^* k_{\mathrm{B}}T}{h^2}\right)^{\frac{3}{2}} \exp\left(-\frac{E_{\mathrm{CB}} - E_{\mathrm{F}}}{k_{\mathrm{B}}T}\right) = N_{\mathrm{C}} \exp\left(-\frac{E_{\mathrm{CB}} - E_{\mathrm{F}}}{k_{\mathrm{B}}T}\right) \tag{1.5}$$

giving the intrinsic hole density n_e^0 in the dark. N_C is the effective density of states, which is a material specific quantity, dependent on $D(E)$. In an actual semiconductor the Fermi energy in the dark is not exactly in the middle of the band gap since $m_\mathrm{e}^* \neq m_\mathrm{h}^*$, nevertheless the approximation is valid. The probability of finding an unoccupied state in the VB, i.e. the occupation probability of holes, is given by $1 - f_\mathrm{F}(E) = f_\mathrm{F}(-E)$. The intrinsic hole concentration n_h^0 in Boltzmann approximation is given by

$$n_\mathrm{h}^0 = N_\mathrm{V} \exp\left(-\frac{E_\mathrm{F} - E_\mathrm{VB}}{k_\mathrm{B}T}\right) \tag{1.6}$$

with E_VB being the upper energetic edge of the valence band and N_V the effective density of states analog to N_C. From the multiplication of equation (1.5) and (1.6) we get the square of the intrinsic charge carrier density n_i

$$n_\mathrm{e}^0 n_\mathrm{h}^0 = n_\mathrm{i}^2 = N_\mathrm{C} N_\mathrm{V} \exp\left(-\frac{E_\mathrm{g}}{k_\mathrm{B}T}\right) \tag{1.7}$$

which is independent of the position of the Fermi energy. In figure 1.3 the band structure, the density of states $D(E_\mathrm{e})$, the Fermi distribution and the resulting intrinsic electron and hole densities n_e^0 and n_h^0 are depicted. The intrinsic charge carrier density consists

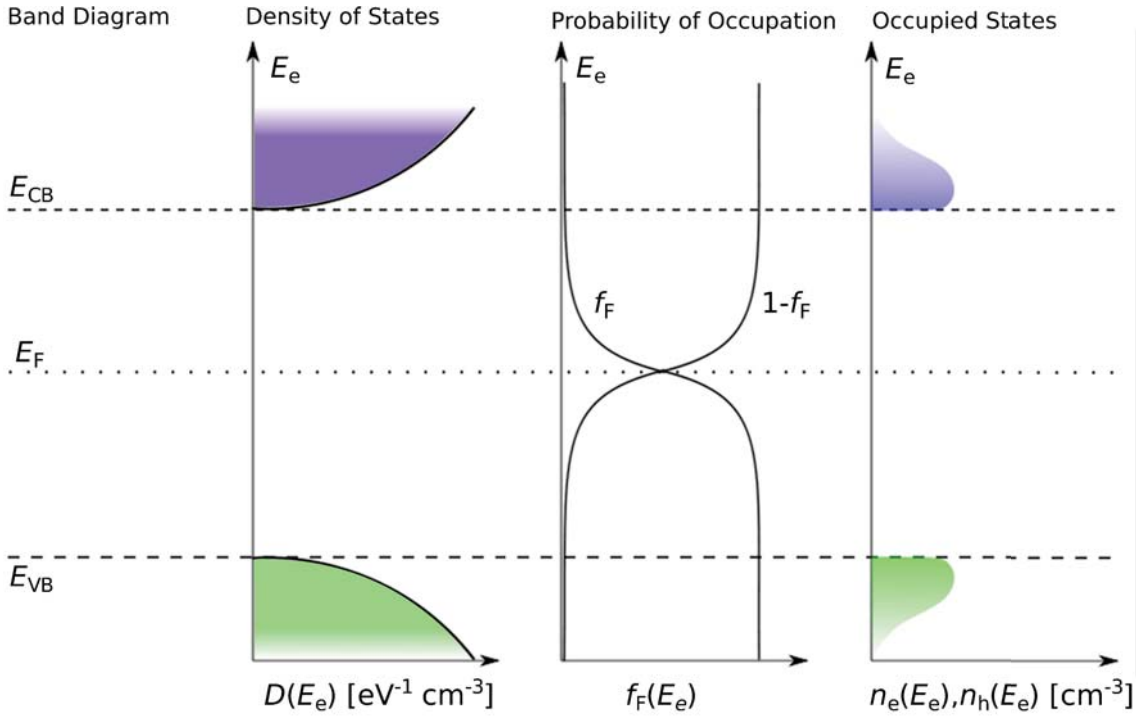

Figure 1.3: Illustration of the band diagram, the density of states $D(E_\mathrm{e})$, the probability of occupation given by the Fermi function $f_\mathrm{F}(E_\mathrm{e})$ and the electrons and hole densities $n_\mathrm{e}(E_\mathrm{e})$ and $n_\mathrm{h}(E_\mathrm{e})$ versus the electron energy E_e. Modified from [25].

of the electrons and holes generated at thermodynamic equilibrium by absorption of the thermal background radiation of the environment. The dark generation rate G_0 can be calculated by

$$G_0 = \int_0^\infty \alpha(h\nu) j_\gamma^0(h\nu) dh\nu = \frac{2\,\Omega}{c^2} \int_0^\infty \frac{\alpha(h\nu)\nu^2}{\exp\left(\frac{h\nu}{k_\mathrm{B}T_0}\right) - 1} d\nu \tag{1.8}$$

using the absorption coefficient $\alpha(h\nu)$ which depend on the photon energy $E_\gamma = h\nu$ of a photon of frequency ν, $j_\gamma^0 = j_\gamma(T = T_0)$ represents the photon flux emitted by a black body (Planck spectra) at (equilibrium) temperature T_0, Ω is the solid angle within which photons are exchanged ($\Omega = 4\pi$ for full solid angle) and $c = \frac{c_0}{n}$ the speed of light in the media, calculated by the vacuum speed of light c_0 and the refractive index n of the media. A comprehensive derivation of $j_\gamma(T)$ using Bose-Einstein statistics and the DOS for photons can be found in [19]. At equilibrium with no current flowing the same number of electrons and holes which are generated per time have to recombine, i.e. the dark generation rate equals the dark recombination rate $G_0 = R_0$. Using the concept of detailed balance, where every process is exactly balanced by its inverse process, all charge carriers diminish by the inverse effect of absorption, i.e. radiative recombination. Thereby, electrons and holes recombine pairwise and the recombination rate is

$$R = k_\mathrm{r} n_\mathrm{e} n_\mathrm{h} \tag{1.9}$$

due to the law of mass action with the recombination coefficient k_r[22, 24] resulting in:

$$G_0 = R_0 = k_\mathrm{r} n_\mathrm{e}^0 n_\mathrm{h}^0 = k_\mathrm{r} n_\mathrm{i}^2 = k_\mathrm{r} N_\mathrm{C} N_\mathrm{V} \exp\left(-\frac{E_\mathrm{g}}{k_\mathrm{B}T_0}\right) \tag{1.10}$$

So the square of the intrinsic charge carrier density in case of solely radiative recombination is:

$$n_\mathrm{i}^2 = \frac{G_0}{k_\mathrm{r}} \tag{1.11}$$

1.2 Doping

Doping is the process of (intentionally) introducing impurity atoms in a semiconductor during production resulting in an extrinsic semiconductor. This can be either done by using electron donor (D) or electron acceptor (A) atoms. Doping with D atoms is called n-doping and doping with A atoms is called p-doping. A donor atom has more valence electrons than required for binding in the prevalent semiconductor lattice, thus

the excess electron is not part of a covalent bond. Due to polarization of the neighboring atoms it remains only weakly bound to the D atom. This results in an occupied energetic state E_D closely beneath the band edge of the conduction band. Typically the D atoms can easily be ionized at room temperature, releasing the electron into the CB. Acceptor atoms in analogy easily accept an electron, i.e. release a hole, while the corresponding energy level E_A is slightly higher in energy than the VB edge. For a donor atom density of n_D or acceptor density n_A, under the assumption of complete ionization, the density of free equilibrium charge carriers inside the corresponding band are $n_\mathrm{e}^0 = n_\mathrm{i} + n_\mathrm{D} \approx n_\mathrm{D}$ or $n_\mathrm{h}^0 = n_\mathrm{i} + n_\mathrm{A} \approx n_\mathrm{A}$ respectively. The Fermi energies of the extrinsic semiconductor are

$$E_\mathrm{F}^\text{n-doping} = E_\mathrm{CB} - k_\mathrm{B}T \ln\left(\frac{N_\mathrm{C}}{n_\mathrm{D}}\right)$$

for n-doping where the Fermi energy moves towards E_E and

$$E_\mathrm{F}^\text{p-doping} = E_\mathrm{VB} + k_\mathrm{B}T \ln\left(\frac{N_\mathrm{V}}{n_\mathrm{A}}\right)$$

for p-doping in which case the Fermi energy is closer to E_VB. It is important to note that equation (1.7) still holds true and the product $n_\mathrm{e}^0 n_\mathrm{h}^0 = n_\mathrm{i}^2$ can not be changed by doping. This implies that a semiconductor can only be either n-doped or p-doped. For e.g. n-doping the hole concentration is strongly reduced and vice versa for p-doping. The species which is enhanced by the doping is commonly referred to as majority charge carrier while the reduced one is called minority charge carrier.

1.3 Semiconductor under Illumination

Under illumination electrons and holes are generated pairwise by the absorption of photons with energies higher than the band gap ($h\nu \geq E_\mathrm{g}$) which is depicted in figure 1.4a. The generation rate of electrons and holes, i.e. the rate of absorbed photons for a given photon flux $j_\gamma(h\nu)$ can be calculated analogously to equation (1.8). We imagine an intrinsic semiconductor illuminated by a Planck spectrum corresponding to the temperature of e.g. the sun ($T_\mathrm{sun} \approx 5800\,\mathrm{K}$). The generation rate $G(T = T_\mathrm{sun})$ is given analog to equation (1.8). At thermodynamic equilibrium the semiconductor is at the same temperature as the sun ($T_\mathrm{SC} = T_\mathrm{sun}$) and would possess an intrinsic charge carrier density $n_\mathrm{i}(T_\mathrm{sun})$ according to equation (1.7) while the Fermi energy of the system would still be located in the middle of the band gap. This scenario is illustrated in figure 1.4b. It is worth to mention here, that under these conditions no energy can be gained

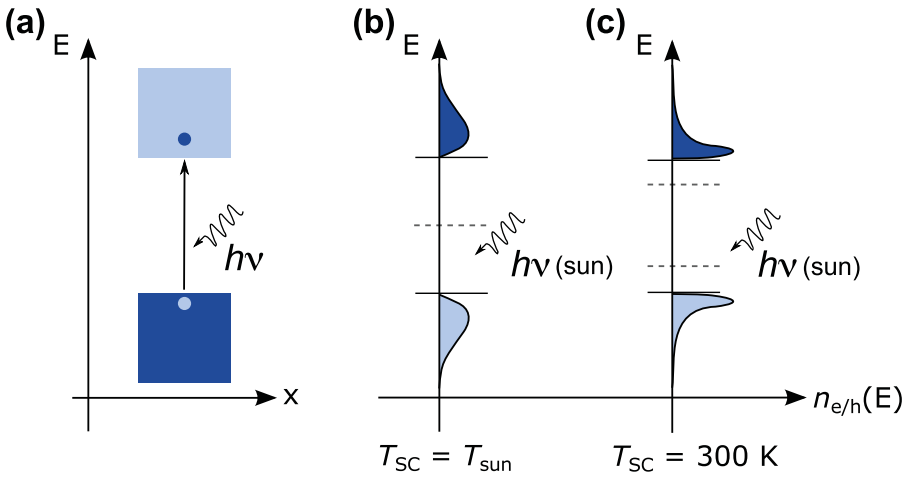

Figure 1.4: **(a)** Absorption of a photon with an energy of $h\nu > E_g$. An electron is excited into the conduction band (light blue) leaving an hole in the valence band. **(b)** and **(c)**: Distribution of electrons in the conduction band (dark blue) and of holes in the valance band (light blue) under illuminatin with sun light given by black body radiation at T_{sun}. For the case of thermodynamic equilibrium when the semiconductor is at a temperature of $T_{SC} = T_{sun}$ (b) and after thermalization for a semiconductor in equilibrium with the environment at $T_{SC} = 300$K (c). Modified from [18] based on [19].

from a semiconductor in an PV application. This gets obvious by the second law of thermodynamics. It implies the Carnot efficiency η_C to be the maximum efficiency for any device converting heat into (entropy-free) electric energy. In the discussed case of thermodynamic equilibrium it is $\eta_C = 1 - \frac{T_{sun}}{T_{sun}} = 0$. If the semiconductor is kept at a lower temperature, e.g. $T_{sun} > T_{SC} = 300\,\mathrm{K}$, the generated electrons and holes thermalize towards the band edges of the corresponding DOS. This is illustrated in figure 1.4c. The resulting electron density in the CB is higher than the intrinsic density $n_i(T = 300K)$ under equilibrium in the dark. Therefore the Fermi energy is shifted towards E_{CB} (analogously to the case of n-doping discussed before). At the same time the Fermi energy has to be located closer to E_{VB}, due to the enhanced hole concentration. This conflict leads to the concept of quasi-Fermi level (QFL) for the case of non equilibrium conditions ($T_{sun} \neq T_{SC}$), to accurately describe electrons and holes at the same time. The QFL $E_{F,CB}$ and $E_{F,VB}$ for electrons in the CB and VB are given by

$$E_{F,CB} = E_{CB} - k_B T \ln\left(\frac{N_C}{n_e}\right)$$
$$E_{F,VB} = E_{VB} + k_B T \ln\left(\frac{N_V}{n_h}\right).$$

The QFL energy $E_{\mathrm{F,CB}}$ is the electrochemical potential of electrons η_{e} and $E_{\mathrm{F,VB}}$ resembles the negative electrochemical potential $-\eta_{\mathrm{h}}$ of holes [19]. The difference of the QFL is called quasi-Fermi level splitting. It is

$$E_{\mathrm{F,CB}} - E_{\mathrm{F,VB}} = \eta_{\mathrm{e}} + \eta_{\mathrm{h}} = \mu_{\mathrm{chem,e}} - e_0\varphi + \mu_{\mathrm{chem,h}} + e_0\varphi = \mu_{\mathrm{chem,e}} + \mu_{\mathrm{chem,h}} \tag{1.12}$$

with the electric potential φ and the sum of the chemical potentials of electrons end holes $\mu_{\mathrm{chem,e}} + \mu_{\mathrm{chem,h}}$. This chemical energy given by the QFL splitting is the free energy of electrons and holes (free of entropy) and thus the maximum energy which can be gained from an electron-hole pair in any solar cell. Therefore the QFL splitting is key, since it translates into the maximum voltage which can be ideally obtained at the electrodes of a solar cell. It will be referred to as internal voltage V_{int} and it is given by

$$\begin{aligned} e_0 V_{\mathrm{int}} &= E_{\mathrm{F,CB}} - E_{\mathrm{F,VB}} = E_{\mathrm{CB}} - E_{\mathrm{VB}} - k_{\mathrm{B}}T \ln\left(\frac{N_{\mathrm{C}}N_{\mathrm{V}}}{n_{\mathrm{e}}n_{\mathrm{h}}}\right) \\ e_0 V_{\mathrm{int}} &= E_{\mathrm{g}} - k_{\mathrm{B}}T \ln\left(\frac{N_{\mathrm{C}}N_{\mathrm{V}}}{n_{\mathrm{e}}n_{\mathrm{h}}}\right). \end{aligned} \tag{1.13}$$

The product of electron and hole densities can be written as

$$n_{\mathrm{e}}n_{\mathrm{h}} = N_{\mathrm{C}}N_{\mathrm{V}} \exp\left(\frac{e_0 V_{\mathrm{int}} - E_{\mathrm{g}}}{k_{\mathrm{B}}T}\right) \tag{1.14}$$

1.4 Generation, Recombination and Transport of Charge Carriers

The charge carriers in a semiconductor satisfy a continuity equation as consequence of charge conservation. It describes the time dependency of the charge carrier density in a volumen element dV for electrons or holes at position x. The carrier density $n_{\mathrm{e,h}}$ gets higher when charge carriers are generated, and lower when they recombine or flow out of dV. The continuity equations for electrons and holes are given by

$$\frac{\partial n_{\mathrm{e}}(x)}{\partial t} = G_{\mathrm{e}}(x) - R_{\mathrm{e}}(x) - \operatorname{div} j_{\mathrm{e}}(x) \tag{1.15}$$

$$\frac{\partial n_{\mathrm{h}}(x)}{\partial t} = G_{\mathrm{h}}(x) - R_{\mathrm{h}}(x) - \operatorname{div} j_{\mathrm{h}}(x) \tag{1.16}$$

with the generation rates $G_{\mathrm{e/h}}$, recombination rates $R_{\mathrm{e/h}}$ and particle current densities $j_{\mathrm{e/h}}$ for electrons and holes respectively. All current densities in this work describe a flux in x direction (perpendicular to the electrodes). The described systems are assumed to be spatially homogeneous in the directions y and z in plane with the electrodes

(div j equals $\frac{\partial}{\partial x} j$ in one dimension). Due to a pairwise generation of electrons and holes $G_\mathrm{e}(x) = G_\mathrm{h}(x) = G(x)$ will be used in the following. The introduced concept is schematically illustrated in figure 1.5. Here, ϵ_0 and ϵ_r are the vacuum and relative permittivity of the medium and ρ the space charge density. The Poisson equation gives the relation of charge density and electric field leading to a coupling of drift and diffusion in case of charged particles. The continuity equations for electrons and holes are coupled by Poisson's equation

$$\frac{\partial^2 \varphi(x)}{\partial x^2} = -\frac{e_0}{\epsilon_\mathrm{r}\epsilon_0} \left(n_\mathrm{h}(x) - n_\mathrm{e}(x) + \rho(x) \right). \tag{1.17}$$

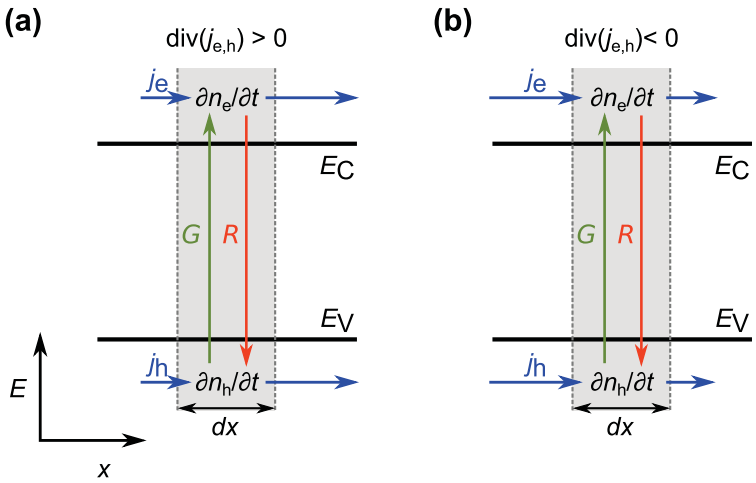

Figure 1.5: Schematic illustration of the contributions to the continuity equation, which describes the temporal change in charge carrier density $\frac{\partial n}{\partial t}$. The generation rate G (green arrows), recombination rate R (red arrows) and electron and hole current densities $j_\mathrm{e,h}$ (blue arrows). In **(a)** the case for $\mathrm{div}(j_\mathrm{e,h}) > 0$ when a current is sourced within the length element dx . In **(b)** the element dx sinks a current ($\mathrm{div}(j_\mathrm{e,h}) < 0$).

1.4.1 Generation

The generation rate $G(x)$ is given by the integral of the product of photon current density and absorption coefficient over all photon energies, according to equating (1.8). The overall generation within a device can be calculated by the integral of $G(x)$ over the thickness d of the absorber. The corresponding photogenerated electric current density J_gen is given by:

$$J_\mathrm{gen} = e_0 \int_0^d G(x) dx \tag{1.18}$$

1.4.2 Recombination

The most fundamental recombination mechanism is radiative or direct recombination under the emission of a photon depicted in figure 1.6(a). It is a fundamental recombination pathway and unavoidable since it is the inverse effect of absorption and absorbtivity equals emissivity ($\alpha_\lambda = \epsilon_\lambda$) according to Kirchhoff's law. Thus exclusively radiative recombination represents the most ideal case. The recombination rate of direct recombination is given by equation (1.9). It is proportional to the product of electron and hole density or n^2 in case of equally large concentrations. The exponent is commonly referred to as reaction or recombination β which is 2 for direct recombination. Often, nonradiative recombination with $\beta = 2$ is prevalent, which is frequently called bimolecular recombination in the field of organic solar cells. In general, other recombination mechanisms with different reaction order will exist or be predominant and a more general recombination rate is given by

$$R = k_\mathrm{r} \left(n_\mathrm{e} n_\mathrm{h}\right)^{\frac{\beta}{2}} \tag{1.19}$$

Figure 1.6(b) illustrates the nonradiative mechanism of Shockley-Read-Hall (SRH) or trap assisted recombination [26]. For this an energetic state is located within the band gap. It gets occupied with either an electron or a hole, depending on the energetic position in respect to the band edges. The captured charge carrier, e.g. an electron from the CB stays trapped until it gets emitted in the VB which is equivalent to the capture of an hole. The recombination over trap states is most efficient if they are located in the middle of the band gap which is commonly referred to as deep trap or recombination center. Then the product of the rates for capturing electrons and holes is highest. In

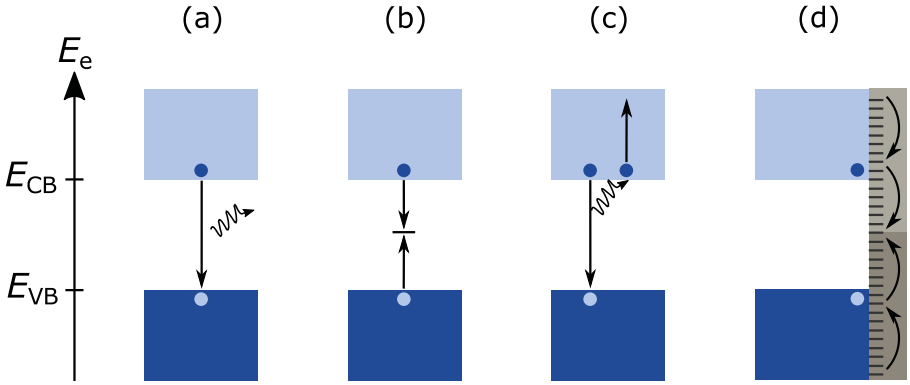

Figure 1.6: Recombination mechanisms of electrons and holes in semiconducting materials. **(a)** Direct or bimolecular recombination under the emission of a photon, **(b)** Trap assisted or monomolecular recombination, **(c)** Auger recombination and **(d)** surface recombination. From [18].

case of shallow traps close to a band edge the probability for the release of a trapped charge carrier is high which is called detrapping. SRH recombination is of reaction order $\beta = 1$.
In case of Auger recombination the energy released during the recombination of an electron-hole pair excites a third, free charge carrier, e.g. an electron, to a higher energetic state within the CB. The process is illustrated in figure 1.6(c). The energy is then dissipated as this electron thermalizes back to the conduction band edge. Thus Auger recombination is an nonradiative process. Since it is a three-particle process it gets more significant for high charge carrier densities and the reaction order is $\beta = 3$.
A further relevant recombination pathway is via energetic states within the band gap located at the surface of a semiconductor. In general, they can result from dangling bonds or impurities at the interface where the lattice ends or by a quasi-continuous density of states, e.g. if the semiconductor is in contact with a metal electrode. In analogy to the photogenerated current density (equation (1.18)) the electric recombination current density can be calculated by:

$$J_{\mathrm{rec}} = e_0 k_{\mathrm{r}} \int_0^d R(x)dx = e_0 k_{\mathrm{r}} \int_0^d \left(n_{\mathrm{e}}(x) n_{\mathrm{h}}(x)\right)^{\frac{\beta(x)}{2}} dx \tag{1.20}$$

A more comprehensive description of surface recombination will be discussed in 1.5 while detailed discussion on specific recombination mechanisms in organic materials will be given in chapter 2.

1.4.3 Transport

In this section the driving forces for charge carrier transport are explained and the corresponding material parameters are introduced.

Drift Current: The term drift current is used to describe a current solely driven by an electric field. For a constant electric field $\vec{E}$, being the only driving force, a charge carrier will move with a constant drift-velocity $\vec{v}$ through a medium with

$$\vec{v} = \mu \vec{E}.$$

The proportionality coefficient μ is the material specific mobility. The electric field is defined in the way that holes drift with the field while electrons move opposite to its

direction. The total electric drift current $J_{\text{drift, e/h}}$ (in one dimension) is described by the microscopic Ohm's law

$$J_{\text{drift}} = e_0(n_\text{e} v_\text{e} + n_\text{h} v_\text{h}) = e_0(n_\text{e}\mu_\text{e} + n_\text{h}\mu_\text{h})E = (\sigma_\text{e} + \sigma_\text{h})F = \sigma E$$

Here, σ is the total conductivity of the system and $\sigma_\text{e} = e_0 n_\text{e}\mu_\text{e}$ and $\sigma_\text{h} = e_0 n_\text{h}\mu_\text{h}$ the electron and hole conductivity. With the electric field being the gradient of the electric potential $E = -\operatorname{grad}(\varphi)$ the individual drift currents $J_{\text{drift,e/h}}$ for electrons and holes are given by:

$$\begin{aligned} J_{\text{drift,e}} &= \frac{\sigma_\text{e}}{e_0}\operatorname{grad}(-e_0\varphi) \\ J_{\text{drift,h}} &= -\frac{\sigma_\text{h}}{e_0}\operatorname{grad}(e_0\varphi). \end{aligned}$$

Diffusion Current: A current is referred to as diffusion current when it is driven by gradients in concentration, i.e. the chemical potential μ_{chem} according to Fick's law

$$\begin{aligned} J_{\text{diff,e}} &= e_0 D\operatorname{grad}(n_\text{e}) = \mu_\text{e} k_\text{B} T\operatorname{grad}(n_\text{e}) = \frac{\sigma_\text{e}}{e_0}\operatorname{grad}(\mu_{\text{chem,e}}) \\ J_{\text{diff,h}} &= -e_0 D\operatorname{grad}(n_\text{h}) = -\mu_\text{h} k_\text{B} T\operatorname{grad}(n_\text{h}) = -\frac{\sigma_\text{h}}{e_0}\operatorname{grad}(\mu_{\text{chem,h}}) \end{aligned}$$

The diffusion coefficient D and the charge carrier mobility are correlated by the Einstein–Smoluchowski relation

$$D = \frac{k_\text{B} T}{e_0}\mu$$

Total Current: The total current is given by the sum of the drift and diffusion current by:

$$J_\text{e} = J_{\text{drift,e}} + J_{\text{diff,e}} = \frac{\sigma_\text{e}}{e_0}\operatorname{grad}(\mu_{\text{chem,e}} - e_0\varphi) = \frac{\sigma_\text{e}}{e_0}\operatorname{grad}(\eta_\text{e}) \tag{1.21}$$

$$J_\text{h} = J_{\text{drift,h}} + J_{\text{diff,h}} = -\frac{\sigma_\text{h}}{e_0}\operatorname{grad}(\mu_{\text{chem,h}} + e_0\varphi) = -\frac{\sigma_\text{h}}{e_0}\operatorname{grad}(\eta_\text{h}) \tag{1.22}$$

With $\eta_{\text{e/h}}$ being the electrochemical potential of electrons and holes respectively. It should be noted here, that the previous summation over drift and diffusion current should not be misinterpreted. In case of equally strong gradients in the electrical $(-e_0\varphi)$ and chemical potentials in opposite direction the average driving forces on electrons cancel out and no current will be driven, in contrast to equally large but opposite currents. Figure 1.7 schematically illustrates the situation in an energy diagram where

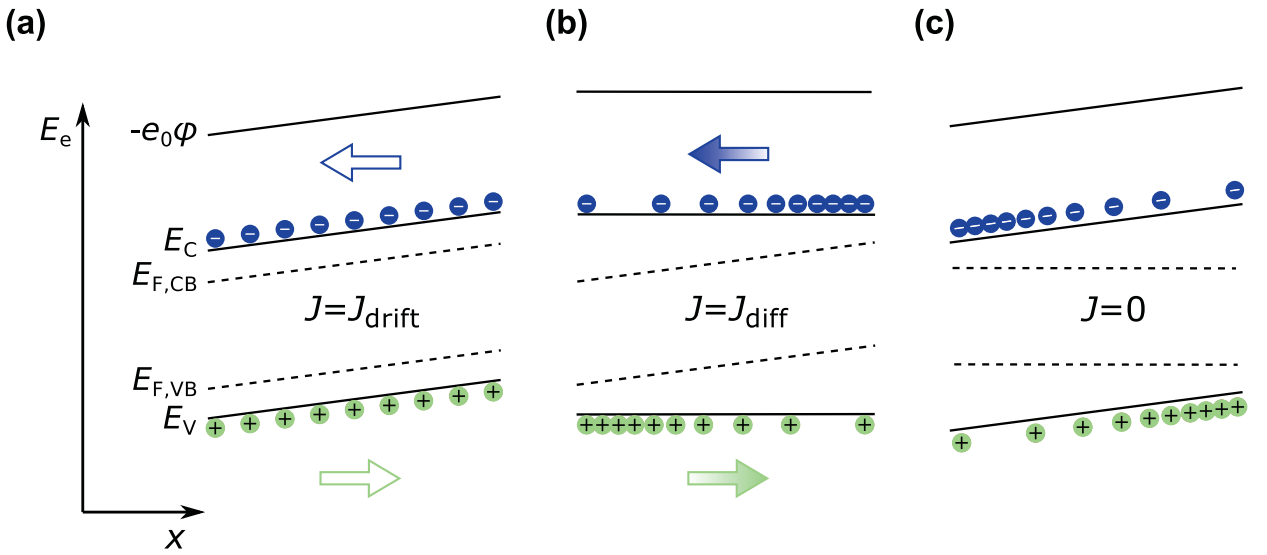

Figure 1.7: Scheme of the enrgy diagram for **(a)** a pure drift current, **(b)** a pure diffusion current and **(c)** the situation where the gradients in electric and chemical potential cancel out and no current is driven. Modified from [18].

the gradients in electric and chemical potential keep balance with no resulting current. In addition, a pure drift and a pure diffusion current with the corresponding bands is depicted. The driving force for a current is the gradient in $\eta_{e/h}$ which is given by the quasi-Fermi energy $E_{F,CB} = \eta_e$ or $E_{F,VB} = -\eta_h$ of the respective charge carrier. Thus the total electric current density is given by the sum of electron- and hole-current

$$J = J_e + J_h = \frac{\sigma_e}{e_0}\,\mathrm{grad}(\eta_e) - \frac{\sigma_h}{e_0}\,\mathrm{grad}(\eta_h) = \frac{\sigma_e}{e_0}\,\mathrm{grad}(E_{F,CB}) + \frac{\sigma_h}{e_0}\,\mathrm{grad}(E_{F,VB}) \quad (1.23)$$

1.5 Selectivity and Contacts

Charge carrier selective regions play an important role in solar cells. Electrons and holes can recombine via energetic states within the band gap located at semiconductor interfaces, as discussed in section 1.4.2. Especially at metal interfaces a rapid recombination due to the quasi continuous DOS will occur. Thus, it is important to ensure that electrons and holes do not reach such an interface simultaneously to avoid surface recombination. There is a more fundamental reason why layers, or regions in general, providing charge carrier selectivity are indispensable for the working principal of solar cells. The quasi-Fermi level splitting under illumination gives the energy which can ideally be gained as electric energy from an electron-hole pair in PV, as discussed in chapter 1.3. Electric power density is given by the product of the extracted current density and the voltage at the contacts ($P_{ext} = J_{ext}V_{ext}$). Thus a preferably high voltage

has to be present at a solar cells electrodes during extraction of charge carriers. This implies that the Fermi energies of the electron and hole contact ($E_{\mathrm{F,el.cont/h.cont}}$) have to differ from each other since $e_0 V_{\mathrm{ext}} = E_{\mathrm{F,el.cont}} - E_{\mathrm{F,h.cont}}$. In the following the conditions resulting in such a situation will be discussed.

To describe the general requirements of an external voltage different from zero a semiconductor under illumination with electrodes on two sides and with external current is assumed. A schematic illustration of the relevant energy levels of a corresponding device is shown in figure 1.8. Under illumination a quasi-Fermi level splitting $e_0 V_{\mathrm{int}}$ is present inside the bulk of the semiconductor. The QFL $E_{\mathrm{F,CB}}$ and $E_{\mathrm{F,VB}}$ of electrons and holes in their respective bands coincide with the Fermi energies of the metal electrodes when brought into contact by Fermi level alignment. To do so, gradients in the QFL have to be present. Since gradients in the QFL are the driving forces for currents we consider a recombination current $J_{\mathrm{rec}} = J_{\mathrm{rec,e}} - J_{\mathrm{rec,h}}$ of electrons and holes towards one contact (while the considerations hold true in the limit of a diminishing J_{rec}). Due to pairwise recombination $|J_{\mathrm{rec,e}}|$ equals $|J_{\mathrm{rec,h}}|$. From figure 1.8 it gets obvious by symmetry conciderations that regions with unsymmetrical gradients have to exist within the device to achieve non-zero external voltage ($V_{\mathrm{ext}} \neq 0$). It can be seen from equation (1.23) that unsymmetrical gradients in the QFL require unsymmetrical conductivities for electrons

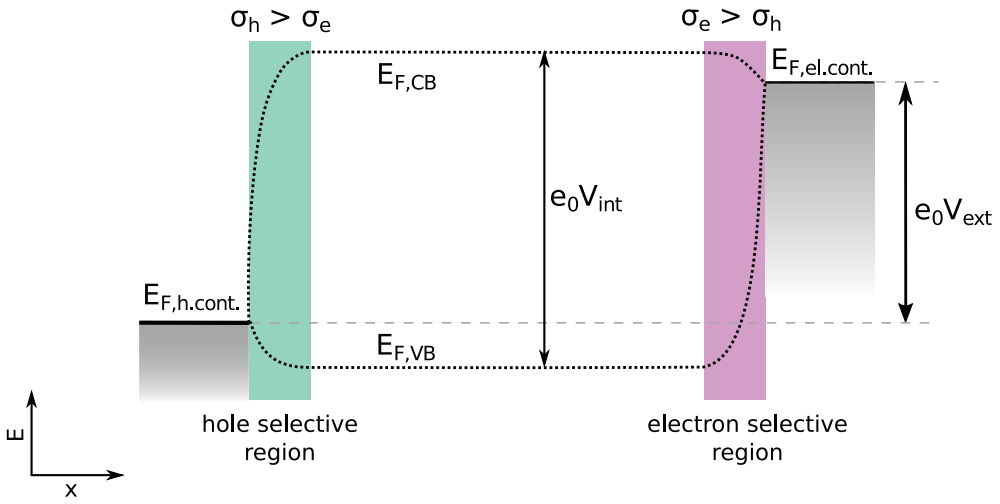

Figure 1.8: Schematic energy diagram for the quasi Fermi level $E_{\mathrm{F,CB}}$ and $E_{\mathrm{F,VB}}$ for electrons and holes in the respective band in a semiconductor under illumination. The external voltage V_{ext} is given by the difference of the Fermi energies of the contacts $E_{\mathrm{F,el.cont}} - E_{\mathrm{F,h.cont}}$. from symmetry contemplation it is obvious that regions with unsymmetrical gradients and hence unsymmetrical conductivities σ have to be present leading to the requirement of $\sigma_{\mathrm{maj}} \gg \sigma_{\mathrm{min}}$ for good selectivity. The hole selective region with $\sigma_{\mathrm{h}} > \sigma_{\mathrm{e}}$ is marked in light green and the electron selective region is colored purple.

and holes in that region to drive equally large recombination currents at open-circuit conditions. Thereby, regions with $\sigma_e > \sigma_h$ or $\sigma_h > \sigma_e$ are a necessary requirement for energy conversion to brake the symmetry within a semiconducting PV device. In general, the unbalance in conductivity can be realized in manifold ways, e.g. by using injecting contacts or charge selective interlayer, via doping like in case of p-n junction solar cells or by regions with unbalanced mobilities for electrons and holes. In the ideal case under open-circuit conditions, where the maximum voltage ($V_{ext} = V_{int}$) is obtained, no gradients in the QFL of charge carriers should exist towards their corresponding electrode. There should be no gradient in the QFL for e.g. electrons (referred to as majority carrier in this case) towards the electron contact. Würfel et al. [27] elaborated the requirement to obtain maximum voltage ($V_{ext} = V_{int}$) as

$$\sigma_{maj} \gg \sigma_{min} \tag{1.24}$$

with the conductivity σ_{maj} of majority carriers (holes in the hole selective regions and electrons in the electron selective region) and σ_{min} for the contrary carriers, respectively. In this case, the entire gradient is carried by the QFL of the minority carriers ($\operatorname{grad} E_{F,min} \gg \operatorname{grad} E_{F,maj}$), i.e. $V_{ext} = V_{int}$. While the discussed condition guarantees a diminishing gradient for majority carriers a current can still be driven by an insignificant gradient in case of high conductivity. Thus (1.24) does not guarantee zero loss of charge carriers by surface recombination. To avoid any detrimental transport of minorities to an electrode, i.e. to guarantee a negligible surface recombination current (compared to the total photogenerated current J_{gen}), the conductivity of minority charge carriers has to be small enough. This leads to a second condition for ideal selectivity:

$$J_{rec} = \frac{\sigma_{min}}{e_0} \operatorname{grad}(E_{F,min}) \ll J_{gen} \tag{1.25}$$

This ensures V_{int} is not reduced through the bulk by a recombination current to an interface.

1.5.1 Surface Recombination

The process of surface recombination, where electrons and holes recombine via states within the bang gap located at semiconductor surface or interface to a neighboring material, is described in 1.4.2. Here a more comprehensive description will be given. How fast a charge carrier finds another one of opposite polarity at a surface and recom-

bines is described by the surface recombination velocity v_{SR}. Typical values range from $v_{\mathrm{SR}} \leq 10\,\mathrm{cm\,s^{-1}}$ for a passivated silicon surface to quasi infinity for metal surfaces. A recombination of an electron from the absorber with a hole from an electrode is equivalent to an extraction. Thus, in general v_{SR} describes injection and extraction properties of electrodes as well as detrimental pairwise recombination of two photogenerated charge carriers. The surface recombination currents $J_{\mathrm{SR,e}}$ and $J_{\mathrm{SR,e}}$ are given by

$$J_{\mathrm{SR,e}} = -e_0 v_{\mathrm{SR,e}}(n_{\mathrm{e}} - n_{\mathrm{e}}^0) \tag{1.26}$$

$$J_{\mathrm{SR,h}} = e_0 v_{\mathrm{SR,h}}(n_{\mathrm{h}} - n_{\mathrm{h}}^0) \tag{1.27}$$

with the equilibrium (dark, $V_{\mathrm{ext}} = 0$) concentration $n_{\mathrm{e/h}}^0$ for electrons and holes at the corresponding contact. When the charge carrier densities at the contacts differ from the equilibrium values, e.g. due to illumination or application of an external voltage, currents will arise.

Metal-Semiconductor Contact: In this section the physics of a metal-semiconductor contact also referred to as Schottky contact are explained. When two materials are brought into contact charge carriers will be exchanged until Fermi levels are aligned and flat through the entire volume i.e. equilibrium is achieved. The Fermi energy of a metal is given by its workfunction W_{F}. The amount of injected charge inside the semiconductor depends on the injection barrier given by the Schottky–Mott rule as (assuming no chargeable surface states, i.e. no Fermi level pinning):

$$\Phi_{\mathrm{B,e}} = E_{\mathrm{CB}} - W_{\mathrm{F}}$$

given by the difference of the W_{F} and the energy of the CB edge for electrons. Respectively, the injection barrier for holes is $\Phi_{\mathrm{B,h}} = \Phi_{\mathrm{B,e}} - E_{\mathrm{g}}$. If the barrier has rectifying character it is referred to as Schottky barrier. Equilibrium charge carrier concentrations n_{e}^0 and n_{h}^0 in the semiconductor at the metal interface are described by

$$n_{\mathrm{e}}^0 = N_{\mathrm{C}} \frac{2}{\sqrt{\pi}} F_{1/2}\left(\frac{-\Phi_{\mathrm{B,e}}}{k_{\mathrm{B}}T}\right)$$

$$n_{\mathrm{h}}^0 = N_{\mathrm{V}} \frac{2}{\sqrt{\pi}} F_{1/2}\left(\frac{\Phi_{\mathrm{B,h}}}{k_{\mathrm{B}}T}\right)$$

with the Fermi integral $F_{1/2}$ of order $\frac{1}{2}$. For $\Phi_{\mathrm{B,e}} > 3k_{\mathrm{B}}T$ or $\Phi_{\mathrm{B,h}} < 3k_{\mathrm{B}}T$ the Fermi integral can be approximated by Boltzmann statistics with $F_{1/2}(x) \approx \sqrt{\pi}/2 \exp(x)$ with less than 2 % deviation [18]. Thus

$$n_{\mathrm{e}}^0 \approx N_{\mathrm{C}} \exp\left(\frac{-\Phi_{\mathrm{B,e}}}{k_{\mathrm{B}}T}\right) \tag{1.28}$$

$$n_{\mathrm{h}}^0 \approx N_{\mathrm{V}} \exp\left(\frac{\Phi_{\mathrm{B,h}}}{k_{\mathrm{B}}T}\right). \tag{1.29}$$

If W_{F} is located e.g. above the edge of the CB, $\Phi_{\mathrm{B,e}}/(k_{\mathrm{B}}T)$ is negative and electrons get injected into the semiconductor, leading to a high electron concentration in vicinity of the contact. At the same time there is an injection barrier for holes which is larger than the band gap. This leads to heavily imbalanced conductivities for electrons and holes, fulfilling the condition (1.24) and thus resulting in a selective electron contact. In an analogous manner, a hole selective contact can be realized by applying a metal with a workfunction energetically lower than the VB edge. A comprehensive overview over other semiconductor contacts can be found in the PhD thesis of Seßler [25].

2 Fundamentals of Photovoltaics and Organic Solar Cells

In the previous chapter, a brief introduction to basic concepts of solid state physics was given and the general effects of generation, recombination and transport were discussed. In the following, the fundamentals of photovoltaics will be introduced, especially the relationship between current density and voltage of a solar cell will be derived and the fundamentals of organic semiconductors are introduced. For this, the description and theory of organic semiconductors are rather discussed based on the picture of orbitals and distinct energy levels in contrast to the model of Bloch waves and energetic bands. While often an alternative or analogous description based on the continuum picture of solid state physics can be found. The nature of the material properties and thus the appropriate description will vary based on e.g crystallinity of the organic material while the transition between a (localized) molecular or a continuum description will undergo a smooth transition.

2.1 Current-Voltage-Curve and Figures of Merit

PV is the direct conversion of light into electrical power. The latter is calculated by the product of voltage V and electrical current I. The amount of provided power is of utmost importance for an energy source which makes the current-voltage-curve (JV-curve) doubtlessly the most important and most frequently determined property of solar cells. A characteristic JV-curve is depicted in figure 2.1 (black line). The red curve in figure 2.1 is the extracted electrical power density $P(V) = -VJ$ which features a maximum where the product of current density and voltage is highest. This point is called the maximum power point (MPP) while the corresponding voltage and current density are referred to as V_{MPP} and J_{MPP}, respectively. The voltage of the cell for zero external current (open-circuit condition) is called open-circuit voltage (V_{OC}). The current density observed under short-circuit conditions, when both electrodes are at the

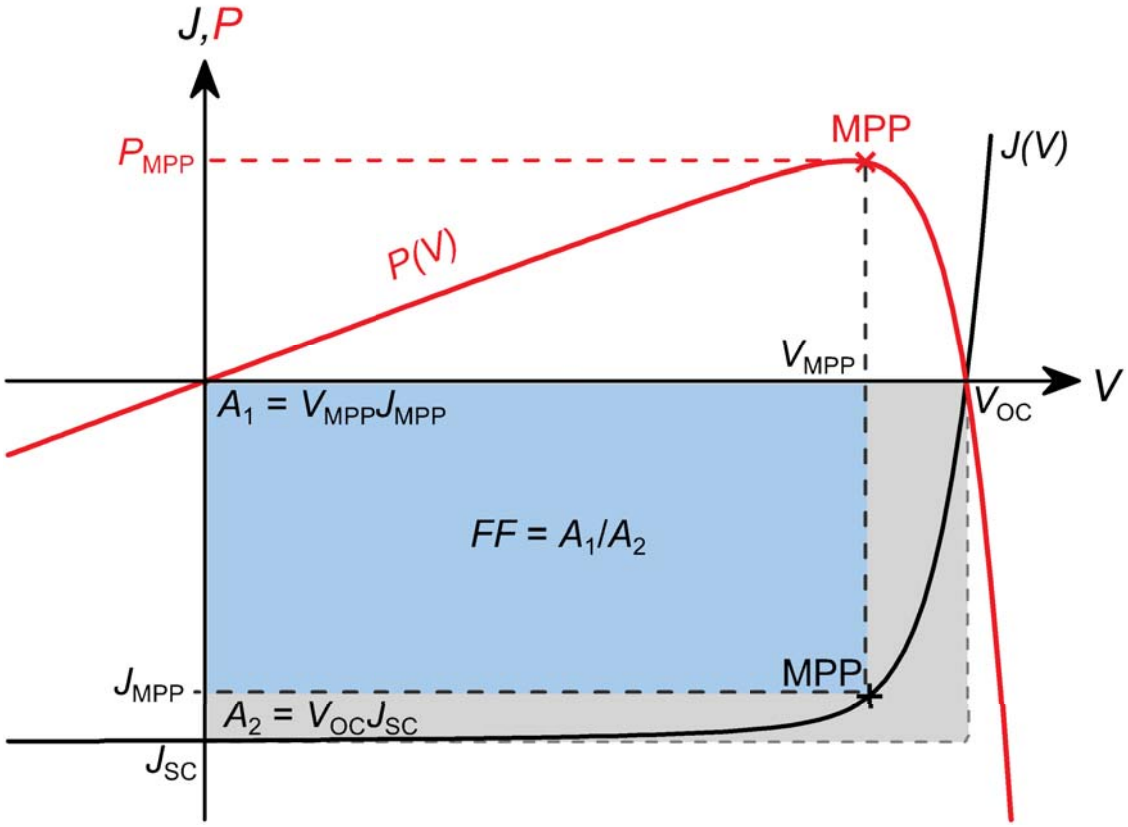

Figure 2.1: Scheme of a characteristic current-voltage curve ($J(V)$) of a solar cell (black curve) with the open-circuit voltage V_{OC} and the short-circuit current density J_{SC} alongside with the electric power ($P(V)$) which can be extracted (red curve) as function of the voltage. The point where the extracted electric power is highest is marked as MPP with the corresponding voltage (V_{MPP}) and current density J_{MPP}.

same potential ($V = 0$), is called short-circuit current (J_{SC}). Beside J_{SC} and V_{OC} the fill factor (FF) is the third key figure of merit. It is defined as

$$FF = \frac{V_{\mathrm{MPP}} J_{\mathrm{MPP}}}{V_{\mathrm{OC}} J_{\mathrm{SC}}} \tag{2.1}$$

It is the ratio of the grey and blue areas depicted in figure 2.1 and is a measure for how rectangular, i.e. ideal, the JV-curve is. From the defined parameters the maximum power density of the solar cell can be calculated by $P_{\mathrm{MPP}} = V_{\mathrm{OC}} J_{\mathrm{SC}}\, FF$. For an input power density P_{light} of illumination the Power Conversion Efficiency (PCE or η) is given by:

$$\eta = \frac{P_{\mathrm{MPP}}}{P_{\mathrm{light}}} = \frac{V_{\mathrm{OC}} J_{\mathrm{SC}}\, FF}{P_{\mathrm{light}}} \tag{2.2}$$

In the following, the theoretically expected current density $J(V)$ as function of the cell's voltage will be derived. For this a cell with solely radiative recombination and a spatially homogeneous total generation rate $G_{\mathrm{tot}} = G + G_0$ throughout the thickness d of the absorber is assumed. G is the rate of additionally generated carriers due to illumination. The total recombination rate $R_{\mathrm{tot}} = R + R_0$ is the sum of the recombination rate of photogenerated carriers R and the dark recombination rate R_0. Using equations (1.9) and (1.10) the recombination rate R of photogenerated carriers is given by:

$$R = R_{\mathrm{tot}} - R_0 = k_{\mathrm{r}}(n_{\mathrm{e}} n_{\mathrm{h}} - n_{\mathrm{i}}^2)$$

Further, we assume ideally selective contacts with no losses due to surface recombination. The continuity equations (1.15) and (1.16) for electrons and holes become:

$$\frac{\partial n_{\mathrm{e,h}}}{\partial t} = G - k_{\mathrm{r}}(n_{\mathrm{e}} n_{\mathrm{h}} - n_{\mathrm{i}}^2) - \frac{\partial}{\partial x} j_{\mathrm{e,h}}$$

Under steady state conditions ($\frac{\partial n}{\partial t} = 0$) we get (using equations (1.7) and (1.14)):

$$\frac{\partial}{\partial x} j_{\mathrm{e,h}} = G - k_{\mathrm{r}} n_{\mathrm{i}}^2 \left[\exp\left(\frac{e_0 V_{\mathrm{int}}}{k_{\mathrm{B}} T} \right) - 1 \right]$$

The recombination inside the semiconductor is determined by the QFL splitting $e_0 V_{\mathrm{int}}$. In case of ideal selective contacts and ideal transport of charge carriers, i.e. flat QFL inside the absorber, the voltage at the electrodes equals the internal voltage $V = V_{\mathrm{int}}$

(see chapter 1.5). The (electric) current density $J(V)$ is calculated by (using equations (1.11) and (1.18)):

$$\begin{aligned} J(V) &= -e_0 \int_0^d \frac{\partial}{\partial x} j_\mathrm{e} dx = -e_0 G d + e_0 k_\mathrm{r} n_\mathrm{i}^2 d \left[\exp\left(\frac{e_0 V}{k_\mathrm{B} T}\right) - 1\right] \\ &= -J_\mathrm{gen} + J_0 \left[\exp\left(\frac{e_0 V}{k_\mathrm{B} T}\right) - 1\right] \end{aligned} \tag{2.3}$$

The photogenerated current density J_gen is the maximum current density which can be extracted from the cell $J_\mathrm{gen} \approx J_\mathrm{SC}$. Equation (2.3) is the ideal Shockley diode equation with the saturation current density J_0, shifted by $-J_\mathrm{SC}$. According to equation (1.13) the V_OC of the ideal solar cell is given by:

$$e_0 V_\mathrm{OC} = E_\mathrm{g} - k_\mathrm{B} T \ln\left(\frac{k_\mathrm{r} N_\mathrm{C} N_\mathrm{V}}{G}\right). \tag{2.4}$$

The more general recombination equation (1.19) for arbitrary reaction order can be expanded to account for the dark generation (analogously to equation (2.3)).

$$R = k_\mathrm{r} (n_\mathrm{e} n_\mathrm{h} - n_\mathrm{i}^2)^{\frac{\beta}{2}} \tag{2.5}$$

Using this in the derivation of $J(V)$ it follows:

$$J(V) = -J_\mathrm{SC} + J_0 \left[\exp\left(\frac{e_0 V}{n_\mathrm{id} k_\mathrm{B} T}\right) - 1\right] \tag{2.6}$$

with the ideality factor $n_\mathrm{id} = \frac{2}{\beta}$. Here V_OC is given by:

$$e_0 V_\mathrm{OC} = E_\mathrm{g} - n_\mathrm{id} k_\mathrm{B} T \ln\left(\frac{k_\mathrm{r} N_\mathrm{C} N_\mathrm{V}}{G}\right). \tag{2.7}$$

Equations (2.3) and (2.6) can be illustrated by an equivalent circuit which consists of a constant current source representing the photogenerated current density J_gen and a diode, representing the recombination current J_rec. The so called diode model of a solar cell is depicted in figure 2.2(a). A more versatile equivalent circuit model is depicted in figure 2.2(b). The series resistance R_S to account for ohmic voltage losses due to transport and the shunt resistance R_P are added. Additional diodes can be used to distinguish between specific recombination mechanisms and a capacitance can be added to the model to account for capacitive effects.

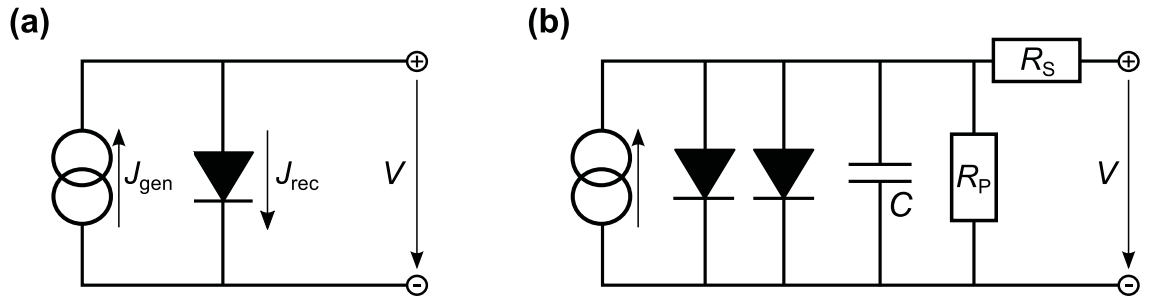

Figure 2.2: Equivalent circuit models of a solar cell. Diode model **(a)** with a current source J_{gen} and a diode to account for the recombination current density J_{rec}. Scheme of a more general model **(b)** with an additional series resistance R_S and parallel resistance R_P, 2 diodes to account for distinct recombination mechanisms and a capacitance C to describe transient effects.

2.2 Organic Semiconductors and Conjugated π-Electron Systems

In this chapter a brief introduction in the semiconducting properties of organic materials based on considerations about molecular orbitals is given. A good overview over orbital theory of organic semiconductors is given in the PhD thesis of Ahme [28] and a comprehensive description can be found in the textbook of Schwörer [22]. Organic semiconductors are carbon (C) based materials with semiconducting properties. In addition to carbon and hydrogen (H), nitrogen , oxygen , sulfur or fluorine are commonly found in these materials, altering electrical and optical properties. There are mainly two groups of organic semiconductors: first, macro molecules, i.e. polymers and second, single molecules smaller in size. Both groups share a C based backbone with alternating single and double bonds responsible for their semiconducting properties. In case of conjugated bonds the C atoms are sp^2 hybridized resulting in the orbitals depicted in figure 2.3(a), while every C atom binds in plane to two other C atoms and one hydrogen by sharing an electron forming σ bonds. The remaining p_z orbitals of two neighboring C atom overlap, forming a π bond containing the forth valence electrons of both atoms. This π orbital can extend over several conjugated bonds forming a delocalized π band. Due to the delocalization, the single and double bonds are not distinguishable.

Figure 2.3(b) shows the energy diagram of the atomic orbitals and the resulting molecular σ and π orbitals for two bound sp^2 hybridized C atoms. There the molecular orbitals are depicted as the linear combination of atomic orbitals while the colors of the orbital represent the sign of the corresponding wave function. The Highest Occupied Molecular Orbital (HOMO) is given by the π orbital depicted in 2.3(a). The Lowest Unoccupied Molecular Orbital (LUMO) is the π^* orbital. It has a node (probability of zero to

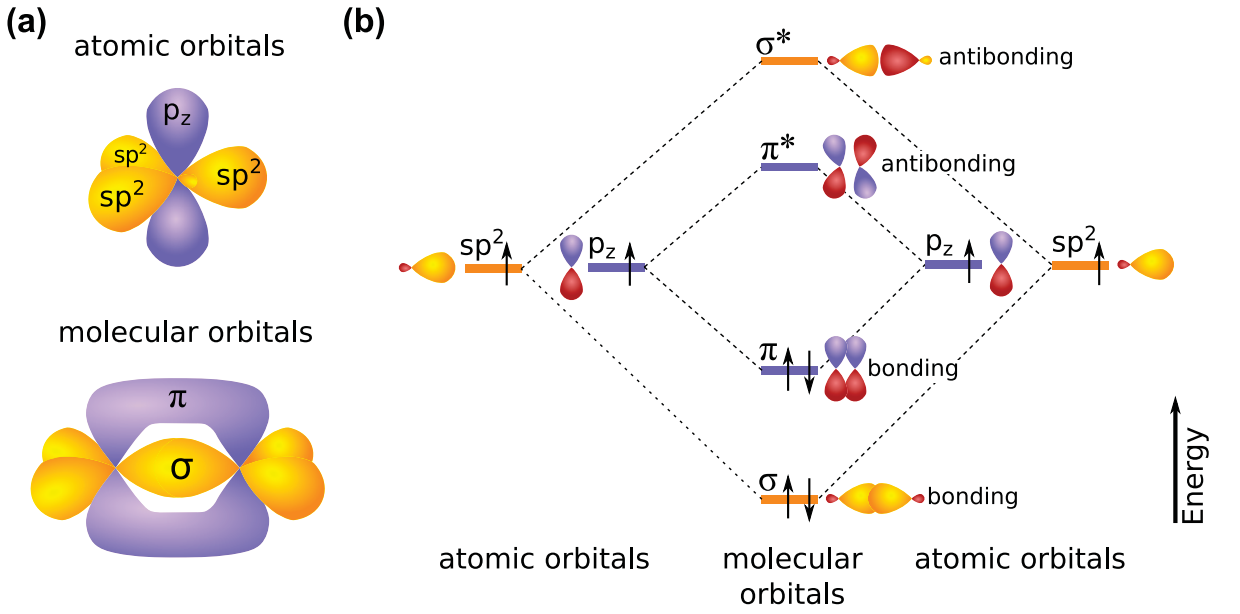

Figure 2.3: **(a)** Illustration of the atomic orbitals of a sp^2 hybridized C atom showing 3 sp^2 and a p orbital and the resulting molecular π and σ orbitals of a C-C bond. **(b)** Energy scheme of the unbound atomic and bound molecular orbitals. The color of the orbital indicates the sign of the corresponding wave function. The bonding π orbital is the HOMO level showing a distinct energetic gap to the LUMO level (antibonding π^* orbital).

find an electron) in between two neighboring C atoms due to the change in sign of the atomic wave functions. The lower probability of the binding electrons to be located between both atoms makes this orbital energetically less favorable and thus destabilizes the bond (in regard to the case of a π orbital). Therefore the π^* orbital is referred to as antibonding orbital while the π orbital is called bonding. This leads to an energetic gap between the HOMO and LUMO orbitals, equivalent to the band gap in inorganic semiconductors. An analogous description of the semiconducting nature of such systems is given by the Peierl's theorem in solid state physics. In case of C-C bonds with equal length the π band would be half filled, since every atom contributes one electron and a one-dimensional metal would be formed [29]. Electron phonon coupling results in the Peierl's instability, so the energy is minimized by dimerization resulting in altering bond lengths. This leads to a fully occupied π and an unoccupied π^* band [30] depicted in figure 2.4.

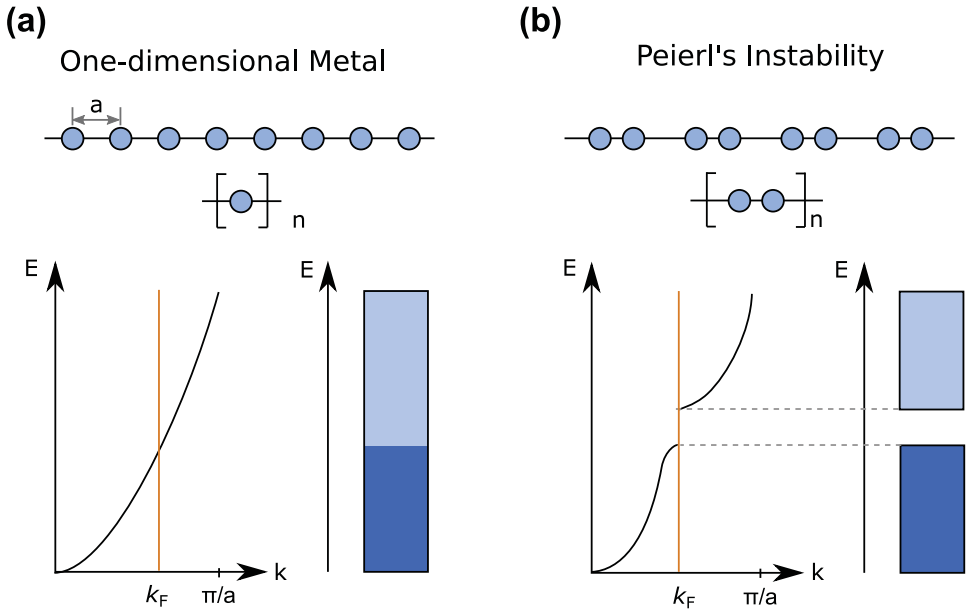

Figure 2.4: Band diagram and schematic DOS as function of electron energy E. Occupied states are highlighted in dark blue and unoccupied states in light blue. A one-dimensional metal is depicted in **(a)**. Peierl's instability leads to the formation of an energetic splitting resulting in a gap at the Fermi wave vector $\vec{k_F}$ **(b)**. From ref. [18].

2.3 Generation and Recombination in Organic Donor-Acceptor Systems

2.3.1 Exciton

Excitons are charge free quasi particles describing bound electron-hole pairs. They can be created during light absorption, i.e. the generation of electron-hole pairs. Thus, they play an important role during the generation of free charge carriers in semiconductors. They are formed due to coulombic interaction the potential energy E_{coul} of an electron and a hole is given by:

$$E_{\text{coul}} = -\frac{e_0^2}{4\pi\epsilon_0\epsilon_r r_0}$$

with the vacuum permittivity ϵ_0, the relative permittivity ϵ_r of the medium and the distance r_0 of an electron and hole, which is typically smaller for organic materials due to the low dielectric constant $\epsilon_r \approx 3$ compared to inorganic materials ($\epsilon_r \approx 12$ for silicon). This results in typical exciton binding energies E_B in organic materials in the range of 0.2–1 eV which is much higher than the thermal activation energy at ambient temperature ($k_B T \approx 25\,\text{meV}$)[7, 31, 32]. The separation distance of electrons and holes

in conventional semiconductors is usually much larger than the unit cell of the lattice. Such excitons are referred to as Mott-Wannier-excitons. They are hydrogen-like quasi particles in the effective mass approximation where the relaxed separation distance r_0 can be understood as the Bohr radius a_0. Their binding energy E_B^MW is given by:

$$E_\mathrm{B}^\mathrm{MW} = \frac{\mu^*}{m_0}\frac{R_\mathrm{y}}{\epsilon_\mathrm{r}^2}\frac{1}{n_\mathrm{ex}^2} \tag{2.8}$$

with the effective mass μ^* of the electron-hole pair, m_0 the intrinsic mass of an electron, the Rydberg energy of $R_\mathrm{y} = 13.6\,\mathrm{eV}$ and n_ex the principle quantum number of excitation. They have typical binding energies in the range of 10 meV in inorganic semiconductors. A scheme of Mott-Wannier-excitons is depicted in 2.5(a). In contrast, the separation distance of bound electrons and holes in amorphous organic materials is typically smaller than the unit cell (one molecule or monomer). Electron and hole are usually localized on the same molecule thus the effective mass approximation is not valid [34, 35]. Such excitons are referred to as Frenkel-excitons. In that case the binding energy must be described on the molecular level by the overlap of the wave functions of electrons and holes. The energies of bound electrons and holes correspond to the energies E_{S_0} and E_{S_1} of the molecular orbitals of the (singlet) excited molecule (M^*). This is illustrated

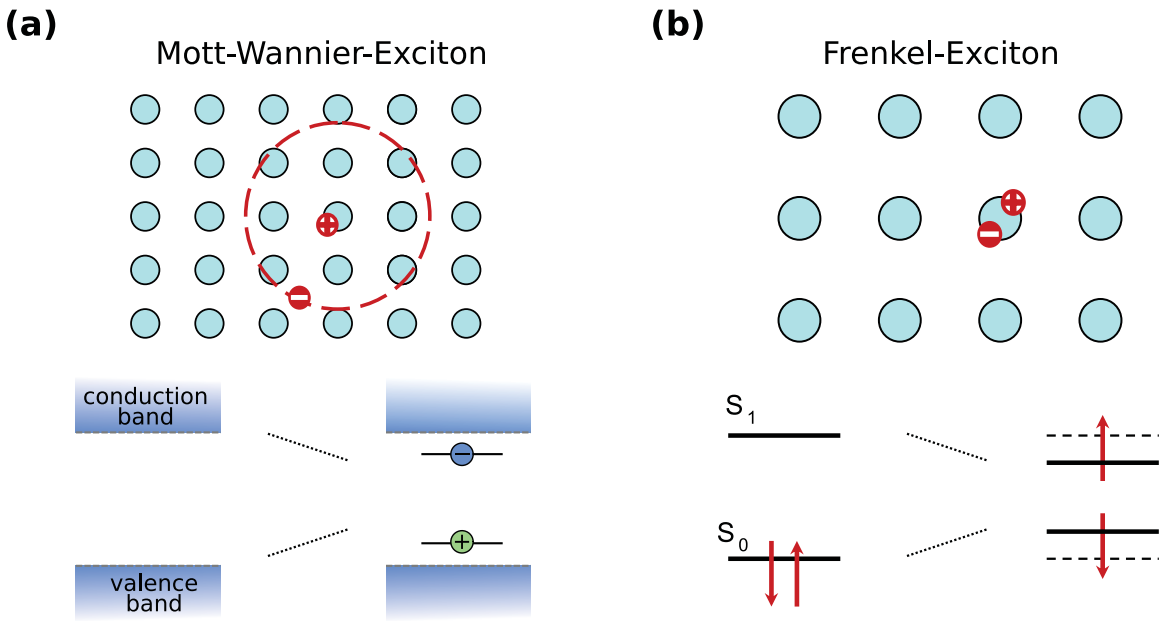

Figure 2.5: Schematic illustration of **(a)** a Mott-Wannier-exciton and its energy levels in the band picture of semiconductor theory and **(b)** a Frenkel-exciton and its energy levels given by molecular orbitals theory. After ref. [33].

in figure 2.5(b). In contrast, the energy levels of free electrons and free holes are given by the energies of the orbitals of the charged (unexcited) molecular species M^- and M^+. This corresponds to the picture of electron or hole polarons in solid state physics. The Frenkel-exciton binding energy E_B^{Fr} in the effective one particle picture can be understood as

$$E_B^{Fr} = E_{HOMO}(M^*) - E_{LUMO}(M^*) - (E_{HOMO}(M^+) - E_{LUMO}(M^-))$$

A comprehensive summary of the quantum mechanical description of Frenkel-excitons can be found in ref [36].

2.3.2 Generation of Free Charges in a Donor-Acceptor System

As discussed in the previous section in organic semiconductors an electron-hole pair forms a strongly bound Frenkel-exciton after photogeneration which hardly can be split by the thermal activation energy at ambient conditions. Thereby photovoltaic devices made from pure polymers have charge generation yields of $\ll 1\,\%$ [37]. Thus, a second molecule is introduced which provides energetically favorable states to spatially separate electrons and holes and thereby generate free charge carriers. This process is referred to as charge transfer (CT). The material which holds the hole after CT is called Donor (D) while the material which hosts the electron is referred to as Acceptor (A). An organic solar cell (OSC) with the described donor-acceptor system was introduced 1986 by Tang et al. [7]. In the further description we will stick to the more common case where light is absorbed by the D molecules and electrons are transferred to the A molecules. Figure 2.6 depicts schematically the processes between light absorption and extraction of charges at the electrodes in an organic D-A solar cell. After absorption of a photon the created electron-hole pair loses a part of the excitation energy by thermalization forming a bound exciton. The electron is transferred to the Electron Transport Level (ETL) at the acceptor, driven by the energy difference ΔE while the hole remains in the Hole Transport Level (HTL) on the D phase. The generated carriers are transported to the electrodes and extracted there. In the picture of molecular energy levels, the ETL and HTL are the corresponding HOMO and LUMO energies of the charged molecular species D^+ and A^-.

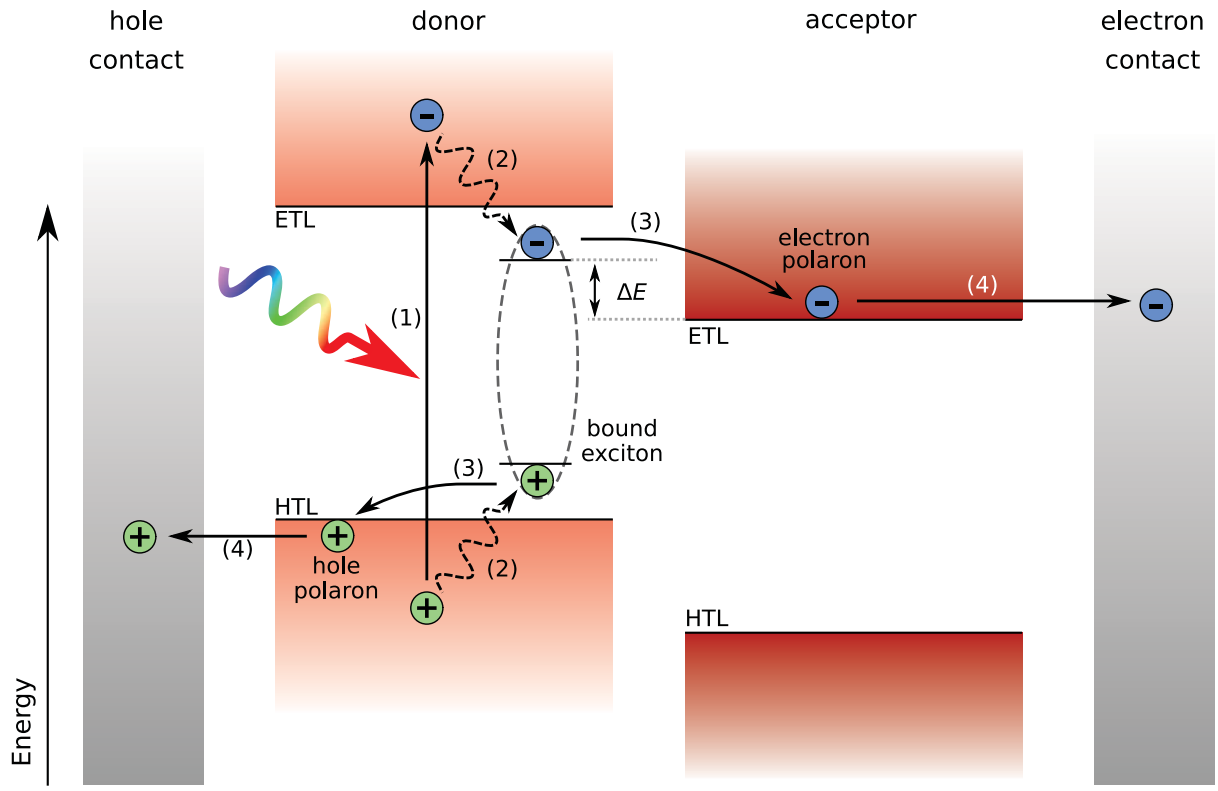

Figure 2.6: Schematic energy diagram of an OSC with the relevant processes involved in the generation of photocurrent. Light is absorbed by the donor material (1) creating an electron-hole pair which relaxes to a bound exciton by thermalization (2). The electron is transferred to the acceptor material (3) driven by the energy difference ΔE. Free electrons and holes are transported to the respective electrodes and extracted (4).

2.3.3 The Charge Transfer State in Donor-Acceptor Systems

Results on the investigation of charge transfer states have been published with the author of this work as first author[38]. Thus concepts and contents of this chapter are closely based on this publication and partially paraphrases it.

CT complexes in solutions have been discovered in 1952 by Mulliken [39] and have been studied intensively ever since. In the commonly used bulk-heterojunction OSC a charge transfer complex is formed at the D-A interface due to interaction of the D and A molecules. The term CT state refers here to the excited state of the CT complex, where the electron is located at the acceptor and the hole at the donor and CT energy (E_{CT}) refers to the excitation energy with respect to the ground state (GS). Figure 2.7 illustrates schematically an exciton on the donor molecule, the CT state and free charge carriers. The relevance of CT states for OPV has recently triggered new interest

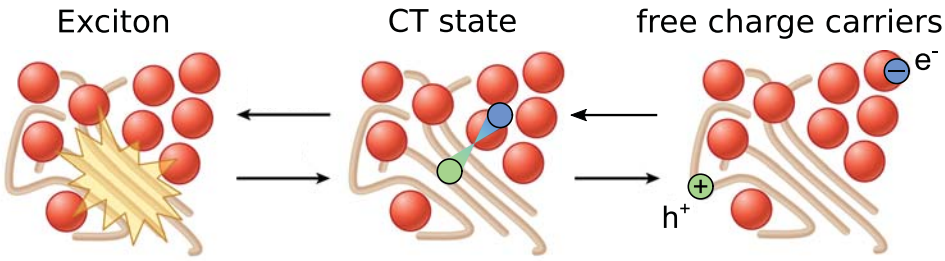

Figure 2.7: Schematic representation of exciton, charge transfer (CT) complex and free charge carriers in a D-A system. The donor molecules are depicted as rod shaped and assumed to be the main absorber while the acceptor molecules are represented by spheres. Modified from [40].

in their properties in condensed matter systems [40–43] while a comprehensive review about charge transfer states in OSC has been published recently by Vandewal [44]. Due to the CT complexes at the D-A interface an absorption and emission band at lower energies compared to the optical gaps of the individual D and A materials is present. Although the CT complex does not contribute significantly to the overall absorption in OSC, CT excitons are intermediate states during charge transfer and thereby involved in charge carrier generation and recombination [41–44]. Figure 2.8(a) shows the energy diagram at a D-A interface with the energy levels relevant for charge transfer and separation into free charges, referred to as charge separated (CS) state here [45]. Within this process photons with energies higher than the optical band gap E_{D^*} of the D molecule are absorbed. This excites electrons to the donor's excited state D^*, i.e., creates excitons with generation rate (G_{D^*}). Excitons can either directly create free charges in the CS state by trespassing the vibrationally relaxed charge transfer state (CT_1) with the rate k^*_{CT} or can thermally relax to the latter with the rate k_{relax}. The relaxed CT_1 state can either dissociate (k_{CS}) forming CS or decay k_{f} (partially radiative) to the GS which is often referred to as geminate recombination in literature since electrons and holes which were originally photogenerated together recombine pairwise. At the same time CT excitons are generated with the rate k_{r} from free charge carriers. This recombination mechanism for free charge carriers is referred to as nongeminate recombination since electrons and holes recombine pairwise which were not photogenerated together initially. It should be noted here that triplet CT states are expected to be formed from free charges with an expected probability of 3/4 due to spin statistics. Nevertheless, triplet states are not included in the energy diagram illustrated in figure 2.8. since they can neither be photoexcited directly and thus not result in absorption nor recombine radiatively, i.e., they do not result in luminescence used in this work for characterization

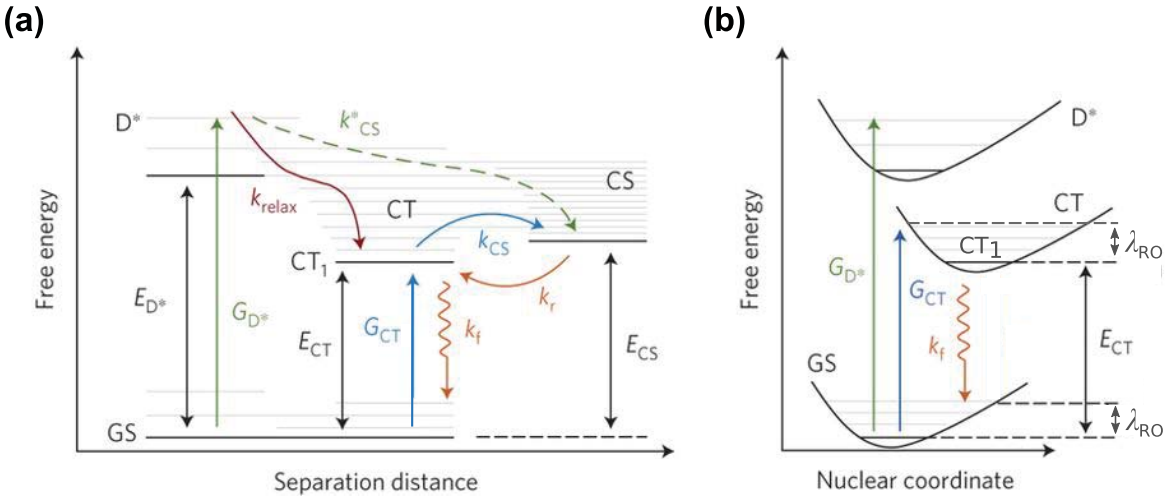

Figure 2.8: State diagram of a D-A system **(a)** with relevant processes involved in free charge generation. Absorption of a photon with energy higher than E_{D^*} generates the donor excited state D^* at a rate G_{D^*}. There are several possible pathways for the generation of free charges in the charge separated (CS) state. Pathways with rate constants k^*_{CS} bypass the vibrationally relaxed and lowest energy CT state (CT_1) and compete with thermal relaxation (k_{relax}). CT^1 can decay radiatively (k_f) to the GS or dissociate (k_{CS}) to free carriers in the CS state. The inverse of the latter process, population of CT_1 from CS, occurs at a rate k_r. Potential energy surfaces of GS, CT and D^* states **(b)**. Optical excitation of CT states (G_{CT}) occurs with highest absorption rate at the photon energy $E_{CT} + \lambda_{RO}$. While the emission of CT recombination peaks at photon energy $E_{CT} - \lambda_{RO}$. Modified from ref [45].

and hence are not discussed in detail. Further, triplet states were reported in literature not to contribute substantially to nonradiative recombination for a large series of typical materials used in organic solar cells due to the energy level alignment between the first triplet state and the CT [46].

The separation of interfacial D^* singlet excitons to CT states (k^*_{CT}) was reported in literature to occur on timescales of 10-100 fs, by far faster than processes like exciton decay (0.1–1 ns, see chapter 2.3.1) and vibrational relaxation of the D^* state [47–49]. Falke et al. showed that vibronic coupling between electronic and nuclear degrees of freedom is the reason for the ultrafast electron transfer [50]. These findings imply a yield of exciton splitting close to unity, independent of the energy difference $E_{D^*} - E_{CT}$ and a strong delocalization of the excited state in contrast to the picture of exciton diffusion. Additionally, the electron transfer being much faster than vibrational relaxation of the excited D^* state implies, that the strong Stokes-shift (i.e. vibrational relaxation) of the exciton in the pure absorber materials in the range of 0.3 – 0.8 eV [51] is not a limiting intrinsic loss mechanism for OSC. The fundamental properties which determine

the separation coefficient k_{CS} of CT to CS states are still under controversial discussion in the field of OSC. Nevertheless, the commonly used picture of energy difference (ΔE_{LL}) of D and A LUMO levels being the driving force for charge separation should be critically reconsidered since it ignores D^* exciton and CT binding energy [44, 52]. Energy transfer losses ($E_{\mathrm{D}^*} - E_{\mathrm{CT}}$) of about 0.1 eV have been reported to be sufficient in polymer-fullerene blends to result in a high free charge carrier generation yield [44, 53–55]. However, the requirements to molecular structures and molecular orbitals allowing such low charge transfer losses are currently unknown.

Figure 2.8(b) shows the energy surfaces of GS, donor excited state D^* and CT state to illustrate the emergence and energetic properties of new absorption and emission bands (only the first excited electric states are depicted). (Singlet) CT states can be optically excited with the generation rate G_{CT} which results in geometrically deformed CT complexs. This deformation is carried by (excited) molecular vibrations. The excited vibrational states relax by thermalization which corresponds to geometric relaxation of the CT complex, referred to as reorganization. Figure 2.9 (a) schematically depicts the corresponding energy diagram of the ground state and the first excited CT state together with exemplary experimental data of the resulting absorption and emission bands. Modified from reference [43]. The highest transition probability, i.e. maximum of the CT absorption spectrum, results at a photon energy of $E_{\mathrm{CT}} + \lambda_{\mathrm{RO}}$ with reorganization energy λ_{RO} according to the Franck–Condon principle. While the emission has a maximum at photon energy $E_{\mathrm{CT}} - \lambda_{\mathrm{RO}}$. Thus, absorption and emission spectra of CT states are Stokes-shifted by $2\lambda_{\mathrm{RO}}$ due to the reorganization of the CT complex [56]. According to Marcus theory the CT state absorption cross section σ and the reduced CT state emission spectrum I_{f}/E are given by [43, 57]:

$$\begin{aligned} \sigma E &= \frac{f_\sigma}{\sqrt{4\pi\lambda_{\mathrm{RO}} k_{\mathrm{B}} T}} \exp\left(\frac{-(E_{\mathrm{CT}} + \lambda_{\mathrm{RO}} - E)^2}{4\lambda_{\mathrm{RO}} k_{\mathrm{B}} T}\right) \\ \frac{I_{\mathrm{f}}}{E} &= \frac{f_{\mathrm{I}}}{\sqrt{4\pi\lambda_{\mathrm{RO}} k_{\mathrm{B}} T}} \exp\left(\frac{-(E_{\mathrm{CT}} - \lambda_{\mathrm{RO}} - E)^2}{4\lambda_{\mathrm{RO}} k_{\mathrm{B}} T}\right) \end{aligned} \tag{2.9}$$

where f_σ and f_{I} are constant prefactors dependent on the electronic coupling matrix element of the D-A system. I_{f} is the spectral photon density of CT emission (in units of $(\mathrm{s\,eV})^{-1}$) and E the photon energy.

CT state energy and occupation of the CT states are crucial as they determine the open-circuit voltage (V_{OC}) and thus are directly correlated to the PCE [23, 43, 58, 59]. Under assumption of thermodynamic equilibrium between free charge carriers and the

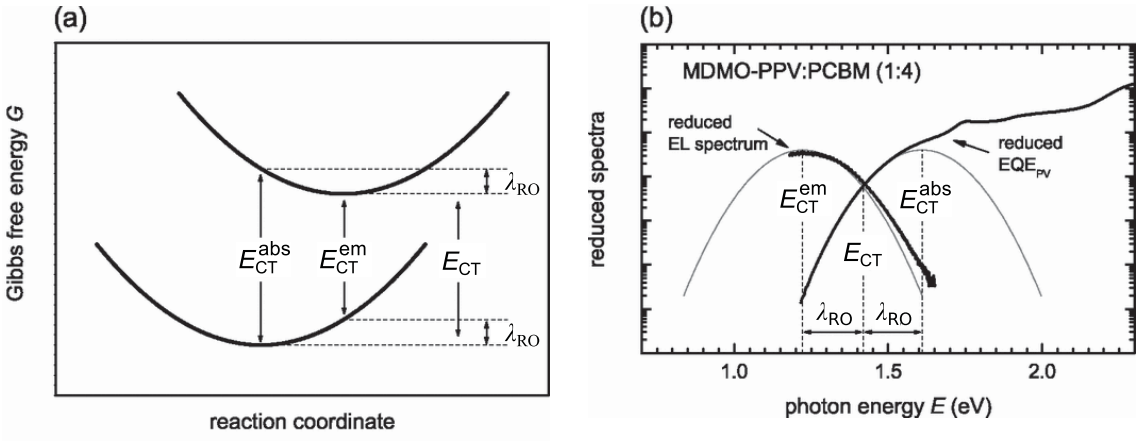

Figure 2.9: Free-energy diagram for the ground state and lowest excited state of the CT complex with an excitation energy E_{CT} as a function of a generalized coordinate. (b) CT absorption and CT emission bands for a MDMO-PPV:PCBM organic solar cell with the energy $E_{\mathrm{CT}}^{\mathrm{abs}}$ of maximal absorption and $E_{\mathrm{CT}}^{\mathrm{em}}$ of maximal emission. Modified from reference [43].

occupation of CT states Burke et al. derived a relation between V_{OC} and E_{CT} and verified it to be valid for OSC [59] given by

$$e_0 V_{\mathrm{OC}} = \underbrace{E_{\mathrm{CT}} - \frac{\sigma_{\mathrm{CT}}^2}{2k_{\mathrm{B}}T}}_{E_{\mathrm{g,eff}}} - k_{\mathrm{B}}T \ln\left(\frac{e_0 f N_{\mathrm{CT}} d_{\mathrm{PAL}}}{\tau_{\mathrm{CT}} J_{\mathrm{rec}}}\right) \tag{2.10}$$

accounting for energetic disorder. For this a Gaussian shaped energetic CT state distribution with a width of σ_{CT} and center E_{CT} is assumed representing the inhomogeneously broadened CT state energies at the D-A interfaces. τ_{CT} is the lifetime of the CT states, J_{rec} the recombination current density under open-circuit conditions ($J_{\mathrm{rec}} = J_{\mathrm{gen}}$), f is the volume fraction of the D-A interfaces, N_{CT} is the density of CT states related to the interfacial volume and d_{PAL} the thickness of the photoactive layer (PAL). For Gaussian disordered CT states the effective band gap $E_{\mathrm{g,eff}}$ is reduced by $\sigma_{\mathrm{CT}}^2/(2k_{\mathrm{B}}T)$ and thus the V_{OC} reduction is proportional to the width of the disorder distribution to the square. Localized CT excitations can not thermalize down to the low energetic tail of the distribution. The energy of an individual CT state dependent on the local environment at the D-A interface at its position. Hence, the quasi-Fermi level splitting $e_0 V_{\mathrm{OC}}$ is only reduced by $\sigma_{\mathrm{CT}}^2/(2k_{\mathrm{B}}T)$.

For the assumed case of a Gaussian energetic disorder the experimentally observed CT spectrum is shifted to $E_{\mathrm{CT}}^{\mathrm{exp}} = E_{\mathrm{CT}} - \sigma^2/(2k_{\mathrm{B}}T)$ with an observed reorganization energy $\lambda_{\mathrm{RO}}^{\mathrm{exp}} = \lambda_{\mathrm{RO}} - \sigma^2/(2k_{\mathrm{B}}T)$. From equation (2.10) it can be seen that the experimentally

observed CT state energy resembles exactly the effective band gap $E_{\mathrm{g,eff}}$ for OSC. Thus V_{OC} can be expressed by the experimentally determined CT state energy $E_{\mathrm{CT}}^{\mathrm{exp}}$ by:

$$eV_{\mathrm{OC}} = E_{\mathrm{CT}}^{\mathrm{exp}} - k_{\mathrm{B}}T \ln\left(\frac{e_0 f N_{\mathrm{CT}} d_{\mathrm{PAL}}}{\tau_{\mathrm{CT}} J_{\mathrm{rec}}}\right) \tag{2.11}$$

From equations (2.9) and (2.11) it is obvious that knowledge about CT state energy E_{CT} and for this the position and width of CT emission or absorption bands are key for a detailed understanding of the origin of V_{OC} in OSC.

2.3.4 Recombination in Organic Donor-Acceptor Systems

The Langevin theory is often used to account for recombination of free carriers in organic donor-acceptor systems [60]. It describes second-order recombination ($R_{\mathrm{L}} = k_{\mathrm{L}} n_{\mathrm{e}} n_{\mathrm{h}}$) in low mobility semiconductors. The Langevin recombination coefficient k_{L} can be calculated from the charge carrier mobilities by

$$k_{\mathrm{L}} = \frac{e_0\,(\mu_{\mathrm{e}} + \mu_{\mathrm{h}})}{\epsilon\epsilon_0} \tag{2.12}$$

It has been studied intensively and observed to be valid for many amorphous organic donor-acceptor blends [59, 61, 62]. In contrast, e.g. for the commonly used P3HT:$PC_{61}BM$ (annealed) the experimentally observed k_{exp} is reduced by 2 – 4 orders of magnitude compared to k_{L} [63–66]. The factor of reduction is referred to as Langevin prefactor $\zeta = k_{\mathrm{exp}}/k_{\mathrm{L}}$ in the literature. As described by Murthy et al., this can be understood as the quotient of the rate constants for recombination of the CT state k_{r} and the dissociation back into free charges k_{CS} as depicted in figure 2.8. Thus, $\zeta = k_{\mathrm{CS}}/k_{\mathrm{r}}$ while the details and driving force of CT state dissociation are still under discussion [67]. It was recently shown by Benduhn et al. [68] that a significant intrinsic nonradiative loss mechanism of carriers exists in polymer:fullerene-based OSC. It is attributed to a high probability of internal conversion of the excited CT complexes in such systems. In this process, the complete excitation energy is dissipated by the excitation of molecular vibrations of the electronic ground state. Considering this unavoidable additional loss, they estimate the theoretical limit for the power conversion efficiency for a single-junction organic polymer:fullerene solar cell to be 25.5 % (The limit for solely radiative recombination is given by the Shockley–Queisser limit of 33.2 %).

2.4 Transport in Organic Materials

In semiconductors the distribution of states is commonly described by energetic bands while the transport of free charge carriers is described by delocalized plane Bloch waves associated with an effective mass due to interactions with the lattice. In organic semiconductors the wavefunctions for electrons and holes can be strongly localized to individual molecules. This leads to a hopping like transport from molecular site to site in disordered organic materials schematically depicted in figure 2.10. This hopping transport can be described by the Bässler model also referred to as Gaussian disorder model which was empirically derived based on Monte-Carlo simulations assuming a Gaussian DOS of transport levels [69]. The mobility in the case of no field-dependence as function of temperature is given by:

$$\mu = \mu_0 \exp\left[-\left(\frac{2\sigma}{3k_\mathrm{B}T}\right)^2\right]$$

with mobility prefactor μ_0 and width σ of the DOS. Hopping like transport with a resulting positive temperature coefficient of mobility is commonly observed for disordered organic semiconductor. Nevertheless, band-like transport was reported at low temperatures in organic crystals [70]. So, the true nature of transport in a real system will be somewhere between band and hopping transport undergoing a continuous transition dependent on the crystallinity of the compound.

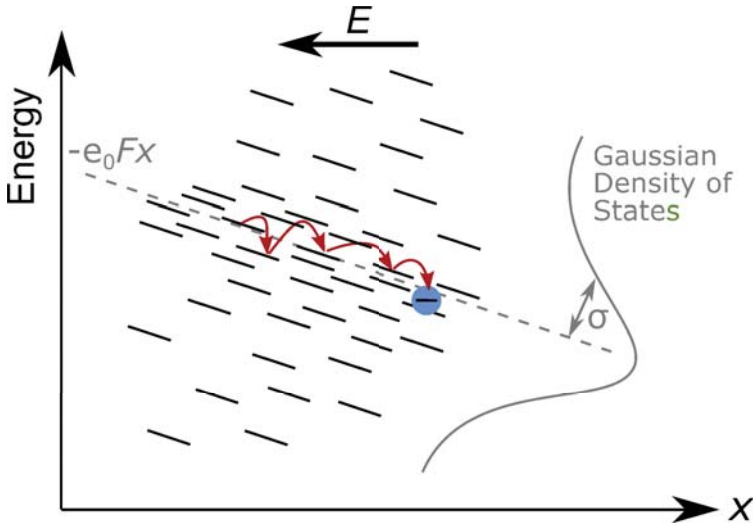

Figure 2.10: Scheme of the hopping transport of an electron in disordered organic semiconductors under an applied electric field E. The disorder of the density of states is represented by a Gaussian distribution with a width of σ. Modified from [18].

2.5 The Organic Bulk-Heterojunction Solar Cell

Free charge carriers are generated via CT at the donor-acceptor interface in organic solar cells as discussed previously. Photogenerated excitons must reach a D-A interface to get split before they recombine. Lifetimes of excitons in organic semiconductors between 1 ps and 1 ns are reported in literature [71] and values about 300 ps to 400 ps [72, 73] are reported as typical of films used in OSC while exciton diffusion lengths in the range of 2.5 nm to 8.5 nm are commonly observed [74–76]. Therefore, the absorber of an OSC should be designed with a phase separation on the nm scale to provide D-A interfaces within the exciton diffusion length to ensure effective generation of free charges. At the same time connected pathways of the D and A material to the respective electrodes must be present for charge carrier extraction. The commonly used and most efficient structure up to now is the bulk-heterojunction (BHJ). It is an interpenetrated network of D and A phases illustrated in Fig. 2.11 introduced by Yu et al. [77, 78] and Halls et al. in 1995 [79]. It is either produced by simultaneous evaporation of two organic compounds or, like in this work, by processing the layer from a blend solution containing D and A molecules. The morphology of the BHJ must be tuned to be fine enough to result in efficient FC generation and coarse enough for good transport and minimal recombination since too small domain sizes enhance nongeminate bimolecular recombination [80]. Morphology can be influenced and controlled by the processing parameters like solvents, processing temperatures and additives.

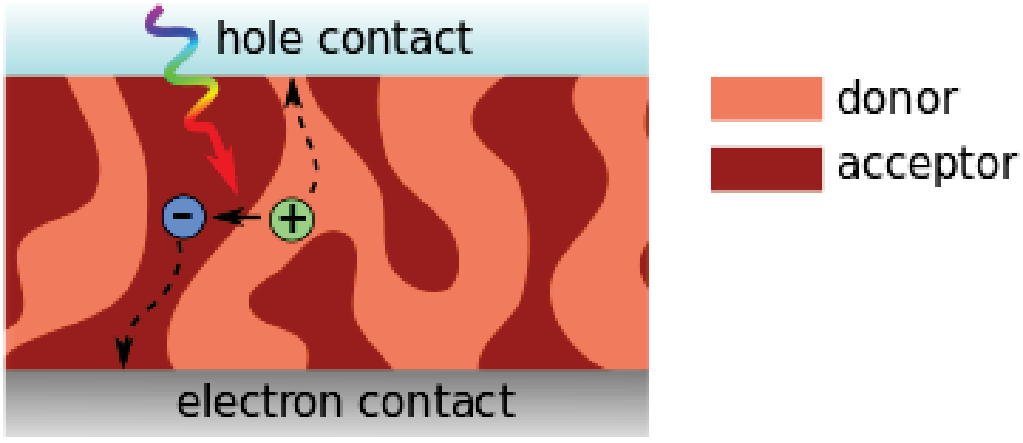

Figure 2.11: Scheme of an organic bulk-heterojunction solar cell consisting of an interpenetrating network of donor and acceptor phases. Photogenerated excitons get split at a D-A interface into free charge carriers. Electrons are transported on the A phase to the electron contact and holes on the D phase to the hole contact. Modified from ref. [25].

Chapter III

Materials and Methods

In this chapter the layout and preparation of organic solar cells used for the presented studies are described and the utilized materials are listed. Further, experimental methods and setups and the applied simulation methods are described.

3 Device Preparation

The preparation of an organic photovoltaic cell using indium tin oxide (ITO) as transparent electrode and a second opaque metal contact is exemplary described here in detail. In case the preparation of a sample differs from the discussed procedure it will be described adequately in the text. Organic solar cells in the described architecture are illuminated through the substrate. To allow the light to enter the cell and be absorbed by the photo-active layer (PAL) a glass substrate in combination with a transparent electrode is used. For this, the 2.5 mm × 2.5 mm substrate is coated with a structured, transparent and conductive ITO layer serving as one electrode depicted in figure 3.1(a). The substrates are cleaned using isopropanol, acetone and deionised water each for 5 min in an ultrasonic bath. Then they are UV-ozone treated for 20 min to remove organic residuals [81] and modify the surface tension ensuring good wetting of solvents for further processing [82], [83]. In the next step a poly(3,4-ethylenedioxythiophene) polystyrene sulfonate (PEDOT:PSS) layer is spin coated on top of ITO to ensure sufficient selectivity of the resulting hole contact. After spincoating the PEDOT:PSS layer is structured by wiping with ethanol (figure 3.1(b)), transferred to an inert nitrogen

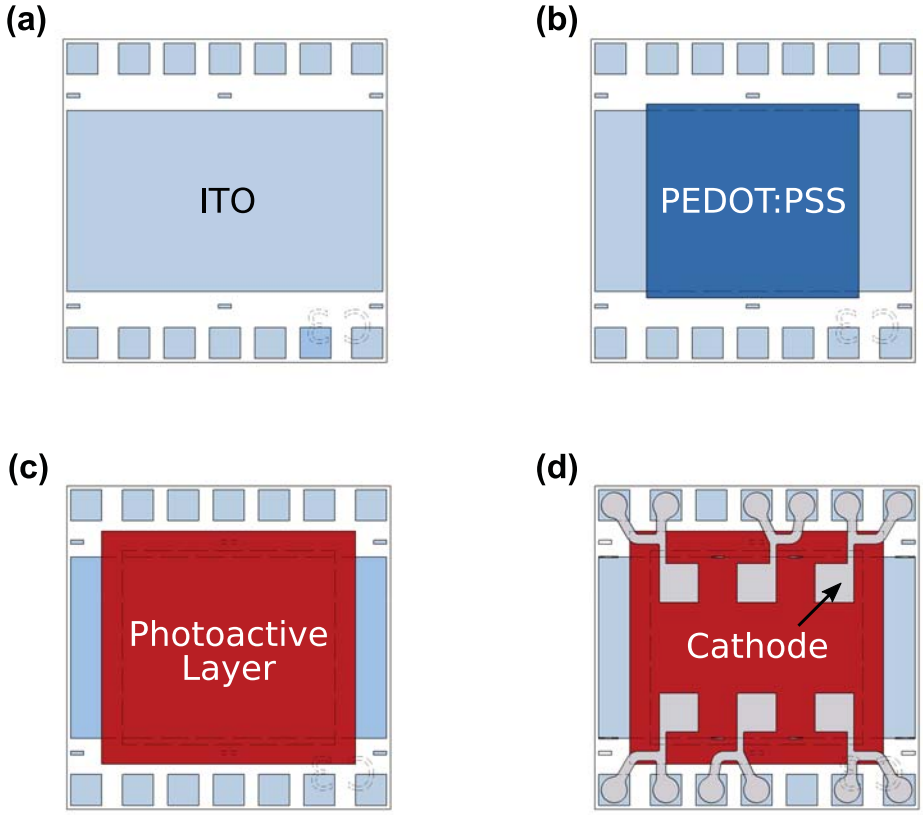

Figure 3.1: Schematic of an ITO based solar cell layout in different processing stages. **(a)** Glass substrate with pre-structured transparent ITO (light blue) electrode. **(b)** The hole selective PEDOT:PSS layer (blue) is added. **(c)** the photoactive layer (red) is processed and the structured electron selective LiF/Al electrode is evaporated **(d)**. Technical drawings were provided by Hans Frieder Schleiermacher.

atmosphere and anealed at 130 °C for 15 min. After that, the PAL is applied via spin coating a blend containing donor and acceptor material solved in an orthogonal solvent to hinder the underlying PEDOT:PSS to get dissolved unintentionally. After structuring the PAL by solvent wiping in the manner depicted in figure 3.1(c) the sample is annealed again to remove remaining solvent from the PAL and affect the morphology of the bulk-heterojunction. In the last step the sample is transferred to an evaporation chamber where a thin (≈ 3 nm) lithium fluoride (LiF) layer for contact selectivity and an opaque aluminum electrode are evaporated as shown in figure 3.1(d) at a pressure below 5×10^{-6} mbar resulting in 6 individual cells (pixels) on one sample with an active area of 0.0925 cm^2 each. Figure 3.2 (a-d) shows an alternative ITO-free device architecture with an opaque chromium-aluminum-chromium (Cr/Al/Cr) metal electrode evaporated on top of the substrate. In this configuration the cell is illuminated through the top anode. The deposition of the subsequent layers is done in the previously described ways

and will not be discussed in detail. The cross-sections of the resulting ITO-based and ITO-free cells are illustrated in figure 3.3.

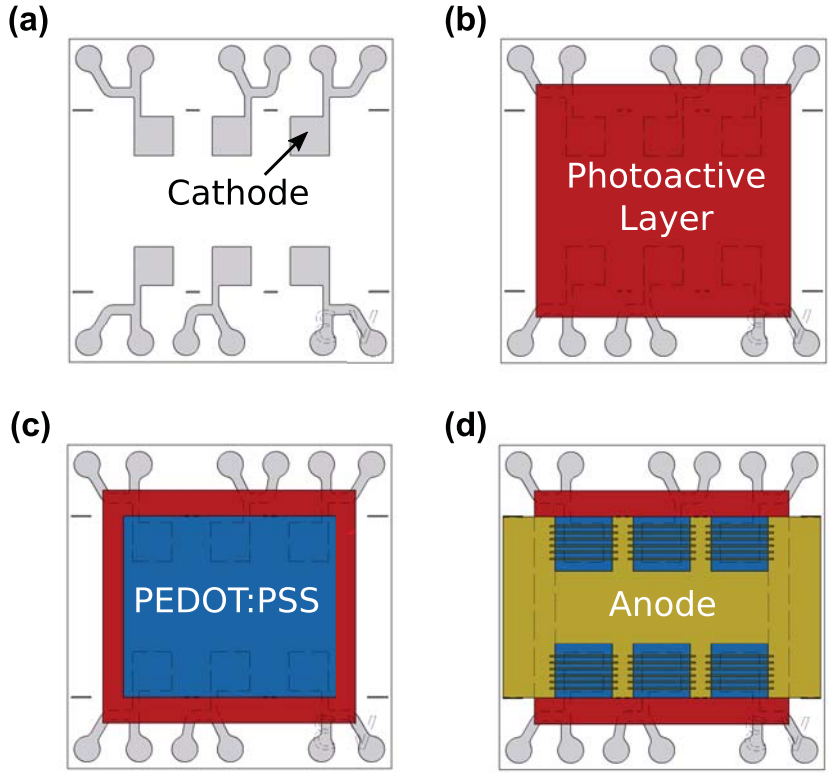

Figure 3.2: Schematic of the layers of an ITO-free solar cell. **(a)** Glass substrate with structured Cr/Al/Cr (grey) electrode and **(b)** with the photoactive layer (red) on top. **(c)** Hole selective PEDOT:PSS layer and **(d)** gold(Au) anode grid with support structure. Technical drawings were provided by Hans Frieder Schleiermacher.

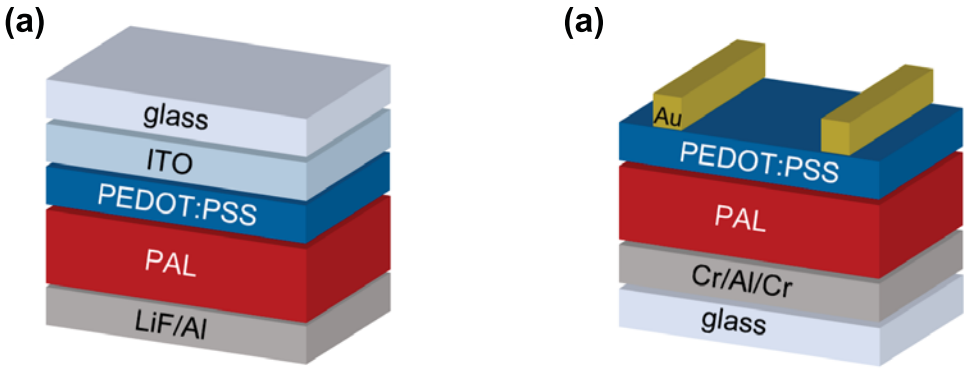

Figure 3.3: Layer stack of an ITO based **(a)** and ITO-free **(b)** organic solar cell with the illumination side at the top. The photoactive layer (PAL) is depicted in red. The electron contacts are lithium fluoride/aluminum (LiF/Al)(a) and chromium/aluminum/chromium (Cr/Al/Cr)(b). Both architectures feature PEDOT:PSS (blue) as hole selective layer but an indium thin oxide (ITO) or gold (Au) anode, respectively.

4 Materials

In the following the used donor, acceptor and inter-layer materials are listed. The IUPAC nomenclature is given and the chemical structure is depicted for the photoacive materials (if available).

Materials for Charge Selective Window-Layer

PEDOT:PSS Clevios^{TM} AI 4083 (PEDOT AI): Poly(3,4-ethylenedioxythiophene) polystyrene sulfonate formulation; purchased from Heraeus

PEDOT:PSS Clevios^{TM} F HC Solar (PEDOT FHC): Formulation; purchased from Heraeus

PEIE: Polyethylenimine ethoxylated; purchased from Sigma-Aldrich

ZnO Avantama N-11: Zinc oxide nanoparticle from solution; purchased from Avantama AG

Donor Materials

P3HT: Poly(3-hexylthiophene-2,5-diyl); purchased from Rieke Metals or from BASF SE

PCDTBT: Poly[N-9'-heptadecanyl-2,7-carbazole-alt-5,5-(4',7'-di-2-thienyl-2',1',3'-benzothiadiazole)]; purchased from 1-Material

PTB7-Th (PCE10): Poly[4,8-bis(5-(2-ethylhexyl)thiophen-2-yl)benzo[1,2-b;4,5-b']dithiophene-2,6-diylalt-(4-(2-ethylhexyl)-3-fluorothieno[3,4-b]thiophene-)-2-carboxylate-2--6-diyl)]; purchased from Solarmer

PBDB-T: Poly[(2,6-(4,8-bis(5-(2-ethylhexyl)thiophen-2-yl) - benzo[1,2-b:4,5-b']dithiophene))- alt -(5,5-(1',3'-di-2-thienyl-5',7'- bis(2-ethylhexyl)benzo[1',2'-c:4',5'-c']dithiophene- 4,8-dione))]; purchased from Solarmer

PBTZT-stat-BDTT-8 (P1): The complete IUPAC nomenclature is not available; purchased from Merck

PV2000: The IUPAC nomenclature and chemical structure are not available; purchased from Raynergy Tek

PffBT4T-2OD: Poly[(5,6-difluoro-2,1,3-benzothiadiazol-4,7-diyl)-alt- (3,3"'-di(2-9 octyldodecyl)-2,2';5',2";5",2"'-quaterthiophen-5,5"'- diyl); purchased from Solarmer

Acceptor Materials

$PC_{61}BM$: Phenyl-C_{61}-butyric acid methyl ester
purchased from Solenne

$PC_{71}BM$: Phenyl-C_{71}-butyric acid methyl ester
purchased from Solenne

ITIC: 3,9-bis(2-methylene- (3-(1,1-dicyanomethylene)-indanone))-5,5,11,11-tetrakis(4-hexylphenyl)- dithieno[2,3-d:2',3'-d']-s-indaceno[1,2-b:5,6-b'] dithiophene)
from Solarmer

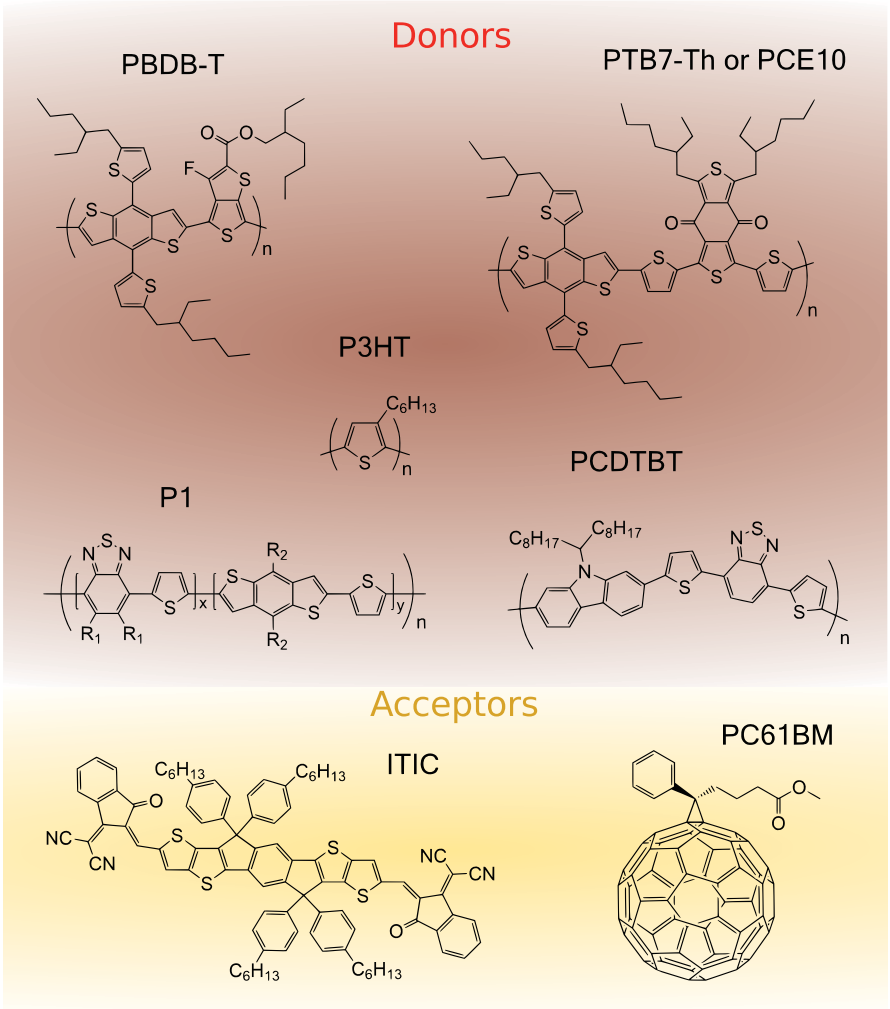

Figure 4.1: Chemical structure of selected donor and acceptor materials that were used within this work. The donor materials PBDB-T, PTB7-Th, P3HT and P1 are illustrated with the acceptors: $PC_{61}BM$ and ITIC. The illustration is taken from the PhD thesis of Spies [18]

5 Characterization Methods

In the following section the characterization methods used in this work are introduced and the experimental setups are explained.

5.1 Current-Voltage Measurement

The Current-Voltage (IV) measurement is usually the first characterization of a solar cell to obtain the figures of merit. The IV-curves presented in this thesis were obtained in a four point measurement configuration by a Keithley 2400 sourcemeter. For comparability solar cells should be measured according to the IEC60904-3 II (2008) guide line. Standard testing conditions prescribe a temperature of 298.15 K and an illumination of AM1.5G. In the applied setup the cells are cooled by a fan, providing air flow to prevent significant deviation from standard conditions. Nevertheless, a reduction in V_{OC} of $10 - 20\,\mathrm{mV}$ due to warming is observed compared to the illumination with a pulsed LED with an intensity corresponding to 1 sun. The samples were illuminated by a SolarCellTest 575 sun simulator (Steuernagel). Since the spectrum of the solar simulator deviates from standard conditions a mismatch correction has to be done to mimic the irradiation of AM1.5G referred to as 1 sun. For the determination of the mismatch factor M a silicon solar cell with known spectral response $\mathrm{SR_{ref}}(\lambda)$, the spectral response of the tested cell $\mathrm{SR_{test}}(\lambda)$, the standard AM1.5G spectrum $\mathrm{E_{AM1.5G}}(\lambda)$ and the spectrum of the solar simulator $\mathrm{E_{SoSi}}(\lambda)$ are needed. M is calculated by:

$$M = \frac{\int_0^\infty E_{\mathrm{AM1.5G}}(\lambda) SR_{\mathrm{ref}}(\lambda) d\lambda}{\int_0^\infty E_{\mathrm{SoSi}}(\lambda) SR_{\mathrm{ref}}(\lambda) d\lambda} \cdot \frac{\int_0^\infty E_{\mathrm{SoSi}}(\lambda) SR_{\mathrm{test}}(\lambda) d\lambda}{\int_0^\infty E_{\mathrm{AM1.5G}}(\lambda) SR_{\mathrm{test}}(\lambda) d\lambda} \tag{5.1}$$

$$= \frac{J_{\mathrm{sc,ref,AM1.5G}}}{J_{\mathrm{sc,ref,SoSi}}} \cdot \frac{J_{\mathrm{sc,\ test,\ SoSi}}}{J_{\mathrm{sc,test,AM1.5G}}} \tag{5.2}$$

The following condition has to be fulfilled under standard condition:

$$J_{\mathrm{SC,test,SoSi}} = J_{\mathrm{SC,test,AM1.5G}}. \tag{5.3}$$

Now equation (5.2) can be written as:

$$J_{\mathrm{SC,ref,SoSi}} = \frac{J_{\mathrm{SC,ref,AM1.5G}}}{M} \tag{5.4}$$

Under the assumption of a constant spectral shape for differing intensities of the sun simulator, the latter can be adjusted till equation (5.4) is fulfilled. Thereafter equation (5.3) is fulfilled as well and the solar cell's J_{SC} equals the one under AM1.5G illumination.

5.2 Illumination and Temperature Dependent Current-Voltage Measurements

Illumination intensity I and temperature dependent measurements of current and voltage can be used to get insight in in the prevalent processes in organic solar cells. In this work especially V_{OC} is studied. The used setup is schematically illustrated in Figure 5.1. A collimated green LED with a custom made driver circuit (sourcing 1 A) was used for illumination while the intensity was varied with neutral density filters with transmittances T_λ (NG glass from Schott AG). To obtain V_{OC} at a desired temperature, it was measured using pulsed light (6.8 Hz) to minimize the effect of heating induced by illumination. Figure 5.2(a) shows the influence of illumination on the measured V_{OC} of a PCDTBT:$PC_{61}BM$ OSC. Especially at low temperatures and for high intensities, heating of the sample affects the results in case of continiuous illumination. A pulse-pause ratio (duty cycle) of illumination of 0.1 % was used in case of high intensities to allow for proper thermalization to the desired temperature while the pulse length t_{illu} was set to reach the steady state ($t_{illu} \approx 50\,\mu s$ for $I \geq 1$ sun). For low intensities t_{illu} had to be increased gradually to obtain steady state conditions. Since at low light intensities the energy input to the system is small, no detrimental loss in V_{OC} is observed. The influence of the input resistance R_p of the voltmeter is plotted in figure 5.2(b). It can be seen that the input impedance of 1 MΩ or 10 MΩ of standard oscilloscope probes is

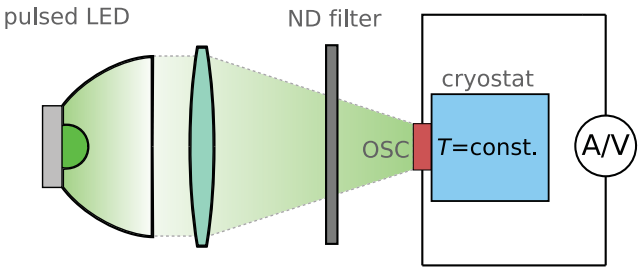

Figure 5.1: Schematic illustration of the setup for intensity and temperature dependent measurements of V_{OC} and J_{SC}. For illumination a pulsed green LED with collimating optics is used to illuminate the OSC (depicted in red). The intensity is varied via neutral density (ND) filters, the cell temperature is controlled by a cryostat (blue) and the J_{SC} or V_{OC} is measured by a ammeter or voltmeter, respectively.

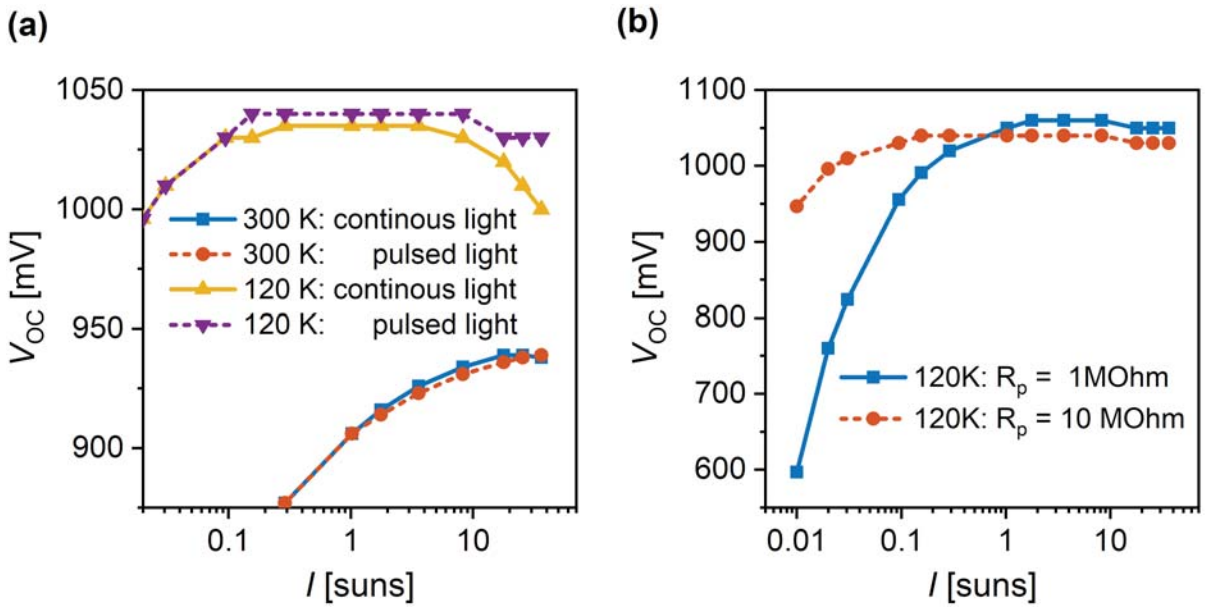

Figure 5.2: V_{OC} of a PCDTBT:$PC_{71}BM$ OSC for pulsed illumination and continuous illumination as function of illumination intensity (a) at different temperatures. V_{OC} as function of illumination intensity (pulsed) for different external shunt resistances (b).

not high enough to hinder a breakdown of the voltage at low intensities in the low temperature regime. To ensure a V_{OC} measurement with negligible external current flow, a custom build buffer amplifier with an input impedance $R_{in} > 10\,G\Omega$ and of appropriate bandwidth was utilized.

The relative intensity $I = J_{SC}/J_{SC,AM1.5G} = T_\lambda/T_{\lambda,AM1.5G}$ is calculated in units of suns. Thus, green illumination with an Intensity of 1 sun results in the same generation current as illumination with AM1.5G ($1000\,W\,m^{-2}$). Here $T_{\lambda,AM1.5G}$ is the filter transmittance resulting in a generation current density $J_{SC,AM1.5G}$ according to 1 sun. It is determined by linear extrapolation of $J_{SC}(T_\lambda) = J_{SC,AM1.5G}$ to the measured J_{SC} values for the individual filters. In the pulsed setup J_{SC} was measured with a trans-impedance amplifier with appropriate bandwidth (TZA400 from Artifex Engineering). Temperature dependent measurements were performed in a low vibration microscopy cryostat (Model ST-550H (450K) from JANIS Cryophysics GmbH in combination with a Wessington Cryogenics TPV-30 container) cooled by liquid nitrogen. The cells are thermally contacted with low temperature Apiezon grease, while temperature of the sample is actively regulated using an electric heater controlled by a model 331 temperature controller from LakeShore. For measurements in the cryo a 260 nm thick MoO_3 cap layer is thermally evaporated on top of the OSC in order to protect the organic materials from being dissolved from the grease. The OSC were protected from dissolving by a thermally evaporated from

the grease. This cap layer had no has no impact on the solar cell performance The setup allows a minimum feasible temperature of 77 K while samples can be illuminated through the window of the cryostat.

5.3 Bias Amplified Charge Extraction

Charge extraction is a common method to investigate the charge carrier density inside organic solar cells [84–91]. In this work a modified bias amplified charge extraction (BACE) setup described by Lange et al. and Kniepert et. al [86, 92] was used to extract charge carriers from OSC. In a BACE experiment the extraction of photogenerated charges is accelerated by a voltage V_{extr} in blocking direction. This extraction voltage reduces the extraction time, thus minimizing recombination losses during extraction [92]. A illustration of the setup is shown in figure 5.3. In the original BACE experiment the cell is illuminated by a light pulse and held at the resulting $V_{\mathrm{OC}}(t)$ to obtain open-circuit conditions ($J = 0$) by a voltage source and charges are extracted immediately after the light is turned off. In the modified setup built for this work, the solar cell is held under open-circuit conditions by an open Metal-Oxide-Semiconductor Field-Effect Transistor (MOSFET) switch. Thereby, charge carriers can be extracted after a variable delay when the illumination is turned off. This enables the investigation of recombination dynamics under open-circuit conditions. A scheme of the transient signals during a BACE experiment is shown in figure 5.4. The cell is illuminated with a green LED until the steady-state is obtained (50 µs) with maximum intensity at a wavelength of 525 nm powered by a custom made driver at a current of $I_{\mathrm{LED}} = 1\,\mathrm{A}$. When the LED is turned off the cell is held under open-circuit conditions for a variable

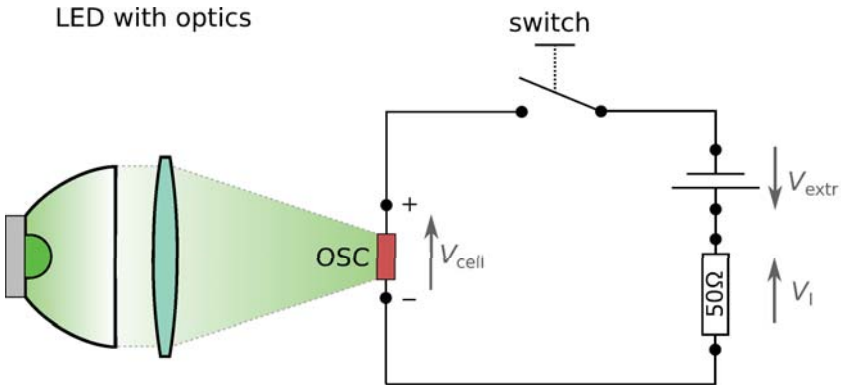

Figure 5.3: Schematic illustration of the BACE setup. The OSC is illuminated by a LED with collimating optics. Charge carriers are exacted via the extraction voltage V_{extr} when the switch is closed. The voltage of the solar cell V_{cell} and the voltage at the current sense resistor V_{I} are measured.

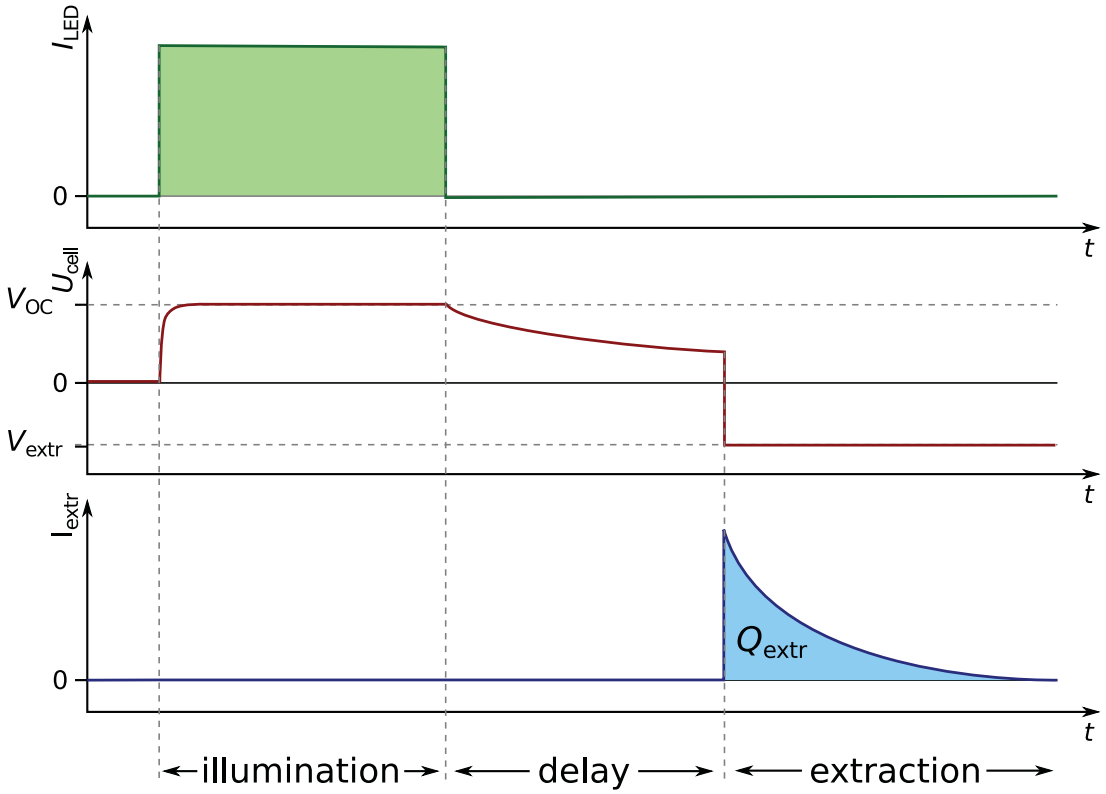

Figure 5.4: Schematic of the signals during BACE. The OSC is illuminated as long as the LED driven by I_{LED} (green area). The cell is kept under open-circuit conditions during a variable delay after illumination was turned off. Then, charge carriers are extracted by applying a negative voltage V_{extr} and the current I is recorded. The extracted charge carriers are given by the time integral over current (light blue area).

delay time. Than it is switched to V_{extr} and the current is measured by the voltage drop V_I across a 50 Ω resistor. The extracted charge is calculated as the time integral over the extraction current I.

LED lighting, delayed switching of the MOSFET and data acquisition are controlled by a custom made LabView program. The LED driver is triggered via a National Instruments multipurpose data acquisition card (Model PCI-6036e with BNC-2210 terminal) while the MOSFET is switched by a programmable Agilent 33220A arbitrary waveform generator. LED trigger signal, MOSFET gate voltage, cell voltage V_{cell} and the voltage V_I at a 50 Ω current sense resistor are recorded with a Tektronix TDS 2014 digital sampling oscilloscope and read out to a computer. The planning, realization, and testing of the described setup was within the scope of this work.

5.4 Luminescence Spectroscopy

Luminescence is the process where an excited system relaxes under the emission of a photon. In general, excitation can happen in any way. In this thesis photoluminescence (PL) and electroluminescence (EL) were used for the characterization of organic semiconductors and solar cells. In a PL experiment the sample is exited via illumination with light of appropriate wavelength. Illumination generates electrons and holes in a classical semiconductor which recombine partially under the emission of light. This radiation is measured in a PL experiment with a spectrometer. In organic BHJ solar cells light is absorbed either in the donor or the acceptor phase forming bound excitons. In a propper working device most excitons are split at the D-A interface generating free electrons and holes. However, excitons which are not split within their lifetime recombine partially under the emission of a photon, while electrons and holes can recombine during the generation process at the D-A interface or when they meet at such interfaces subsequently. Both processes, the decay of excitons and free charge can be accompanied by the emission of radiation. Figure 5.5(a) shows a schematic of the radiative recombination pathways within an OSC.

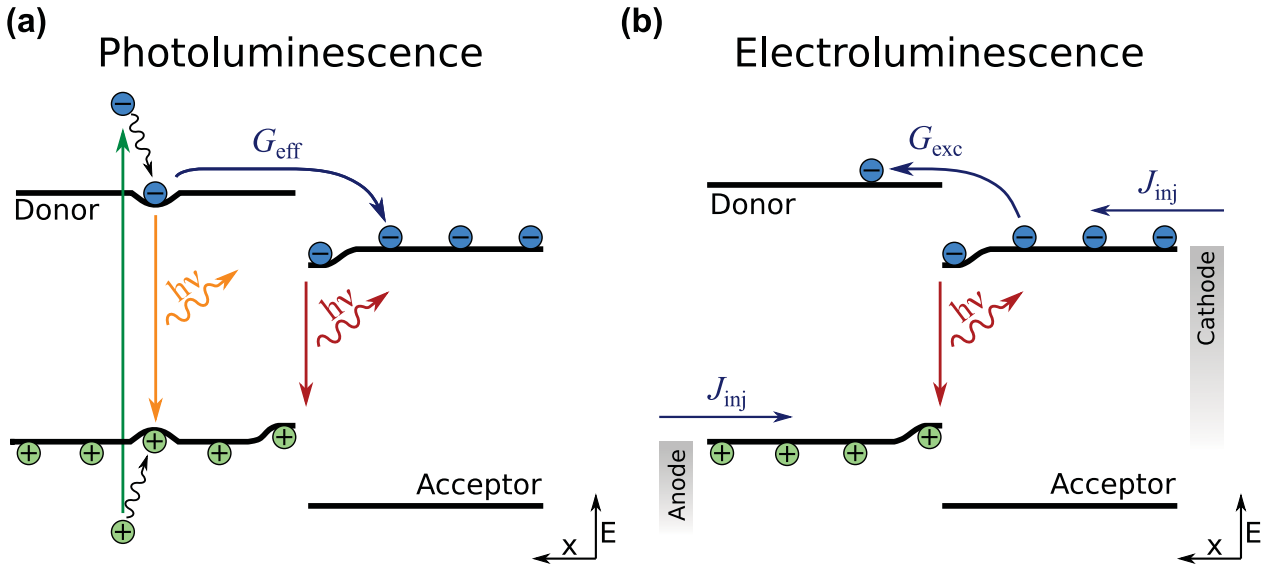

Figure 5.5: (State diagram with the relevant processes for photoluminescence (PL) **(a)** and **(b)** electroluminescence (EL). For PL the photo-excitation is depicted with a green arrow. The generated excitons on the donor material can either decay (orange) or dissociate into free charge (G_{eff}). The latter can recombine radiatively at a DA interface (red). For EL charge carriers are injected (J_{inj}). They either recombine (red) or generate excitons (G_{exc}) on the donor while the latter was not observed within this work.

In an EL measurement electrons and holes are injected into the semiconductor by their corresponding contacts. Free electrons and holes meet at the D-A interface where they recombine partially radiative which is depicted in figure 5.5(b). In general injected electrons and holes could generate excitons (depicted as G_{exc}) by overcoming the energetic barrier at the D-A interface. However, this effect was not observed in this work. Extension, testing and characterization of the luminescence setup described below was part of the present work and done in close cooperation with T. Sarkar. A comprehensive description and detailled information about the performance and charactristics of the setup can be found in the master thesis of Sarkar [51]. The luminescence spectra presented in this manuscript were measured in a setup consisting of a Czerny-Turner spectrograph (Andor Shamrock 193i) with an Indium Gallium Arsenide (InGaAs) photo diode array (Andor iDus DU490A) which was cooled to -70 °C. The spectrograph is equipped with two interchangeable diffraction gratings optimized for 860 nm and 1200 nm, both featuring 300 lines/mm. The present InGaAs detector has a usable range of approximately 600 nm to 1600 nm with a peak quantum efficiency of over 85%. To prevent the background from drifting over the required measurement time (up to 45 min) an active temperature control utilizing Peltier elements was installed to the enclosure of the spectrograph, since a significant part of the field of view of the detector measures the inner walls of the spectrograph. The sample is imaged to the plane of the entrance slit of the spectrograph by a collimating system with an angle of acceptance of approximately 10° (full angle), consisting of 2 planar-convex lenses with a 1050 nm to 1600 nm anti reflection coating (Thorlabs, c-coating). For photoexcitation in PL experiments a frequency doubled neodymium-doped yttrium aluminum garnet (Nd:YAG)-laser with a wavelength of 532 nm was used passing through a convex diffuser lens to give a homogeneous illumination of the sample. A schematic of the luminescence setup is shown in figure 5.6. If not stated differently, the laser intensity was set to generate a J_{SC} approximately equal to AM1.5G illumination of the corresponding sample. In all cases PL was performed at illumination intensities comparable to realistic operation conditions of solar cells. To avoid peaks from the second diffraction order of the grating a 640 nm dielectric long pass filter (Edmund Optics) was placed before the collimator to stop the green excitation light from entering the spectrograph. An additional 720 nm long pass color glass filter (Thorlabs) was utilized for measurements up to 1300 nm and a 850 nm filter (Thorlabs) for measurements up to 1600 nm. The spectra are corrected for the setup's spectral sensitivity using a custom built reverence lamp (reference spectrum was measured by Fraunhofer ISE CalLab). The given intensities are not absolute values,

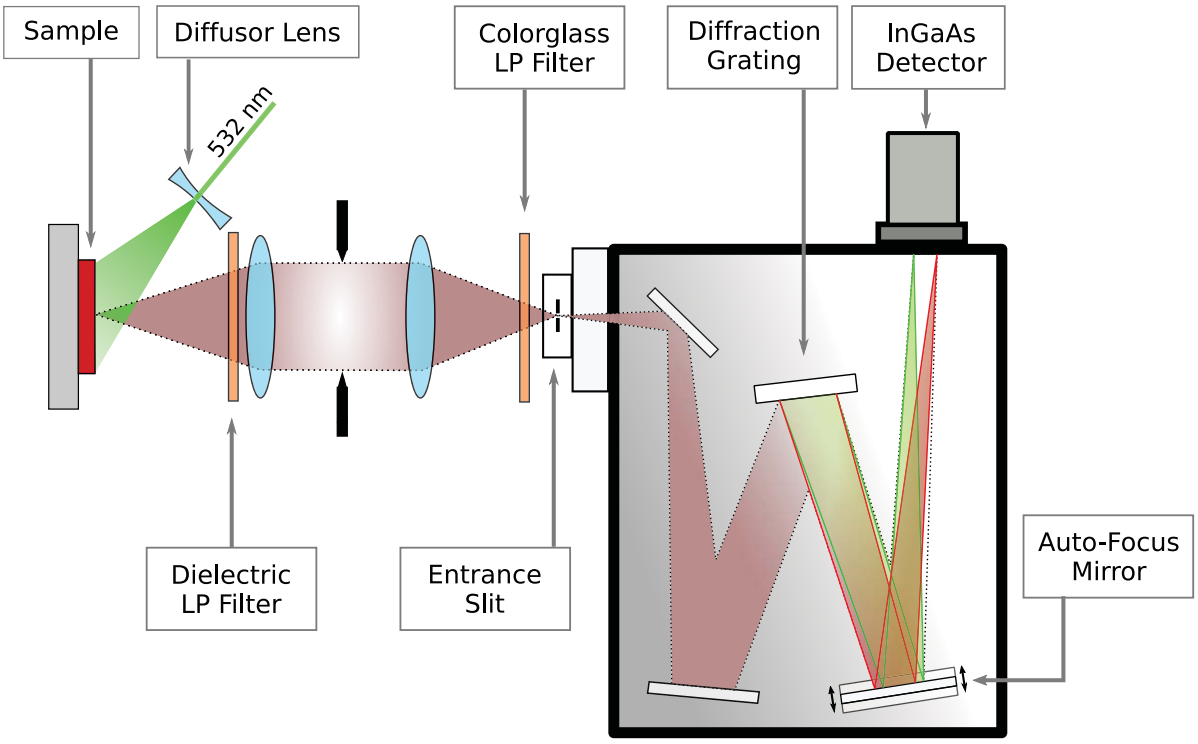

Figure 5.6: Illustration of the setup used for luminescence spectroscopy measurements presented in this work. Within the setup the sample can be excited by a laser for PL. The cell can be connected to an electric sourcemeter to control the working point of the device or inject charge carriers for EL.

nevertheless all measured spectra have the same relative unit (in respect to the reference lamp) and the magnitudes can be compared among each other. The working points of the OSC were controlled by a Keithley 2400 sourcemeter. All presented luminescence spectra in this work are measured in an inert nitrogen atmosphere. The width of the entrance slit of the spectrograph was 2 mm for P3HT:$PC_{61}BM$ and 0.5 mm for all other materials.

5.5 Reflection and Transmission Measurements

Reflection and transmission measurements were performed to obtain the refractive index n and extinction coefficient k of materials included in optical simulations within this work. The reflectance R_λ and transmittance T_λ were measured with a UV-Vis-NIR (PerkinElmer LAMBDA 950) equipped with an integrating sphere. The n and k values were determined by fitting dielectric functions from theoretical models to the experimental data with the commercial software SCOUT from W. Theiss Hard- and Software. A comprehensive description of the procedure including theoretic fundamentals, common

dielectric models and the fitting procedure can be found in the PhD thesis of Seßler [25]. The layer thicknesses, needed to create the optical models of the investigated materials, were measured with an Veeco Dektak 150 surface profilometer. The author thanks Annika Spies for the contribution of many n and k values utilized within this work and Patricia Schulze for reflection and transmission measurements.

6 Numerical Simulation Methods

Interpretation of experimental results often requires the comparison to simulated predictions from different theoretical models, thus numerical simulation tools are indispensable in the research of organic electronics. Dependent on the spatial resolution and the degree of physical detail a variety of simulation methods exists. Starting from a rather coarse description of the system by a network of electrical components in an equivalent circuit model, to detailed simulation of certain phenomena on the molecular level (e.g. density functional theory or Monte Carlo simulations). So, it is dependent on the underlying phenomena which simulation technique is expedient. A good overview and detailed introduction to the simulation of organic solar cells is given by Tress [93].

6.1 Drift-Diffusion Simulations

Drift diffusion simulations are an continuum approach to simulate the position-dependent properties within a solar cell and thus an intermediate approach between more detailed simulations on the atomic level and, e.g., the more coarse equivalent circuit or diode model introduced in chapter 2.1. It was shown that the detail of drift-diffusion simulations is sufficient for an accurate description of the most relevant physical processes in semiconducting devices and in particular for the description of organic solar cells [18, 93–99]. Although the author did not perform any drift-diffusion simulations, results from simulations are a key factor in the description and understanding of the experimental observations shown in the following. Therefore, only a short description of the theoretical framework of drift-diffusion simulations will be given here. These simulations mathematically describe the transport of quasi-free charged particles by solving the continuity equations (1.15) and (1.16) and transport equations (1.21) and (1.22) for electrons and holes which are coupled by the Poisson equation (1.17). A detailed derivation from the Boltzmann transport equation can be found, e.g., in the textbook of Jacoboni [100]. The set of differential equations is numerically solved using boundary conditions given by equations (1.26), (1.27) and (1.28), (1.29) describing Schottky contacts for the simula-

tions in this work. The electric potential φ of one contact is set to zero. The electrostatic potential of the second contact is described by $e_0\varphi = E_\mathrm{F} - \Phi_\mathrm{B} + k_\mathrm{B}T \ln(N_\mathrm{C}/n_\mathrm{i})$. Here, E_F is the Fermi energy at the contact and equals the applied external voltage and Φ_B the injection barrier introduced in section 1.5.1. A more comprehensive description of the fundamentals of drift-diffusion simulations, a detailed discussion on the applicability of the drift-diffusion approach on OSC, a description of the used software and a detailed description of the individual simulations shown in this work can be found in the PhD thesis of Spies [18].

6.1.1 The Effective Semiconductor Model

Here the one-dimensional effective semiconductor (ES) model used in drift-diffusion simulations is introduced. In the ES model the complex morphology of a donor-acceptor bulk-heterojunction is replaced by a homogeneous medium referred to as effective semiconductor as depicted in figure 6.1 for the case of a one-dimensional ES. The obvious benefits of the one-dimensional ES model are the reduction of dimension and required parameters which results in reduced computation time. Material properties influenced by the morphology (e.g. mobility) or by the energy level of the underlying D-A system (e.g. generation rates) are transferred into effective parameters. Thus, e.g., the complex mechanism of generation of free carriers via the separation of excitons involving a CT state is transferred into an effective generation rate G_eff for free electrons and holes. The ES model can resemble the results of a two-dimensional A-D model for varying transport properties and doping densities quite accurately as shown in the PhD thesis of Stelzl [95]. However, the ES model is limited and not capable to reproduce characteristics specific to heterogeneous system like e.g. simultaneous n-doping of the acceptor and p-doping of the donor phase.

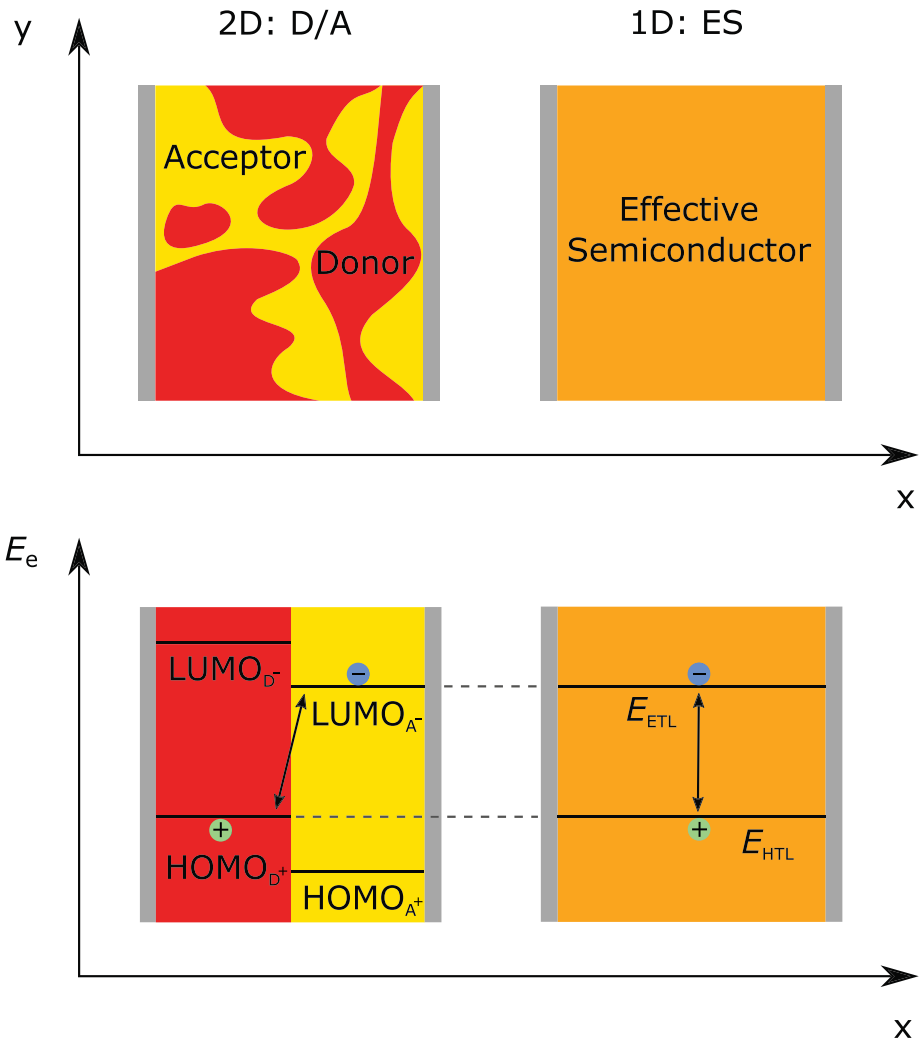

Figure 6.1: Illustration of the transformation from a 2-dimensional donor acceptor (D/A) to a 1-dimensional ES Model. On the top the morphology and on the bottom the respective energy level diagrams are depicted. For a one-dimensional ES model, only transport normal to the electrodes is considered. Modified from ref [18].

6.2 Optical Scattering-Matrix Simulations of Radiative Out Coupling

In this section the scattering-matrix (S-matrix) formalism will be introduced very briefly while a detailed description of the specific simulations used in this work and their analysis is given in the results section. A comprehensive description of the S-matrix formalism is however beyond the scope of this work. The utilized MATLAB code is based on the work of Oliver Höhn [101] and on the bachelor thesis of Florian Bödicker [102], where an in-depth description and derivation of the formalism can be found. Their work is mainly based on the parameterization given in [103, 104].

The S-matrix method describes the propagation of electromagnetic waves in a multilayered system. The propagation through a layer is described by the (scattering-) matrix **S**. It connects the amplitudes $\vec{I}_i$ of the incoming and $\vec{O}_i$ of the outgoing waves by:

$$\begin{bmatrix} \vec{O}_1 \\ \vec{O}_2 \end{bmatrix} = \begin{bmatrix} S_{11} & S_{12} \\ S_{21} & S_{22} \end{bmatrix} \cdot \begin{bmatrix} \vec{I}_1 \\ \vec{I}_2 \end{bmatrix}$$

Here $\vec{I}_1$ and $\vec{O}_1$ are the amplitudes before (to the left of) and $\vec{I}_2$ and $\vec{O}_2$ after the layer as depicted in figure 6.2. The diagonal elements S_{11} and S_{22} describe the reflections at the interfaces according to the Fresnel equations and the elements S_{12} and S_{21} give the transmission through the layer. The construction of the S-matrix describing the propagation through multiple layers is a recursive process described in the appendix of [101]. There the implementation of an electromagnetic dipole emitter at an interface used in this work is explained in detail, as well.

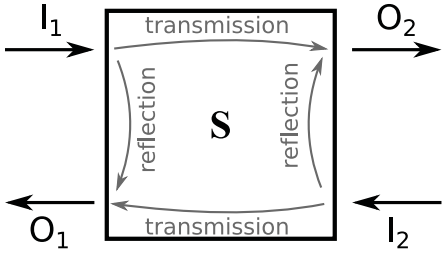

Figure 6.2: Schematic illustratin of the S-matrix methid. I_1 and O_1 are the amplitudes of the electromagnetic wave before and $_2$ and O_2 after a layer.

Chapter IV

Results and Discussion

Experimental results from the characterization of organic solar cells are presented, analyzed and discussed in this chapter. The individual studies focus on charge extraction to determine the bulk recombination properties of different absorber materials, V_{OC} losses due to surface recombination and their underlying processes, temperature and intensity dependent electronic measurements to obtain the effective band gap of organic donor-acceptor systems and a correction procedure for luminescence spectra to determine the charge transfer state energy accurately. The results of the individual studies are compared among each other and with literature, which leads to a more comprehensive understanding of the origin of V_{OC} of OSC.

7 Charge Extraction from Organic Solar Cells

This chapter presents results from charge extraction experiments, explains the origin of capacitive charges in organic solar cells as well as their influence on common transient experiments and introduces a novel technique to determine bulk recombination coefficients.

The densities of electrons and holes in the photocative layer of solar cells are figures of great interest. They determine the QFL splitting and recombination within the bulk of a semiconductor. Charge carrier densities are commonly obtained from extraction experiments in literature [84–92]. For this work, carriers were extracted with the BACE method using the setup described in chapter 5.3. There, the OSC is initially under

open-circuit conditions and a light pulse generates excess carriers. After generation the carriers will recombine for a variable period (delay). After that, a voltage V_{extr} in reverse direction is applied for fast collection of charge carriers. The extraction is repeated for a series of delay times to investigate recombination dynamics.

7.1 Capacitance of Organic Solar Cells

This section explains the presence and origin of capacitive charges in OSCs, their occurrence in transient extraction experiments and shows exemplary data from a P3HT: $PC_{61}BM$ solar cell. Figure 7.1(a) shows a scheme of the space charge ρ in an exemplary device in the dark ($V = 0\,\mathrm{V}$) with selective semiconductor-metal contacts as described in chapter 1.5. At the electron contact, the metal injects electrons into the ETL and at the hole contact, holes into the HTL. This results in charged regions in the semiconductor and corresponding charges in the metal. By applying a voltage V_{extr} in blocking direction, these regions get recharged. As a result, the hole contact region gets more negative and the electron contact region more positive, as depicted in figure 7.1(b). A transient capacitive current observed during BACE accompanies this recharging.
Note that a corresponding charge exists for all contact types, which becomes obvious by considerations about the voltage between the electrodes of a solar cell. It is zero in the dark when no external voltage is applied. Thus the Fermi energies of the contacts are equal. Dependent on the workfunctions of the metal electrodes a characteristic shift of

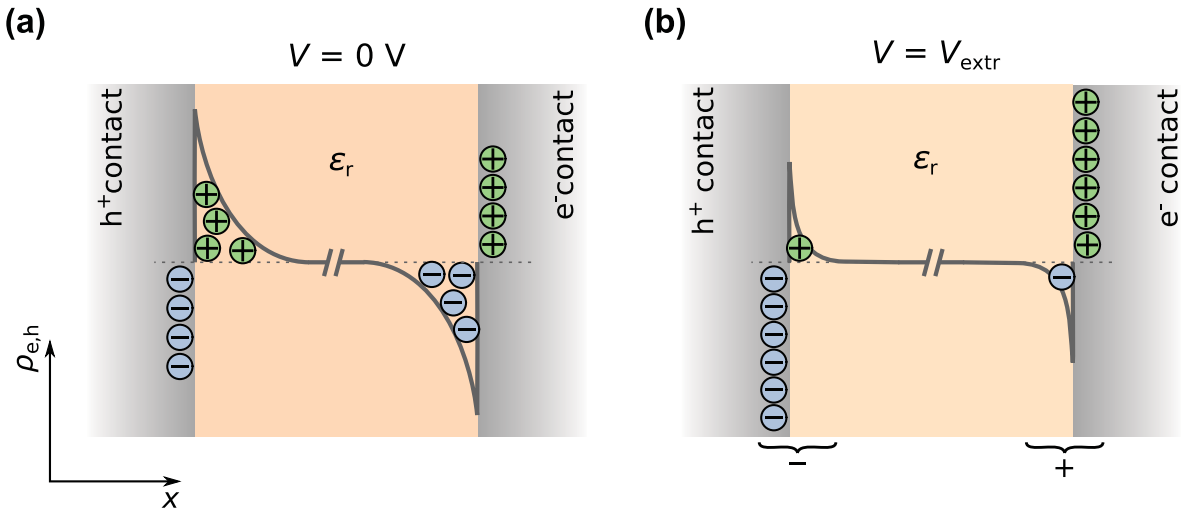

Figure 7.1: Space charge ρ as a function of the position x within the solar cell for metal-semiconductor contacts. **(a)** Shows the case of thermodynamic equilibrium at $V = 0\,\mathrm{V}$ between electron and hole contact. **(b)** the space charge regions get recharged when an extraction voltage V_{extr} is applied across the electrodes.

$e_0 V_{\mathrm{bi}} = W_{\mathrm{F,e.cont}} - W_{\mathrm{F,h.cont}}$ the vacuum level between both contacts arises. This shift is referred to as built-in voltage V_{bi}. When an external voltage e.g. V_{extr} is applied, the Fermi energies of the contacts differ by $e_0 V_{\mathrm{extr}}$. Hence, the alignment of the vacuum levels must change by $e_0 V_{\mathrm{extr}}$. The latter is causes by a corresponding change of the electric potential between the contacts (although $e_0 V_{\mathrm{extr}}$ is an electrochemical potential). This requires recharging across the device since a change in electric charge is needed to alter the electric field.

Figure 7.2(a) shows transient extraction currents I_{extr} for different extraction voltages V_{extr} from a P3HT:$PC_{61}BM$ solar cell measured in the dark[1]. The cell was switched from $V = 0\,\mathrm{V}$ to V_{extr}. It can be seen that most carriers are extracted in the first 500 ns. The observed fall-time of the dark extraction current compares well with the characteristic RC-time of the system. It is $\tau_{\mathrm{RC}} = R_{\mathrm{S}} \cdot C_{\mathrm{geo}} = 50\,\Omega \cdot 1.6\,\mathrm{nF} = 80\,\mathrm{ns}$, considering the $50\,\Omega$ series resistor used for current sensing during BACE. Figure 7.2(b) shows the extracted charge $Q_{\mathrm{extr}} = \int_0^\infty I_{\mathrm{extr}}(t)dt$ as function of V_{extr} together with a linear fit to the data. The slope there is the capacitance (C_{cell}) of the OSC according to the differential

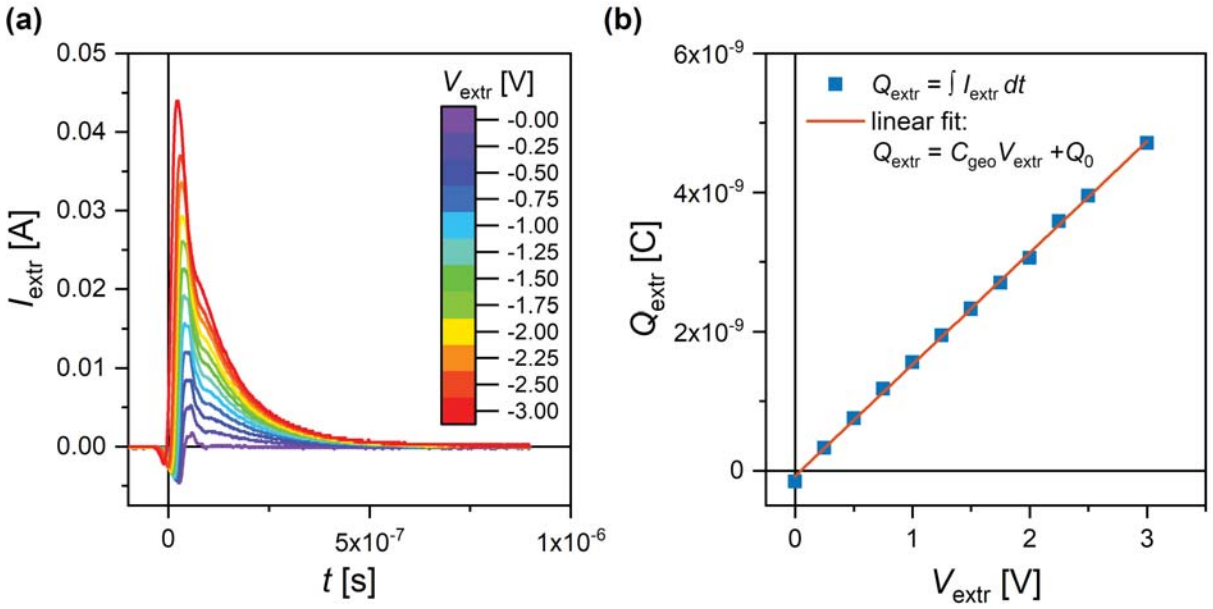

Figure 7.2: **(a)** Dark extraction current I_{extr} for different extraction voltages V_{extr} over time of a P3HT:$PC_{61}BM$ OSC. **(b)** Extracted charge as a function of V_{extr} with a linear fit to the data.

[1] The measured device was built in the architecture depicted in figure 3.3(a) with a 220 nm thick absorber layer, a PEDOT:PSS hole contact and a LiF/Al electron contact. The used P3HT was purchased from Rieke Metals.

definition of capacitance $C(V) = \frac{\partial Q}{\partial \varphi}$. A linear fit with a slope of $C = 1.603\,\mathrm{nF}$ (with y-axis intercept of $Q_0 = 0.015\,\mathrm{nF}$) describes the data accurately. Thus, the cell shows a constant dark capacitance in blocking direction over the investigated voltage range. It originates in the geometry of the cell stack. For an OSC with D-A materials with no significant doping, the intrinsic conductivity in the bulk is negligible. Thus it can be considered as a dielectric medium with dielectric constant ϵ_r sandwiched between the contacts (neglecting the expansion of the charged regions due to injection from the contacts). This geometry corresponds to a plate capacitor with a theoretical geometric capacitance C_geo of:

$$C_\mathrm{geo} = \epsilon_0 \epsilon_r \frac{A}{d} \tag{7.1}$$

with the cell area A and the distance d between the electrodes. Using this a dielectric constant of $\epsilon_\mathrm{r} = 4.3$ results for $A = 0.0925\,\mathrm{cm}^2$, $d = d_\mathrm{PAL} = 220\,\mathrm{nm}$ and $C_\mathrm{geo} = C_\mathrm{cell} = 1.603\,\mathrm{nF}$. The width of injected space charges from the electrodes may reduce the thickness of the intrinsic region of the PAL in the real device. Thus a reduced effective layer thickness $d_\mathrm{PAL,eff}$ may be considered for an accurate description of the capacitance within this model. The latter results in a lower ϵ_r[1]. This in the expected range of of 3 – 4 commonly observed values for organic materials used for OSC. Regardless of this deviations, the simple models of a plate capacitor has proven to approximate the observed capacitance of OSCs in blocking direction in the dark quite accurately during this work, thus, $C_\mathrm{cell} \approx C_\mathrm{geo}$ is found to be a reasonable assumption under these conditions.

The capacitive charge originates from the change of space charge within the device. It causes no additional recombination within the absorber layer in the dark. The dark recombination rate is given by $R(x) = k_\mathrm{r} \left(n_\mathrm{e}^0(x) n_\mathrm{h}^0(x)\right)^{\beta/2} = k_\mathrm{r} n_\mathrm{i}^\beta = R_0$ (using the Boltzmann approximation). This holds true for every position, even in the contact regions with high injection. Thus capacitive charge must be considered and subtracted respectively when recombination is studied in extraction experiments.

The model of a simple geometric capacitance is a good approximate for an OSC's capacitance in blocking direction in the dark due to the dielectric character of the absorber. This situation changes drastically under illumination when the conductivity[2] of the photoactive layer rises alongside with n_pg. The capacitance of the cell under illumination is altered. It was reported in literature that C_cell in forward-direction is strongly voltage

[1] E.g. $\epsilon_\mathrm{r} = 3.9$ for $d_\mathrm{PAL,eff} = 200\,\mathrm{nm}$.

[2] The conductivities $\sigma_\mathrm{e,h}$ for electrons or holes is given by $\sigma_\mathrm{e,h} = e_0 n_\mathrm{e,h} \mu_\mathrm{e,h}$.

and illumination intensity dependent, showing a peak at about V_{OC}. $C_{\mathrm{cell}}(V)$ in forward-direction was reported to vary by 20 – 400 % determined experimentally by impedance spectroscopy and from simulatinos [105, 106]. An exemplary $C(V)$ plot from Cho et al. is shown in figure B.1 in the appendix B. Unfortunately, the capacitance under illumination describing the change of space charge near the electrodes is not directly accessible within the presented experimental setup. It could be determined via e.g. impedance spectroscopy for a given illumination intensity. However, the cell undergoes the transition from initial open-circuit conditions under illumination to a voltage in blocking direction in the dark during BACE. Thus, the question about the correct capacitance that should be considered and its experimental determination remains.

7.2 Excess Carrier Density and Capacitive Correction

Recombination in a semiconductor depends on the product of electron and hole concentrations. In the following, the recombination of the previously described injected charge carriers in close vicinity of the contacts with photogenerated carriers is neglected[1] and no significant doping is assumed. Doing so, the photogenerated carrier densities under open-circuit conditions are much higher than the dark concentrations for illumination intensities relevant for solar cells, i.e., $n_{\mathrm{e/h}}^{\mathrm{pg}} \gg n_{\mathrm{e/h}}^{0}$. Thus, recombination in the absorber is dominated by the excess carriers under these conditions. Using equation (1.19) the recombination rate is:

$$\begin{aligned} R(x) &= k_{\mathrm{r}} \left(n_{\mathrm{e}} n_{\mathrm{h}}\right)^{\frac{\beta}{2}} \\ &= k_{\mathrm{r}} \left((n_{\mathrm{e}}^{\mathrm{pg}} + n_{\mathrm{e}}^{0}) \cdot (n_{\mathrm{h}}^{\mathrm{pg}} + n_{\mathrm{h}}^{0}) \right)^{\frac{\beta}{2}} \\ &\approx k_{\mathrm{r}} \left(n_{\mathrm{e}}^{\mathrm{pg}} n_{\mathrm{h}}^{\mathrm{pg}}\right)^{\frac{\beta}{2}} \end{aligned} \tag{7.2}$$

Hence, the photogenerated excess carrier densities are key for the investigation of bulk recombination in an intrinsic semiconductor.

The extracted charge originating from photogenerated carriers Q_{pg} is calculated by subtracting the capacitive charge Q_{cap}, with origin in recharging of the contact regions, from the total extracted charge Q_{ext}. For this, the capacitive charge is commonly considered

[1] For metal-semiconductor contacts with significant injection of carriers the high, e.g., electron density in the vicinity of the electron contact will lead to enhanced recombination of photogenerated holes in this region under illumination which can considerably contribute there, i.e. $R \approx k_{\mathrm{r}}(n_{\mathrm{pg}}^2 + n_{\mathrm{e}}^0 n_{\mathrm{pg}}) \neq k_{\mathrm{r}} n_{\mathrm{pg}}^2$. The contribution to the total recombination is neglected, since this regions are thin compared to the absorber thickness.

as the recharge of the constant geometric capacitance determined from a dark extraction for a corresponding voltage jump ΔV [92] by:

$$\begin{aligned} Q_{\mathrm{pg}}(t_{\mathrm{d}}) &= Q_{\mathrm{extr}}(t_{\mathrm{d}}) - Q_{\mathrm{cap}}(t_{\mathrm{d}}) \\ &= Q_{\mathrm{ext}}(t_{\mathrm{d}}) - C_{\mathrm{geo}}\Delta V(t_{\mathrm{d}}) \\ &= Q_{\mathrm{ext}}(t_{\mathrm{d}}) - C_{\mathrm{geo}}(V_{\mathrm{extr}} - V_{\mathrm{OC}}(t_{\mathrm{d}})) \end{aligned} \tag{7.3}$$

Here, t_{d} is the delay time between the end of illumination and the extraction, $\Delta V = |V_{\mathrm{extr}}| + |V_{\mathrm{OC}}(t_{\mathrm{d}})|$ (since the cell is pulled from V_{OC} to V_{extr} during BACE) and $V_{\mathrm{OC}}(t_{\mathrm{d}})$ is the measured open-circuit voltage of the cell immediately before extraction. Since the capacitance in forward direction deviates from C_{geo}, this correction is flawed and introduces an certain error.

Figure 7.3(a) shows the transient extraction currents I_{extr} for a P3HT:$PC_{61}BM$ solar cell using an extraction voltage of $V_{\mathrm{extr}} = -1\,\mathrm{V}$[1]. The cell was illuminated with an intensity corresponding to approximately 17 suns until a steady-state was established and charge carriers were extracted after a variable delay time t_{d}. For short delays, a significant extraction current is observed for more than 2 µs. The extraction after previ-

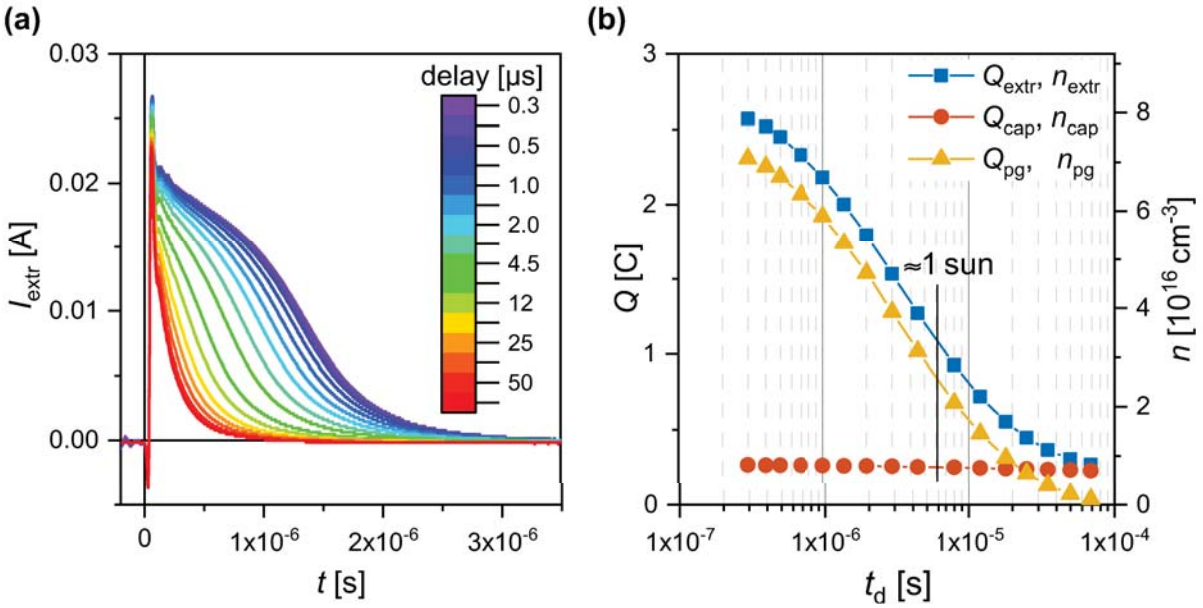

Figure 7.3: **(a)**: Extraction current I_{extr} for different delays between photogeneration and extraction over time of a P3HT:$PC_{61}BM$ OSC. **(b)** Extracted charge Q_{extr}, capacitive charge Q_{cap} and photogenerated charge $Q_{\mathrm{pg}} = Q_{\mathrm{extr}} - Q_{\mathrm{cap}}$ as function of delay time t_{d} between illumination and extraction for a P3HT:$PC_{61}BM$ OSC.

[1] The same cell that was used for the determination of $C_{\mathrm{geo}} = 1.603\,\mathrm{nF}$ in a dark extraction.

ous illumination is significantly slower than in the dark, where only the space charged regions close to the electrodes are recharged. It gets obvious here, that the extraction of photogenerated carriers from the bulk of the absorber is limited by transport due to the low mobilities in the organic semiconductor.

Figure 7.3(b) depicts Q_{extr}, Q_{cap} and Q_{pg} calculated according to equation (7.3) as a function of t_{d}. Assuming equally large and spatial homogeneous charge carrier densities for electrons and holes ($n_{\mathrm{e}}^{\mathrm{pg}} = n_{\mathrm{h}}^{\mathrm{pg}} = n_{\mathrm{pg}}$) and no further recombination during extraction[1] the excess charge carrier density as a function of delay time t_{d} can be calculated by:

$$n_{\mathrm{pg}}(t_{\mathrm{d}}) = \frac{Q_{\mathrm{pg}}(t_{\mathrm{d}})}{e_0 d_{\mathrm{PAL}} A} \tag{7.4}$$

This excess carrier density gives the spatially averaged value $n_{\mathrm{pg}} = d_{\mathrm{PAL}}^{-1} \int_0^{d_{\mathrm{PAL}}} n_{e/h}^{\mathrm{pg}}(x)dx$ over the thickness of the absorber. An axis corresponding to the carrier densities n_{extr}, n_{cap}[2] and n_{pg} is added to figure 7.3. The plots of Q_{extr}, Q_{cap} and Q_{pg} over t_{d} for a PCDTBT:$PC_{71}BM$ OSC with an absorber thickness of 220 nm a PEDOT:PSS hole contact and a LiF/Al electron contact are shown in figure 7.4. The initial illumination intensity before extraction was about 11 suns. For the P3HT:$PC_{61}BM$ OSC about 90 % of the extracted charge carriers shortly after illumination are photogenerated (see figure 7.3). In contrast, for the PCDTBT:$PC_{71}BM$ only about 50 % of the initially extracted carriers are excess carries. For long delay times, the calculated excess carrier density gets even negative there, which is not physically meaningful. This points at an overcompensation by an insufficient correction for capacitive charges. Hence, low photogenerated carrier concentrations ($Q_{\mathrm{pg}} < Q_{\mathrm{cap}}$) demand for an accurate correction for capacitive effects. The simple correction using the constant geometric capacitance does not sufficiently account for the complex voltage dependence of the capacitance of an OSC in the presence of excess carriers. The impact of an inaccurate capacitive correction is further examined below.

[1] Since extraction takes about 2 µs, values for $t_{\mathrm{d}} \lessapprox 2\,\mu\mathrm{s}$ may contain notable errors due to additional recombination losses during extraction.

[2] The picture of homogeneous carrier densities n_{cap} and n_{extr} have only a comparative character, since they not occur physically throughout the absorber. The extracted capacitive charge originates from narrow space charge regions at the contacts.

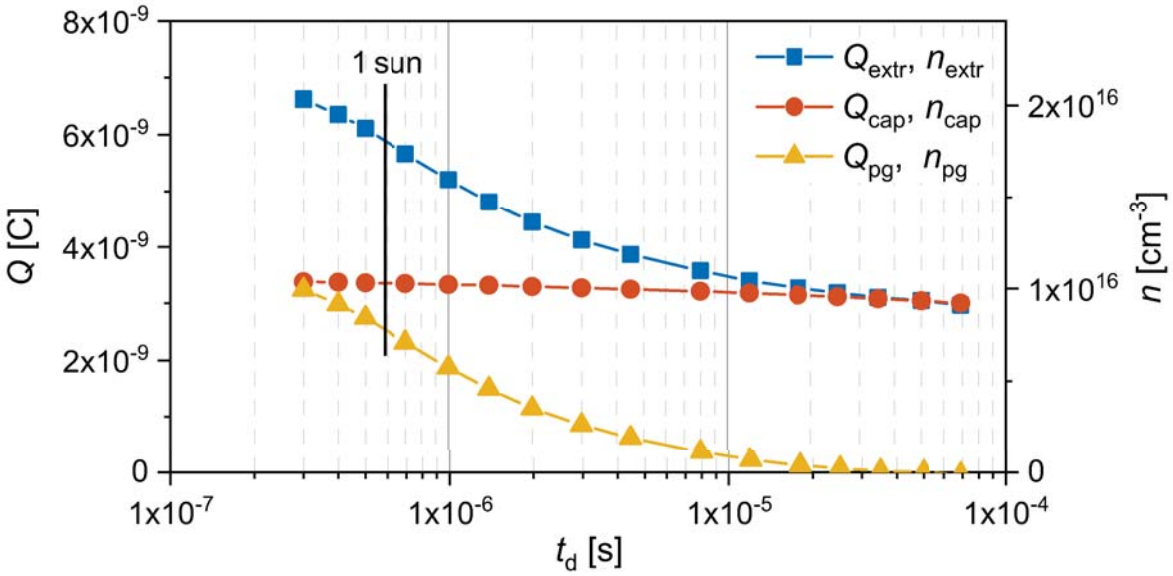

Figure 7.4: Extracted charge Q_{extr}, capacitive charge Q_{cap} and excess charge Q_{pg} as function of delay time t_{d} between illumination and extraction for an ITO based PCDTBT:$PC_{71}BM$ OSC.

7.3 Capacitive Currents under Open-Circuit Conditions

In the following, the influence of the cell capacitance on the excess carrier density during decay after photogeneration is analyzed. The considerations are of a more general nature and valid for other transient electrical characterization methods. They are for example directly applicable to the method of transient photo-voltage, where the solar cell is kept, after an initial illumination, under open-circuit conditions in the dark as well.
Although the cell is held under open-circuit conditions during the delay in BACE, the current within the cell is not zero. The occurring currents are depicted in a corresponding equivalent circuit model of the system in figure 7.5. The excess carriers within the absorber are represented by the chemical capacitance C_{chem}. It is given by the change of excess carriers with voltage and can be calculated from the theoretical steady state carrier density given by equation (1.14) by:

$$C_{\mathrm{chem}} = \frac{\partial Q_{\mathrm{pg}}}{\partial V} = e_0 d_{\mathrm{PAL}} \frac{\partial n_{\mathrm{pg}}}{\partial V} = \frac{e_0^2 d_{\mathrm{PAL}}}{2k_{\mathrm{B}}T} \sqrt{N_{\mathrm{C}} N_{\mathrm{V}}} \exp\left(\frac{e_0 V - E_{\mathrm{g,eff}}}{2k_{\mathrm{B}}T}\right) \tag{7.5}$$

C_{chem} is given here in units of electric charge per area and voltage ($\mathrm{F\,cm^{-2}}$) to match the picture of an electric circuit. After the illumination is turned off, the voltage decays over time due to recombination of excess carriers depicted by the recombination current

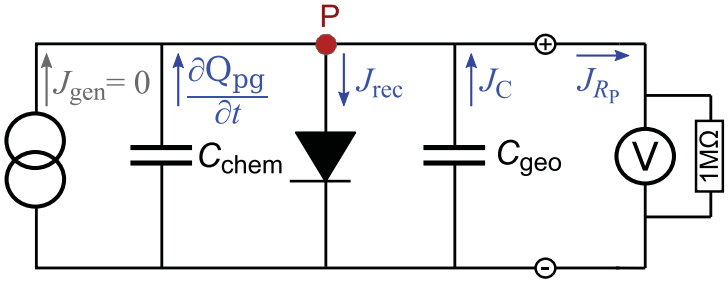

Figure 7.5: Equivalent circuit model of an OSC under open-circuit conditions after photogeneration. Consisting of the capacitances C_{chem} of the excess carriers and C_{geo} of the contacts, a diode to account for recombination and the input impedance of 1 MΩ of the voltmeter in parallel.

J_{rec}[1]. The capacitance of the space charge in the contact regions is taken into account by the capacitance C_{geo} (considered here as constant again for reasons of simplicity). The sum of all currents in point P depicted in figure 7.5 must be zero due to Kirchhoff's current law. Hence, the temporal change $\partial Q_{\mathrm{pg}}/\partial t$ of excess carriers is described by a continuity equation analogous to equation (1.15) by:

$$\begin{aligned}\frac{\partial Q_{\mathrm{pg}}}{\partial t} &= -J_{\mathrm{rec}} - J_{\mathrm{C}} - J_{\mathrm{R_P}} \\ &= -J_{\mathrm{rec}} - \underbrace{\left(C_{\mathrm{geo}}\frac{\partial V}{\partial t} + \frac{V}{R_{\mathrm{P}}}\right)}_{J_{\mathrm{inj}}} \end{aligned} \tag{7.6}$$

$$\frac{\partial n_{\mathrm{pg}}(t)}{\partial t} = -k_{\mathrm{r}} n_{\mathrm{pg}}(t)^2 - \frac{1}{e_0 d_{\mathrm{PAL}} A} J_{\mathrm{inj}} \tag{7.7}$$

Here, ideal transport[2] and selective contacts ($V_{\mathrm{int}}(x) = V_{\mathrm{ext}}$) as well as direct recombination are assumed. J_{C} and $J_{\mathrm{R_P}}$ were summarized to an effective injection current J_{inj}. $J_{\mathrm{R_P}}$ is added to account for shunt resistance[3]. When V_{OC} decays, C_{geo} discharges by the current $J_{\mathrm{C}} = \partial V/\partial t \cdot C_{\mathrm{geo}}$. It has the sign of a generation current when V_{OC} decays ($\partial V/\partial t < 0$). This capacitive current is partially injected into the bulk where the

[1] The recombination current J_{rec} is considered as electric currents here. In reality homogeneous pairwise recombination in an electrically neutral semiconductor does not require transport of carriers and thus no actual electric current.

[2] In the commonly used materials for OSC transport plays an important role due to the rather low mobilities and flat QFL are unusual if currents are present, hence recombination is not homogeneous. V_{OC} can even get decoupled from V_{int} and thereby from the excess carrier density, due to strong gradients of the QFL as discussed in chapter 1.5.1.

[3] $R_{\mathrm{P}} \leq 1\,\mathrm{M\Omega}$ is common since V_{OC} is measured with an oscilloscope with an input resistance of 1 MΩ.

carriers recombine. The other part flows over the external resistor. When carriers get injected into the bulk during this process, part of the excess carriers originate from the discharge of the contact regions and are no longer photogenerated carriers. For infinite parallel resistance (no external current) all photogenerated plus all capacitive carriers have to recombine within the PAL. Thus, more charge carriers recombine in total than the number of excess carriers that are initially present after illumination. Since $n_{\mathrm{pg}}(t)$ is known as a function of (delay) time the derivative $^{\partial n_{\mathrm{pg}}}/_{\partial t}$ can be calculated. Figure 7.6 depicts $^{-\partial n_{\mathrm{pg}}}/_{\partial t}$ over n_{pg} for P3HT:PC_{61}BM and PCDTBT:PC_{71}BM solar cells alongside with the contribution from the injection current $J_{\mathrm{inj}} \cdot (e_0 d_{\mathrm{PAL}} A)^{-1}$ according to equation (7.7)[1]. To compare this to the influence of errors in the correction for capacitive charges exemplary values corrected with a 5 % higher and a 5 % lower geometric capacitance are added. For the P3HT:PC_{61}BM cell the injection current from the contacts plays a minor role. In contrast, for the PCDTBT:PC_{71}BM devices the capacitive injection current has the same order of magnitude as the experimentally determined change of excess carrier over time for low carrier densities (long delays). Thus, small deviations

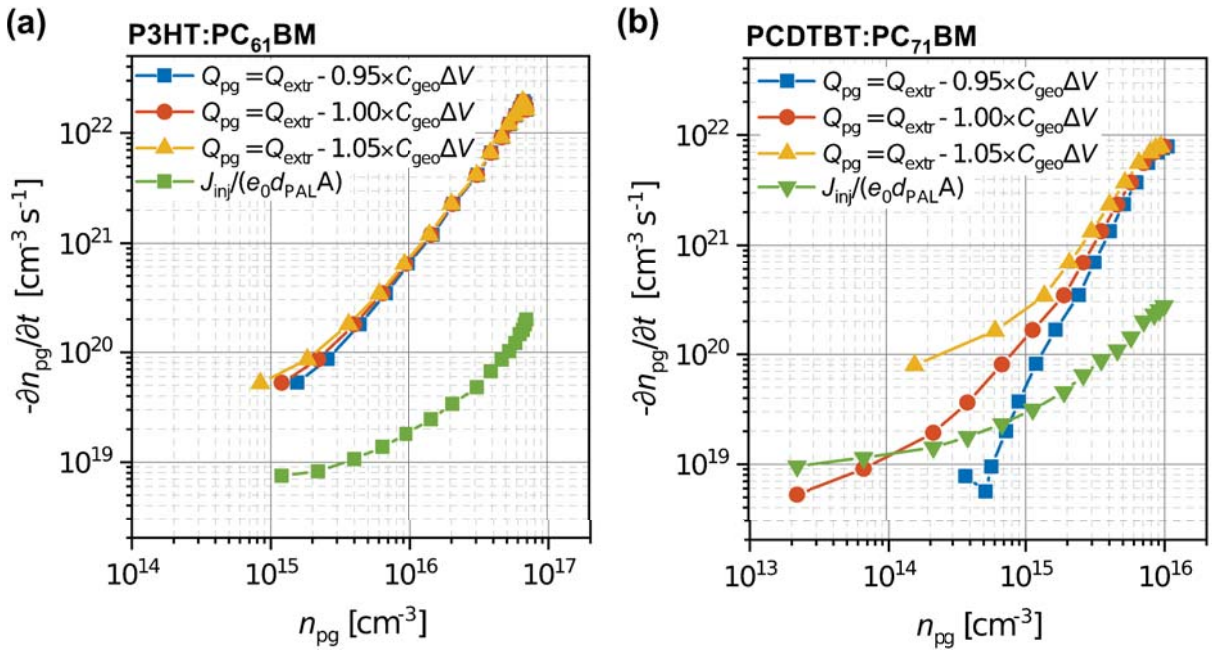

Figure 7.6: Negative time derivative of excess carrier density $^{-\partial n_{\mathrm{pg}}}/_{\partial t}$ as a function of carrier density $n_{\mathrm{pg}} = Q_{\mathrm{pg}}/(e_0 d_{\mathrm{PAL}} A)$ for a variation of the capacitive correction for a P3HT:PC_{61}BM based (a) and a PCDTBT:PC_{71}BM based (b) OSC alongside with the injected charge carriers per time $J_{\mathrm{inj}}/(e_0 d_{\mathrm{PAL}} A)$ from the recharge of the contact regions. Plots using 5 % percent higher and lower values than the experimentally determined dark capacitance C_{geo} are added for comparison.

[1] $R_{\mathrm{P}} = 1\,\mathrm{M\Omega}$ was used to account for the input resistance of the used oscilloscope.

in capacitive correction and the injection from the contact regions, have a significant effect on the calculated excess carrier density in the investigated range. This is due to the lower share of excess carrier in the extracted charge ($Q_{\mathrm{pg}}(t=0)/Q_{\mathrm{cap}} \approx 2$ compared to ≈ 10 for P3HT:PC_{61}BM). However, for both absorber systems small changes in the capacitive correction of the data results in notable changes in ${}^{\partial n_{\mathrm{pg}}}/_{\partial t}(n)$, especially for low excess carrier concentrations. Thus a adequate correction of capacitive charges is indispensable in this regime.

The ratio of capacitive and excess carriers is further exemplified in figure 7.7. It depicts exemplary geometric capacitances calculated by equation (7.1) for different layer thicknesses using $\epsilon_{\mathrm{r}} = 3.5$ over voltage and generation rate alongside with the chemical capacitance for P3HT:PC_{61}BM and PCDTBT:PC_{71}BM calculated by equation (7.5) using the values[1] in table 7.1. The capacitive charge Q_{cap} and the charge originating from excess carrier Q_{pg}, extracted during BACE, are given by the integrals of the capacitances over the corresponding voltage range $Q = \int_{V_{\mathrm{extr}}}^{V_{\mathrm{OC}}} C(V)dV$ (area under the $C(V)$

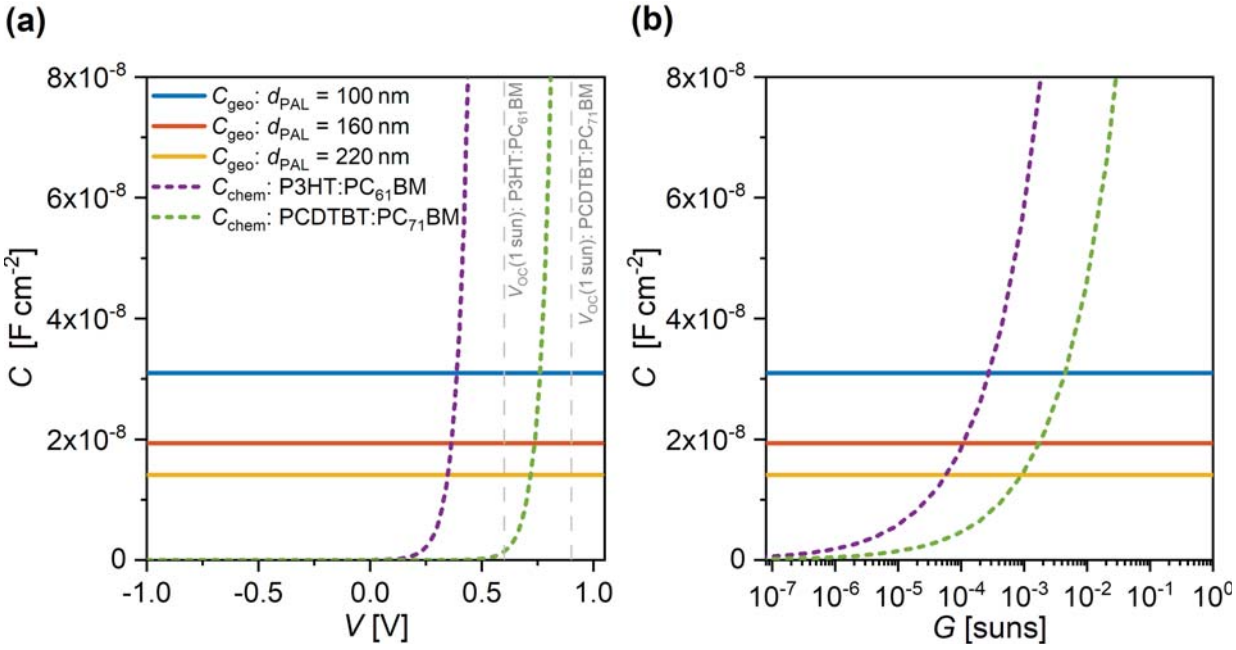

Figure 7.7: Geometric capacitance C_{geo} of the electrodes for different layer thicknesses and chemical capacitance C_{chem} over the cells voltage V (a) and over the corresponding steady state generation rate G (b) for a P3HT:PC_{61}BM and PCDTBT:PC_{71}BM OSC.

[1] The V_{OC} and J_{SC} at an illumination of AM1.5G are values commonly observed and the effective band gaps are values from temperature dependent measurements (see chapter 9). The product of the effective densities of states was calculated by $N_{\mathrm{C}}N_{\mathrm{V}} = J_{\mathrm{SC}}(1\,\mathrm{sun})/(e_0 d_{\mathrm{PAL}} k_{\mathrm{r}}) \cdot (\exp((e_0 V_{\mathrm{OC}}(1\,\mathrm{sun}) - E_{\mathrm{g,eff}})/(k_{\mathrm{B}}T)))^{-1}$ for an absorber thickness of $d_{\mathrm{PAL}} = 220\,\mathrm{nm}$.

Table 7.1: Parameters used for the calculation of the chemical capacitance.

absorber material	$J_{SC}(1\,\text{sun})$ [mA cm^{-2}]	$V_{OC}(1\,\text{sun})$ [V]	$E_{g,\text{eff}}$ [eV]	k_r [cm^3 s^{-1}]	$N_c N_V$ cm^{-6}
P3HT:PC$_{61}$BM	10	0.6	0.984	3.9×10^{-12}	9.6×10^{38}
PCDTBT:PC$_{71}$BM	10	0.9	1.350	9.1×10^{-11}	1.1×10^{39}

plots). The extracted capacitive charge scales linearly with the extraction voltage by $Q_{cap} = C_{geo}(V - V_{ext})$. In contrast, the number of extracted excess carriers does not depend considerably on the extraction voltage since $C_{chem}(V)$ is very small in the blocking direction due to its exponential dependence on the voltage. Thus, low extraction voltages and thick layers (low C_{geo}) help to minimize capacitive effects and thus the ratio Q_{pg}/Q_{cap}. Altogether the discussed limitation for an accurate correction for the capacitive charge and the injection of the latter under open-circuit conditions during BACE only allows for a reliable analysis of bulk recombination in the regime where $Q_{pg} \gtrapprox Q_{cap}$. The overall recombination in the absorber according to equation (7.6) is given by:

$$J_{rec} = \frac{\partial V}{\partial t}\Big(C_{geo}(V) + C_{chem}(V)\Big)$$

Here, $\partial Q_{pg}/\partial t = \partial V/\partial t\, C_{chem}$ and $R_P = \infty$ is assumed. Whether the recombination in the absorber is dominated by excess carriers or capacitive currents from the electrodes depends on the dominant capacitance for a given voltage. Thus the prevalent regime has severe consequences on the interpretation of observed effects. As depicted in figure 7.7(b) C_{chem} gets bigger than C_{geo} at a generation of about $G \approx 6 \times 10^{-5}$ suns for a 220 nm thick for P3HT:PC$_{61}$BM cell. For a 100 nm thick PCDTBT:PC$_{71}$BM the same occurs at $G \approx 1 \times 10^{-2}$ suns. This leads to a significantly higher number of excess carriers compared to capacitive charges in P3HT:PC$_{61}$BM at carrier densities corresponding to the same steady state generation rates.

In general, the injection of capacitive currents can be avoided in BACE by an immediate extraction (no delay) and by varying the initial illumination intensity. However, this approach is still restricted by the limited capacitive correction. In addition the explicit time dependence of excess carrier density can no longer be obtained, thus k_r can not be determined by the method described hereinafter.

7.4 Determination of the Bulk Recombination Coefficient

Here, the recombination coefficient k_r is determined from the time dependence of the excess carrier density. The determined excess charge Q_{pg} from BACE for short delays for P3HT:$PC_{61}BM$ and PCDTBT: $PC_{71}BM$ solar cells exceed the capacitive charge by a factor of two or more (see figures 7.3 and 7.4). Hence, the impact of errors in the capacitive correction and of capacitive injection current are rather low. By neglecting the injection current in equation (7.7) the continuity equation for excess carriers gets:

$$\frac{\partial n_{pg}(t)}{\partial t} = -k_r n_{pg}(t)^2 \tag{7.8}$$

Here homogeneous bimolecular recombination is considered to be the only loss mechanism for excess carriers. This is commonly reported to be the predominant mechanism in many organic DA systems [80, 107] and thus is often used as recombination model in numerical simulations [18, 99, 108–112]. Figure 7.8 shows ${}^{\partial n_{pg}}/_{\partial t}(n_{pg})$ for a P3HT:$PC_{61}BM$ and a PCDTBT:$PC_{71}BM$ OSC with fits according to equation (7.8) to the upper nine values (shortest delay) which resemble the experimental data quite accurately. Thus the investigated OSC indeed shows bimolecular-like recombination for high charge carrier densities. The deviation for low carrier densities orig-

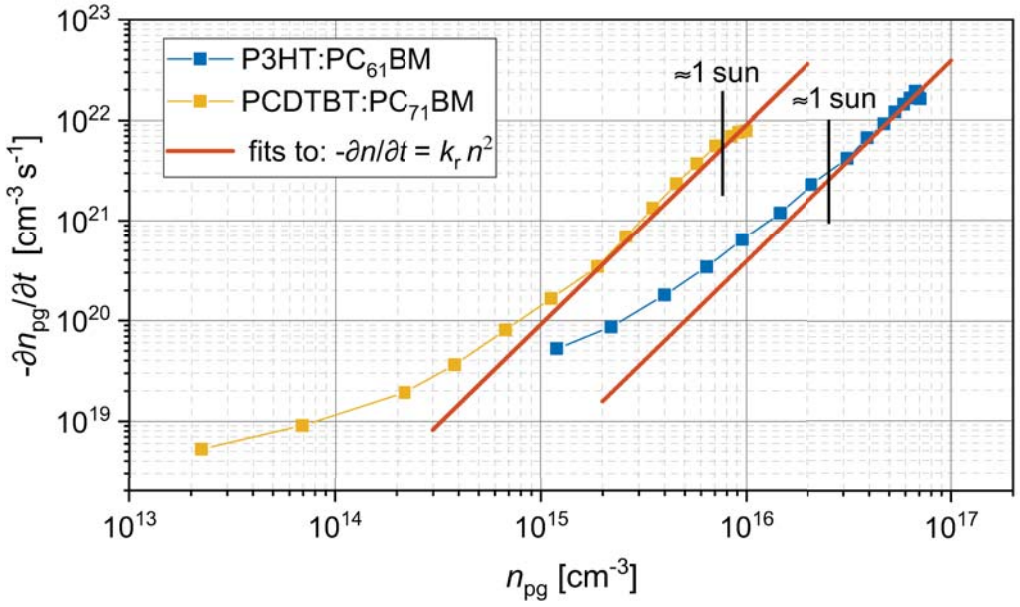

Figure 7.8: Time derivative of excess carrier density ${}^{-\partial n_{pg}}/_{\partial t}(n_{pg})$ for a P3HT:$PC_{61}BM$ and a PCDTBT:$PC_{71}BM$ OSC from BACE. Fits to the nine highest values of each data set for bimolecular recombination ($-{}^{\partial n_{pg}}/_{\partial t} = k_r^{bi} n^2$) are added (solid red lines).

inates from a combination of errors in the capacitive correction and capacitive currents during recombination. Bimolecular recombination is shown to be predominant in the investigated samples over a wide range of intensities in chapter 9. The fits result in recombination coefficients of $k_{\mathrm{r}}^{\mathrm{bi}} = 3.9 \times 10^{-12}\,\mathrm{cm^3\,s^{-1}}$ for P3HT:PC_{61}BM and $k_{\mathrm{r}}^{\mathrm{bi}} = 9.1 \times 10^{-11}\,\mathrm{cm^3\,s^{-1}}$ for PCDTBT:PC_{71}BM. The experimentally determined bimolecular recombination coefficient for P3HT:PC_{61}BM compare well with values reported in literature of $(2-3)\times10^{-12}\,\mathrm{cm^3\,s^{-1}}$ obtained at comparable conditions [92, 113]. For PCDTBT:PC_{71}BM a recombination coefficient between $(0.9-3)\times10^{-11}\,\mathrm{cm^3\,s^{-1}}$ was reported which is lower by a factor of >3 [62]. However, there k_{r} was calculated from the carrier mobility assuming Langevin recombination, as described in chapter 2.3.4, and not obtained directly from the recombination dynamics of excess carrier. The introduced analysis method allows the determination of the bimolecular bulk recombination coefficients from BACE measurements in the excess carrier dominated regime where $Q_{\mathrm{pg}} > Q_{\mathrm{cap}}$ and $C_{\mathrm{chem}} > C_{\mathrm{geo}}$. It gives direct[1] excess to an important material parameter e.g. demanded as an input parameter in numerical simulations.

7.5 Summary of Charge Extraction Experiments

A BACE setup was established and excess charge carrier dynamics were studied. The capacitance of OSCs was studied, it was shown that it can have a significant impact on the results in the measured range. Explicitly, uncertainties of the capacitive correction and injection of capacitive currents under open-circuit conditions in transient experiments were identified (assuming ideal transport). It was concluded that the use of low extraction voltages and thick absorber layers are beneficial to reach the excess carrier dominated regime. Unfortunately, a minimum voltage or corresponding steady state generation rate for this regime depends on the properties of the studied absorber and therefore a general limit can not be given. Altogether, capacitive effects are quite complex, and an accurate description and detailed understanding of such experiments over a wide range of conditions require complex time and spatially resolved simulations tailored to the particular system, especially if transport is considered. Nevertheless, bimolecular recombination coefficients of $k_{\mathrm{r}}^{\mathrm{bi}} = 3.9\times10^{-12}\,\mathrm{cm^3\,s^{-1}}$ for P3HT:PC_{61}BM and $k_{\mathrm{r}}^{\mathrm{bi}} = 9.1\times10^{-11}\,\mathrm{cm^3\,s^{-1}}$ for PCDTBT:PC_{71}BM were determined from the excess carrier dominated regime where Q_{pg} exceeds Q_{cap} significantly.The introduced method enables the direct determination of recombination coefficients of the photoactive material at

[1] Only the volume of the absorber $d_{\mathrm{PAL}}A$ is needed for the calculation of the carrier density.

carrier densities relevant for the operation of the solar cell and in a complete device, i.e. the real morphology of the donor acceptor bulk-heterojunction.

8 Recombination Losses due to Poor Selectivity of Contacts

Results on recombination losses at electrode surfaces were published [99] with co-authorship of the author of this thesis, who contributed the experimental results. The presented study was carried out in close cooperation with Annika Spies who contributed the numerical simulations. The experiments and simulations were planned and the results and conclusions were subsequently discussed and developed by U. Würfel, A. Spies and the author of this work. Results, ideas and conclusions of the following chapter partially paraphrase this publication.

Organic solar cells with selective and less selective contacts are investigated in this study and the dependence of recombination losses on contact selectivity and on transport properties are investigated. Charge carrier selective contacts are commonly used in OSC to separate charge carriers (in contrast to e.g. doped regions in a pn-junction). Due to the variety of possible requirements for organic solar cells like flexibility, stability and roll-to-roll production capability many electrode materials have been tested for OSC [111, 114–117]. Important electrode properties like transparency, reflectivity and conductivity are straight forward to measure. However, the selectivity of an electrode material in combination with a certain absorber material is quite challenging to determine. Contacts with insufficient selectivity cause a loss of electrons and holes due to recombination at the interface of the electrode. This effect will be referred to as surface recombination in this work. It is accompanied by a V_{OC} loss. It will be shown that the reduction of V_{OC} is the main contribution to power conversion efficiency loss originating from surface recombination in OSC. Thus, a detailed understanding of this V_{OC} loss is of great interest.

Recombination of electrons and holes at electrodes with insufficient selectivity have been studied in literature in detail. E.g. Tress et al. investigated the influence of carrier mobility on recombination due to the loss of charge carriers at the surface and concluded that μ acts as an indirect enhancement factor [118]. It was found that, finite mobilities give the best performance since there is a trade-off between the transport of carriers to the respective electrodes (high fill factor) and their loss due to surface recombination (low

open-circuit voltage) [118–120]. Further, Sandberg et al. compared the impact of reduced surface recombination velocities, interfacial minority carrier doping and majority carriers traps to the case of an increased injection barrier at the electrode. They provide means to determine the dominating effect of the V_{OC} reduction and derive an analytical expression that relates the injection barrier of the electrodes to the open-circuit voltage [121]. More recently, Wheeler et al. reported that the quasi-Fermi level splitting in the bulk is hardly affected by surface recombination in OSCs by applying charge carrier extraction and transient photovoltage measurements to probe recombination kinetics [122]. They point out that understanding surface recombination is important to avoid misinterpretation of the correlation between V_{OC} values and bulk recombination. The presented work elucidates this correlation further by identifying two distinct contributions to the V_{OC} reduction caused by insufficient contact selectivity. Their magnitudes are determined by measurements of the radiative bulk recombination from an advanced combination of photo- and electroluminescence for the first time and complemented by charge extraction experiments. In addition, the influence of charge carrier mobilities on surface recombination losses is studied quantitatively by means of numerical simulations.

8.1 Open-Circuit Voltage Loss due to Recombination at Electrodes

Recombination at contacts is examined in a study on OSCs built with different contact materials for three absorber materials. Figure 8.1 shows the measured JV-curves for solar cells made from the photoactive materials P3HT:$PC_{61}BM$, PTB7-Th:$PC_{71}BM$ and PffBT4T-2OD:$PC_{61}BM$ with lithium fluoride/aluminum (LiF/Al) and copper (Cu) electron contacts, respectively[1] (symbols). A severe reduction of the open-circuit voltages from 602 mV to 358 mV (P3HT:$PC_{61}BM$), from 802 mV to 576 mV (PTB7-Th:$PC_{71}BM$) and from 784 mV to 583 mV (PffBT4T-2OD:$PC_{61}BM$) is observed for the Cu contact compared to the LiF/Al contact while the short-circuit current densities and the fill factors are hardly affected. Thus the V_{OC} reduction is the main contribution to PCE loss for the investigated OSC. The observed V_{OC} loss is caused by losses at the electron contact, since the devices for an individual photoactive material are identical apart from the material of the electron contact. The JV-curves plotted as solid lines in figure 8.1 are obtained from drift-diffusion simulations in the effective semiconductor model (see

[1] All cells were built in the layout and layer stack depicted in figures 3.1 and 3.3(a) with absorber thicknesses of 220 nm (P3HT(Rieke Metals):$PC_{61}BM$), 80 nm (PTB7-Th:$PC_{71}BM$) and 260 nm (PffBT4T-2OD:$PC_{61}BM$) using PEDOT:PSS as hole contact.

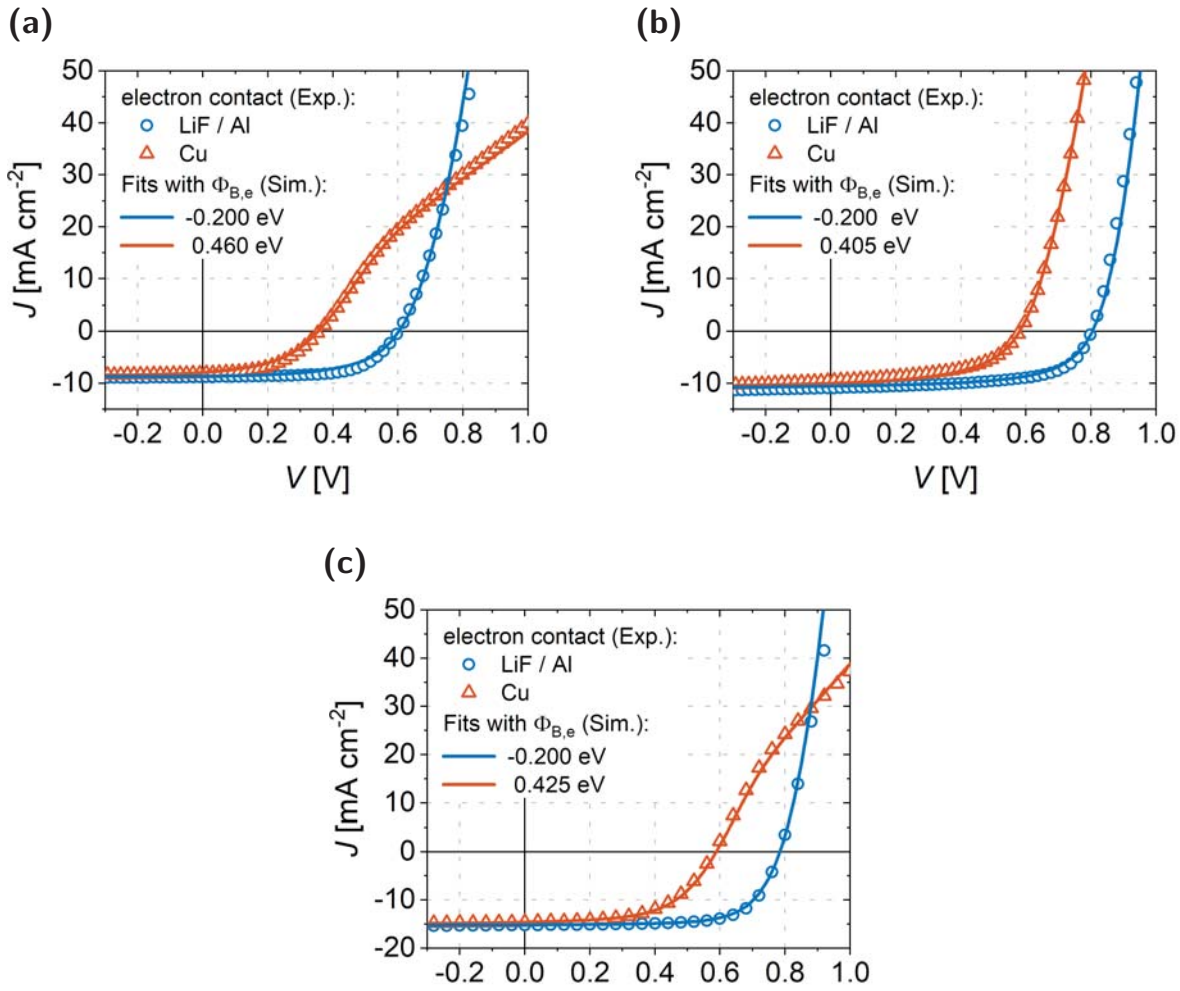

Figure 8.1: Experimental (symbols) and simulated (solid lines) JV-curves of solar cells with selective LiF/Al (blue) and less selective Cu (red) metal contact for three different donor:acceptor blends (a) P3HT:$PC_{61}BM$, (b) PTB7-Th:$PC_{71}BM$ and (c) PffBT4T-2OD:$PC_{61}BM$. The injection barrier $\Phi_{B,e}$ of the electron contact was the only parameter varied in the drift-diffusion simulations.

chapter 6.1). There, the selectivity of the modeled metal-semiconductor contacts[1] is tuned by the work function of the electrode (see chapter 1.5). For selective contacts (reproducing LiF/Al), the work function (WF) is set 0.2 eV above the electron transport level, i.e. an electron injection barrier of $\Phi_{B,e} = -0.2\,eV$ is used. For the less selective contact the WF is empirically shifted towards the middle of the band gap to match the experimental curves for Cu electrodes. Injection barriers of $\Phi_{B,e} = 0.46\,eV$

[1] The conclusions in this work about arising gradients in the QFL due to surface recombination currents in OSC are valid in general. The example of window layers from wide band gap semiconductors is discussed in reference [99].

(P3HT:$PC_{61}BM$), 0.405 eV (PTB7-Th:$PC_{71}BM$) and 0.425 eV (PffBT4T-2OD:$PC_{61}BM$) are found to reproduce accurately the measured curves[1] A comprehensive description of the simulations presented in this chapter is given in the PhD thesis of Spies [18].
In the following the V_{OC} loss caused by surface recombination is discussed and quantified. For this, zero external current is assumed. The internal voltage $V_{int}(x)$ at a position x is given by equation (1.12) as

$$e_0 V_{int}(x) = E_{g,eff} - k_B T \ln\left(\frac{N_{ETL} N_{HTL}}{n_e(x) n_h(x)}\right)$$

In an OSC with ideally selective contacts all photogenerated carriers recombine solely within the bulk of the absorber ($G = R$). Assuming spatially homogeneous generation G and thus no currents, generation and recombination cancels out and $G_{e,h} = R_{e,h}$ for every position within the absorber. For equal charge carrier densities ($n_e = n_h$) the recombination rate is $R = k_{rec} n^{\beta}$ and the quasi-Fermi level splitting V_{int} can be written as

$$e_0 V_{int}^{ideal} = E_{g,eff} - k_B T \ln\left(\frac{N_{ETL} N_{HTL}}{(G/k_{rec})^{\frac{2}{\beta}}}\right)$$

We get the ideal internal voltage V_{int}^{ideal}, only dependent on the generation rate G and the material specific effective band gap $E_{g,eff}$, bulk recombination coefficient k_{rec} with the corresponding reaction order β and the effective densities of states N_{ETL} and N_{HTL}. V_{int}^{ideal} represents the ideal, i.e. the maximum, quasi-Fermi level splitting for a given material and generation rate and thus the maximum attainable V_{OC}. Thus the open-circuit voltage will be $V_{OC} < V_{int}^{ideal}$ in a system with additional losses.

The previous consideration describes the quasi-Fermi level splitting inside the bulk of the semiconductor. The open-circuit voltage $e_0 V_{OC}$ measured externally at the contacts is given by the difference between the Fermi energies of the contacts $E_{F,\,el.cont}$ and $E_{F,\,h.cont}$.

$$e_0 V_{OC} = E_{F,el.cont} - E_{F,h.cont}$$

Since no excess carriers are lost for ideally selective contacts, the quasi-Fermi level splitting in the bulk is not altered by the electrodes[2] and the Fermi energy (the work

[1] A scheme of the used energetic levels is drawn in figure B.2 in appendix B and the complete parameter sets used in simulations are listed in tables C.1, C.2 and C.3 in appendix C.

[2] Except in close proximity of the contacts. There the QFL of the minority carriers can strongly vary, dependent on the boundary conditions.

function) of the contact resembles the quasi-Fermi level of the corresponding majority charge carrier. Hence, V_{OC} is given by

$$e_0 V_{\mathrm{OC}} = E_{\mathrm{F,el.cont}} - E_{\mathrm{F,h.cont}} = E_{\mathrm{F,ETL}}(d) - E_{\mathrm{F,HTL}}(0) = e_0 V_{\mathrm{int}}^{\mathrm{ideal}}$$

Here, the hole contact is located at position $x = 0$ and the electron contact at $x = d$ as depicted in figure 8.2(a), with d being the thickness of the photoactive layer.
In case of a loss of excess carriers at an electrode by surface recombination, x_{max} is defined as the position within the absorber where the product $n_{\mathrm{e}} n_{\mathrm{h}}$ of the charge carrier densities is highest. The corresponding internal voltage is referred to as maximum internal voltage $V_{\mathrm{int}}^{\mathrm{max}} = V_{\mathrm{int}}(x_{\mathrm{max}})$, respectively.
Figure 8.2(b) depicts schematically the band diagram of an OSC where the WF of the electron contact is located in the middle of the band gap, which results in a contact with unideal selectivity[1]. This causes gradients in the QFL, which act as the driving forces for the surface recombination current. In the depicted case, the internal voltage equals the ideal voltage $V_{\mathrm{int}}^{\mathrm{max}} = V_{\mathrm{int}}^{\mathrm{ideal}}$, i.e. the charge carrier densities at some distance of the contact is not altered. So, no considerable number of carriers is lost to the unselective electrode from these regions. However, the open-circuit voltage is significantly reduced

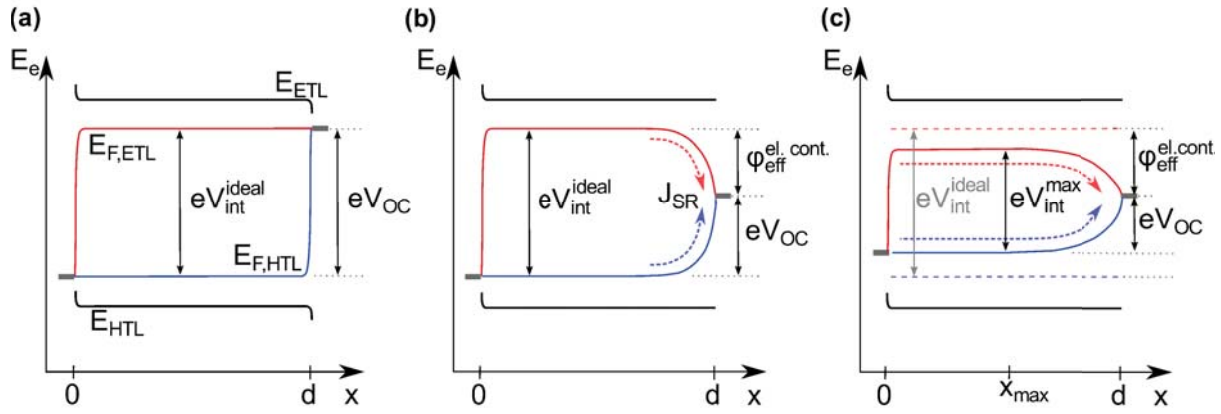

Figure 8.2: Schematic illustration of the energy levels inside solar cells with the hole contact at $x = 0$ and the electron contact at $x = d$. (a) For two highly selective contacts, showing the maximum attainable internal voltage $V_{\mathrm{int}}^{\mathrm{ideal}}$ characteristic for the absorber material and $V_{\mathrm{OC}} = V_{\mathrm{int}}$. (b) For a less selective electron contact with a surface recombination current J_{SR} towards the contact reducing V_{OC} by $\varphi_{\mathrm{eff}}^{\mathrm{el.cont.}}$ while $V_{\mathrm{int}}^{\mathrm{max}} = V_{\mathrm{int}}^{\mathrm{ideal}}$. (c) For a less selective electron contact with loss of carriers from the entire volume of the absorber. Thus, $V_{\mathrm{int}}^{\mathrm{max}} \neq V_{\mathrm{int}}^{\mathrm{ideal}}$ at every position.

[1] The metal does not inject a considerable number of electrons into the ETL. Hence, $n_{\mathrm{e}} \approx n_{\mathrm{h}}$ and thereby $\sigma_{\mathrm{e}} \approx \sigma_{\mathrm{h}}$ in the vicinity of the contact which results in bad selectivity according to chapter 1.5.

by the gradient of the QFL of electrons in the conduction band, i.e. of the majority charge carrier. The quantity $\Delta V_{\mathrm{OC,1}}$ is defined here as the loss of open-circuit voltage due to the gradient in the QFL of the majority carriers

$$\Delta V_{\mathrm{OC,1}} = -\frac{1}{e_0}\int_{x_{\max}}^{d} \mathrm{grad}(E_{\mathrm{F,\,ETL}})dx$$

in the case of an unideal electron contact. In this case ($V_{\mathrm{int}}^{\max} = V_{\mathrm{int}}^{\mathrm{ideal}}$) for a metal-semiconductor contact assuming balanced mobilities, $\Delta V_{\mathrm{OC,1}}$ is the difference between the WF of the electrode and the ideal value of the quasi-Fermi energy of the majority charges. This difference is introduced as the effective injection barrier[1] φ_{eff} by

$$\Delta V_{\mathrm{OC,1}} = E_{\mathrm{F,ETL}}^{\mathrm{ideal}} - W_{\mathrm{F,el.cont}} = \varphi_{\mathrm{eff,el.cont}} \tag{8.1}$$

for the electron contact. Figure 8.2(c) illustrates a system with an electron contact with unideal selectivity where the internal voltage does not reach the ideal voltage ($V_{\mathrm{int}} < V_{\mathrm{int}}^{\mathrm{ideal}}$). Therefore, charge carriers flow from the entire thickness of the absorber to the electrode and recombine, reducing the electron and hole densities significantly throughout the whole cell ($V_{\mathrm{int}} \sim \ln(n^2)$). This loss in open-circuit voltage due to a reduced maximum QFL splitting, i.e. reduced carrier densities through the entire photoactive layer, is defined by $\Delta V_{\mathrm{OC,2}}$ as

$$\Delta V_{\mathrm{OC,2}} = V_{\mathrm{int}}^{\mathrm{ideal}} - V_{\mathrm{int}}^{\max}$$

Two contributions to the loss in V_{OC} due to surface recombination are distinguished, $\Delta V_{\mathrm{OC,1}}$ due to a gradient in the QFL of the majority carriers and $\Delta V_{\mathrm{OC,2}}$, caused by the reduction of the charge carrier density through the entire thickness of the absorber.
The previously shown JV-curves from drift-diffusion simulations (figure 8.1) are in excellent agreement with the experimental results. Figure 8.3 depicts the corresponding simulated band diagram of the P3HT:PC_{61}BM OSC in the effective semiconductor model for a selective and a less selective electron contact. The surface recombination in the case of the poorly selective electron contact results in a severe gradient of the QFL of electrons in the vicinity of the electron contact. V_{int} is gradually reduced towards the latter while it approaches the ideal value $V_{\mathrm{int}}^{\mathrm{ideal}}$ at some distance. From this region, no considerable amount of carriers is lost to the unselective contact. The simulations

[1] In contrast to the injection barrier $\Phi_{\mathrm{B,e}} = E_{\mathrm{ETL}} - W_{\mathrm{F,el.cont}}$, defined in chapter 1.5 as the difference between the electron transport level and the workfunction of the cathode.

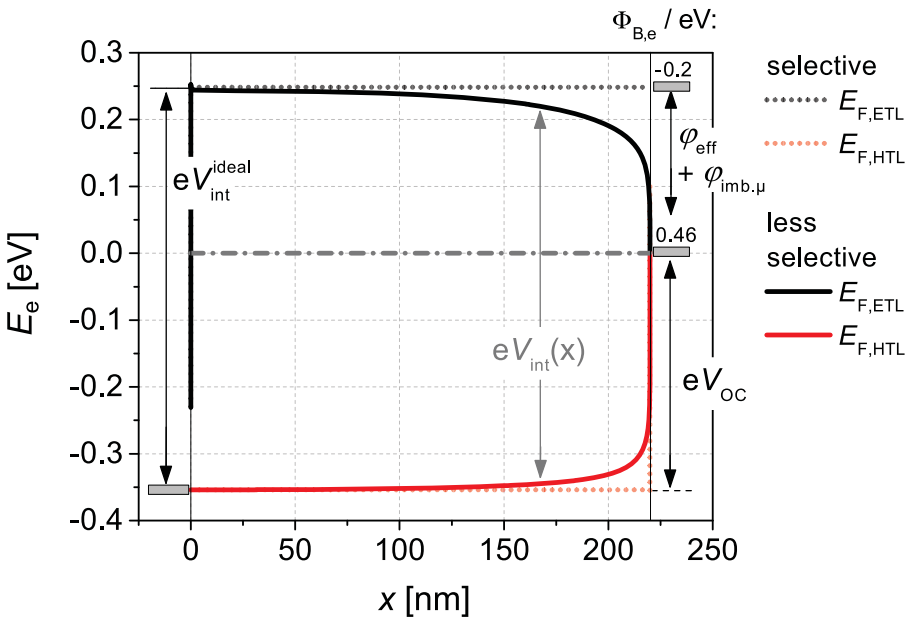

Figure 8.3: Simulated quasi-Fermi energies for P3HT:$PC_{61}BM$ cells with selective contacts (dotted lines) and a selective hole contact but less selective electron contact (solid lines) showing strong gradients in the quasi-Fermi energy of electrons towards the cathode.

suggest the gradient of the QFL of electrons, i.e. $\Delta V_{\mathrm{OC},1}$, to be the main reason for the V_{OC} loss, correspondent to the case illustrated in figure 8.2(b). The main loss of V_{OC} is due to a strong gradient of the QFL, while the QFL splitting is hardly affected at some distance of the electrode where it is almost ideal ($V_{\mathrm{int}} \approx V_{\mathrm{int}}^{\mathrm{ideal}}$). Thus the carrier densities and thereby recombination in the absorber are not reduced significantly compared to the ideal case in these regions.

The simulations for P3HT:$PC_{61}BM$ use a higher electron mobility ($1.7 \times 10^{-4}\,\mathrm{cm^2\,(V\,s)^{-1}}$) than the hole mobility ($4.5 \times 10^{-4}\,\mathrm{cm^2\,(V\,s)^{-1}}$) to fit the JV-data. Imbalanced mobilities are often observed in common donor acceptor system used in OSC [123–125]. The acceptor phase, commonly a fullerene derivative, often possesses a higher mobility than the donor phase which commonly consists of a polymer. A given surface recombination current to, e.g. the electron contact, requires a smaller driving force for a larger electron mobility, i.e. a smaller gradient in the QFL of electrons. A lower hole mobility leads to a pileup of a positive space charge and with that to an electric potential difference $\varphi_{\mathrm{imb.\mu}}$ which will influence V_{OC}. The resulting $\Delta V_{\mathrm{OC},1}$ in case of imbalanced mobilities is

$$\Delta V_{\mathrm{OC},1} = \varphi_{\mathrm{eff}}^{\mathrm{el.cont.}} - \varphi_{\mathrm{imb.\mu}}$$

V_{OC} will be further reduced for a contact with low selectivity if $\mu_{maj} < \mu_{min}$ ($\varphi_{imb.\mu} < 0$) and it will be less reduced if $\mu_{min} < \mu_{maj}$ ($\varphi_{imb.\mu} > 0$). The fact that in many organic solar cells the electron mobility is higher than the hole mobility makes it often more difficult to realize a selective hole contact and more facile to ensure a selective electron contact. An analysis by means of numeric simulations on the impact of imbalanced mobilities on the contributions $\Delta V_{OC,1}$ and $\Delta V_{OC,2}$ to the overall loss in V_{OC} due to surface recombination is given in chapter 8.3.
The simulations yield a total recombination[1] in the absorber layer of $\int_0^{d_{PAL}} R(x)dx = 5.5 \times 10^{16}\,cm^{-2}\,s^{-1}$ for selective contacts and $2.8 \times 10^{16}\,cm^{-2}\,s^{-1}$ for the less selective contact. Even though V_{OC} is reduced by 244 mV for the less selective contact, still 51 % of the generated carriers recombine within the volume of the photoactive layer and only 49 % recombine at the electrode. Hence, the theoretical results predict a severe reduction of V_{OC} while the average carrier density in the absorber and thereby the overall bulk recombination is barely reduced.

8.2 Spectroscopic Investigation of Surface Recombination

In this chapter, the underlying mechanism of V_{OC} loss is investigated by means of luminescence spectroscopy and charge extraction experiments. The recombination in the absorber under open-circuit, and hence the QFL splitting and carrier density, is determined to give an experimental proof for strong gradients of the QFL under open-circuit conditions. Figures 8.4 (a) to (c) present the electroluminescence spectra of the investigated cells measured at a forward current density of $76\,mA\,cm^{-2}$ in the setup described in chapter 5.4. For the selective LiF/Al contacts injected electrons and holes meet at the donor–acceptor interface and recombine partially radiatively as illustrated in figure 8.5(a). The observed peak in the EL spectra originate from the charge-transfer state which is formed by an electron and a hole during recombination[58]. For the much less selective Cu contact, no EL could be observed within the detection limit of the setup. The effect that increased surface recombination reduces the EL signal was demonstrated previously [108, 111]. An unsuited work function of the cathode causes an injection barrier $\Phi_{B,e}$ for electrons. Hence, the electron injection is impeded. The lack of recombination partners in the absorber causes holes to travel through the whole photoactive layer to the surface of the poorly selective electron contact where they recombine nonradiatively

[1] Bimolecular recombination according to equation (1.9) is used in simulations as recombination model.

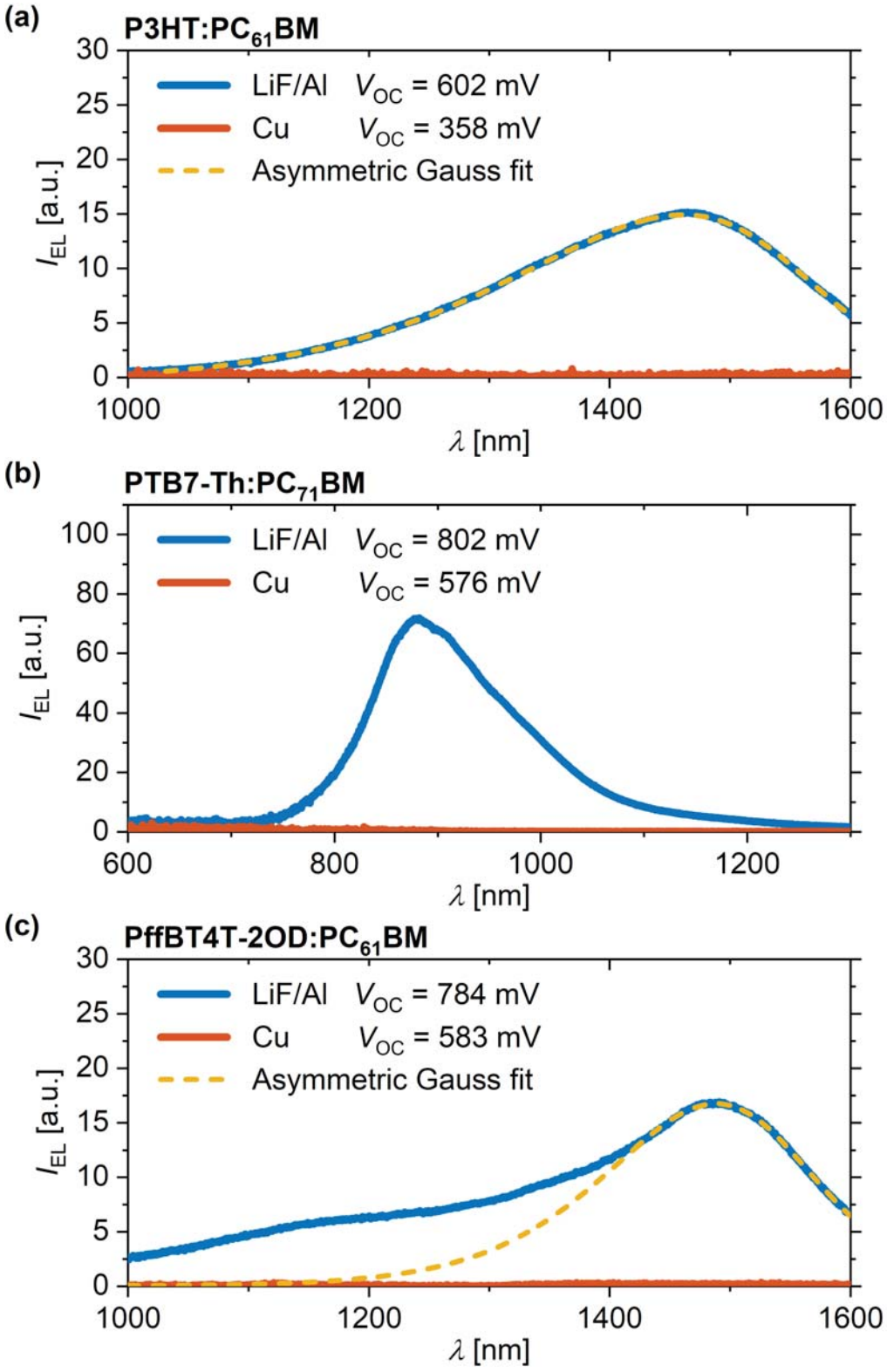

Figure 8.4: Electroluminescence spectra of solar cells with a selective LiF/Al and a less selective Cu contact made from different photoactive materials. (a) P3HT:$PC_{61}BM$, (b) PTB7-Th:$PC_{71}BM$ and (c) PffBT4T-2OD:$PC_{61}BM$ obtained at a current density of 76 mA cm^{-2}. The fitted asymmetric Gauss peaks are characteristic fingerprint of recombination of free charge carrier.

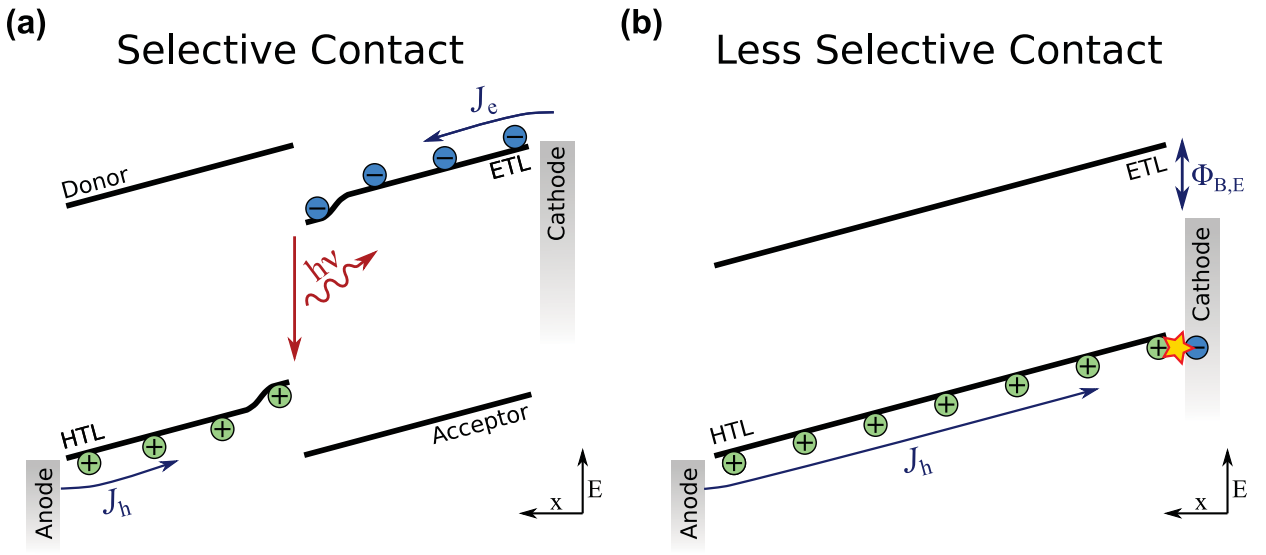

Figure 8.5: Scheme of recombination processes for in injected carrier for different contacts, present during EL measurements in an OSC. For selective contacts (a) electrons and holes recombine partially radiatively at the DA interface. In case of a poorly selective electron contact (b), the injected holes travel to the cathode and recombine nonradiatively with electrons, which are hardly injected due to the injection barrier $\Phi_{B,e}$.

as illustrated in figure 8.5(b). Thus, EL is not suited to investigate bulk recombination in the presence of unselective contacts but confirms surface recombination as the reason for the V_{OC} loss in the investigated solar cells. In addition, the characteristic peak shapes for the recombination of free charge carriers in the respective DA systems are obtained from a fit of an asymmetric Gaussian function to the EL spectra for the cells with selective contacts. The used fit function and results are given in chapter D.1 in appendix D the resulting curves are drawn as yellow dashed lines in figure 8.4. These peak shapes are used later on for the discussion of photoluminescence results.

To examine the recombination in the absorber under illumination, photoluminescence was measured at illumination intensities of $\approx 1\,\text{sun}$[1]. Figure 8.6 depicts the PL spectrum[2] of a P3HT:$PC_{61}BM$ OSC with LiF/Al contact at open-circuit conditions. The spectrum consists of the signal from the radiative decay of excitons with a maximum intensity at $\approx 750\,\text{nm}$ and the charge-transfer (CT) state signal, originating from the recombination of free carriers, with a peak at $\approx 1450\,\text{nm}$. A schematic state diagram of

[1] The intensity of the monochromatic LASER was adjusted to generate the same short-circuit current as under an illumination of AM1.5G.

[2] The luminescence of the used ITO coated glass substrate is subtracted from the presented PL spectra. The substrate PL spectrum is depicted alongside with the PL of a P3HT:$PC_{61}BM$ OSC for comparison in figure B.3 in appendix B.

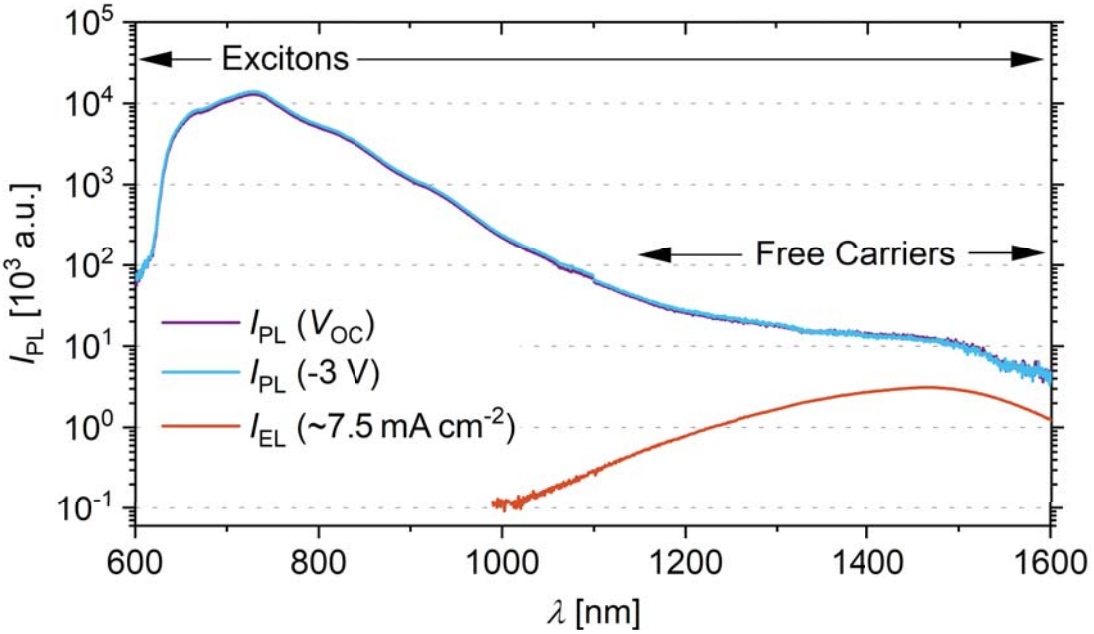

Figure 8.6: Luminescence spectra of a P3HT:$PC_{61}BM$ solar cell with selective LiF/Al contact. The PL at V_{OC} and $V = -3\,V$ are plotted as blue lines and the EL scaled to $J_{inj} \approx 7.5\,mA\,cm^{-2}$ is given as red line. This corresponds to the photogenerated current density under illumination used for PL.

a donor-acceptor system under open-circuit conditions is drawn in figure 8.7(a). Photogenerated excitons either recombine or split up into free charges (G_{eff}). For ideally selective contacts, all generated carriers recombine within the absorber. This can happen at the DA interface via the intermediate CT state under the emission of a photon. The comparison of the PL at open-circuit conditions to the EL at a corresponding injection current density J_{inj} indicates the presence of the CT signal. Despite most excitons commonly dissociate to free carriers in P3HT:$PC_{61}BM$, the observed CT peak intensity is about four orders of magnitude smaller than the exciton luminescence. The weak signal from free carriers originates from the low quantum yield for radiative decay of free carriers between 10^{-6} to 10^{-9}[58, 126][1]. Due to the strong overlap of the free carrier signal with the low energetic tail of the exciton signal, CT state emission is not trivial to determine. To access CT recombination, i.e. the recombination of free carriers, PL

[1] The high nonradiative recombination in OCS can be explained e.g. by recombination via trap states within the band gap. The latter are commonly present in the used absorber materials [127]. However, Tvingstedt and Deibel found recently that the non-radiative recombination mechanism in OPV is not recombination of free carriers with trapped carriers in an exponential density of tail states [128]. Furthermore, a high intrinsic probability for nonradiative CT state decay, due to internal conversion was recently reported by Benduhn et al. [68]. Therefore, the true nature of nonradioactive recombination in OPV is still under discussion.

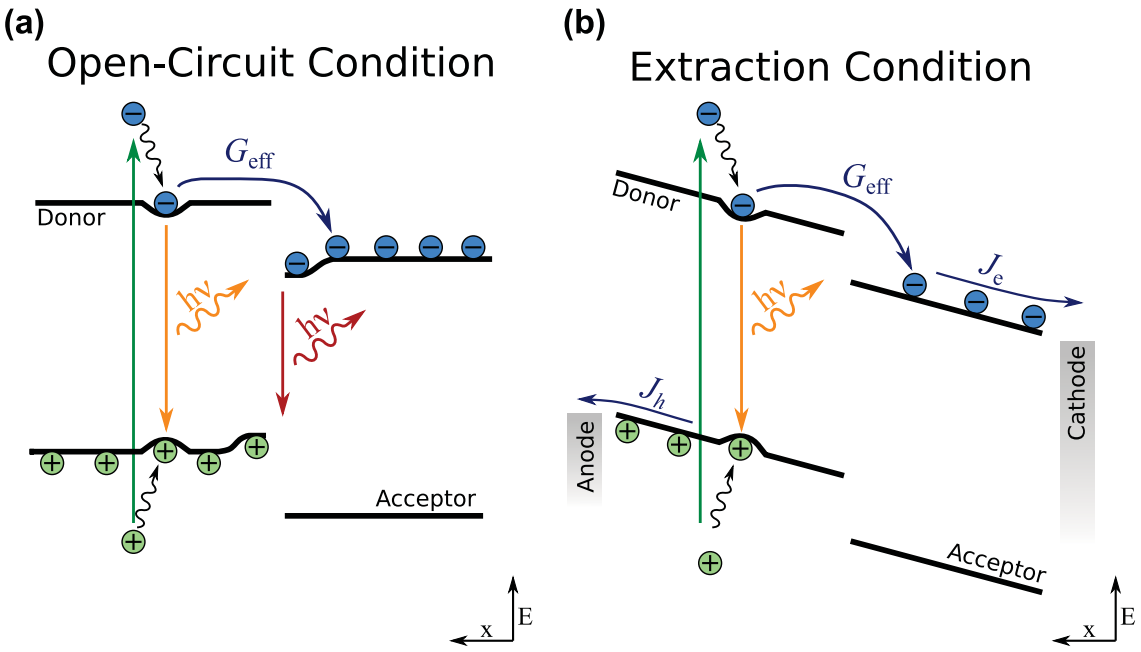

Figure 8.7: Schematic energy diagram of an OSC under open-circuit conditions (a). Photogenerated excitons decay or dissociate, generating free charge carriers with the rate G_{eff}. The latter can recombine radiatively at the DA interface. In the case of carrier extraction (b) the radiative recombination of free charges is quenched.

of the solar cell is measured at different working points of the solar cell. By applying an extraction voltage the signal from free charges should diminish since the charge carrier density within the bulk is reduced [129]. This case is depicted in figure 8.7(b).
In figure 8.8 the PL spectra at V_{OC} and at an applied extraction voltage of $-3\,\text{V}$ for P3HT:PC_{61}BM OSC with (a) a selective LiF/Al and (c) a less selective Cu contact are plotted in the relevant wavelength range. The change in luminescence $\Delta I_{\text{PL}} = I_{\text{PL}}(V_{\text{OC}}) - I_{\text{PL}}(-3\,\text{V})$ for the cells is given in (b) and (d), respectively. The data is fitted by a combination of the characteristic peak shape of free carriers[1] and the tail of a negative Gaussian, accounting for the increase in exciton PL when carrier density is reduced, which is known from literature [130, 131]. The amplitude $\Delta I_{\text{PL}}^{\text{CT}}$ from the fit gives the amount of CT recombination. It is a measure for the recombination of free charge carriers, i.e. for the carrier density within the absorber. It should be stated that $\Delta I_{\text{PL}}^{\text{CT}}$ is not the absolute CT emission but the amount of quenched CT luminescence. A comparison with the absolute PL signal I_{PL} at 1450 nm) of ≈ 13 a.u. (arbitrary units $\sim \text{W m}^{-2}\,\text{nm}^{-1}$) in figure 8.8 shows that $\Delta I_{\text{PL}}^{\text{CT}}$ (≈ 1 a u at 1450 nm) is about 8 % of the

[1] The peak shape of free carrier recombination is known from EL measurements. The explicit peak shape from the fit to the EL of the cell, shown as yellow dashed line in 8.4(a) is used for fitting ΔI_{PL}.

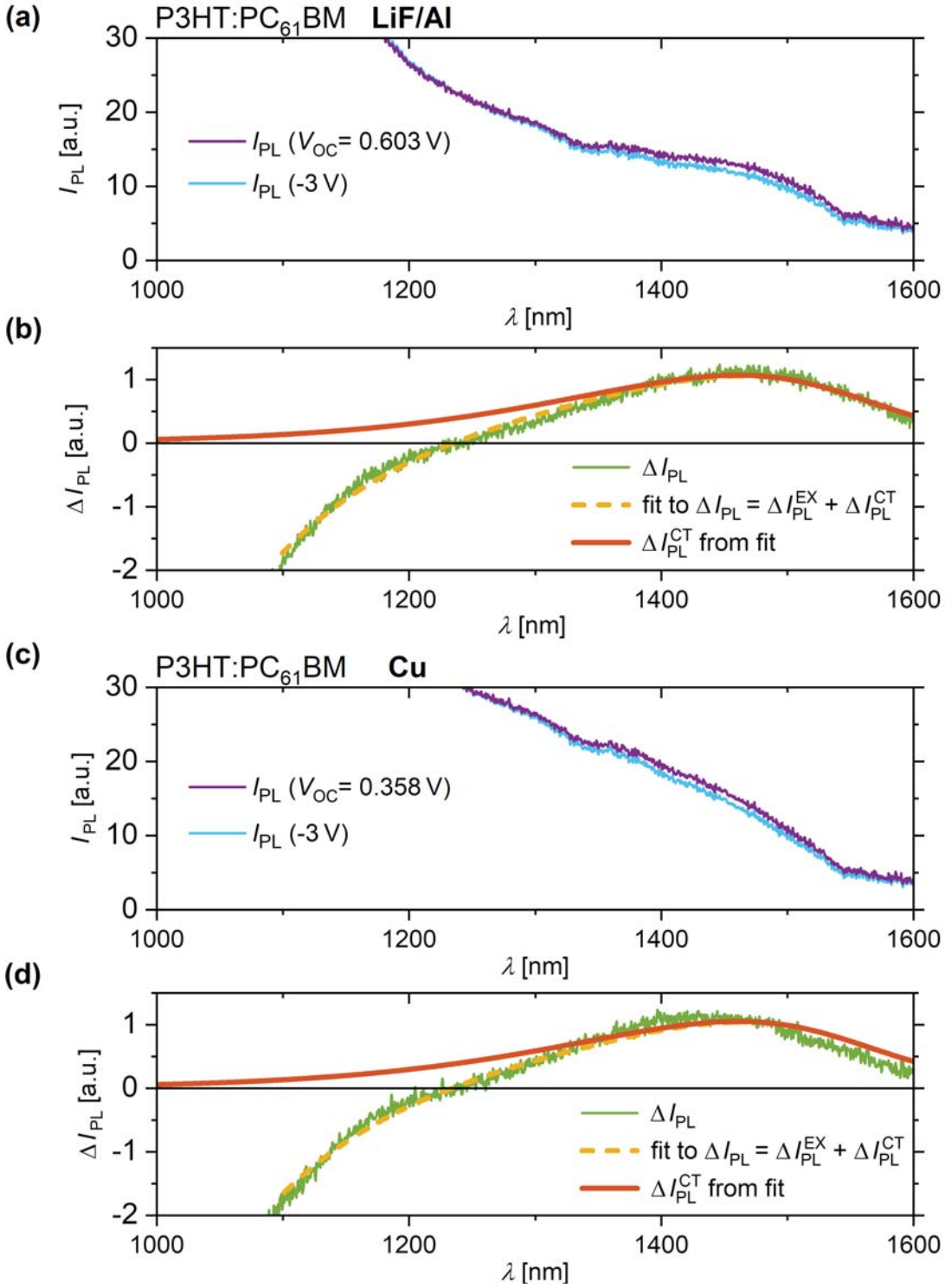

Figure 8.8: PL Intensity at V_{OC} and at $V = -3\,V$ for a P3HT:$PC_{61}BM$ OSC with a selective LiF/Al (a) and a less selective Cu contact (c). PL quenching $\Delta I_{PL} = I_{PL}(V_{OC}) - I_{PL}(-3\,V)$ (b) and (d) for the respective systems. The data was fitted by a combination of an asymmetric Gaussian peak (PL of free charge carrier) and a negative Gaussian tail (representing the rise in exciton PL). ΔI_{PL}^{CT} (peak size from fit) is a measure for the free carrier PL.

total luminescence. Its proportion of the total CT luminescence is even higher when the amount of the exciton signal in the relevant wavelength region is considered. Therefore, $\Delta I_{\mathrm{PL}}^{\mathrm{CT}}$ has the same order of magnitude as the total CT emission and can be used as an approximate measure for the magnitude of total radiative recombination of free charges. The total intensity of free carrier recombination $I_{\mathrm{tot}}^{\mathrm{CT}}$ is calculated by the integral of $\Delta I_{\mathrm{PL}}^{\mathrm{CT}}$ over wavelength as 3.5 a.u. ($\sim$ W m^{-2}) for both, the selective (LiF/Al) and the less selective (Cu) contact. Within the accuracy of the analysis[1], the amount of PL from free charges for the cell with a less selective contact is comparable to the PL of the cell with highly selective contacts.

The PL spectra $I_{\mathrm{PL}}(\lambda)$ and $\Delta I_{\mathrm{PL}}(\lambda)$ of the PffBT4T-2OD:$PC_{61}BM$ cells for LiF/Al and Cu contacts are plotted in figure 8.9. The analysis for PffBT4T-2OD:$PC_{61}BM$ was carried out analogously to P3HT:$PC_{61}BM$. For the PTB7-Th:$PC_{71}BM$ based solar cell, the change in PL intensity for different bias conditions is more pronounced. Thus the quenched luminescence from free carriers $\Delta I_{\mathrm{PL}}^{\mathrm{CT}} \approx \Delta I_{\mathrm{PL}}$ could be obtained directly and no fitting is needed to obtain $I_{\mathrm{tot}}^{\mathrm{CT}}$. The corresponding PL spectra are shown in figure 8.10. The resulting $I_{\mathrm{tot}}^{\mathrm{CT}}$ from excess carriers for all absorber materials are summarized in table 8.1 alongside with the V_{OC} of the cells. The data is complemented with the carrier densities n_{pg} obtained from BACE. In addition, the calculated $\Delta V_{\mathrm{OC},1}$ and $\Delta V_{\mathrm{OC},2}$ from simulations are listed. For the poorly selective Cu contact V_{OC} is reduced by 200 – 250 mV for the different photoactive materials. However, the measured overall recombination of free carriers $I_{\mathrm{tot}}^{\mathrm{CT}}$ in the absorber for the LiF/Al and the Cu cathode is comparable in case of P3HT:$PC_{61}BM$ and PTB7-Th:$PC_{71}BM$ and reduced by a factor of 2 for the

Table 8.1: Results from PL and charge extraction measurements for devices with the polymers P3HT, PTB7-Th, and PffT4TBT-2OD and fullerene acceptors for selective (LiF/Al) and less selective (Cu) electron contacts.

Blend	el. cont.	V_{OC} [mV]	$I_{\mathrm{tot}}^{\mathrm{CT}}$ [$\sim$ W m^{-2}]	n_{pg} [10^{16} cm^{-3}]	$\Delta V_{\mathrm{OC},1}$ [mV]	$\Delta V_{\mathrm{OC},2}$ [mV]
P3HT:$PC_{61}BM$	LiF/Al	602	3.5	2.3	0	0
	Cu	358	3.5	2.0	248	0
PTB7-Th:$PC_{71}BM$	LiF/Al	802	550	0.9	0	0
	Cu	576	500	1.2	224	2
PffT4BT-2OD:$PC_{61}BM$	LiF/Al	784	6.9	0.9	0	0
	Cu	583	3.5	0.7	191	10

[1] A discussion on the errors of luminescence measurements is given in chapter D.2 in appendix D. They do not affect the qualitative conclusions of this study.

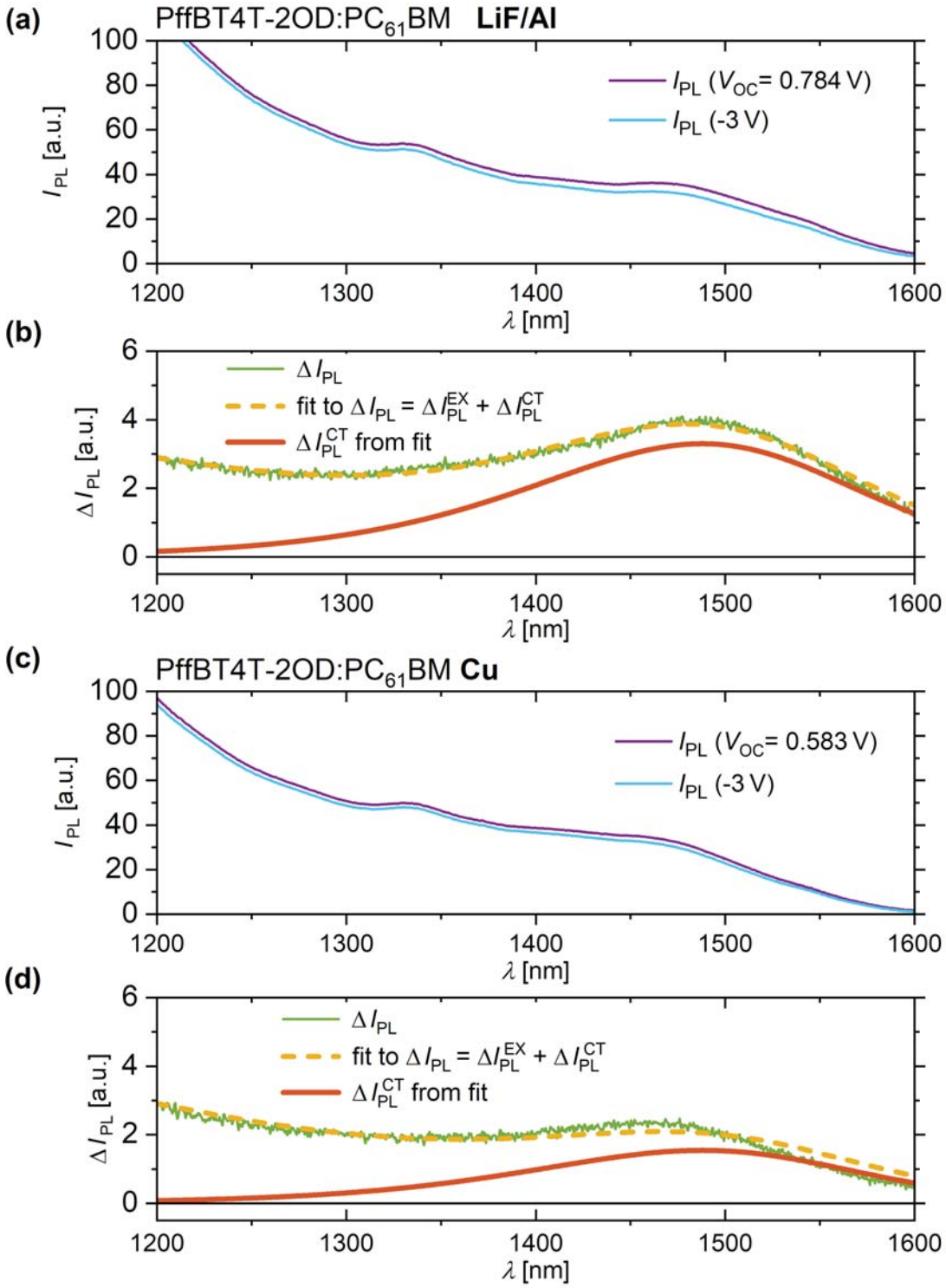

Figure 8.9: PL Intensity at V_{OC} and at $V = -3\,V$ for a PffBT4T-2OD:$PC_{61}BM$ OSC with a selective LiF/Al (a) and a less selective Cu contact (c). PL quenching $\Delta I_{PL} = I_{PL}(V_{OC}) - I_{PL}(-3\,V)$ (b) and (d) for the respective systems. The data was fitted by a combination of an asymmetric Gaussian peak (PL of free charge carrier) and a negative Gaussian tail (representing the rise in exciton PL). ΔI_{PL}^{CT} (peak size from fit) is a measure for the free carrier PL.

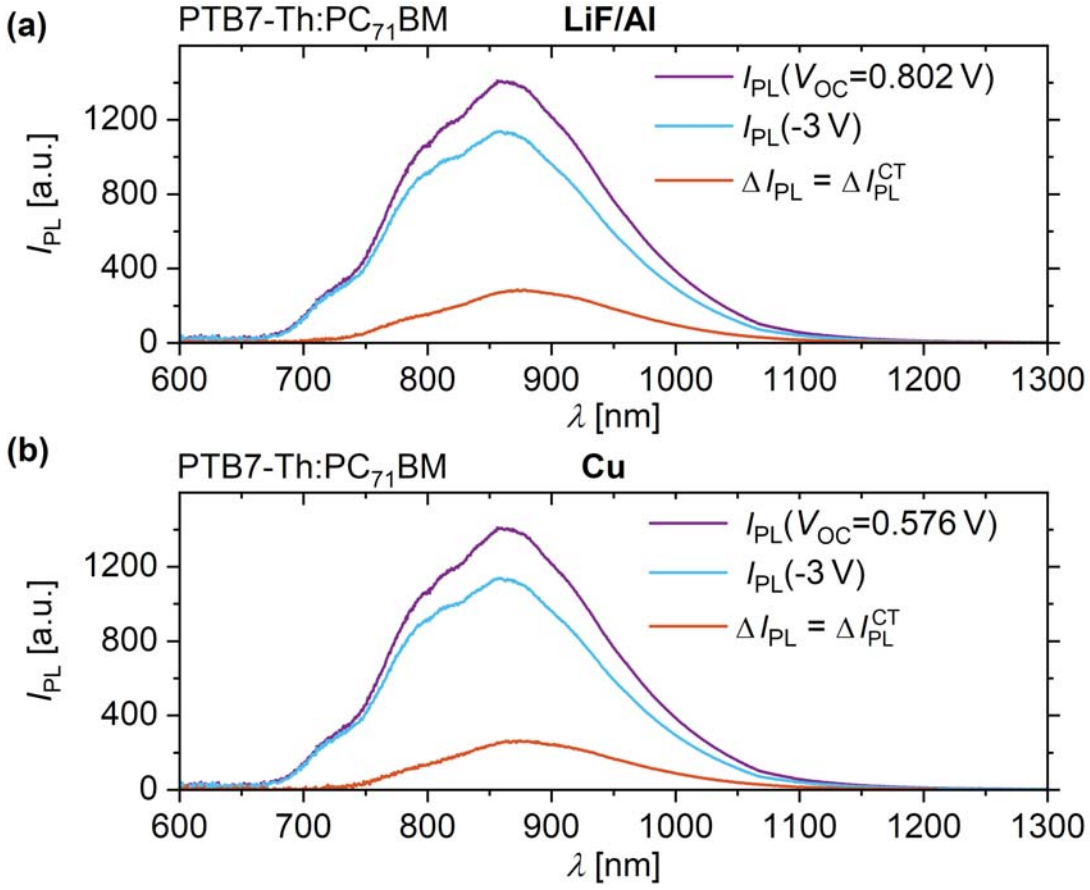

Figure 8.10: PL Intensity at V_{OC} and at $V = -3\,V$ for a PTB7-Th:$PC_{71}BM$ OSC with a selective LiF/Al (a) and a less selective Cu contact (b) with the corresponding PL quenching signals $\Delta I_{PL} = I_{PL}(V_{OC}) - I_{PL}(-3\,V)$. ΔI_{PL}^{CT} is a measure for the free carrier luminescence.

PffT4BT-2OD:$PC_{61}BM$ cell. This leads to the conclusion that the overall carrier density is barely altered by surface recombination in OSC. The measured excess carrier densities from BACE corroborates this result. They are comparable for both contact materials for each absorber material. However, this quantity comprises significant systematic errors from capacitive effects at the investigated intensity of $\approx 1\,sun$. The ratio of capacitive to excess charge is $\frac{n_{pg}}{n_{cap}} \approx 3$ for P3HT:$PC_{61}BM$, ≈ 2 for PffBT4T-2OD:$PC_{61}BM$ and only ≈ 1 for PTB7-Th:$PC_{71}BM$ at $1\,sun$[1]. In contrast, the introduced steady-state method of PL quenching is not affected by the capacity of the OSC. The uncertainty of the obtained numbers is estimated to be about 50 %[2]. However, the experimental results prove, that recombination in the bulk, and thus the overall carrier densities

[1] A comprehensive discussion on the systematic errors of this method is given in chapter 7.

[2] The accuracy of the method is limited mainly by incomplete quenching of the CT signal, variations between samples, inhomogeneities within one sample and systematic errors of the setup.

($R \sim n^{\alpha}$), have the same order of magnitude for selective contacts and those contacts where severe V_{OC} losses from surface recombination are observed. Thus, the drawn picture from simulations, that strong gradients of the QFL of electrons and holes towards an unselective contact are the main reason for V_{OC} losses in OSC is verified. From the simulated values of $\Delta V_{\mathrm{OC},1}$ and $\Delta V_{\mathrm{OC},2}$ in table 8.1 it becomes apparent that the V_{OC} loss for P3HT:$PC_{61}BM$ originates completely from the gradient of the QFL of electrons ($\mu_{\mathrm{e}} = 1.7 \times 10^{-4}\,\mathrm{cm}^2\,(\mathrm{V\,s})^{-1}$, $\mu_{\mathrm{h}} = 4.5 \times 10^{-4}\,\mathrm{cm}^2\,(\mathrm{V\,s})^{-1}$). Whereas, for the photactive material with the high mobility polymer PTB7-Th:$PC_{71}BM$ ($\mu_{\mathrm{e}} = 6 \times 10^{-4}\,\mathrm{cm}^2\,(\mathrm{V\,s})^{-1}$, $\mu_{\mathrm{h}} = 7 \times 10^{-3}\,\mathrm{cm}^2\,(\mathrm{V\,s})^{-1}$) a contribution of $\Delta V_{\mathrm{OC},2}$ arises, i.e. a loss of carriers throughout the entire thickness of the absorber, due to the better transport properties. The influence of carrier mobility on the overall V_{OC} loss is discussed hereinafter.

8.3 Impact of Charge Carrier Mobility on Surface Recombination

The effect of transport properties of the absorber on surface recombination and the resulting losses is studied by a variation of the carrier mobilities in simulations within this section. Figure 8.11(a) shows the band diagram for a 220 nm thick solar cell with a

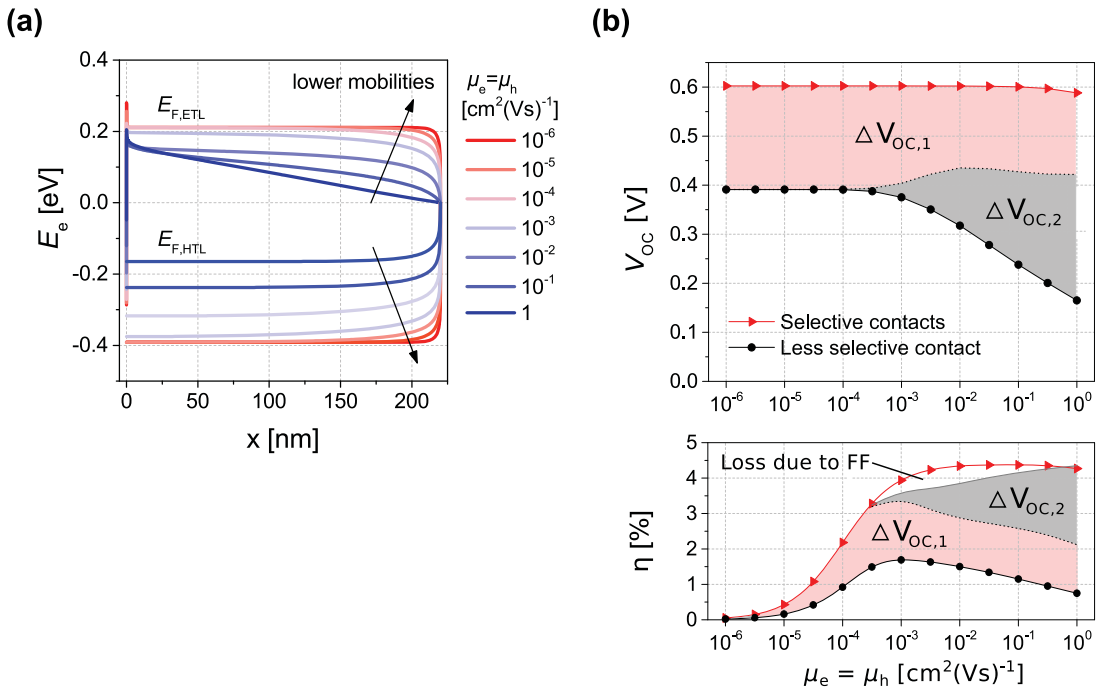

Figure 8.11: (a) Simulated energy diagram of a solar cell with a selective hole contact and a poorly selective electron contact for different mobilities. (b) V_{OC} and the power conversin efficieny η for the cases depicted in (a) as a function of mobility with the losses (compared to the case without surface recombination). Modified from[99].

selective hole contact and a less selective electron contact for different balanced ($\mu_e = \mu_h$) carrier mobilities. For a low mobility, the QFL splitting, and thus the carrier density, is only altered in the proximity of the cathode. For mobilites lower than $\lessapprox 10^{-3}\,\mathrm{cm^2\,(V\,s)^{-1}}$, the gradient of the QFL of electrons is the main contribution to the overall V_{OC} loss ($\Delta V_{OC,1}$). Therefore, hardly any carriers do actually flow from the bulk to the unselective contact and recombine, hence the surface recombination current diminishes. However, even small currents need strong gradients as a driving force for mobilities that low. For higher mobilities, the internal voltage gets more and more reduced by the loss of carriers throughout the entire absorber, resulting in rising surface recombination currents. The contribution from the gradient of the majority carriers ($V_{OC,1}$) and from the loss of electrons and holes to the surface ($V_{OC,2}$) to the overall voltage loss and power conversion efficiency loss are plotted as function of carrier mobility in figure 8.11(b)(in comparison to cell with two selective contacts). It can be seen there that the loss in power conversion efficiency is mainly caused by losses of the open-circuit voltage over the entire investigated mobility range. For typical mobilities of photoactive materials used in OPV in the range of $10^{-4}\,\mathrm{cm^2\,(V\,s)^{-1}}$ to $10^{-3}\,\mathrm{cm^2\,(V\,s)^{-1}}$, the gradients of the corresponding QFL are the main contribution to the V_{OC} loss.

8.4 Summary of the Investigation of Surface Recombination in OSC

In this chapter, the effect of surface recombination on the charge carrier densities in organic solar cells was investigated. Electron contacts with strongly different selectivity (LiF/Al and Cu) were applied as top electrode on devices with different photoactive layers. Charge carrier density was determined by charge extraction and an advanced combination of photo- and electroluminescence. The method of photoluminescence quenching has been established to determine the PL intensity originating from free charge carrier. Using this method, the recombination of photogenerated electrons and holes in P3HT:PC_{61}BM via the CT state could be (to the knowlege of the author) determined experimentally for the first time under illumination. The results prove that the overall carrier densities is only slightly reduced by the poorly selective Cu contacts in the investigated organic solar cells. This implies, that V_{OC} does not equal the internal QFL splitting for OSC when surface recombination is present. Thus V_{OC} is not suited to investigate bulk recombination in this case. All experimental results could be reproduced consistently by drift-diffusion simulations where the work function of the electron contact was the only varied parameter. From the combination of these results, two distinct contributions to the overall V_{OC} reduction have been identified. First: the gradient of

the quasi-Fermi energy of the majority carriers towards their respective contact as the driving force for the recombination current and second: the reduction of the maximum charge carrier density in the absorber due to recombination at the electrode interface. Their contributions depend strongly on the charge carrier mobilities. For materials with rather poor transport properties, which is the case for many photoactive materials that are used in OSC, the main loss of the V_{OC} is caused by the gradient of the quasi-Fermi energy of the majority charge carriers in the vicinity of the corresponding contact (whereas the carrier densities at some distance of a contact with insufficient selectivity are barely reduced). For imbalanced mobilities, these losses from gradients in the QFL are reduced for the case of a higher majority carrier mobility. The fact that in many organic solar cells the electron mobility is higher than the hole mobility explains the observation that it often is more difficult to realize a selective hole contact and more facile to ensure a selective electron contact.

9 Illumination and Temperature Dependence of the Open-Circuit Voltage

This study presents results from temperature and illumination dependent measurements of the open-circuit voltage of organic solar cells made from different photoactive materials. From that, the effective band gaps of organic donor-acceptor materials are determined. The data was obtained in a cryogenic setup described in chapter 5.2. To avoid a change in temperature of the absorber under illumination pulsed light (530 nm) from a green LED is used. It emerged during this study that V_{OC} is (10–20) mV lower when measured under continuous illumination of 1 sun (1000 W m^{-2} AM1.5G) on a sun simulator[1] compared to the value measured with pulsed light of comparable intensity. For this study V_{OC} was measured using a buffer amplifier with an input impedance of $R_{in} > 10\,G\Omega$ to ensure open-circuit conditions. This is crucial at low temperatures and low illumination intensities as discussed in chapter 5.2.

[1] There the cell is passively cooled by an airflow from a fan.

9.1 Determination of the Effective Band Gap

For ideally selective electrodes ($V_{\mathrm{int}} = V_{\mathrm{OC}}$) and homogeneous generation the V_{OC} of an OSC is given by equation (2.7) as

$$e_0 V_{\mathrm{OC}}(T) = E_{\mathrm{g,eff}} - n_{\mathrm{id}} k_{\mathrm{B}} T \ln\left(\frac{N_{\mathrm{C}} N_{\mathrm{V}} k_{\mathrm{r}}}{G_{\mathrm{eff}}}\right) \tag{9.1}$$

Here, recombination of reaction order $\beta = \frac{2}{n_{\mathrm{id}}}$ according to equation (1.19) and the Boltzmann approximation is used. From this equation V_{OC} is expected to increase linearly with decreasing temperature and to increase logarithmically with increasing illumination intensity[1]. Figure 9.1 shows the measured V_{OC} as a function of temperature and intensity[2] for solar cells made from P3HT:$PC_{61}BM$ purchased from Rieke Metals (a) and BASF (b), PCDTBT:$PC_{71}BM$ (c), P1:$PC_{61}BM$ (d), PffBT4T-2OD:$PC_{61}BM$ (e) and PBDB-T:ITIC (f). The used contact materials are listed in table 9.1. The breakdown in V_{OC} for the P3HT:$PC_{61}BM$ cell (figure 9.1(a)) at low temperatures and intensities is caused by the shunt resistance of the investigated OSC. The mobility of charge carriers in organic semiconductors typically drops exponentially with temperature (see chapter 2.4) and the transport properties get limited drastically. Hence, a parasitic current causes a severe ohmic voltage loss in the absorber at low temperatures, reducing the external voltage at the contacts. At low temperatures the voltage of an OSC is already reduced significantly for comparatively small external currents flowing over parasitic shunt resistances[3]. Therefore, special attention must be payed on shunt resistance during sample selection for these measurements. The strong drop in V_{OC} for PBDB-T:ITIC (figure 9.1) at a temperature of 125 K was caused by a temporal shunt during the measurement and is not considered in the following discussion.

According to equation (9.1), $e_0 V_{\mathrm{OC}}$ at $T = 0\,\mathrm{K}$ is expected to resemble the effective band gap[4] $E_{\mathrm{g,eff}}$ of the absorber material. Hence, $E_{\mathrm{g,eff}}$ can be determined from a linear extrapolation of $V_{\mathrm{OC}}(T)$ to $T = 0\,\mathrm{K}$. V_{OC} is plotted as a function of the temperature for

[1] Assuming a temperature independent effective generation rate of free carriers G_{eff}, a constant recombination coefficient k_{r} with recombination mechanism n_{id} as well as a constant product $N_{\mathrm{C}} N_{\mathrm{V}}$ of the effective densities of states .

[2] The calculation of the intensities in multiples of 1 sun (1000 $\mathrm{W\,m^{-2}}$ AM1.5G) for the green illumination is described in chapter 5.2.

[3] An example for the V_{OC} reduction for defined external shunt resistances of 1 MΩ and 10 MΩ at low temperatures is shown in figure 5.2 on page 37.

[4] $E_{\mathrm{g,eff}}$ resembles the energy difference of the electron-transport level in the acceptor phase and the hole-transport level in the donor material in the effective semiconductor picture as discussed in chapter 2.

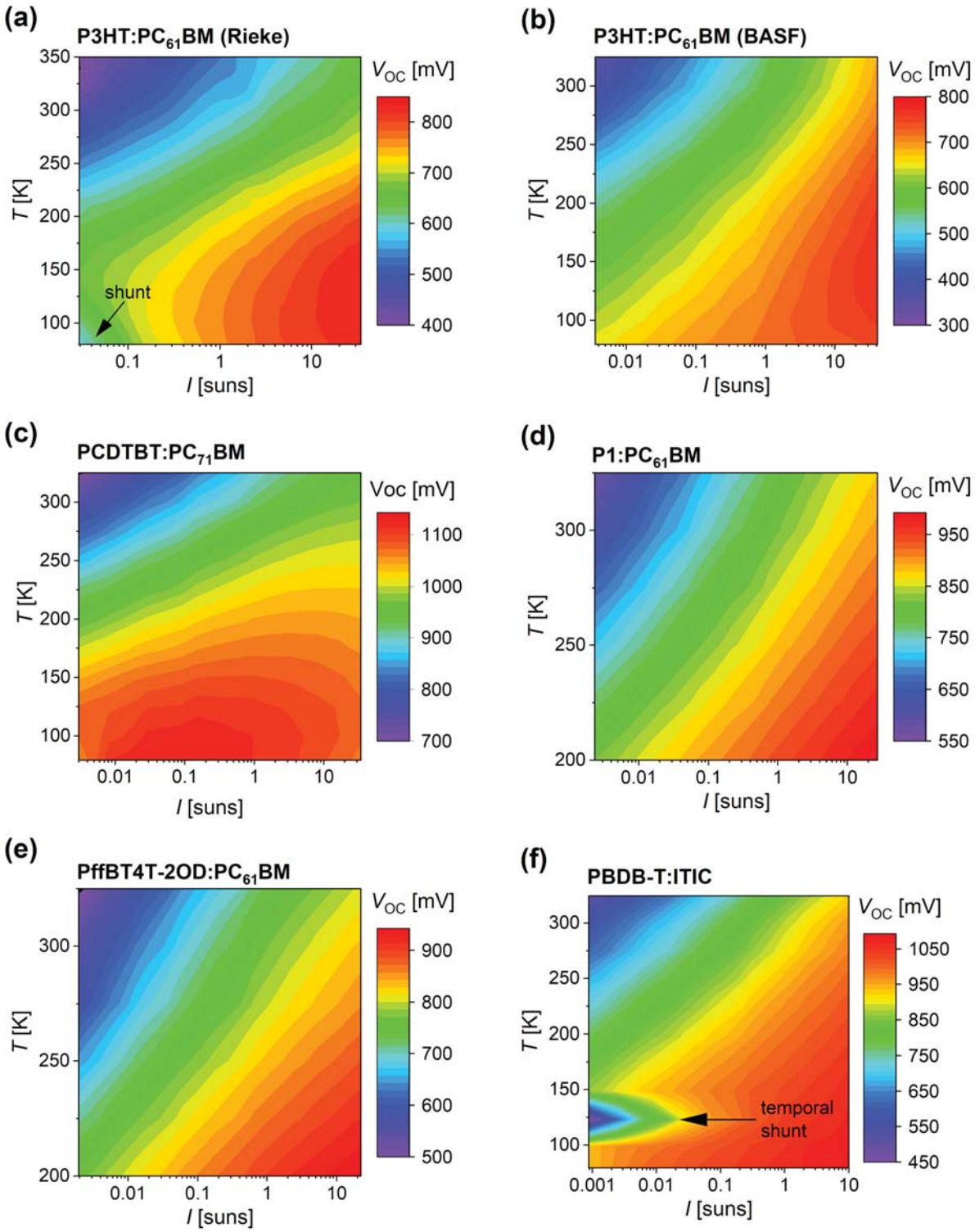

Figure 9.1: V_{OC} as a function of temperature and intensity for OSC with the photoactive materials P3HT:$PC_{61}BM$ purchased from (a) Rieke Metals and (b) BASF, (c) PCDTBT:$PC_{71}BM$, (d) P1:$PC_{61}BM$, (e) PffT4T-2OD:$PC_{61}BM$ and (f) PBDB-T:ITIC.

different intensities in figure 9.2 for P3HT:$PC_{61}BM$ (from BASF) (a), PBDB-T:ITIC (b) and PCDTBT:$PC_{71}BM$ (c). Figure 9.3 shows the same data for OSC made from PffBT4T-2OD:$PC_{61}BM$ (a), P1:$_{61}BM$ (b) and P3HT:$PC_{61}BM$ (from Rieke Metals). For temperatures above 200 K the V_{OC} increases linearly with decreasing temperature for all intensities and materials as expected from theory. Line fits to the data in this linear regime are extrapolated to $T = 0\,K$. $E_{g,eff}$ is calculated as the mean value of the results from extrapolation for the individual illumination intensities. For PCDTBT:$PC_{71}BM$ only the values for intensities $I < 1\,sun$ were considered. The resulting $E_{g,eff}$ of the individual absorber materials with errors (mean deviation) are summarized in table 9.1. The deviations from the expected linear behavior and the systematic shift of the extrapolated effective gap for PCDTBT:$PC_{71}BM$ for intensities >1 sun are discussed in the next section.

Table 9.1: Effective band gaps $E_{g,eff}$ for different absorber materials obtained from linear extrapolation of V_{OC} to $T = 0\,K$.

absorber material	el. contact	h. contact	$E_{g,eff}$ [meV]
P3HT:$PC_{61}BM$ (BASF)	LiF/Al	PEDOT:PSS AI	881 ± 7
P3HT:$PC_{61}BM$ (Rieke)	LiF/Al	PEDOT:PSS AI	984 ± 29
PffBT4T-2OD:$PC_{61}BM$	LiF/Al	PEDOT:PSS AI	1175 ± 9
P1:$PC_{61}BM$	ITO/PEIE	PEDOT:PSS AI/Ag	1196 ± 16
PCDTBT:$PC_{71}BM$	LiF/Al	PEDOT:PSS AI	1350 ± 6
PBDB-T:ITIC	ZnO	MoO_3	1237 ± 15

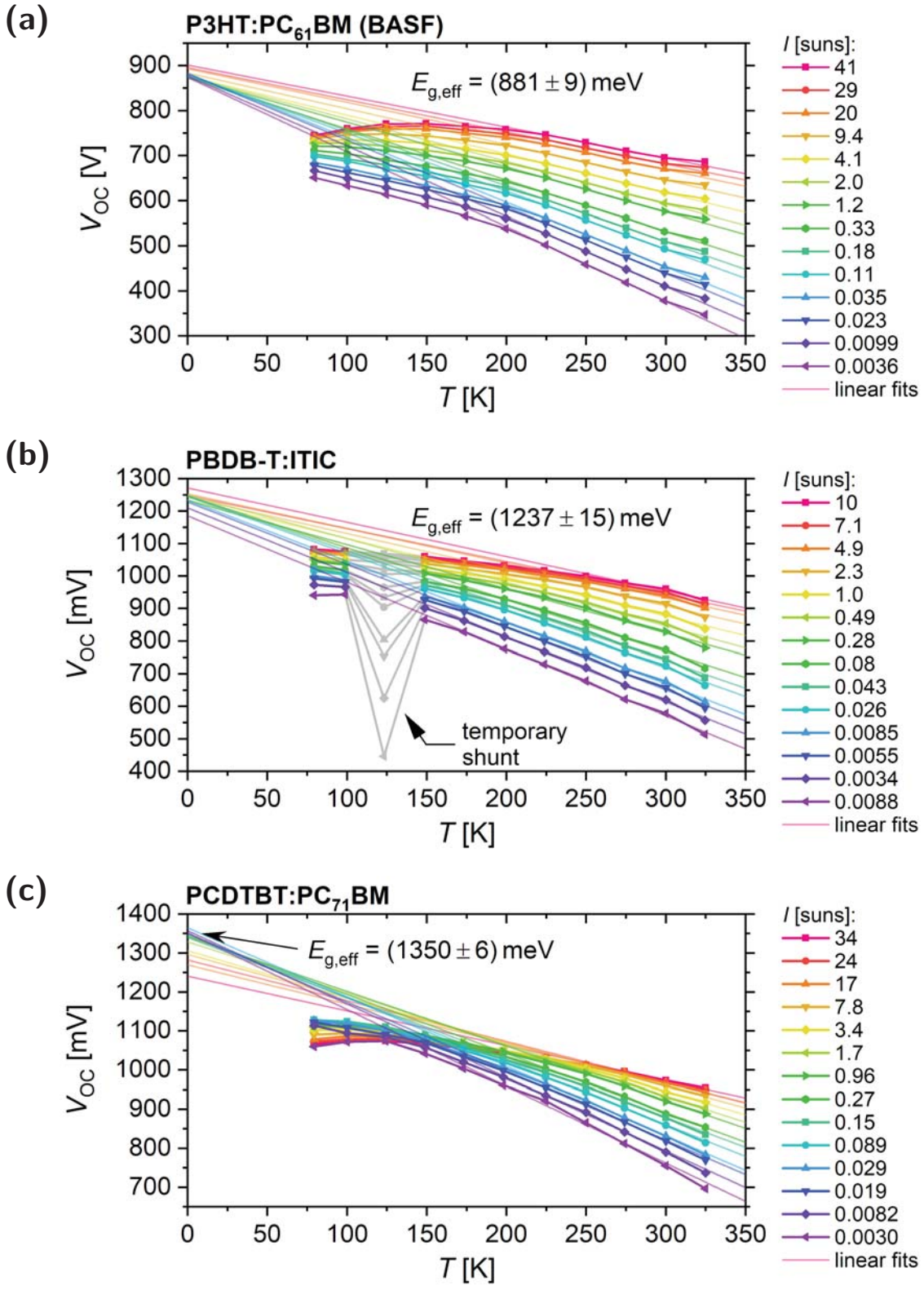

Figure 9.2: V_{OC} as a function of temperature for different intensities for the photoactive materials (a) P3HT:$PC_{61}BM$ purchased from BASF, (b) PBDB-T:ITIC and (c) PCDTBT:$PC_{71}BM$. The effective band gap $E_{g,eff}$ is obtained by extrapolation to $T = 0\,K$ of the line fits to the data in the range where a linear behavior is observed.

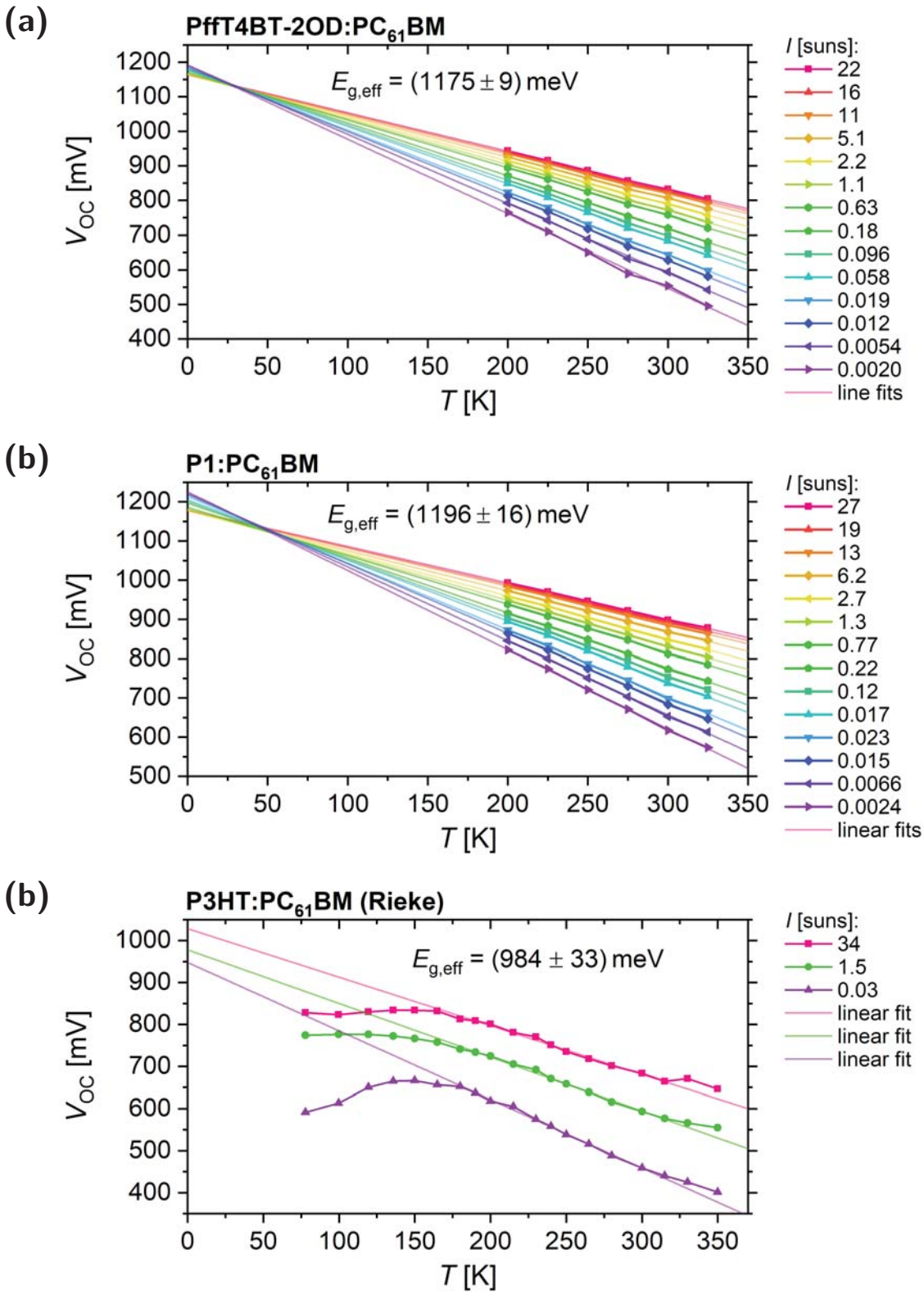

Figure 9.3: V_{OC} as a function of temperature for different intensities for the photoactive materials (a) PffBT4T-2OD:$PC_{61}BM$, (b) P1:$PC_{61}BM$ and (c) P3HT:$PC_{61}BM$ purchased from BASF. he effective band gap $E_{g,eff}$ is obtained by extrapolation to $T = 0\,K$ of the line fits to the data in the range where a linear behavior is observed.

9.2 Open-Circuit Voltage Saturation at Low Temperatures

V_{OC} measured at lower intensities and at high temperatures changes linearly with temperature in figures 9.2 and 9.3 for all materials as expected from equation (9.1). For falling temperatures and high illumination intensities, the measured V_{OC} deviates from the expected behavior. The reasons for this are worked out in this section by a successive discussion of possible reasons.

The quantum yield for photogeneration of free charge carriers in P3HT:PCBM blends was reported in literature to be virtually temperature independent in the range of (10–280) K in transient absorption experiments [132]. Hence, reduced generation of carriers for a given illumination intensity is excluded to contribute considerably to the observed saturation of V_{OC} at low temperatures (at least for P3HT:PC_{61}BM) and G_{eff} is assumed temperature independent, i.e. $G_{eff} \sim I$, in the following discussion. Further, a significant contribution from a temperature or illumination dependence of $N_C N_V$ is excluded. A contribution would require changes in orders of magnitude, since V_{OC} depends logarithmically on $N_C N_V$, which seems not to be reasonable. It is worth to mention here, that these assumptions ($G_{eff} \sim I$, $N_C N_V \approx$ const.) imply a temperature independent recombination coefficient k_r in the range where a linear temperature dependence of V_{OC} is observed e.g. at $T < 200\,\mathrm{K}$ for P3HT:PC_{61}BM.

For P3HT:PC_{61}BM, V_{OC} saturates at about 780 mV. At a corresponding QFL splitting, the energetic difference to the determined band gap of 880 meV is $E_{eff} - e_0 V_{OC} \approx 100\,\mathrm{meV}$. When assumed equally large[1], the difference between the QFL of electrons and holes to the respective band edges is $E_{F,e} - E_C = E_V - E_{F,h} \approx 50\,\mathrm{meV} \approx 4\,k_B T$ (for $T = 150\,\mathrm{K}$). In case of asymmetric energetic states, one QFL is located even closer to its corresponding band. Thus, deviations from the Boltzmann approximation may arise. However, for PCDTBT:PC_{71}BM, $E_{eff} - e_0 V_{OC}$ is about 300 meV $\approx 35\,k_B T$ at 100 K, thus no significant deviations from the Boltzmann approximation are expected and thus they can be excluded as the dominant reason for the observed V_{OC} saturation.

Hence, a transition in the predominant recombination mechanism, i.e. change in n_{id} or k_r, is obvious.

$V_{OC}(I)$ is expected to increase linearly with the logarithm of the illumination intensity with a slope of $n_{id} \cdot e_0^{-1} k_B T \ln(10)$ for a given temperature (for constant k_r and n_{id}). Therefore, the slope of $V_{OC}(I)$ gives insights in the recombination mechanism. V_{OC} is shown in a semi-logarithmic plot over I in figure 9.4 (a) for the P3HT:PC_{61}BM (BASF)

[1] Assuming no significant doping and equal effective densities of states for electron and holes

and the PCDTBT:$PC_{71}BM$ OSCs. For P3HT:$PC_{61}BM$ at high temperature, a constant slope is observed over the entire intensity range. At low temperatures, the slope flattens toward high intensities. In contrast, V_{OC} for PCDTBT:$PC_{71}BM$ shows a curvature over the entire voltage and intensity range. Figures 9.4 (b) and (c) depict n_{id} as a function of illumination intensity, calculated from the slope of $V_{OC}(I)$ by $n_{id} = \frac{\partial V(I)}{\partial \log(I)} \cdot \frac{e_0}{k_B T \ln(10)}$. For P3HT:$PC_{61}BM$, n_{id} is nearly constant at ≈ 1.3 for all intensities at $T > 200\,K$, i.e. recombination with intensity independent k_r of reaction order $\beta = \frac{2}{n_{id}} \approx 1.5$ is predominant. At lower temperatures (higher QFL splittings) n_{id} rises slightly and gets considerably voltage dependent for 80 K and 100 K. For PCDTBT:$PC_{71}BM$ n_{id} is tem-

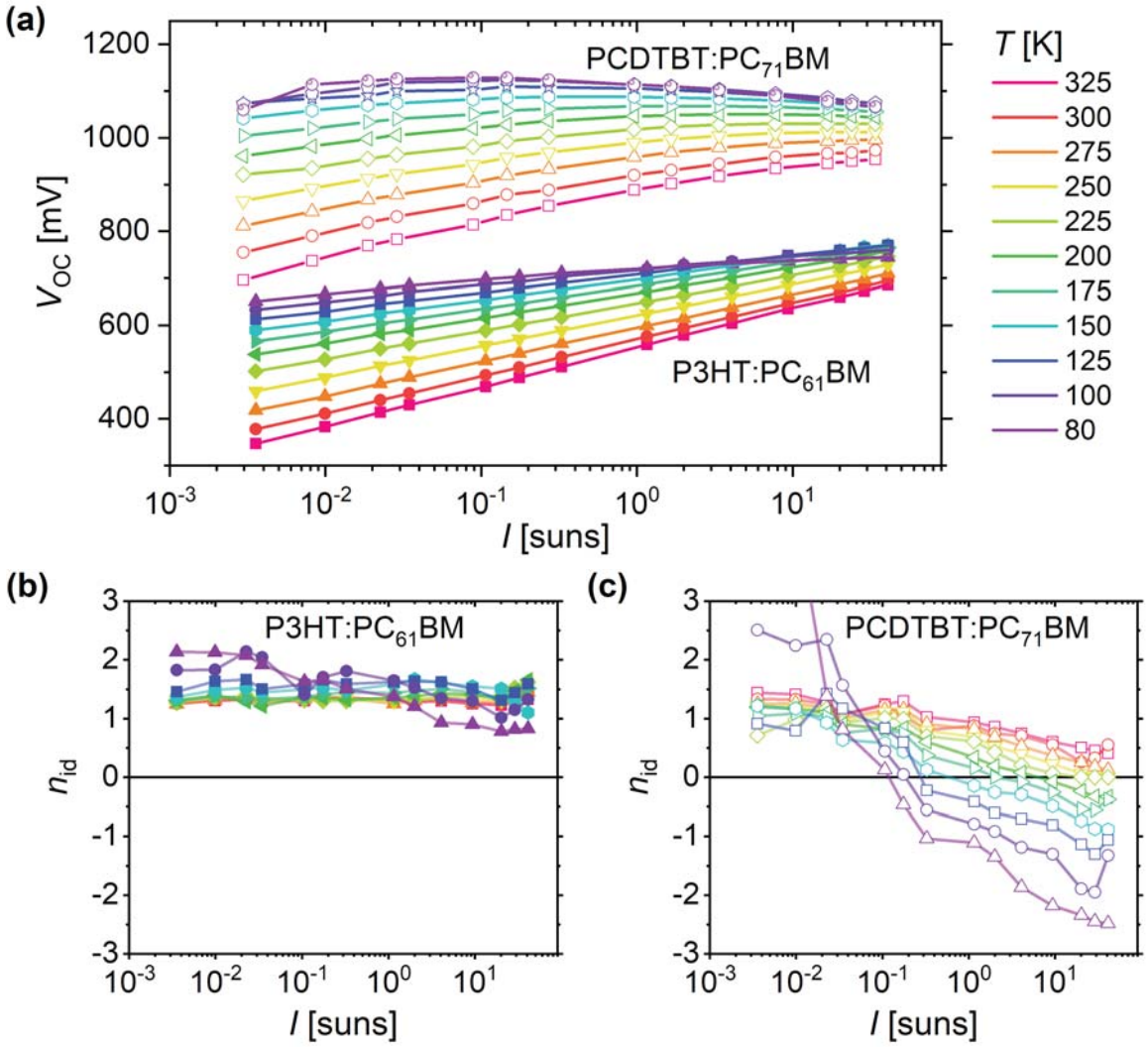

Figure 9.4: V_{OC} as function of illumination intensity I (a) of a P3HT:$PC_{61}BM$ solar cell (full symbols) and a PCDTBT:$PC_{71}BM$ cell (open symbols. The corresponding ideality factors n_{id} as function of I are plotted in (b) and (c) (the two points for the lowest intensities at 80 K are 5 and 8, respectively. They originate from the drop of V_{OC} at these conditions due to the shunt resistance of the cell).

perature and intensity dependent over the entire range. At low temperatures and high intensities (high QFL splitting) it gets smaller then 1 and even negative.
The observations can be explained by arising surface recombination with increasing QFL splitting in the absorber. When the QFL splitting in the absorber increases, the quasi-Fermi energies of electrons and holes move toward or even above the work function of the contacts, increasing the driving force for surface recombination currents. It was shown in chapter 8 that in such a case a V_{OC} loss at the electron contact of $\Delta V_{\mathrm{OC}} = E_{\mathrm{F,ETL}}^{\mathrm{ideal}} - W_{\mathrm{F,el.cont}}$ arises for a metal-semiconductor contact and balanced mobilites[1]. In this case, V_{OC} is limited to the built-in voltage $V_{\mathrm{bi}} = 1/e_0\,(W_{\mathrm{F,h.cont}} - W_{\mathrm{F,el.cont}})$ and a saturation of V_{OC} can be explained. In addition, the effect of an ideality factors < 1 obseverd at illumination intensity dependent V_{OC} measurements was reported in literature [133]. The hypothesis of increased surface recombination from increased QFL splitting is further supported by the fact that the saturation is observed already at lower intensities and at higher temperatures for PCDTBT:PC_{71}BM, which has a significantly higher QFL splitting than P3HT:PC_{61}BM under the same conditions. It can be seen from figure 9.4(a) that saturation effects start at comparable voltages ($\approx 700\,\mathrm{mV}$), which is reasonable, since the samples feature the same contacts and hence, the similar built-in voltage. However, the observed decrease of V_{OC} with increasing QFL splitting, i.e. decreasing temperature, requires a more extensive explanation. Unfortunately, the investigation of surface recombination and internal QFL splitting in the absorber is not possible with the methods of charge extraction and PL quenching as used in chapter 8 for this purpose. Due to the very poor transport properties at low temperatures, no relevant amount of carriers can be extracted with reasonable voltages. Nevertheless, surface recombination is suggested to determine V_{OC} under the discussed conditions.
As proven in chapter 8, strong gradients of the QFL are present in the photoactive layer of OSC when V_{OC} is reduced by surface recombination and $V_{\mathrm{OC}} < V_{\mathrm{int}}$. Hence, the open-circuit voltage is not given by the internal QFL splitting in the absorber and equation (9.1) is not valid anymore, i.e conclusions about the bulk recombination can not be obtained from measurements of V_{OC} in that regime. This explains the observed systematic shift of the extrapolated $E_{\mathrm{g,eff}}$ towards lower energies at high illumination intensities for PCDTBT:PC_{71}BM in figure 9.2 (c). For illumination intensities > 1 sun the V_{OC} of PCDTBT:PC_{71}BM is already reduced by surface recombination at high temperatures

[1] $E_{\mathrm{F,ETL}}^{\mathrm{ideal}}$ is the ideal quasi-Fermi energy of electrons without losses of carriers to the contact. For other contact types and imbalanced mobilities the V_{OC} loss due to surface recombination is much more complex and can not be given as easy.

for the used PEDOT:PSS and LiF/AL contacts. When the temperature is lowered, the QFL splitting in the absorber gets bigger, which increases surface recombination even further. Thus, V_{OC} rises less than V_{int} and $V_{\mathrm{OC}}(T)$ is extrapolated to values lower than the band gap.

9.3 Comparison of V_{OC} to the Effective and the Absorption Band Gap

The previously determined effective band gap resembles the energy difference between the electron transport level in the acceptor phase and the hole transport level in the donor phase. It describes the difference between the energy levels of free carriers in the effective semiconductor model. However, bound electron-hole pairs (excitons) are photogenerated in the pristine phases and split at the D-A interface. This requires an energetic driving force to overcome the binding energy of the excitons. Figure 9.5 shows absorption spectra for a variety of photoactive D-A materials from reference [18]. The low energetic tail of the absorption spectra of the investigated materials is typically given rather by a Gaussian tail then by a step-like edge, due to the wide vibration spectra. Thus the absorption band edge in such materials remains a question of definition. The absorption band gap $E_{\mathrm{g,abs}}$ was obtained here by the intersection of tangents fitted to the absorption tail at lower energies. Thus, it is a measure for the onset of considerable absorption. The corresponding $E_{\mathrm{g,abs}}$ are listed in table 9.2 together with the effective band gap for free charge carriers $E_{\mathrm{g,eff}}$ and representative values of V_{OC} of the respective solar cells. The differences $\Delta E_{\mathrm{exc}} = E_{\mathrm{g,abs}} - E_{\mathrm{g,eff}}$ between the absorption band gap and

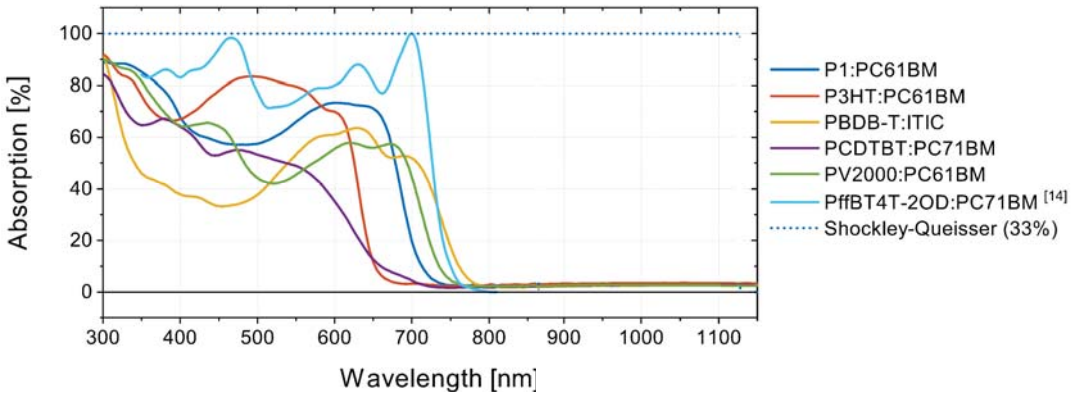

Figure 9.5: Absorption spectra for the photoactive D-A materials P1:$PC_{61}BM$, P3HT:$PC_{61}BM$, PBDB-T:ITIC, PCDTBT:$PC_{71}BM$, PV2000:$PC_{61}BM$ and PffBT4T-2OD:$PC_{71}BM$. Modified from ref. [18].

Table 9.2: Absorption band gaps $E_{g,abs}$ from reference [18], effective band gap for free electrons and holes $E_{g,eff}$ and typical values of $e_0 V_{OC}$ at 1 sun illumination.

absorber material	$E_{g,abs}$ [meV]	$E_{g,eff}$ [meV]	ΔE_{exc} [meV]	$e_0 V_{OC}$ [meV]	ΔE_{rec} [meV]
P3HT[a] :$PC_{61}BM$	1900	881	1019	567	314
P3HT[b] :$PC_{61}BM$	1900	984	916	592	392
PffBT4T-2OD:$PC_{61}BM$	1660	1175	485	773	402
P1:$PC_{61}BM$	1740	1196	544	801	395
PCDTBT:$PC_{71}BM$	1730	1350	380	904	446
PBDB-T:ITIC	1620	1237	383	884	353

[a] Purchased from BASF.
[b] Purchased from Rieke Metals.

the effective band gap and $\Delta E_{rec} = E_{eff} - e_0 V_{OC}$ between the effective band gap and V_{OC} are added for comparison. ΔE_{exc} is the driving force for exciton splitting and is lost during the generation of free carriers. ΔE_{rec} is the energy loss due to recombination of free carriers as illustrated in figure 9.6. $E_{g,abs}$ and ΔE_{exc} were simultaneously lowered over the last years from about $E_{g,abs} \approx 2\,\text{eV}$ with a loss of $\Delta E_{exc} \approx 1\,\text{eV}$ for P3HT:$PC_{61}BM$ with typical power conversion efficiencies of $\eta \approx 3.5\,\%$, to $E_{g,abs} \approx 1.6\,\text{eV}$ with a loss of $\Delta E_{exc} < 0.4\,\text{eV}$ for the state-of-the-art non-fullerene system PBDB-T:ITIC where efficiencies of $\eta > 9\,\%$ are achieved. The recombination losses of free carriers are between (0.3 – 0.45) eV for all investigated materials. The highest value of $\Delta E_{rec} = 0.45\,\text{eV}$ for PCDTBT:$PC_{71}BM$ may be overestimated, since surface recombination losses reduce the given V_{OC} at 1 sun as discussed in the previous section. These losses, arising from recombination in the absorber, are comparable to other PV technologies[1] like thin film GaAs solar cells with $\Delta E_{rec} \approx 0.31\,\text{eV}$ ($E_g = 1.43\,\text{eV}$, $V_{OC} = 1.122\,\text{V}$), crystalline Si solar cells with $\Delta E_{rec} \approx 0.38\,\text{eV}$ ($E_g = 1.12\,\text{eV}$, $V_{OC} = 0.738\,\text{V}$) and hybrid organic–inorganic perovskite solar cells with $\Delta E_{rec} \approx 0.37\,\text{eV}$ ($E_g \approx 1.51\,\text{eV}$, $V_{OC} = 1.144\,\text{V}$) [134, 135]. Thus, the energy loss involved in the dissociation of excitons to free charge carriers, which causes the need for a higher absorption band gap, is still the main limiting factor for the efficiency of OSCs. Hence, these losses must be further reduced by sophisticated chemical synthesis of donor and acceptor materials with beneficial energy levels or by the development of novel materials with reduced exciton binding energy to enable the direct generation of free charge carriers in organic semiconductors. The latter can be

[1] Values from current record cells.

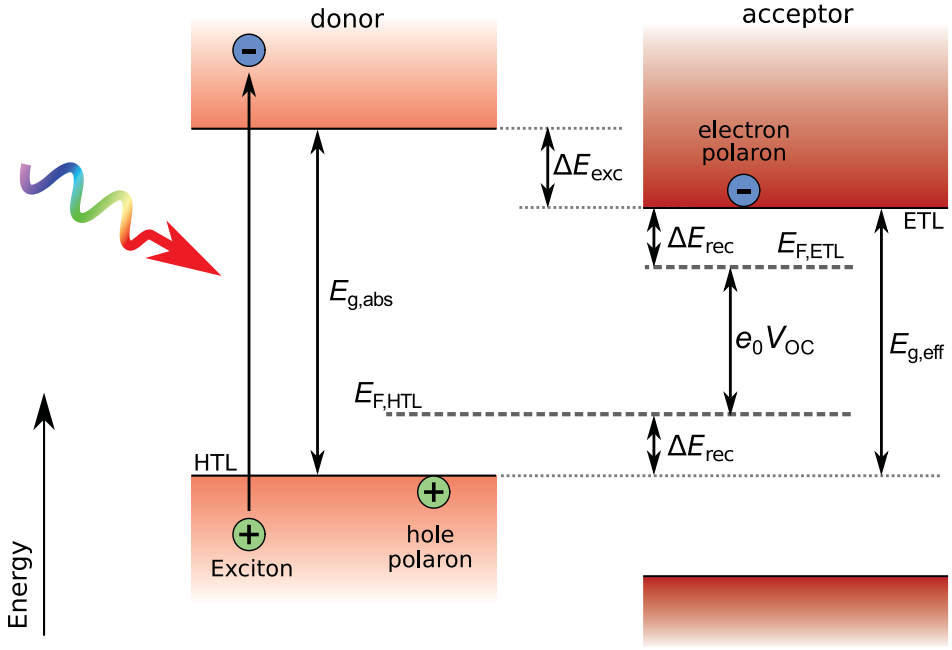

Figure 9.6: Energy diagram of an organic BHJ solar cell with the absorption band gap $E_{g,abs}$ and effective band gap $E_{g,eff}$. In addition, the energy losses ΔE_{exc}, needed as driving force for exciton splitting, and ΔE_{rec} from the recombination of free carriers are depicted alongside with the quasi-Fermi level splitting $e_0 V_{OC}$.

adressed by the development of novel organic semiconductors with increased dielectric constant to reduce the exciton binding energy according to equation (2.8).

9.4 Summary of Illumination and Temperature Dependent Measurements

The temperature and illumination dependence of the V_{OC} of organic solar cells was studied for six different absorber materials. This was used to determine the effective band gap of the individual donor-acceptor material. The observed saturation of V_{OC} at low temperatures and high illumination intensities was attributed to surface recombination caused by a high quasi-Fermi level splitting in the absorber. The voltage losses originating from the energetic offset needed for excition splitting and from recombination of free carriers were determined and compared among each other and to other PV technologies. The recombination losses of free carriers of (0.3 – 0.45) eV were found to be comparable to other materials utilized in commercially available solar cells. It was shown that the energetic offset for exciton splitting was reduced with increasing efficiency of OSCs in recent years. However, with about 0.4 eV for the state-of-the-art non-fullerene absorber PBDB-T:ITIC ($\eta > 9\,\%$) it is still drastically limiting the power conversion efficiency.

10 Correction of Luminescence Spectra for Optical Out Coupling Effects

Results on optical out coupling properties of OSC have been published with the author of this work as first author [38]. The presented ideas, results and conclusions of the following section partially paraphrase the mentioned publication and figures are adopted with minor changes.

The following section will discuss the impact of optical interference on detected luminescence from an OSC as well as the importance for a proper interpretation of experimental data. Furthermore, a theoretical method to correct experimental spectra for the optical out coupling properties is introduced. Further, the energy of the charge transfer state of different absorber materials is accurately determined from corrected electroluminescence spectra.

10.1 Simulation of the Out Coupling of Luminescence from Organic Solar Cells

The simulation of the coupling of light from organic solar cells is described in this section. These out coupling properties will be used for a correct interpretation of experimental luminescence spectra of OSC. According to the Fresnel equations, electromagnetic waves are partially reflected at material interfaces in case of differences in the refractive index n or the extinction coefficient k of the materials. The reflected and the direct waves superimpose which leads to interference. When light is emitted from a material inside a solar cell, reflections at electrodes and other interfaces can cause interference. This can alter the emitted intensity spectrum $I(\lambda)$ compared to the intrinsic emission line shape $I_{\mathrm{hom}}(\lambda)$ of the material. The latter is the emission spectrum in the absence of interference, i.e. the emission in a homogeneous medium. The out coupling factor γ_{OC} of radiation is defined as the quotient of $I(\lambda)$ and $I_{\mathrm{hom}}(\lambda)$ by [137]:

$$\gamma_{\mathrm{OC}}(\lambda) = \frac{I(\lambda)}{I_{\mathrm{hom}}(\lambda)} \tag{10.1}$$

The out coupling factor of a system can be simulated within the S-matrix formalism introduced in chapter 6.2. For this, luminescence in the photoactive layer (PAL) is implemented by a dipole-like emitter at position x (x-direction is perpendicular to the

surfaces of the electrodes). For the calculation of the optical properties of the system, the layer stack is split into two parts at the position of emission x and two S matrices are calculated (one for the lower and one for the upper half of the layer stack). The emitted radiance $I_{\mathrm{PAL}}(x)$ from the layer stack in direction of the transparent electrode was calculated for each dipole position x from the time-averaged Poynting-vector $\bar{S}$ in observation direction (perpendicular to the electrodes). With the assumption of a relative permeability of $\mu_{\mathrm{r}} = 1$, $\bar{S}$ of plane electromagnetic waves by can be calculated from the amplitude of the electric field $|\vec{E}|$ [138]

$$\bar{S} = \frac{1}{2}\sqrt{\frac{\epsilon_{\mathrm{r}}\epsilon_0}{\mu_0}}|\vec{E}|^2$$

With the permeability of free space μ_0. In order to realize spherically symmetrical emission from the photoactive layer, the dipole was oriented in x-, y- and z-direction successively and the resulting radiances were averaged. As a reference the free space radiance I_{hom} of a homogeneous system with infinite elongation was calculated. The radiance of the emission at position x from the solar cell was divided by the reference radiance according to equation (10.1), to get the out coupling factor $\gamma_{\mathrm{OC}}(x)$. Assuming spatially homogeneous recombination and thus homogeneous luminescence within the PAL of an OSC, the out coupling factor of the solar cell $\bar{\gamma}_{\mathrm{OC}}$ was calculated as the spatial average of $\gamma_{\mathrm{OC}}(x)$, i.e., the spatial average over all emission positions x in the PAL with thickness d_{PAL}

$$\bar{\gamma}_{\mathrm{OC}} = \frac{1}{d_{\mathrm{PAL}}}\int_0^{d_{\mathrm{PAL}}} \gamma_{\mathrm{OC}}(x)\, dx = \frac{1}{d_{\mathrm{PAL}}}\int_0^{d_{\mathrm{PAL}}} \frac{I_{\mathrm{PAL}}(x)}{I_{\mathrm{hom}}}\, dx \tag{10.2}$$

The emission position was varied throughout d_{PAL} with a sampling of $\Delta x = \frac{d_{\mathrm{PAL}}}{100}$ in the simulations. The error was proven to be less than 1 % for $N \geq 100$ (relative to $N \geq 1000$). For the construction of the S-matrices, the n and k values of the featured materials are used as input parameters. Their determination from fitting of an optical model to experimental reflectance and transmittance data is described in chapter 5.5. Exemplary results for ITO are given in figure 10.5. All used n and k values can be found in figures B.4 and B.5 in appendix B. All layer thicknesses used for S-matrix simulations are listed in chapter D.3 in appendix D. Super- and substrate are air ($n = 1$) and glass ($n = 1.67$), respectively, or vice versa depending on the investigated layer stack of the OSC. When the luminescence is observed through the 1.1 mm thick glass substrates, the latter is modeled as superstrate i.e. with infinite elongation. Thereby no reflection at the

glass air interface is included in the simulation, i.e., the back reflection at the 1.1 mm distant glass-air boundary is assumed to be not coherent and does not contribute to interference.

10.2 Impact of Interference on Electroluminescence Spectra

The influence of interference on the observed EL spectra of OSC is shown for an exemplary device in this section. The electroluminescence spectrum[1] $I_{\mathrm{EL}}(\lambda)$ of a P3HT:$PC_{61}BM$ OSC with a transparent PEDOT:PSS FHC electrode, depicted as device type A in figure 10.1 (a), is plotted as a blue solid line in figure 10.2. The spectrum was obtained at a forward current density of $75\,\mathrm{mA\,cm^{-2}}$. The emission features a rather wide peak with a maximum at approximately 1360 nm. After measuring the EL spectrum, the very same device (type A) was modified by depositing a 10 nm thick (and thus semitransparent) Ag layer on top of the transparent electrode and renamed to type B, depicted in figure 10.1 (b). The drastically changed spectrum when the cell is remeasured can be seen from the solid red line in figure 10.2 which shows a narrower peak with a central wavelength of about 1250 nm. It should be pointed out that the PAL and contact materials were not changed and morphological changes of the absorber are not expected by mere deposition of such a thin Ag layer on top of the PEDOT:PSS layer. So, the recombination properties are also not expected to change. Therefore, the different spectrum has to originate from the change of the optical properties of the system. In addition, the calculated radiant out coupling factor $\bar{\gamma}_{\mathrm{OC}}$ for the corresponding layer stacks are plotted in figure 10.2 (dashed lines). For the device type B the out coupling factor resembles the spectral shape quite accurately proving further that the spectrum

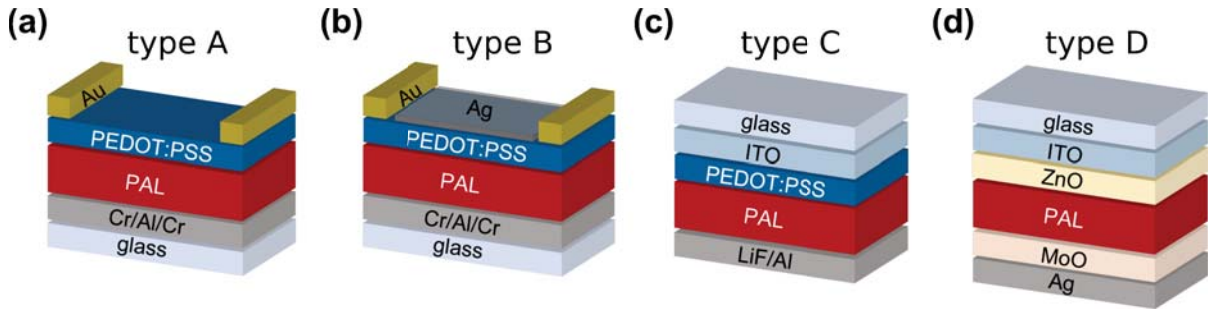

Figure 10.1: Used layer stacks of (a) an optically inverted OSC (b) with additional semitransparent Ag layer. (c) ITO based architecture using PEDOT:PSS and LiF/Al electrodes or (d) inverted ITO based architecture using ZnO and MoO_3 as charge selective layers.

[1] Given in arbitrary units (a.u. $\sim \mathrm{W\,m^{-2}\,nm^{-1}}$) relative to a reference spectrum.

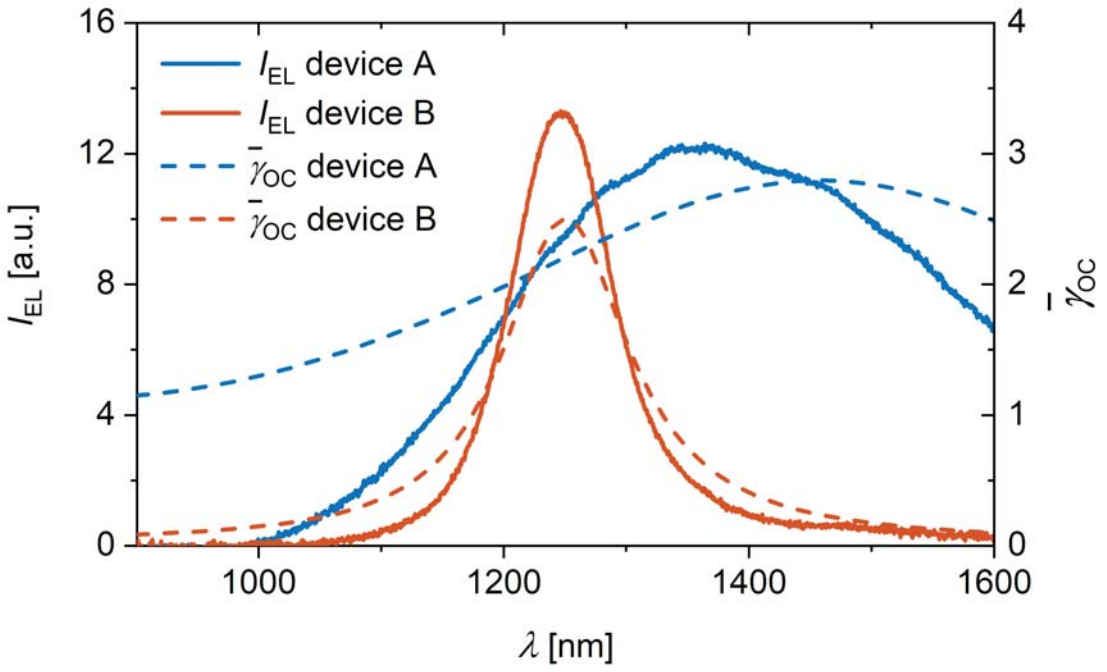

Figure 10.2: EL spectra of a P3HT:$PC_{61}BM$ cell without (type A, see figure 10.1) and with a thin, semitransparent Ag layer on top (type B) together with the calculated radiant out coupling factors $\bar{\gamma}_{OC}$.

is very strongly governed by out coupling effects. Therefore, the data hardly allows for any statement about the spectral fingerprint of the emitting photoactive material.
The wavelength dependence of $\bar{\gamma}_{OC}$ for the device without the additional mirror (type A) originates from the interference of the direct emission and the reflected portion at the back mirror, i.e., wide-angle interference. This is schemed in figure 10.3 (a) alongside with γ for different emission positions x for a simple model system (emission in front of an ideal mirror). The path difference between direct and reflected light (solid green line) depends on the distance x of the photon emission from the reflective surface, hence γ does. Averaging over all emission positions leads to a rather homogeneous out coupling $\bar{\gamma}_{OC}$ (dashed red line). Still, aspects of the observed spectral shape of the type A device, like an asymmetry, can be partially explained by optical out coupling. In contrast, the additional highly reflective surface in the type B stack forms an optical micro-cavity leading to a pronounced peak in $\bar{\gamma}_{OC}$, i.e. multi-beam interference as depicted in figure 10.3 (b) for a model system. While the amplitude of the out coupled radiance $I_{PAL}(x)$ and thus $\gamma(x)$ still depend on the position of emission within the cavity, the peak position is determined by the optical distance $n \cdot d_{PAL}$ between the mirrors. It is given by the thickness d_{PAL} and the refractive index n of the photoactive layer.
The previously discussed case has a more exemplary character since a reflective surface

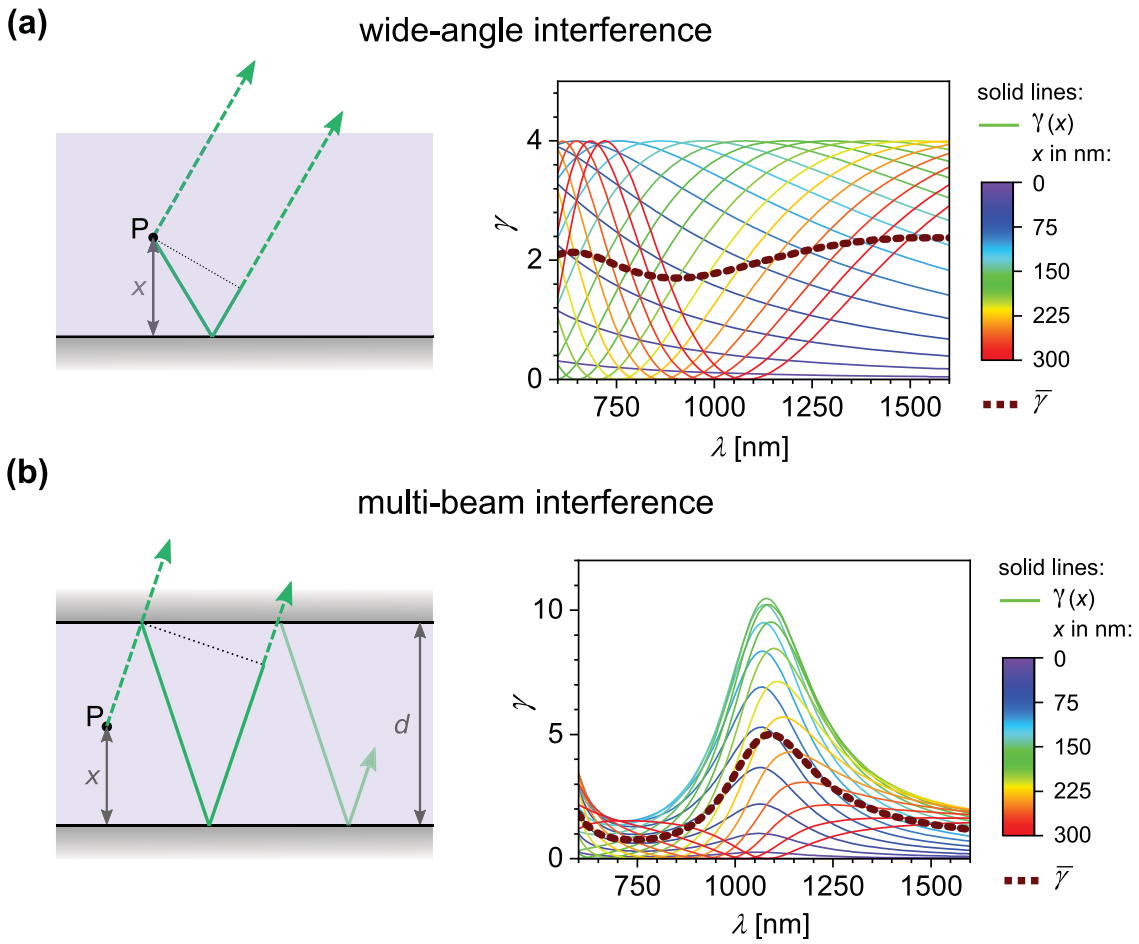

Figure 10.3: Schematic illustration of the path of light (dashed green line) emitted at point P at position x in front of a reflective surface (a) with the path length difference of the reflected beam drawn as solid green lines and the corresponding $\gamma(x)$ values for different positions x (solid lines) alongside with the averaged $\bar{\gamma}_{\mathrm{OC}}$ (dashed line). (b) A system with emission between two reflecting surfaces and the out coupling factor γ showing multi-beam interference.

at the illumination side reduces photon absorption and hence is avoided in the design of a solar cell. The next section focuses on EL from typical architectures of OSC.

10.3 Correct Determination of Charge Transfer State Energy in Organic Solar Cells from Luminescence Spectra

Generation and recombination of electrons and holes in organic solar cells occur via charge transfer (CT) states located at the donor-acceptor interface. The energy of these CT states is a crucial factor for the attainable open-circuit voltage and its correct determination is thus of utmost importance for a detailed understanding of such devices. It was shown in literature, assuming equilibrium between the occupation of the excited

charge transfer (CT) state and the densities of free carriers ($\mu_{CT} = e_0 V_{int}$), that the CT state energy E_{CT} resembles the effective band gap as discussed in chapter 2.3.3. Thereby, E_{CT} contributes directly to V_{OC} as described by equation (2.10). It is obvious that knowledge about the CT state energy is key for a detailed understanding and thus optimization of V_{OC} of OSCs. To investigate CT state emission, EL spectroscopy was performed for a variety of photoactive D-A systems and layer stacks, since it is dominated by CT state emission [58, 139].

The EL spectra of P3HT:PC_{61}BM devices (type A) measured at a current density of 75 mA cm^{-2} for varying PAL thicknesses d_{PAL} are shown in figure 10.4 (a) along with the corresponding $\bar{\gamma}_{OC}(\lambda)$ and the corrected spectra $I_{EL,corr} = I_{EL} \cdot \bar{\gamma}_{OC}{}^{-1}$. The corrected intensity $I_{EL,corr}$ represents the expected free space radiance without the optical environment, i.e., the emission in a homogeneous medium. The same quantities are plotted in figure 10.4 (b) for ITO based devices (type C in figure 10.1 (c)). The raw spectra depend

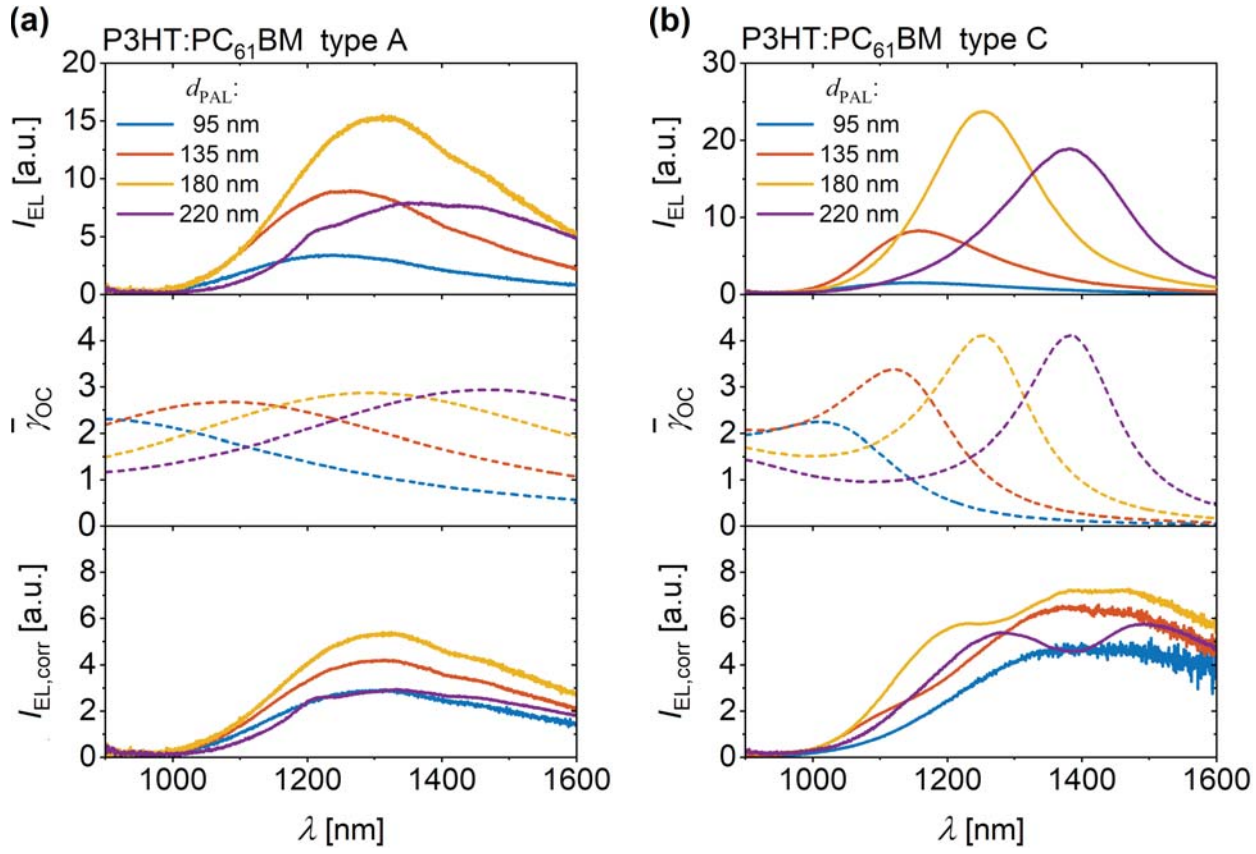

Figure 10.4: EL spectra $I_{EL}(\lambda)$ of P3HT:PC_{61}BM solar cells for different thicknesses d_{PAL} of the photoactive layer for ITO-free devices type A (a) and ITO-based devices type C (b), the calculated radiant out coupling factors $\bar{\gamma}_{OC}(\lambda)$ for the corresponding layer stacks and the spectra $I_{EL,corr} = I_{EL} \cdot \bar{\gamma}_{OC}{}^{-1}$ corrected for the optical out coupling.

sensitively on d_{PAL} and show peak positions between 1240 nm and 1370 nm for device type A and between 1050 nm and 1380 nm for type C devices. The peak amplitudes range from 3.4 to 15.3 for type A and from 1.5 to 23.8 for type C.

In great contrast, all corrected intensities $I_{\mathrm{EL,corr}}$ are quite similar regarding shape and amplitude for all absorber thicknesses and for both device architectures. This could be expected for the same photoactive material used in these devices. It thus shows clearly that the measured spectra are strongly influenced by the optical properties of the layer stacks[1]. The measured spectra for the transparent PEDOT:PSS contact (type A) are wider compared to the spectra of the ITO based devices (type C) which show more narrow peaks. For both architectures the overall intensities vary as a function of d_{PAL}. This is more severe for the ITO based cells. The out coupling in the PEDOT:PSS device is quite homogeneous, since it is governed by wide-angle interference. This was discussed in the previous section where an additional mirror was added on a cell in the same architecture. The out coupling of the ITO based devices feature clear peaks. These peaks originate from the high reflectance of ITO at the relevant wavelengths. The reflectances of ITO and PEDOT:PSS are shown in figure 10.5 (measured on glass). In combination with the reflective back mirror of the OSC, the high reflectance of ITO

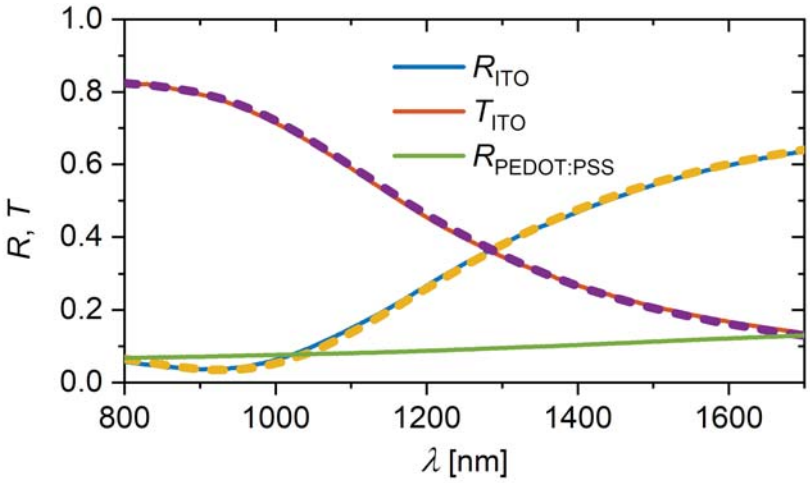

Figure 10.5: Reflectance R and transmittance T of ITO and the reflectance of PEDOT:PSS measured on glass (solid lines) and the fits (dashed lines) to the ITO data for the determination of n and k values.

[1] It should be noted that a variation of the absorber thickness can result in morphological and also energetic changes which may influence I_{EL} [140]. The deviations present in the corrected spectra are due to slight offsets in peak position and peak width between measurement and simulation. Nevertheless, the corrected spectra clearly demonstrate the strong impact of interference effects on the observed phenomena.

results in the formation of an optical micro-cavity. In contrast, PEDOT:PSS (measured on glass) does not show a comparable increase of its reflectance in the infrared part of the spectrum.

In addition to P3HT:$PC_{61}BM$, for which power conversion efficiencies of $\approx 3.5\,\%$ are typically achieved, the polymer PV2000 as an example for a high-performing polymer in combination with $PC_{61}BM$ as well as the state of the art non-fullerene DA system PBDB-T:ITIC are investigated in ITO based solar cells [141]. The used layer stack (type D) is shown in figure 10.1 (d). The PV2000:$PC_{61}BM$ solar cells yield a PCE between 4.9 % ($d_{PAL} = 80\,nm$) and 7.9 % ($d_{PAL} = 240\,nm$) and the PBDB-T:ITIC cells between 7.2 % ($d_{PAL} = 50\,nm$), 8.2 % ($d_{PAL} = 132\,nm$) and a maximum of 9.3 % at $d_{PAL} = 88\,nm$. EL spectra for the PV2000:$PC_{61}BM$ devices are plotted in figure 10.6 (a) for layer thicknesses in the range of $80\,nm \leq d_{PAL} \leq 240\,nm$ at a current density of $108.1\,mA\,cm^{-2}$ alongside with $\bar{\gamma}_{OC}$ and $I_{EL,corr}$. The measured spectra peak between

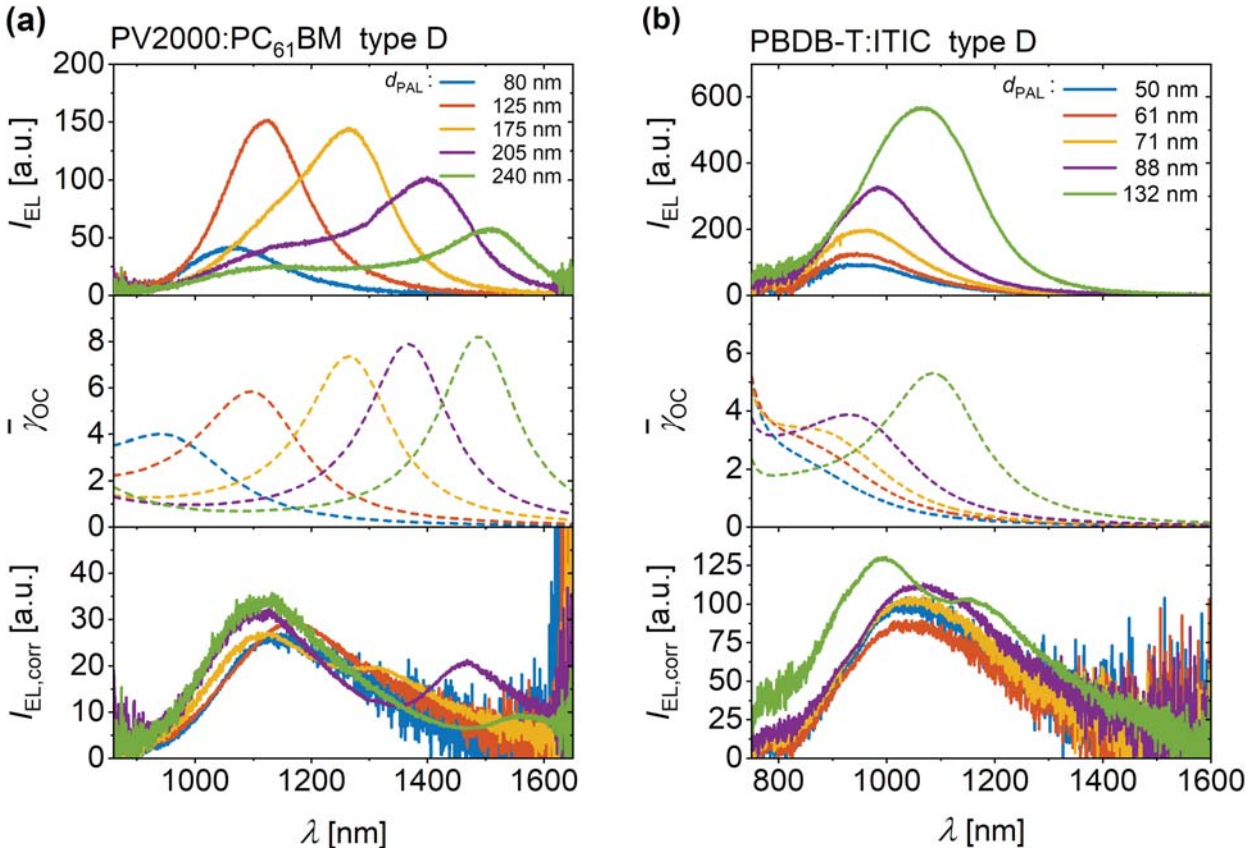

Figure 10.6: EL spectra $I_{EL}(\lambda)$ of PV2000:$PC_{61}BM$ solar cells (a) and PBDB-T:ITIC solar cells (b) for different thicknesses d_{PAL} of the photoactive layer in an ITO based design (type D in figure 10.1), the calculated radiant out coupling factors $\bar{\gamma}_{OC}(\lambda)$ for the corresponding layer stacks and the spectra $I_{EL,corr}$ corrected for the out coupling.

1050 nm and 1500 nm with intensities between 40 to 150 (a.u.). All corrected spectra feature a peak between 1120 nm and 1170 nm with maximum intensities between 26 and 34 (a.u.). In the uncorrected spectra these devices show a shift in wavelength of the peak of almost 500 nm and a significant change in overall emission for different thicknesses of the absorber layer. This can clearly be attributed to changes in the optical out coupling properties originating from the variation of the absorber thickness. I_{EL} at a current density of 100 mA cm^{-2}, $\bar{\gamma}_{\mathrm{OC}}$ and $I_{\mathrm{EL,corr}}$ for the PBDB-T:ITIC devices are shown in figure 10.6 (b) for absorber thicknesses 50 nm $\leq d_{\mathrm{PAL}} \leq$ 132 nm. Thicker photoactive layers could not be realized due to a poor resulting film quality. the peaks in I_{EL} are located between 940 nm and 1070 nm with maximum peak intensities in the range of 100 to 600 (a.u.) whereas all corrected spectra feature a peak at approx. 1070 nm with maximal intensities between 85 and 125 (a.u.). The strong s-shape in the corrected spectrum of the device with an average absorber thickness of 132 nm originates from strong fluctuations of d_{PAL} of about 30 nm (as measured by profilometry). This results in an inaccurate correction when only the average thickness is taken into account. To determine the CT state energy the previously shown spectra $I_{\mathrm{EL}}(\lambda)$ (inW nm^{-1} m^{-2}) are converted to the reduced emission spectra $I_{\mathrm{f}}/E = I_{\mathrm{EL}}(\lambda)/E^3$ (in photons per unit spectral energy and per area) [142]. The normalized reduced I_{f}/E are plotted in figure 10.7 alongside with the corrected reduced spectra $I_{\mathrm{f,corr}}/E$ for all systems[1]. Gaussian functions are fitted by means of equation (2.9), which describes radiative CT state emission, to all spectra and added to figure 10.7. The resulting CT state energy E_{CT}, reorganization energy λ_{RO} and the energy of maximum CT emission $E_{\mathrm{CT}}^{\mathrm{em}} = \max(I_{\mathrm{f}}/E)$ from the fits for all systems and photoactive layer thicknesses are listed in table 10.1. The corrected spectra for all absorber thicknesses resemble each other quite accurately for each DA system while the raw spectra differ strongly as was the case when the intensity was plotted over wavelength. It gets obvious from figure 10.7 that the high energetics tails, i.e., the apparent reorganization energy λ_{RO}, and thus the estimated CT energy $E_{\mathrm{CT}} = E_{\mathrm{CT}}^{\mathrm{em}} + \lambda_{\mathrm{RO}}$ are significantly affected by interference effects. The spectra of the ITO based P3HT:PC_{61}BM and PBDB-T:ITIC devices show that the uncorrected data sets differ from the corrected spectra for all absorber thicknesses and in case of P3HT:PC_{61}BM for layer thicknesses $>$ 135 nm, micro-cavity effects can cause significant deviations of the observed spectra from the expected Gaussian shape. This results in a strong dependence of the fit results on the chosen data range. In case of

[1] The corrected spectra of PBDB-T:ITIC are smoothened by a floating average over 20 data points to reduce noise and to ensure proper normalization.

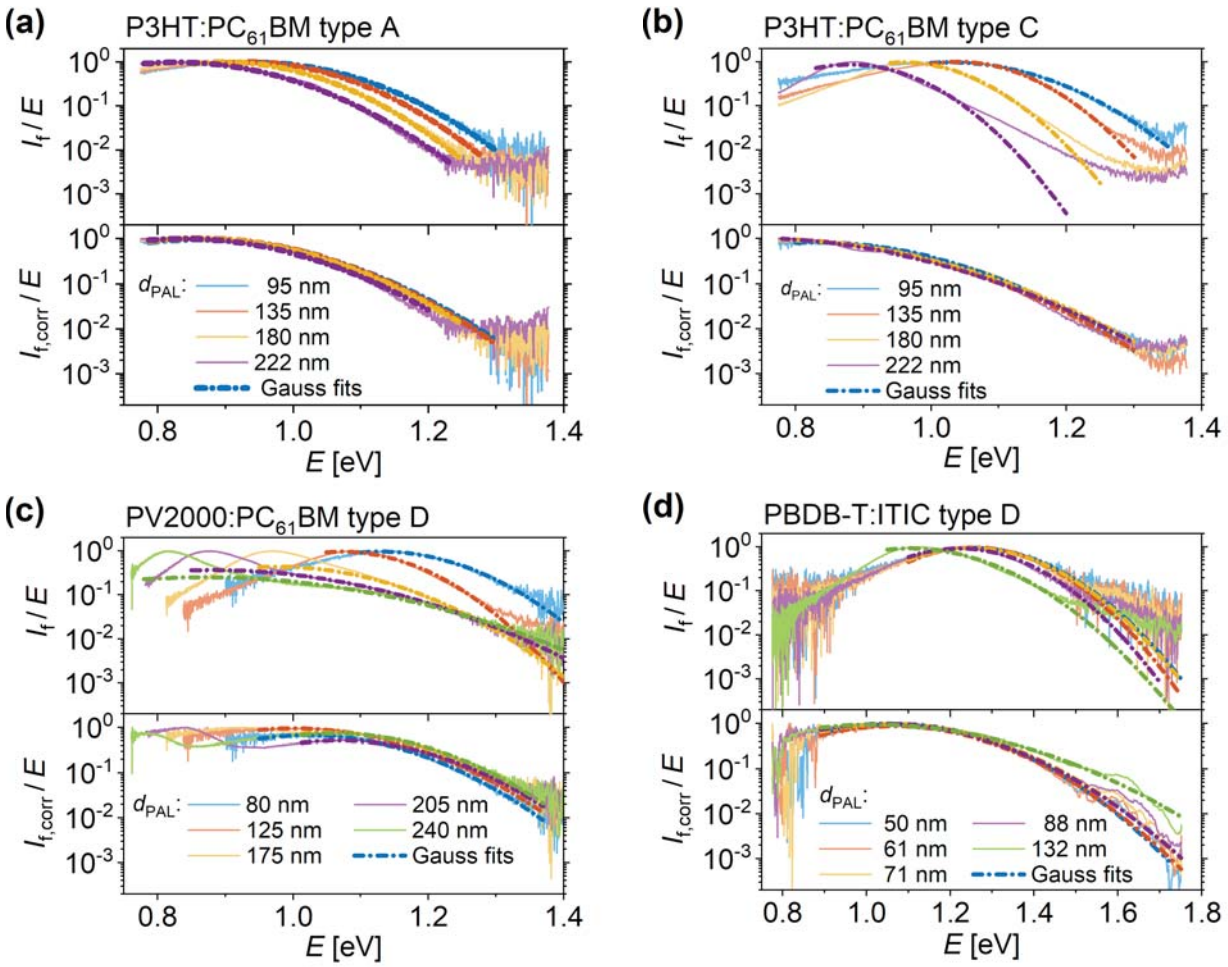

Figure 10.7: Reduced emission spectra I_f/E and corrected spectra $I_{f,corr}/E$ with Gaussian fits according to equation (2.9) for P3HT:$PC_{61}BM$ devices of type A in (a) and type C in(b) as well as type D devices made from (c) PV2000:$PC_{61}BM$ and (d) PBDB-T:ITIC.

PV2000:$PC_{61}BM$ (figure 10.7 (c)) the uncorrected spectra look like a superposition of two peaks for $d_{PAL} \geq 175\,nm$ due to the resonance peak of the micro-cavity. These strongly altered spectral shapes make a meaningful analysis of the uncorrected data difficult and prone to misinterpretation. Interestingly, there are cases where two effects compensate each other when the CT state energy is determined from the results of the Gaussian fits. E.g., the uncorrected PBDB-T:ITIC spectra feature higher E_{CT}^{em} values with lower λ_{RO} (peak width) compared to the corrected spectra. This results in comparable CT energies from the raw and the corrected spectra although the values for $E_{CT,corr}^{em}$ and λ_{RO} differ significantly for both cases. Hence, even in this case, the correction procedure is indispensable to achieve a deeper understanding of the underlying processes and material properties.

Table 10.1: Results of Gaussian fits to the experimental and corrected reduced EL spectra for different photoactive materials and varying absorber thicknesses d_{PAL} plotted in figure 10.7.

d_{PAL} [nm]	$E_{\mathrm{CT}}^{\mathrm{em}}$ [eV]	λ_{RO} [eV]	E_{CT} [eV]	$E_{\mathrm{CT,corr}}^{\mathrm{em}}$ [eV]	$\lambda_{\mathrm{RO,corr}}$ [eV]	$E_{\mathrm{CT,corr}}$ [eV]
P3HT:PC_{61}BM (type A)						
95	0.947	0.262	1.209	0.86	0.364	1.224
135	0.934	0.233	1.167	0.858	0.35	1.208
180	0.896	0.236	1.133	0.856	0.345	1.201
220	0.828	0.300	1.128	0.837	0.353	1.190
P3HT:PC_{61}BM (type C)						
95	1.028	0.227	1.256	0.830	0.388	1.218
135	1.040	0.131	1.171	0.764	0.493	1.256
180	0.957	0.131	1.089	0.762	0.54	1.302
220	0.88	0.127	1.007	0.727	0.594	1.321
PV2000:PC_{61}BM (type D)						
80	1.13	0.190	1.32	1.021	0.270	1.292
125	1.072	0.152	1.224	1.001	0.307	1.308
175	0.977	0.301	1.278	1.051	0.262	1.313
205	0.881	0.565	1.446	1.067	0.263	1.330
240	0.868	0.718	1.586	1.060	0.259	1.319
PBDB-T:ITIC (type D)						
50	1.251	0.353	1.604	1.067	0.586	1.653
61	1.254	0.308	1.562	1.062	0.62	1.682
71	1.249	0.351	1.6	1.056	0.666	1.723
88	1.222	0.316	1.538	1.039	0.696	1.736
132	1.101	0.455	1.556	0.997	1.168	2.166[a]

[a] Value not reliable due to layer thickness fluctuation (see text and figure 10.7).

10.4 Summary of Out Coupling Effects in OSC

This study reports on drastic changes in the CT emission spectra of organic solar cells upon variation of the absorber layer thickness. This was demonstrated for a variety of different bulk-heterojunction organic solar cells based on four different device architectures, three different photoactive materials and various thicknesses of the absorber layer. For each device, an electroluminescence spectrum was recorded, and it was found that the spectra for a given photoactive material differ strongly for different device architectures and different thicknesses of the absorber layer. In harsh contrast, the CT state energy as a fundamental property of the donor-acceptor blend is expected to be rather independent of the exact device configuration and the thickness of the absorber layer. Therefore, the optical out coupling properties of the different devices were calculated by means of a scattering matrix formalism based on experimentally determined optical diffraction and extinction coefficients. After correction of the luminescence spectra for the specific out coupling properties, all spectra for each photoactive material were very similar. These findings demonstrate clearly that the measured spectra are strongly influenced by micro-cavity effects and that the described correction for the optical out coupling is indispensable in order to achieve reliable information about the nature of the emissive states within the photoactive layer. The energy of these CT states is a crucial factor for the attainable open-circuit voltage, thus its correct determination is of utmost importance for a detailed understanding and improvement of V_{OC} in organic bulk-heterojunction solar cells.

Chapter V

Summary

The work *Advanced Electrical and Optical Characterization of Recombination in Organic Solar Cells* aims for the correct determination of important material parameters and a better understanding of device physics, recombination mechanisms and the origin of the open-circuit voltage of organic solar cells. It focuses on the evaluation of characterization methods for organic solar cells and the determination of material parameters with a strong focus on recombination and effects decisive for the V_{OC}. The work comprises four experimental studies dealing with different aspects contributing to energy losses and thus the reduction of V_{OC} in organic solar cells. This includes recombination of free charge carriers in the bulk of the absorber, additional losses at surfaces and the correct determination of relevant energetic levels involved in the recombination of charge carriers.

Charge Extraction from Organic Solar Cells This study deals with the determination of recombination of free charge carriers in the absorber of an organic bulk-heterojunction solar cell. For this, an experimental setup for bias amplified charge extraction was established within this work. Herewith, the capacitance and the excess charge carrier dynamics of organic solar cells were studied. It was shown that the solar cell's capacitance significantly affects the results of transient electrical characterization of OSCs. Explicitly, uncertainties of the capacitive correction and injection of capacitive charges under open-circuit conditions were identified as limiting factors to the utilized method. It was shown that the extracted charge originating from excess carriers must have a

significant share in the total extracted charge to obtain reliable results. To reach the excess-carrier-dominated regime, the use of low extraction voltages and thick absorber layers is beneficial. Unfortunately, the conditions for this regime depend on the properties of the studied absorber material and a general limit can not be given. It was further concluded, that an in-depth description and understanding of transient electrical characterization of organic solar cells requires complex time- and spatial-resolved simulations tailored to the particular system, especially if transport should be explicitly considered. Nevertheless, bimolecular recombination coefficients of $k_{\mathrm{r}}^{\mathrm{bi}} = 3.9 \times 10^{-12}\,\mathrm{cm}^3\,\mathrm{s}^{-1}$ for P3HT:PC_{61}BM and $k_{\mathrm{r}}^{\mathrm{bi}} = 9.1 \times 10^{-11}\,\mathrm{cm}^3\,\mathrm{s}^{-1}$ for PCDTBT:PC_{71}BM were determined from the excess-carrier-dominated regime, where the number of extracted excess carriers significantly exceeds the charge from capacitive currents. The introduced method enables the direct determination of recombination coefficients of the photoactive material at carrier densities relevant for the operation of the solar cell, in a complete device, i.e. the real morphology of the donor-acceptor bulk-heterojunction.

Recombination Losses due to Poor Selectivity of Electrodes Further, V_{OC} losses due to additional recombination of electrons and holes at electrodes were studied. For this, electron contacts with strongly different selectivity (LiF/Al and Cu) were applied as top electrodes on devices with differing photoactive layers. Charge carrier density was determined by charge extraction and an advanced combination of photo- and electroluminescence. A novel method of photoluminescence quenching has been established to determine the PL intensity originating from free charge carrier. Using this method, the recombination of free electrons and holes in P3HT:PC_{61}BM under illumination via the CT state could be determined experimentally for the first time (to the knowlege of the author). The results prove that the overall carrier densities are only slightly reduced by the poorly selective Cu contacts in the investigated organic solar cells whereas V_{OC} is reduced drastically. This implies, that V_{OC} does not equal the internal QFL splitting in an typical OSC when surface recombination is present. Thus, V_{OC} is not suited to investigate bulk recombination in this case. All experimental results could be reproduced consistently by drift-diffusion simulations where the work function of the electron contact was the only varied parameter (the simulations were carried out by A. Spies [18]). From the combination of these results, two distinct contributions to the overall V_{OC} reduction have been identified. First: the gradient of the quasi-Fermi energy of the majority carriers towards their respective contact as the driving force for the surface recombination current and, second: the reduction of the maximum charge carrier den-

sity in the absorber due to recombination at the electrode. Their contributions depend strongly on the charge carrier mobilities. For materials with rather poor transport properties, which is the case for many photoactive materials that are used in OSCs, the main loss of V_{OC} is caused by the gradient of the quasi-Fermi energy of the majority charge carriers in the vicinity of the corresponding contact. In contrast, the carrier densities at relatively small distance to a contact with insufficient selectivity are barely reduced.

Temperature and Intensity Dependence of the Open-Circuit Voltage Temperature and illumination dependence of V_{OC} of organic solar cells was studied for six different absorber materials. From that, the effective band gaps of the individual donor-acceptor materials were determined. The observed saturation of V_{OC} at low temperatures and high illumination intensities was attributed to surface recombination caused by the high quasi-Fermi level splitting in the absorber under this conditions. Voltage losses originating from the energetic offset needed for exciton splitting and from recombination of free carriers were determined and compared among each other and to other PV technologies. Recombination losses of free carriers were found to be comparable to those in other materials utilized in commercially available solar cells like Si or GaAs and to those of other novel technologies like provskite solar cells. It was shown that the energetic offset for exciton splitting was reduced with increasing efficiency of OSCs in recent years from $> 1\,\mathrm{V}$ to $\approx 0.4\,\mathrm{V}$. However, with $\approx 0.4\,\mathrm{eV}$ for the state-of-the-art non-fullerene system PBDB-T:ITIC ($\eta > 9\,\%$) it is still drastically limiting the power conversion efficiency in OPV.

Correction of Luminescence Spectra for Optical Out Coupling Effects This study reports on drastic changes of the CT emission spectra of organic solar cells upon variation of the absorber layer thickness. This was demonstrated for a variety of different bulk-heterojunction organic solar cells based on four different device architectures, three different photoactive materials and various thicknesses of the absorber layer. For each device, an electroluminescence spectrum was recorded, and it was found that the spectra for a given photoactive material differ strongly for different device architectures and different thicknesses of the absorber layer. In harsh contrast, the CT state energy as a fundamental property of the donor-acceptor blend is expected to be rather independent of the exact device configuration and the thickness of the absorber layer. Therefore, the optical out coupling properties of the different devices were calculated by means of a scattering matrix formalism based on experimentally determined optical diffraction

and extinction coefficients. After correction of the luminescence spectra for the specific out coupling properties all spectra for each photoactive material were very similar. These findings demonstrate clearly that the measured spectra are strongly influenced by micro-cavity effects and that the described correction for the optical out coupling is indispensable in order to achieve reliable information about the nature of the emissive states within the photoactive layer. The energy of these CT states is a crucial factor for the attainable open-circuit voltage, thus its correct determination is of utmost importance for a detailed understanding and improvement of V_{OC} in organic bulk-heterojunction solar cells.

Final Conclusions and Outlook In a broader perspective, this thesis contributes to a deeper understanding of device physics, recombination mechanisms and the origin of the open-circuit voltage in organic bulk-heterojunction solar cells and establishes experimental methods for a comprehensive characterization of recombination in OSCs. The relevant recombination mechanisms are theoretically discussed and experimentally investigated, including recombination of free charge carriers in the absorber, additional recombination at interfaces and the characteristic energy levels as well as energy losses in donor-acceptor systems. In particular, a novel method of photoluminescence quenching has been established to determine the radiative recombination of free charge carriers in organic solar cells under illumination. Further, the presence of strong gradients of the charge carrier densities in case of surface recombination in OSCs has been experimentally proven. In addition, the strong influence of interferences on luminescence spectra of OSC has been discovered, theoretically described and a novel method for the correction for optical out coupling effects has been established, allowing an accurate interpretation of luminescence spectra. It has been shown that the energy loss originating from the recombination of free electrons and holes is comparable to the recombination losses in record cells of other technologies like crystalline silicon, gallium arsenide or hybrid organic–inorganic perovskite solar cells. The rather high dielectric constant of crystalline semiconductors typically used for solar cells result in low exciton binding energies which leads to a direct generation of free charge carriers. The same holds true for hybrid organic–inorganic perovskite solar cells which have received special attention in research since their power conversion efficiency was rapidly increased to over 23 % in recent years [135, 136]. The utilized perovskite materials feature a high dielectric constant because of the incorporated heavy elements like Pb and polarizable organic cations. In contrast, the energy loss involved in the dissociation of the strongly bound

excitons, i.e. the separation of electrons and holes, and the resulting low V_{OC} compared to the energy of absorbed photons is still a main limiting factor for the power conversion efficiency in current OSCs. These losses must be further reduced by sophisticated chemical synthesis of donor and acceptor materials with beneficial energy levels or by the development of neat materials with reduced exciton binding energy, e.g. by a significant increase of the dielectric constant, to enable the direct generation of free charge carriers in organic semiconductors. The reduction of this losses is a key challenge in the field of OPV and is required to enable power conversion efficiency comparable to other arising material classes like hybrid organic–inorganic perovskites and to compete with established technologies.

Zusammenfassung

Diese Arbeit *Advanced Electrical and Optical Characterization of Recombination in Organic Solar Cells* zielt auf die korrekte Bestimmung wichtiger Materialkenngrößen und auf ein besseres Verständnis der Rekombination von Ladungsträgern, des Ursprungs der offenen Klemmenspannung (V_{OC}) und der Physik der organischen Solarzelle (OSC) ab. Der Fokus liegt hierbei auf der Evaluation von Charakterisierungsverfahren für organische Solarzellen und der Bestimmungen wichtiger Materialparameter. Ein besonderes Augenmerk liegt hierbei auf der Rekombination freier Ladungsträger und Effekten, welche die V_{OC} beeinflussen. Die Arbeit besteht aus vier experimentellen Studien, die verschiedene Mechanismen zum Energieverlust freier Ladungsträger untersuchen und damit zur Verringerung von V_{OC} beitragen. Dies umfasst die Rekombination freier Ladungsträger in der photoaktiven Schicht, zusätzliche Verluste an rekombinationsaktiven Oberflächen und die korrekte Bestimmung der energetischen Zustände, welche an der Rekombination freier Ladungsträger beteiligt sind.

Extraktion freier Ladungsträger aus organischen Solarzellen

Dieses Kapitel behandelt die Rekombination freier Ladungsträger in der photoaktiven Schicht einer OSC. Im Rahmen dieser Arbeit wurde hierfür speziell ein experimenteller Aufbau geplant, ein Messplatz eingerichtet und die Kapazität und Überschussladungsträgerdynamik untersucht. Hierbei wurde gezeigt, dass die Kapazität organischer Solarzellen die Ergebnisse transienter elektrischer Charakterisierungsmethoden maßgeblich beeinflussen kann. Für die verwendete Methode wurden die experimentellen Unsicherheiten in der Bestimmung kapazitiver Ladungen und die Injektion kapazitiver Ladungen unter offenen Klemmen als limitierende Faktoren identifiziert. Es wurde gezeigt, dass für eindeutige Ergebnisse die Ladungsmenge, welche aus der Extraktion photogenerierter Ladungsträger herrührt, einen signifikanten Anteil der gesamten extrahierten Ladung ausmachen muss. Um diese Situation zu erreichen sind große Schichtdicken und geringe Extraktionsspannungen von Vorteil. Die genau erforderlichen Bedingungen hängen jedoch vom untersuchten photoaktiven Material ab und eine allgemeingültige Grenze für das benötigte Überschussladungsträgerdominierte-Regime kann nicht gegeben werden. Eine detaillierte Beschreibung des transienten Verhaltens einer individuellen OSC benötigt komplexe zeit- und ortsaufgelöste Simulationen, insbesondere wenn die Transporteigenschaften des organischen Halbleiters berücksichtigt werden sollen. Unter Bedingungen, in denen die Überschussladungsträger dominieren, konnte der bi-molekulare

Rekombinationskoeffizient für P3HT:$PC_{61}BM$ als $k_r^{bi} = 3.9 \times 10^{-12}\,cm^3\,s^{-1}$ und für PCDTBT:$PC_{71}BM$ als $k_r^{bi} = 9.1 \times 10^{-11}\,cm^3\,s^{-1}$ bestimmt werden. Die neu eingeführte Methode erlaubt die Bestimmung des Rekombinationskoeffizienten des photoaktiven Materials unter anwendungsrelevanten Beleuchtungsstärken in einer kompletten Solarzelle und somit der realen Morphologie des organischen Halbleiters.

Rekombinationsverluste an Elektroden mit unzureichender Selektivität

Darüber hinaus wurden zusätzliche Verluste durch Rekombination von Elektronen und Löchern an Elektroden untersucht. Hierzu wurden Elektronenkontakte mit stark unterschiedlicher Selektivität auf organische Solarzellen für mehrere photoaktive Materialien aufgebracht. Die Ladungsträgerdichte in der photoaktiven Schicht wurde mittels Ladungsträgerextraktion und einer Kombination aus Elektro- und Photolumineszenz bestimmt. Dafür wurde eine neuartige Methode der Fluoreszenzlöschung zur Bestimmung der Lumineszenz freier Ladungsträger unter Beleuchtung eingeführt. Mit dieser Methode konnte die Rekombination freier Elektronen und Löcher in P3HT:$PC_{61}BM$ zum ersten Mal unter Beleuchtung experimentell bestimmt werden (nach bestem Wissen des Autors). Die Ergebnisse beweisen, dass die Gesamtladungsträgerdichten in den untersuchten organischen Solarzellen durch die Verwendung von Kupferkontakten mit geringer Selektivität nur geringfügig verringert werden, wobei die offene Klemmenspannung drastisch sinkt. Daraus folgt, dass sich die äußere Spannung einer typischen organischen Solarzellen unter offenen Klemmen erheblich von der Aufspaltung der Quasi-Fermi-Energien in der absorbierenden Schicht unterscheidet, wenn Oberflächenrekombination auftritt. Demzufolge ist für die Untersuchung der Rekombination im Volumen des organischen Halbleiters die äußere Klemmenspannung im Falle von Oberflächenrekombination nicht geeignet. Die experimentellen Ergebnisse konnten mittels Drift-Diffusion-Simulationen, in welchen lediglich die Austrittsarbeit der Kontakte variiert wurde, konsistent reproduziert werden (die Simulationen wurden durch A. Spies durchgeführt [18]). Mittels dieser Ergebnisse konnten zwei Beiträge zur Verringerung der V_{OC} durch Oberflächenrekombination unterschieden werden. Erstens: Der Gradient in der Quasi-Fermi-Energie der Majoritätsladungsträger als Triebkraft für den Oberflächenrekombinationsstrom hin zum Kontakt und zweitens: Die Reduktion der maximalen Ladungsträgerdichte in der absorbierenden Schicht durch den Rekombinationsverlust an der Oberfläche. Ihr Beitrag hängt stark von den Ladungsträgermobilitäten ab. In Materialien mit eher schlechten Transporteigenschaften, was für viele photoaktive Materialien zutrifft die in organischen Solarzellen verwendet werden, ist der Hauptbeitrag zum V_{OC} Verlust der Gradient der

Quasi-Fermi-Energie der Majoritätsladungsträger hin zum entsprechenden Kontakt. Im Gegensatz dazu sind die Ladungsträgerdichten in geringer Entfernung zum Kontakt mit unzureichender Selektivität kaum verringert.

Temperatur- und Intensitätsabhängigkeit der offenen Klemmenspannung

Die Temperatur- und Intensitätsabhängigkeit der V_{OC} von organischen Solarzellen wurde für sechs photoaktive Materialien untersucht. Hieraus wurde die effektive Bandlücke des jeweiligen Donor-Akzeptorsystems bestimmt. Die auftretende Sättigung der V_{OC} bei tiefen Temperaturen und hohen Beleuchtungsintensitäten wurde auf Oberflächenrekombination zurückgeführt, welche durch die hohe Aufspaltung der Quasi-Fermi-Energien unter diesen Bedingungen verursacht wird. Die Spannungsverluste aus der Trennung der stark gebundenen photogenerierten Excitonen und aus der Rekombination von freien Ladungsträger wurden bestimmt und sowohl untereinander als auch mit Werten anderer Photovoltaik-Technologien verglichen. Die Verluste aus der Rekombination von freien Ladungsträgern sind vergleichbar mit denen in kommerziell erhältlichen GaAs oder Si Solarzellen und mit denen anderer neuartiger Technologien wie Perowskit Solarzellen. Es wurde gezeigt, dass die Energie welche als treibende Kraft für die Trennung der gebundenen Excitonen benötigt wird, mit steigender Effizienz der organischen Solarzellen in den letzten Jahren von $> 1\,\mathrm{V}$ auf $\approx 0.4\,\mathrm{V}$ verringert werden konnte. Mit $\approx 0.4\,\mathrm{eV}$ im aktuellen „non-Fullerene“ System PBDB-T:ITIC ($\eta > 9\,\%$) limitiert diese den Wirkungsgrad organischer Solarzellen jedoch nach wie vor stark.

Korrektur von Lumineszenzspektren auf optischs Emissionsvermögen

Diese Untersuchung zeigt drastische Veränderungen der CT Emissionsspektren von organischen Solarzellen durch Variation der Dicke der photoaktiven Schicht. Dies wurde für eine Vielzahl organischer Solarzellen unter Verwendung vier verschiedener Zellarchitekturen und drei verschiedenen photoaktiven Materialien demonstriert. Die Elektrolumineszenz aller Solarzellen wurde gemessen und damit gezeigt dass sich die Spektren eines gegebenen photoaktiven Materials für verschieden Schichtdicken und Zellarchitekturen stark voneinander unterscheiden. Im Gegensatz dazu wird erwartet, dass die Energie des CT Zustandes als fundamentale Eigenschaft des Donor-Akzeptorsystems nicht nennenswert von der Schichtdicke und dem genauen Zellaufbau abhängt. Aus diesem Grund wurde das optische Emissionsvermögen der verschiedenen Solarzellen durch Streu-Matrix Simulationen anhand experimentell bestimmter Brechungs- und Extinktionskoeffizienten berechnet. Nachdem die experimentell gemessenen Spektren auf das

Emissionsvermögen des Schichtstapels korrigiert wurden, ähneln sie sich für jedes photoaktive Material sehr. Die Ergebnisse zeigen, dass die gemessenen Spektren stark durch Interferenzeffekte in der gebildeten Mikrokavität beeinflusst werden und die eingeführte Korrektur für das Emissionsvermögen unverzichtbar sind, um verlässliche Informationen über die Energie strahlender Zustände in der photoaktiven Schicht zu erhalten. Die Energie des CT Zustandes spielt eine entscheidende Rolle für die erreichbare offene Klemmenspannung. Dadurch ist ihre genaue Bestimmung für ein tieferes Verständnis und eine Verbesserung der V_{OC} äußerst wichtig.

Fazit und Ausblick

Diese Arbeit trägt zu einem tieferen Verständnis der Zellphysik, der Rekombination und des Ursprungs der offenen Klemmenspannung organischer Bulk-Heteroübergangsolarzellen bei. Weiterhin beschreibt sie experimentelle Verfahren für eine umfassende Charakterisierung von Rekombination in OSC. Relevante Rekombinationsmechanismen wurden theoretisch beschrieben und experimentell untersucht. Dies umfasst die Rekombination von freien Ladungsträgern in der photoaktiven Schicht, zusätzliche Rekombination an Oberflächen und die Bestimmung wichtiger Energieniveaus und charakteristischer Energieverluste in Donor-Akzeptorsystemen. Hierzu wurde ein neuartiges Verfahren der Lumineszenzlöschung eingeführt und erfolgreich angewandt, um die strahlende Rekombination freier Ladungsträger in OSC unter Beleuchtung zu bestimmen. Zudem wurde, im Fall von Oberflächenrekombination in organischen Solarzellen, die Existenz starker Gradienten der Ladungsträgerdichten experimentell nachgewiesen. Des Weiteren wurde der starke Einfluss von Interferenz auf Lumineszenzspektren in OSC entdeckt, theoretisch beschrieben und ein Verfahren zur Berücksichtigung des Emissionsvermögens der Zellen eingeführt, was eine korrekte Interpretation der Spektren erlaubt. Darüber hinaus wurde gezeigt, dass der Energieverlust, der aus der Rekombination freier Ladungsträger in organischen Solarzellen herrührt, vergleichbar zu dem in Rekordzellen anderer Photovoltaik Technologien wie GaAs, Si oder hybrider organisch-anorganischen Perowskitsolarzellen ist. Die typischerweise hohe Dielektrizitätskonstante solcher kristallinen Halbleiter führt zu einer geringen Excitonenbindungsenergie und erlaubt eine direkte Generation freier Ladungsträger. Das ist aufgrund der verwendeten schweren Elemente, wie Blei, und der polarisierbaren, organischen Kationen auch für organisch-anorganische Perowskite der Fall. Diese fanden in den letzten Jahren große Beachtung in der Wissenschaft, da ihr Wirkungsgrad rasant auf über 23 % gesteigert werden konnte [135, 136]. Im Gegensatz dazu begrenzen der Energieverlust, der mit der Trennung stark

gebundener Excitonen einhergeht, und die damit verbundene niedere V_{OC} im Vergleich zur Energie der absorbierten Photonen, den Wirkungsgrad von modernen organischen Solarzellen nach wie vor erheblich. Diese Verluste müssen in der Zukunft, durch die Synthese geeigneter Donor- und Akzeptormaterialien mit vorteilhaften Energieniveaus oder neuartiger organischer Halbleiter mit kleiner Excitonbindungsenergien, z.B. durch Erhöhung der Dielektrizitätskonstanten, weiter reduziert werden. In der Reduzierung dieser Verluste liegt die zentrale Herausforderung im Feld der organischen Photovoltaik, um vergleichbare Wirkungsgrade zu anderen aufstrebenden Materialklassen, wie hybride organisch-anorganische Perowskite und zu etablierten PV-Technologien, zu erreichen.

Appendices

Appendix A

Sub- and Superscripts, Symbols, Constants and Abbreviations

A.1 Sub- and Superscripts

The sub- and superscripts that repeat most often with the following list of symbols are listed separately for a better readability. If the sub- and superscripts are separated with a comma it needs to be interpreted as an "and". When separated via "/" it needs to be interpreted as "or".

Sub- or Superscript	Description
Subscripts	
0	in Equilibrium at 300 K
A	of Acceptor
AM1.5G	Illumination with Am1.5G
CB	of the Conduction Band
corr	Corrected for Optical Out Coupling
CT	of Charge Transfer State
D	of Donor
e	of Electrons
e/h	of Electrons or Holes respectivly
eff	(of) Effective (Semiconductor)
el.cont	at the electron contact
ETL	of the Electron transport Level
h	of Holes
h.cont	at the hole contact
HTL	of the Hole Transport Level
i	Intrinsic Value

maj	of Majority Carriers
min	of Minority Carriers
MPP	at the Maximum Power Point
OC	under Open-Circuit Conditions
PAL	Phot Active Layer
pg	Photogenerated or Excess Value
ref	of Reference Solar Cell
SC	under Short-Circuit Conditions
SoSi	Illumination with Sun Simulator
test	of Measured Solar Cell
VB	of the Valence Band

Superscripts

0	in Equilibrium at 300 K
*	Excited Species
exp	Experimantally Observed Value
Fr	of Frenkel-excitons
ideal	ideal Value
max	Maximum Value
MW	of Mott-Wannier-excitons
n-doping	for Doping with an Elcetron Donor
p-doping	for Doping with an Electron Acceptor
pg	Photogenerated or Excess Value

A.2 Symbols

Symbol	Description	SI-Unit
α	absorption coefficient	m^{-1}
α_λ	Absorptivity	
β	Reaction Order	
ΔE_{exc}	Energy loss due to Exciton Splitting	J
ΔE_{rec}	Energy loss due to Recombination	J
ΔI_{PL}	Quenched Photoluminesence Intensity	a.u. $\sim \mathrm{W\,m^{-2}\,nm^{-1}}$
$\Delta I_{\mathrm{PL}}^{\mathrm{CT}}$	Quenched Photoluminesence Intensity of Charge-Transfer State	a.u. $\sim \mathrm{W\,m^{-2}\,nm^{-1}}$
ΔV	Voltage Jump	V
$\Delta V_{\mathrm{OC},1}$	Voltage Loss Related To Contribution 1	V
$\Delta V_{\mathrm{OC},2}$	Voltage Loss Related To Contribution 2	V
Δx	Step Size for Position Variations	m
ϵ_λ	Emissivity	
ϵ_{r}	Relative Permittivity	
η	Power Conversion Efficiency	
η_{e}	Electrochemical Potential of electrons	J
η_{h}	Electrochemical Potential of holes	J
γ_{OC}	Out Coupling Factor for Electromagnetic Waves	
$\bar{\gamma}_{\mathrm{OC}}$	Averaged Out Coupling Factor	
λ	Wavelength	m
λ_{RO}	Reorganization Energy	J
μ	Charge Carrier Mobility	$\mathrm{m^2\,(V\,s)^{-1}}$
μ^*	Effective Mass Of Electron-Hole Pair	kg
$\mu_{\mathrm{chem,e}}$	Chemical Potential of Elecrons	J
$\mu_{\mathrm{chem,h}}$	Chemical Potential of Holes	J
μ_r	Relative Permeability	
μ_0	Mobility Prefactor	$\mathrm{m^2\,(V\,s)^{-1}}$
ν	Frequency	s^{-1}
Ω	Solid Angle	sr
Φ_{B}	Injection Barrier	J

ρ	Space Charge Density	m^{-3}
σ	Total Electrical Conductivity	$\Omega^{-1}\,\mathrm{m}^{-1}$
σ_e	Electron Conductivity	$\Omega^{-1}\,\mathrm{m}^{-1}$
σ_h	Hole Conductivity	$\Omega^{-1}\,\mathrm{m}^{-1}$
σ_CT	Width of Gaussian Energetic Dissorder Distribution of CT Complexes	m^{-3}
τ_CT	Lifetime of excited CT states	s
τ_RC	RC Time	s
φ	Electiric Potential	V
φ_eff	Effective Injection Barrier	J
$\varphi_\mathrm{imb.\mu}$	Electric Potential Related To Imbalanced Mobilities	V
$\vec{v}$	Drift Velocity	$\mathrm{m\,s}^{-1}$
ζ	Langevin Prefactor	
A	Area	m^2
c	Speed of Light in Medium	$\mathrm{m\,s}^{-1}$
C	Capacitance	F
C_cell	Capacitance of the Solar Cell	F
C_chem	Chemical Capacitance	F
C_geo	Geometric Capacitance	F
D	Diffusion Coefficient	$\mathrm{m}^2\,\mathrm{s}^{-1}$
d	Layer Thickness	m
$D(E)$	Density of States	m^{-3}
d_PAL	Thickness of the Photoactive Layer	m
$\vec{E}$	Electric Field	$\mathrm{V\,m}^{-1}$
E	Energy	J
$\vec{E}$	Electric Field	$\mathrm{V\,m}^{-1}$
E_A	Acceptor Energy Level	J
E_abs	Acceptor Energy Level	J
E_B	Binding Energy	J
E_CB	Conduction Band Energy	J
E_coul	Potential Energy from Coulomb Interaction	J
E_CT	Energy of the Excited Charge-Transfer State	J
$E_\mathrm{CT}^\mathrm{abs}$	Energy of Maximum CT Absorption	J
$E_\mathrm{CT}^\mathrm{em}$	Energy of Maximum CT Emission	J

$E^{\mathrm{em}}_{\mathrm{CT,corr}}$	Corrected Energy of Maximum CT Emission	J
E_{D}	Donor Energy Level	J
E_{F}	Fermi Energy	J
$E_{\mathrm{g,abs}}$	Bandgap of Absorber	J
E_{g}	Bandgap	J
$E_{\mathrm{g,eff}}$	Effective Bandgap	J
E_{VB}	Valence Band Energy	J
F	Free Energy	J
f	Volume Fraction of the D-A Interfaces	
f_{F}	Fermi Function	
$F_{1/2}$	Fermi Integral Of Order 1/2	
FF	Fill Factor	
G	Generation Rate	$\mathrm{m^{-3}\,s^{-1}}$
G_{D^*}	Generation Rate for Excited Donor Molecules	$\mathrm{m^{-3}\,s^{-1}}$
G_{CT}	Generation Rate for Excited CT states	$\mathrm{m^{-3}\,s^{-1}}$
G_{eff}	Effective Generation Rate of Free Carriers	$\mathrm{m^{-3}\,s^{-1}}$
G_{exc}	Rate for Exciton Generation from Free Carriers	$\mathrm{m^{-3}\,s^{-1}}$
I	Illumination or Luminescence Intensity (*multiples of AM1.5G at $1000\,\mathrm{W\,m^{-2}}$)	$\mathrm{W\,m^{-2}}$ or suns*
I_{EL}	Electroluminesence Intensity	a.u. $\sim \mathrm{W\,m^{-2}\,nm^{-1}}$
$I_{\mathrm{EL,corr}}$	Corrected Electroluminesence Intensity	a.u. $\sim \mathrm{W\,m^{-2}\,nm^{-1}}$
I_{f}/E	Reduced Electroluminescence Intensity	a.u. $\sim \mathrm{m^{-2}\,(eV)^{-1}}$
$I_{\mathrm{f,corr}}/E$	Corrected Reduced Electroluminescence Intensity	a.u. $\sim \mathrm{m^{-2}\,(eV)^{-1}}$
$\vec{I_i}$	Amplitude of the Incoming Wave	$\mathrm{W\,m^{-2}}$
$I^{\mathrm{CT}}_{\mathrm{tot}}$	Total Photoluminesence Intensity from Free Carriers	a.u. $\sim \mathrm{W\,m^{-2}\,nm^{-1}}$
I_{hom}	Emitted Radiance from a Homogeneous System	a.u. $\sim \mathrm{W\,m^{-2}\,nm^{-1}}$
I_{PAL}	Emitted Radiance from the Solar Cell	a.u. $\sim \mathrm{W\,m^{-2}\,nm^{-1}}$
I_{PL}	Photoluminesence Intensity	a.u. $\sim \mathrm{W\,m^{-2}\,nm^{-1}}$
I_{extr}	Extraction Current	A
j	Particle Current Density	$\mathrm{s^{-1}\,m^{-2}}$

J	Electric Current Density	$\mathrm{A\,m^{-2}}$
J_C	Capacitive Current Density	$\mathrm{A\,m^{-2}}$
J_diff	Diffusion Current Density	$\mathrm{A\,m^{-2}}$
J_drift	Drift Current Density	$\mathrm{A\,m^{-2}}$
J_EL	Current Density for Electroluminesence Measurement	$\mathrm{A\,m^{-2}}$
J_gen	Generation Current Density	$\mathrm{A\,m^{-2}}$
J_inj	Injected Current Density	$\mathrm{A\,m^{-2}}$
J_rec	Recombination Current Density	$\mathrm{A\,m^{-2}}$
$J_{\mathrm{R_P}}$	Current Density the Parallel Resistance	$\mathrm{A\,m^{-2}}$
J_SR	Surface Recombination Current Density	$\mathrm{A\,m^{-2}}$
j_γ	Photonflux from Black Body	$\mathrm{s^{-1}\,m^{-2}}$
J_0	Saturation Current Density	$\mathrm{A\,m^{-2}}$
k	Extinction Coefficient	
$\vec{k}$	Wave Vector	$\mathrm{m^{-1}}$
$\vec{k}_\mathrm{F}$	Fermi Wave Vector	$\mathrm{m^{-1}}$
k_CS	Coefficient of CT State to Free Charges Dissociation	$\mathrm{m^3\,s^{-1}}$
k_f	Recombination Coefficient of CT State Decay	$\mathrm{m^3\,s^{-1}}$
k_L	Langevin Recombination Coefficent	$\mathrm{m^3\,s^{-1}}$
k_r	Recombination Coefficient of Free Charriers	$\mathrm{m^3\,s^{-1}}$
k_relax	Coefficient of Exciton to CT State Dissociation	$\mathrm{m^3\,s^{-1}}$
$k^*{}_\mathrm{CS}$	Coefficient of Exciton to Free Carrier Dissociation	$\mathrm{m^3\,s^{-1}}$
M	Mismatch Factor	
m_e^*	Effective Mass Of Electron	kg
m_0	Rest Mass of the Electron	kg
N	Number of Atoms	
n	Charge Carrier Density	$\mathrm{m^{-3}}$
n	Refractive Index in the Medium	
n_ex	Principle Quantum Number	
n_id	Ideality Factor	
n^pg	Excess Charge Carrier Density	$\mathrm{m^{-3}}$

N_{ETL}	Effective Density of States of Electron Transport Level	m^{-3}
N_{HTL}	Effective Density of States of Hole Transport Level	m^{-3}
n_{A}	Acceptor-like Dopant Density (p-Doping)	m^{-3}
N_{C}	Effective Density of States of the Conduction Band	m^{-3}
N_{CT}	Density of CT States	m^{-3}
n_{D}	Donor-like Dopant Density (n-Doping)	m^{-3}
n_{i}	Intrinsic Charge Carrier Density	m^{-3}
N_{V}	Effective Density of States of the Valence Band	m^{-3}
$\vec{O}_i$	Amplitude of the Outgoing Wave	$\mathrm{W\,m}^{-2}$
P	Power Density	$\mathrm{W\,m}^{-2}$
P_{in}	Incident Power Density	$\mathrm{W\,m}^{-2}$
P_{MPP}	Power Density at Maximum Power Point	$\mathrm{W\,m}^{-2}$
r_0	Distance of an Electron and a Hole	m
Q	Electric Charge	C
Q_{cap}	Capacitive Charge	C
Q_{extr}	Extracted Charge	C
Q_{pg}	Charge from Excess Carriers	C
R	Recombination Rate	$\mathrm{m}^{-3}\,\mathrm{s}^{-1}$
R_{P}	Parallel Resistance	Ω
R_{S}	Serial Resistance	Ω
R_{tot}	Total Recombination Rate	$\mathrm{m}^{-3}\,\mathrm{s}^{-1}$
R_λ	Reflectance	
S	Entropy	$\mathrm{J\,K}^{-1}$
$\bar{S}$	Time Averaged Pointing-Vector	$\mathrm{W\,m}^2$
$\mathbf{S}$	Scattering Matrix	
S_{ij}	Scattering Matrix Element	
SR	Spectral Response	$\mathrm{A\,W}^{-1}$
t	Time	s
t_{illu}	Illumintion Pulse Length	s
T	Temperature	K
T_λ	Transmittance	

T_{SC}	Temperature of the Semiconductor	K
T_0	Equilibrium Temperature under Dark Conditions	T
$\vec{v}$	Drift Velocity	$\mathrm{m\,s^{-1}}$
v_{SR}	Surface Recombination Velocity	$\mathrm{m\,s^{-1}}$
V	Volume	$\mathrm{m^3}$
V	Voltage	V
V_{bi}	Built-In Voltage	V
V_{ext}	Externally Applied Voltage	V
V_{extr}	Extraction Voltage	V
V_{int}	Internal Voltage	V
$V_{\mathrm{int}}^{\mathrm{ideal}}$	Ideal Internal Voltage	V
$V_{\mathrm{int}}^{\mathrm{max}}$	Maximum Internal Voltage	V
W_{F}	Workfunction	J
$W_{\mathrm{F,el.cont}}$	Workfunction of Electron Contact	J
$W_{\mathrm{F,h.cont}}$	Workfunction of Hole Contact	J
x	Position (Permpendicular to the Electrodes)	m
x_{max}	Position where Internal Voltage Is Maximum	m
y	Position	m
z	Position	m

A.3 Constants

Constant	Description	value
c_0	Speed of Light in Vacuum	$2.9979 \times 10^8\,\mathrm{m\,s^{-1}}$
ϵ_0	Vacuum Permittivity	$8.8542 \times 10^{-12}\,\mathrm{A\,s\,(V\,m)^{-1}}$
e_0	Elementary Charge	$1.6022 \times 10^{-19}\,\mathrm{C}$
h	Planck Constant	$6.6261 \times 10^{-34}\,\mathrm{kg\,m^2\,s^{-1}}$
$\hbar$	Reduced Planck Constant ($\hbar = \frac{h}{2\pi}$)	$1.0546 \times 10^{-34}\,\mathrm{J\,s}$
k_{B}	Boltzmann Constant	$1.380\,65 \times 10^{-23}\,\mathrm{J\,K^{-1}}$
m_0	Rest Mass of the Electron	$9.1094 \times 10^{-31}\,\mathrm{kg}$
μ_0	Vacuum Permeability	$4\pi \times 10^{-7}\,\mathrm{H\,m^{-1}}$
T_{sun}	Temperature of the Sun (5800 K)	5800 K
R_{y}	Rydberg Energy	$2.1799 \times 10^{-18}\,\mathrm{J}$

A.4 Abbreviations

Abbreviation	Full Expression
A	Acceptor
Ag	Silver
Al	Aluminium
AM1.5G	Air Mass 1.5 Global Spectrum
Au	Gold
BHJ	Bulk Heterojunction
C	Carbon
CB	Conduction Band
Cr	Chromium
CS	Charge Seperated State
CT	Charge-Transfer
Cu	Copper
D	Donor
D-A	Donor-Acceptor
DOS	Density of States
EL	Electroluminescence
ETL	Electron Transport Level
F	Fluorine
GS	Ground State
GaAs	Gallium Arsenide
HOMO	Highest Occupied Molecular Orbital
HTL	Hole Transport Level
InGaAs	Indium Gallium Arsenide
ITO	Indium Doped Zincoxide
JV-curve	Current Density-Voltage Characteristic
LED	Light-Emitting Diode
LiF	Lithium Fluoride
LUMO	Lowest Unoccupied Molecular Orbital
M	Molecule
MoO_3	Molybdenum Oxide
MPP	Maximum Power Point

OC	Open-Circuit
OPV	Organic Photovoltaic
OSC	Organic Solar Cell
PAL	Photoactive Layer
PCE	Power Conversion Efficiency
PL	Photoluminesence
PV	Photovoltaics
QFL	Quasi Fermi-Level
S_0	Ground State
S_1	first (Singlet) Exctation
Si	Silicon
SC	Short-Circuit
VB	Valence Band
ZnO	Zinc Oxide

Appendix B

Supporting Figures

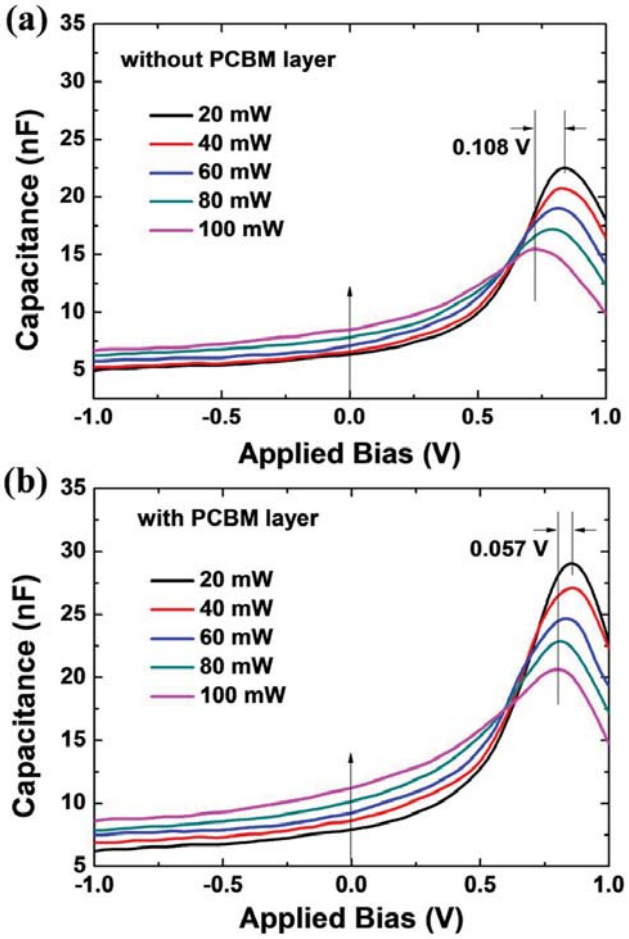

Figure B.1: Photo-assisted capacitance-voltage characteristics at various photo-excitation intensities from 20 to 100 mW cm^{-2} (a) for a inverted PTB7-F20:$PC_{71}BM$ solar cells without a $PC_{61}BM$ layer and (b) for solar cells with a $PC_{61}BM$ layer. From reference [105].

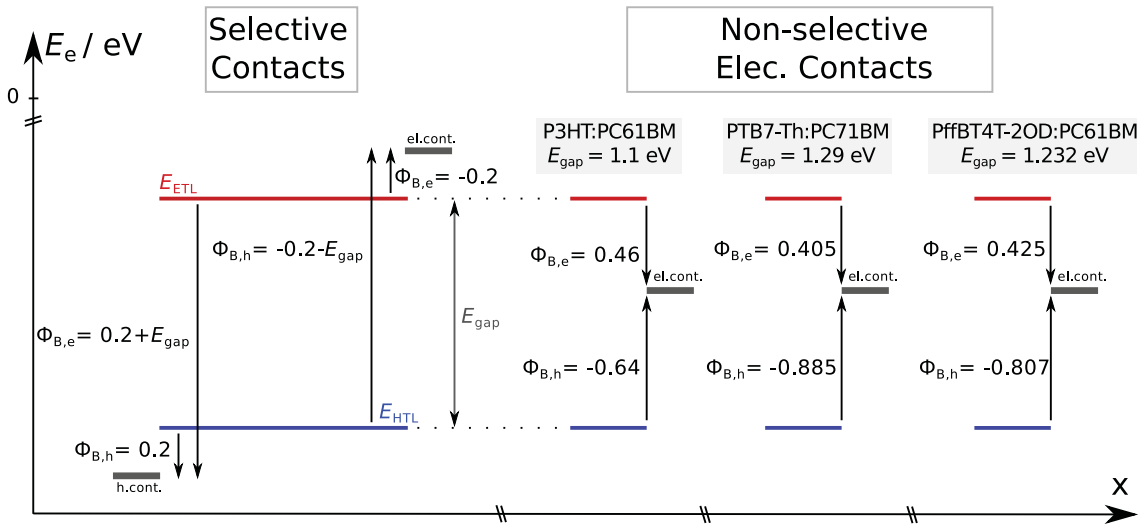

Figure B.2: Scheme of the energy levels of the effective semiconductor and the work functions of the electrodes in the case of selective and a non-selective electron contact for P3HT:PC_{61}BM, PTB7-Th:PC_{71}BM and PffBT4T-2OD:PC_{61}BM. Modified from [99].

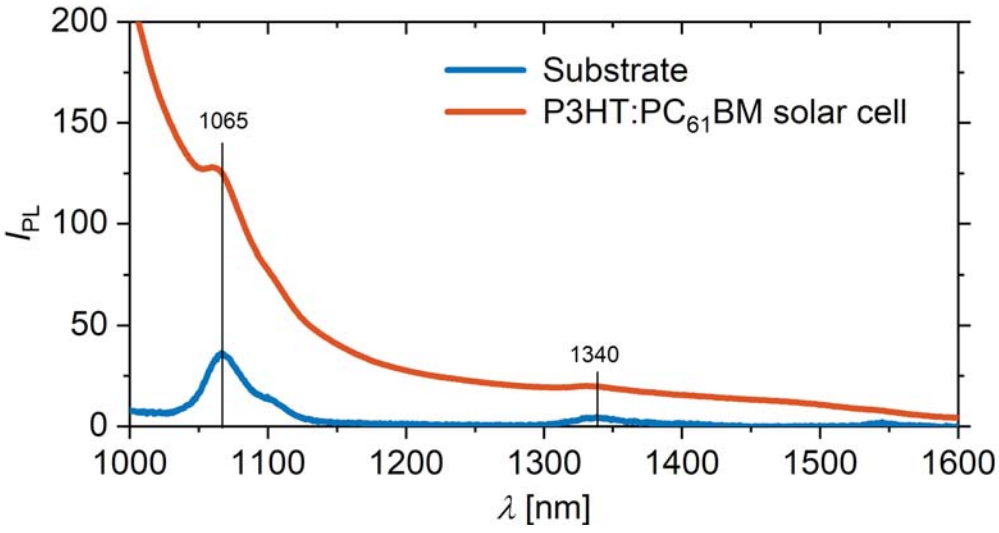

Figure B.3: PL spectra of an ITO coated glass substrate and a P3HT:PC_{61}BM OSC processed on a respective substrate measured at comparable intensities. The peaks at $\approx$ 1065 nm (including the small side peak) and at $\approx$ 1340 nm originate from neodymium (Nd^{3+}) impurities in the glass [143].

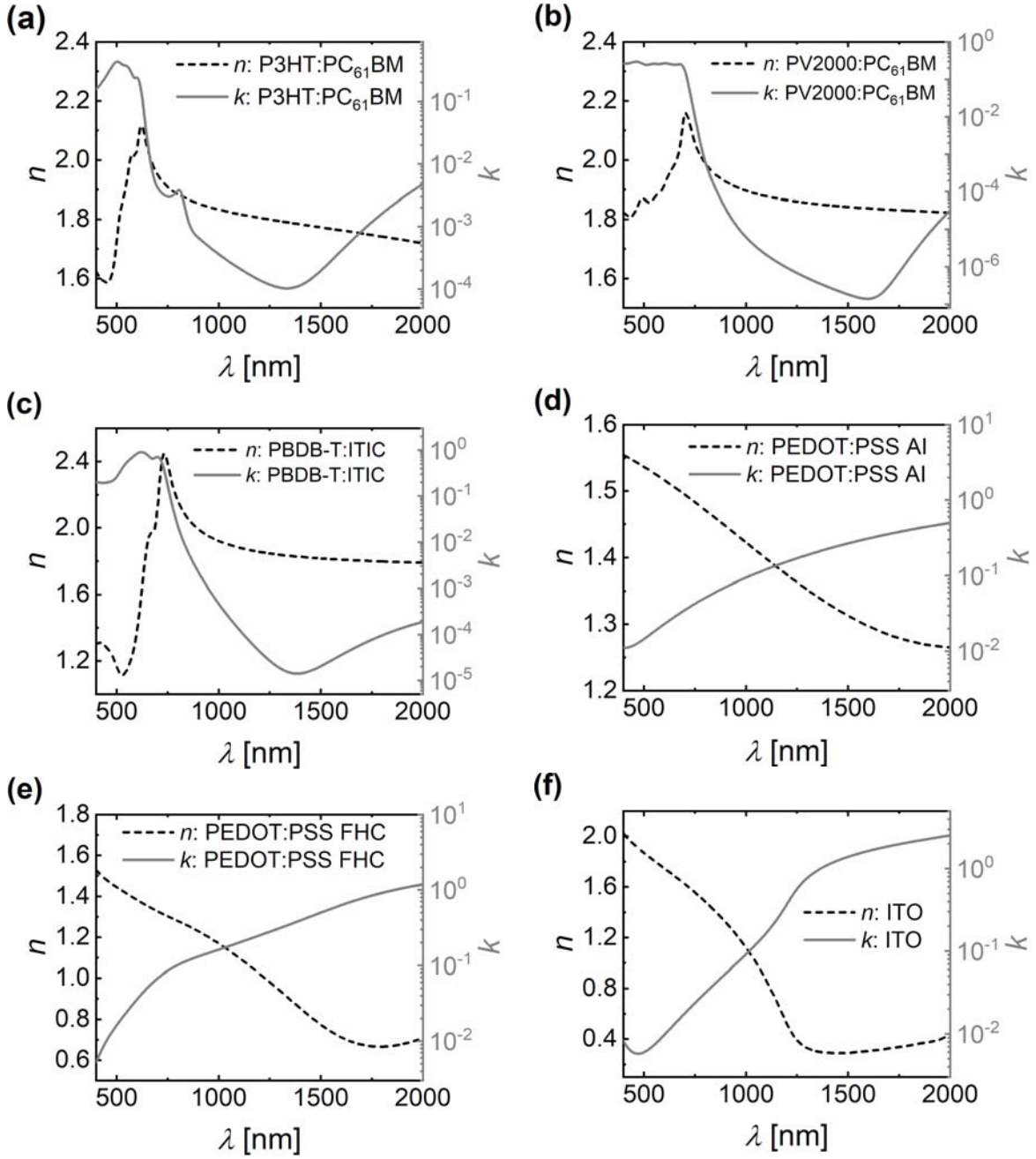

Figure B.4: Refractive index n and extinction coefficient k of (a) P3HT:$PC_{61}BM$, (b) PV2000:$PC_{61}BM$, (c) PBDB-T:ITIC, (d) PEDOT:PSS AI, (e) PEDOT:PSS FHC and (f) ITO.

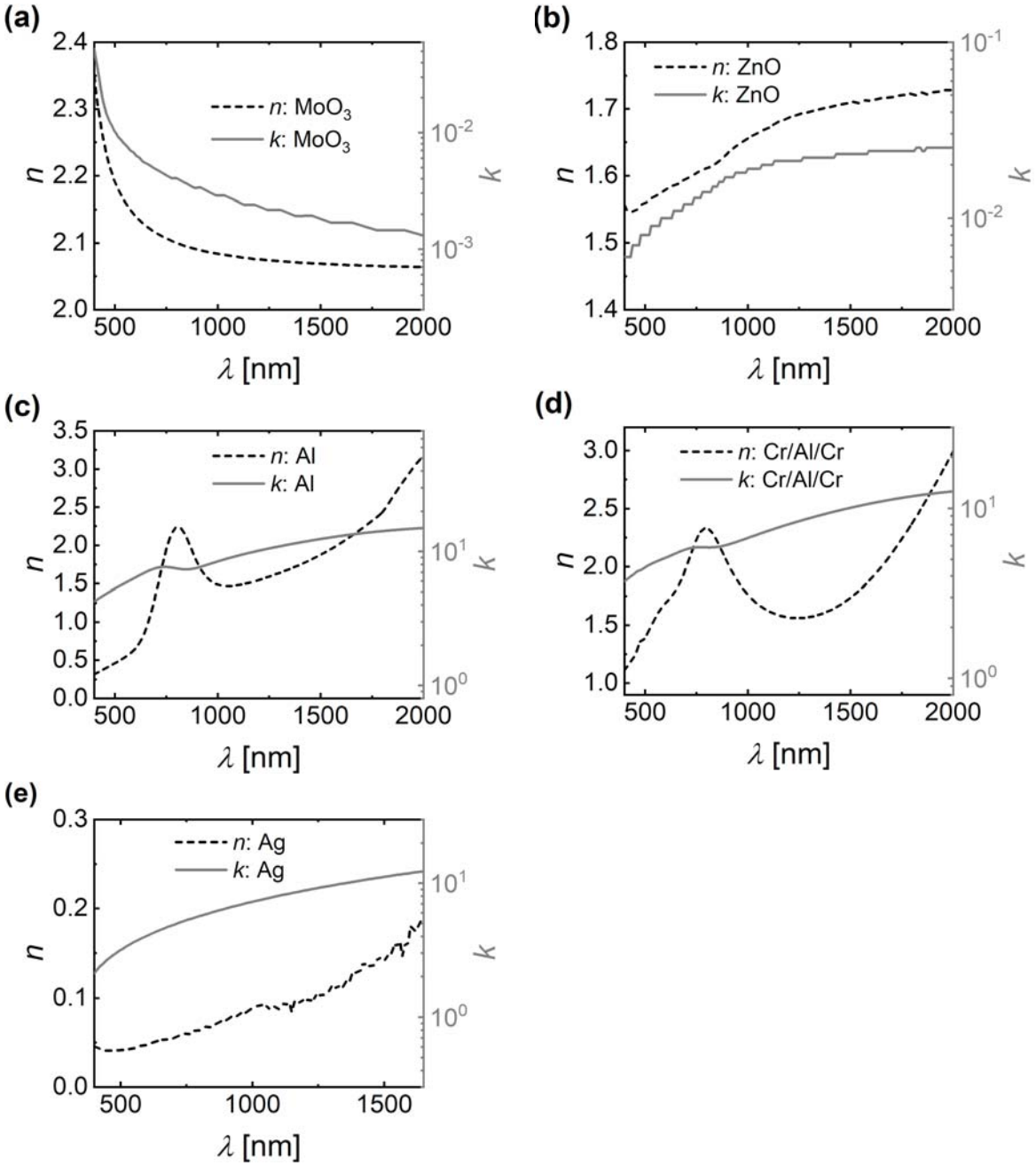

Figure B.5: Refractive index n and extinction coefficient k of (a) MoO_3 from reference [144], (b) ZnO from reference [145], (c) Al, (d) Cr/Al/Cr and (e) Ag from reference [146].

Appendix C

Supporting Tables

Table C.1: Parameter set for drift-diffusion simulations used for the JV-curves of P3HT:$PC_{61}BM$ shown in figure 8.1(a) [18].

Parameter (Symbol)	Value
Global parameters	
Temperature (T)	300 K
Work function of electron contact ($W_{\mathrm{F,e.cont}}$) (selective)	3.6 eV
Work function of electron contact ($W_{\mathrm{F,e.cont}}$) (less selective)	4.26 eV
Work function of hole contact ($W_{\mathrm{F,h.cont}}$)	5.1 eV
Surface recombination velocity of electrons and holes($\nu_{\mathrm{SR,h/h}}$)	$10^{12}\,\mathrm{cm\,s^{-1}}$
Parameters of photoactive layer	
Generation rate (G)	$2.5{\times}10^{-21}\,\mathrm{cm^{-3}\,s^{-1}}$
Layer thickness (d)	220 nm
Dielectric permittivity (ϵ)	3.4
Effective density of states in ETL / HTL $N_{\mathrm{ETL/HTL}}$	$5{\times}10^{20}\,\mathrm{cm^{-3}}$
Recombination coefficient k_{rec}	$2.3{\times}10^{-12}\,\mathrm{cm^{-3}\,s^{-1}}$
Energy of ETL (E_{ETL})	3.8 eV
Energy of HTL (E_{HTL})	4.9 eV
Mobility of electrons (μ_{e})	$1.7{\times}10^{-4}\,\mathrm{cm^2\,(V\,s)^{-1}}$
Mobility of holes (μ_{h})	$4.5{\times}10^{-4}\,\mathrm{cm^2\,(V\,s)^{-1}}$

Table C.2: Parameter set for drift-diffusion simulations used for the JV-curves of PTB7-Th:$PC_{71}BM$ shown in figure 8.1(b) [18].

Parameter (Symbol)	Value
Global parameters	
Temperature (T)	300 K
Work function of electron contact ($W_{\mathrm{F,e.cont}}$) (selective)	3.6 eV
Work function of electron contact ($W_{\mathrm{F,e.cont}}$) (less selective)	4.205 eV
Work function of hole contact ($W_{\mathrm{F,h.cont}}$)	5.29 eV
Surface recombination velocity of electrons and holes($\nu_{\mathrm{SR,h/h}}$)	$10^{12}\,\mathrm{cm\,s^{-1}}$
Parameters of photoactive layer	
Generation rate (G)	$8.9{\times}10^{-21}\,\mathrm{cm^{-3}\,s^{-1}}$
Layer thickness (d)	80 nm
Dielectric permittivity (ϵ)	3.4
Effective density of states in ETL / HTL $N_{\mathrm{ETL/HTL}}$	$1.8{\times}10^{20}\,\mathrm{cm^{-3}}$
Recombination coefficient k_{rec}	$4.0{\times}10^{-11}\,\mathrm{cm^{-3}\,s^{-1}}$
Energy of ETL (E_{ETL})	3.8 eV
Energy of HTL (E_{HTL})	5.09 eV
Mobility of electrons (μ_{e})	$6{\times}10^{-5}\,\mathrm{cm^2\,(V\,s)^{-1}}$
Mobility of holes (μ_{h})	$7{\times}10^{-4}\,\mathrm{cm^2\,(V\,s)^{-1}}$

Table C.3: Parameter set for drift-diffusion simulations used for the JV-curves of PffBT4T:$PC_{61}BM$ shown in figure 8.1(d) [18].

Parameter (Symbol)	Value
Global parameters	
Temperature (T)	300 K
Work function of electron contact ($W_{\mathrm{F,e.cont}}$) (selective)	3.8 eV
Work function of electron contact ($W_{\mathrm{F,e.cont}}$) (less selective)	4.425 eV
Work function of hole contact ($W_{\mathrm{F,h.cont}}$)	5.432 eV
Surface recombination velocity of electrons and holes($\nu_{\mathrm{SR,h/h}}$)	$10^{12}\,\mathrm{cm\,s^{-1}}$
Parameters of photoactive layer	
Generation rate (G)	$3.7{\times}10^{-21}\,\mathrm{cm^{-3}\,s^{-1}}$
Layer thickness (d)	260 nm
Dielectric permittivity (ϵ)	3.4
Effective density of states in ETL / HTL $N_{\mathrm{ETL/HTL}}$	$0.5{\times}10^{20}\,\mathrm{cm^{-3}}$
Recombination coefficient k_{rec}	$5.0{\times}10^{-11}\,\mathrm{cm^{-3}\,s^{-1}}$
Energy of ETL (E_{ETL})	4.0 eV
Energy of HTL (E_{HTL})	5.232 eV
Mobility of electrons (μ_{e})	$2.8{\times}10^{-4}\,\mathrm{cm^2\,(V\,s)^{-1}}$
Mobility of holes (μ_{h})	$2.1{\times}10^{-4}\,\mathrm{cm^2\,(V\,s)^{-1}}$

Appendix D

Supporting Information

D.1 Fitting Procedure for the Luminescence Data of P3HT:$PC_{61}BM$ and PffBT4T-2OD:$PC_{61}BM$ in chapter 8

Here the fitting of EL data used in chapter 8 is discussed in more detail as explained analogously in the supporting information of reference [99]. The share of luminescence from the recombination of free charge carriers in the PL was distinguished by a fitting routine. The shape of the characteristic luminescence peak originating from free charges was determined from the EL spectra of the donor:acceptor system. This characteristic peak in the EL spectra was fitted with an asymmetric Gaussian function given by

$$y = y_0 + A\frac{1}{1+\exp\left(\frac{-(x-x_c+w_{1/2})}{w_2}\right)}\left(1+\exp\left(\frac{-(x-x_c+w_{1/2})}{w_3}\right)\right)$$

Where x_c is the peak position,$w_{1/2}$ is the effective width, w_2 is the left width and w_3 is the right width. The offset y_0 was set to zero. The resulting parameters for P3HT:$PC_{61}BM$ are: $x_c = 1466\,\text{nm}$, $w_{1/2} = 164\,\text{nm}$, $w_2 = 111\,\text{nm}$ and $w_3 = 50\,\text{nm}$. For PffBT4T-2OD:$PC_{61}BM$ the parameters are $x_c = 1495\,\text{nm}$, $w_{1/2} = 86\,\text{nm}$, $w_2 = 67\,\text{nm}$ and $w_3 = 45\,\text{nm}$ respectively. In case of PffBT4T-2OD:$PC_{61}BM$ only the characteristic peak at 1495 nm was included in the fit. Since the resulting function is used to identify the amount of PL from free charge carriers the luminescence at shorter wavelength is not considered, because it is strongly superimposed by the luminescence of the exciton decay in PL.

D.2 Experimental Uncertainties of JV, EL, PL and Charge Extraction

In this chapter the experimental uncertainties for the data shown in chapter 8 are estimated analog to the discussion in the supporting information of reference [99].

Luminescence: The used cell layout contains 6 individual solar cells per substrate. The JV-characteristics showed minor variation between the cells within one substrate. All used data (JV, BACE, EL and PL) were measured on the same respective cell. EL and PL spectra were measured at the same positions. While the luminescence measurement itself is quite accurate, the signal shows fluctuations of up to 50 % when measured on different positions of the active area. The calculated $\Delta I_{\mathrm{PL}}^{\mathrm{CT}}$ from the fit can be used as an approximate value of the PL of free charge but does not give a precise value of the latter as discussed previously. Therefore, the values (both EL and PL) have an uncertainty of at least 50 % but give the correct order of magnitude of the measured quantity. Nevertheless, the uncertainties do not affect the qualitative conclusions in this study.

Charge Extraction Charge extraction: The accuracy of the measured extraction current is high (less than 5 % uncertainty considering the accuracy of the used oscilloscope and the measurement of resistance). The photogenerated charge carrier density n_{pg} is calculated from the difference of the extracted and the calculated capacitive charge (divided by the geometric volume of the cell). The systematic errors of the applied BACE method are discussed in detail in chapter 7. However, no systematic studies on the influence of the less selective contact (injection barrier) on the extraction current and on the model of a constant geometric capacitance in the presence of free charge carriers have been made so far. Therefore, the systematic error from the applied analysis method is unknown. Hence, the uncertainty in BACE is considered being rather high, even in the excess carrier dominated regime (potentially more than 50 %). However, the high uncertainty of the determined n_{pg} does not affect the qualitative conclusions in this work since only the order of magnitude of n_{pg} is crucial.

D.3 Layer Thicknesses used For S-Matrix Simulations in Chapter 10

The layer thicknesses used for S-matrix simulations are listed in this section. The layer stacks are listed, starting from the side of observation in luminescence measurements, i.e. the illumination side.

Type A:
The layer thicknesses for the P3HT:$PC_{61}BM$ cells are:
Air (∞) / PEDOT:PSS FHC (70 nm) / P3HT:$PC_{61}BM$ (variable) / Cr/Al/Cr (100 nm) / glass (∞).

Type B:
The layer thicknesses for the P3HT:$PC_{61}BM$ solar cells with additional semitransparent Ag mirror are:
Air (∞) / Ag (10 nm) / PEDOT:PSS FHC (70 nm) / P3HT:$PC_{61}BM$ (variable) / Cr/Al/Cr (100 nm) / glass (∞).

Type C:
The thicknesses of the different layers for the ITO-based P3HT:$PC_{61}BM$ cells are:
Glass (∞) / ITO (230 nm) / PEDOT:PSS AI (30 nm) / P3HT:$PC_{61}BM$ (variable) / LiF (0.3 nm) / Al (10 nm) / air(∞).

Type D:
The layer thicknesses for the ITO-based PV2000:$PC_{61}BM$ cells are:
Glass (∞) / ITO (180 nm) / ZnO (25 nm) / PV2000:$PC_{61}BM$ (variable) / MoO_3 (10 nm) / Ag (100 nm) / air (∞).
For the ITO-based PBDB-T:ITIC solar cells:
Glass (∞) / ITO (180 nm) / ZnO (20 nm) / PBDB-T:ITIC (variable) / MoO_3 (2 nm) / Ag (100 nm) / air (∞).

Appendix E

Publications

Publications in Peer-Reviewed Journals

1. M. List, T. Sarkar, P. Perkhun, J. Ackermann, C. Luo and U. Würfel. **Correct determination of charge transfer state energy from luminescence spectra in organic solar cells** *Nat. Commun.* 9(1), 125204 (2018).

2. A. Spies, M. List, T. Sarkar, U. Würfel. **On the Impact of Contact Selectivity and Charge Transport on the Open-Circuit Voltage of Organic Solar Cells**. *Adv. Energy Mater* 7(5), 1601750 (2016).

3. U. Würfel, M. Seßler, M. Unmüssig, M. List, E. Mankel, T. Mayer, G. Reiter, J.-L. Bubendorff, L. Simon, M. Kohlstädt. **How Molecules with Dipole Moments Enhance the Selectivity of Electrodes in Organic Solar Cells – a Combined Experimental and Theoretical Approach**. *Adv. Energy Mater.* 6(19), 1600594 (2016).

4. T. Amann, A. Kailer, N. Oberle, K. Li, M. Walter, M. List, J. Rühe. **Macroscopic superlow friction of steel and diamond-like carbon lubricated with a formanisotropic 1,3-diketone**. *ACS omega* 2(11), 8330 (2017).

5. K. Li, T. Amann, M. List, M. Walter, M. Moseler, A. Keiler, J. Rühe. **Ultralow Friction of Steel Surfaces Using a 1,3-Diketone Lubricant in the Thin Film Lubrication Regime**. *Langmuir* 31(40), 11033 (2015).

Book Chapters

A. Spies, J. Reinhardt, M. List, B. Zimmermann, U. Würfel. **Impact of Charge Carrier Mobility and Electrode Selectivity on the Performance of Organic Solar Cells**. In K. Leo (editor). *Elementary Processes in Organic Photovoltaics*, 401–418. Springer International Publishing, Cham (2017).
ISBN 978-3-319-28338-8.

Presentations and Posters

Presentations

M. List, A. Spies, T. Sarkar, U. Würfel. **Electro and Photoluminescence Measurements for Characterization of Surface Recombination**. *Freiburg Material Research Center Kolloquium*, Schluchsee, Germany (2015).

M. List, J. Herterich, M. Kohlstädt, U. Würfel, S. Glunz. **Lumineszenzspektroskopie an Perowskit-Solarzellen**. *Freiburg Material Research Center Kolloquium*, Schluchsee, Germany (2017). -price for best abstract-

M. List, A. Spies, J. Reinhardt, U. Würfel. **Luminescence Spectroscopy and Thin-Film Interference Effects in Organic Solar Cells**. *EMRS Spring Meeting*, Strasbourg, France (2017).

Poster Presentations

M. List, A. Spies, J. Reinhardt, U. Würfel. **Impact of Surface Recombination on the Charge Carrier Profile in Organic Solar Cells**. *EMRS-Spring Meeting*, Lille , France (2015).

M. List, A. Spies, J. Reinhardt, U. Würfel. **Impact of Surface Recombination on the Charge Carrier Profile in Organic Solar Cells**. *Next Generation Organic Photovoltaics*, Groningen, Netherlands (2015).

Bibliography

[1] International Energy Agency. *Key World Energy Statistics 2018*. IEA, Paris (2018). ISBN 978-92-64-30125-2.

[2] International Energy Agency. *World Energy Outlook 2014*. IEA Publications, Paris (2014). ISBN 978-92-64-20805-6.

[3] G7. 'Leader's Declaration G7 Summit, 7-8 June 2015' (2015). URL `https://www.g7germany.de/Content/DE/_Anlagen/G7_G20/2015-06-08-g7-abschluss-eng___blob=publicationFile&v=6.pdf` (accessed: 12/20/2018).

[4] R. Fu, D. J. Feldman, R. M. Margolis, M. A. Woodhouse, K. B. Ardani. 'U.S. Solar Photovoltaic System Cost Benchmark: Q1 2017' (2017). URL `https://www.nrel.gov/docs/fy17osti/68925.pdf` (accessed: 11/10/2018).

[5] Fraunhofer Institut für Solare Energiesysteme ISE. 'Photovoltaic Report' (2018). URL `https://www.ise.fraunhofer.de/content/dam/ise/de/documents/publications/studies/Photovoltaics-Report.pdf` (accessed: 11/26/2018).

[6] NobelPrize.org. 'Der Nobelpreis in Chemie 2000' (2000). URL `https://www.nobelprize.org/prizes/chemistry/2000/8940-pressemitteilung-der-nobelpreis-in-chemie-2000/` (accessed: 11/06/2018).

[7] C. W. Tang. 'Two-layer organic photovoltaic cell'. *Appl. Phys. Lett.* 48(2), 183 (1986).

[8] F. Zhao, S. Dai, Y. Wu, Q. Zhang, J. Wang, L. Jiang, Q. Ling, Z. Wei, W. Ma, W. You, C. Wang, X. Zhan. 'Single-Junction Binary-Blend Nonfullerene Polymer Solar Cells with 12.1% Efficiency'. *Adv. Mater.* 29(18), 1700144 (2017).

[9] L. Meng, Y. Zhang, X. Wan, C. Li, X. Zhang, Y. Wang, X. Ke, Z. Xiao, L. Ding, R. Xia, H.-L. Yip, Y. Cao, Y. Chen. 'Organic and solution-processed tandem solar cells with 17.3% efficiency'. *Science* 361(6407), 1094 (2018).

[10] C. H. Peters, I. T. Sachs-Quintana, J. P. Kastrop, S. Beaupré, M. Leclerc, M. D. McGehee. 'High Efficiency Polymer Solar Cells with Long Operating Lifetimes'. *Adv. Energy Mater.* 1(4), 491 (2011).

[11] M. Jørgensen, K. Norrman, S. A. Gevorgyan, T. Tromholt, B. Andreasen, F. C. Krebs. 'Stability of polymer solar cells'. *Adv. Mater.* 24(5), 580 (2012).

[12] S. B. Sapkota, A. Spies, B. Zimmermann, I. Dürr, U. Würfel. 'Promising long-term stability of encapsulated ITO-free bulk-heterojunction organic solar cells under different aging conditions'. *Sol. Energy Mater. Sol. Cells* 130, 144 (2014).

[13] D. Baran, R. S. Ashraf, D. A. Hanifi, M. Abdelsamie, N. Gasparini, J. A. Röhr, S. Holliday, A. Wadsworth, S. Lockett, M. Neophytou, Emmott, Christopher J. M., J. Nelson, C. J. Brabec, A. Amassian, A. Salleo, T. Kirchartz, J. R. Durrant, I. McCulloch. 'Reducing the efficiency-stability-cost gap of organic photovoltaics with highly efficient and stable small molecule acceptor ternary solar cells'. *Nat. Mater.* 16(3), 363 (2017).

[14] SOLARTE. 'Schmidhuber and BELECTRIC OPV bring energy into the German pavilion' (2014). URL `https://www.schmidhuber.de/sites/default/files/field/file/140626_pm_belectric_schmidhuber_expo_en_final.pdf` (accessed: 11/06/2019).

[15] S. H. Park, A. Roy, S. Beaupré, S. Cho, N. Coates, J. S. Moon, D. Moses, M. Leclerc, K. Lee, A. J. Heeger. 'Bulk heterojunction solar cells with internal quantum efficiency approaching 100%'. *Nat. Photonics* 3(5), 297 (2009).

[16] A. Armin, M. Velusamy, P. Wolfer, Y. Zhang, P. L. Burn, P. Meredith, A. Pivrikas. 'Quantum Efficiency of Organic Solar Cells: Electro-Optical Cavity Considerations'. *ACS Photonics* 1(3), 173 (2014).

[17] J.-D. Chen, Y.-Q. Li, J. Zhu, Q. Zhang, R.-P. Xu, C. Li, Y.-X. Zhang, J.-S. Huang, X. Zhan, W. You, J.-X. Tang. 'Polymer Solar Cells with 90% External Quantum Efficiency Featuring an Ideal Light- and Charge-Manipulation Layer'. *Adv. Mater.* 30(13), e1706083 (2018).

[18] A. Spies. *Numerical Simulations and Advanced Characterization of Organic Solar Cells*. Phd thesis, Albert Ludwig University of Freiburg (2018).

[19] P. Würfel, U. Würfel. *Physics of solar sells: From basic principles to advanced concepts*. Wiley-VCH, Weinheim, 3rd edition edition (2016). ISBN 978-3-527-41312-6.

[20] J. Nelson. *The physics of solar cells.* Imperial College Press, London (2003). ISBN 9781860943492.

[21] C. Kittel. *Introduction to Solid State Physics, 12th Edition.* John Wiley & Sons, Inc (1999). ISBN 9780471415268.

[22] M. Schwoerer, H. C. Wolf. *Organic Molecular Solids.* Physics textbook. Wiley-VCH, Weinheim (2007). ISBN 978-3-527-40540-4.

[23] U. Würfel, M. Thorwart, E. R. Weber (editors). *Quantum Efficiency in Complex Systems, Part II - From Molecular Aggregates to Organic Solar Cells.* Semiconductors and Semimetals. Elsevier (2011). ISBN 9780123910608.

[24] P. Würfel. *Physik der Solarzellen.* Spektrum-Hochschultaschenbuch. Spektrum Akademischer Verlag, Heidelberg and Berlin, 2. auflage edition (2000). ISBN 978-3-8274-0598-2.

[25] M. Seßler. *Selektive Fensterschichten in Organischen Tandemsolarzellen.* Phd thesis, Albert Ludwig University of Freiburg (2015).

[26] W. Shockley, W. Read. 'Statistics of the Recombinations of Holes and Electrons'. *Phys. Rev.* 87(5), 835 (1952).

[27] U. Würfel, A. Cuevas, P. Würfel. 'Charge Carrier Separation in Solar Cells'. *IEEE J. Photovoltaics* 5(1), 461 (2015).

[28] H. Ahme. *Spectroscopic Investigations of Transfer and Transport of Charge Carriers in the Donor/ Acceptor Network of Organic Solar Cells.* Phd thesis, Albert Ludwig University of Freiburg (2014).

[29] A. J. Heeger. 'Semiconducting and Metallic Polymers: The Fourth Generation of Polymeric Materials (Nobel Lecture)'. *Angew. Chem., Int. Ed.* 40(14), 2591 (2001).

[30] J. Patterson, B. Bailey. *Solid-State Physics.* Springer-Verlag, Berlin and Heidelberg (2010). ISBN 978-3-642-02588-4.

[31] B. A. Gregg, M. C. Hanna. 'Comparing organic to inorganic photovoltaic cells: Theory, experiment, and simulation'. *J. Appl. Phys.* 93(6), 3605 (2003).

[32] D. Hertel, H. Bässler. 'Photoconduction in amorphous organic solids'. *ChemPhysChem* 9(5), 666 (2008).

[33] M. Pope, C. E. Swenberg. *Electronic processes in organic crystals and polymers*, *Monographs on the physics and chemistry of materials*, volume #56. Oxford University Press, New York, 2nd ed edition (1999). ISBN 9780195129632.

[34] M. Reufer. *Exziton- und Spindynamik organischen Halbleiterlasern*. Cuvillier Verlag, Göttingen, 1st ed. edition (2006). ISBN 9783865378798.

[35] C. F. Klingshirn. *Semiconductor Optics*. Graduate Texts in Physics. Springer-Verlag, Berlin and Heidelberg, 4th ed. 2012 edition (2012). ISBN 978-3-642-28362-8.

[36] D. Abramavicius, V. Butkus, L. Valkunas. 'Interplay of Exciton Coherence and Dissipation in Molecular Aggregates'. In 'Quantum Efficiency in Complex Systems, Part II - From Molecular Aggregates to Organic Solar Cells', *Semiconductors and Semimetals*, volume 85, 3–46. Elsevier, New York (2011). ISBN 9780123910608.

[37] G. A. Chamberlain. 'Organic solar cells: A review'. *Solar Cells* 8(1), 47 (1983).

[38] M. List, T. Sarkar, P. Perkhun, J. Ackermann, C. Luo, U. Würfel. 'Correct determination of charge transfer state energy from luminescence spectra in organic solar cells'. *Nat. Commun.* 9(1), 125204 (2018).

[39] R. S. Mulliken. 'Molecular Compounds and their Spectra. II'. *J. Am. Chem. Soc.* 74(3), 811 (1952).

[40] K. Vandewal, J. Benduhn, K. S. Schellhammer, T. Vangerven, J. E. Rückert, F. Piersimoni, R. Scholz, O. Zeika, Y. Fan, S. Barlow, D. Neher, S. R. Marder, J. Manca, D. Spoltore, G. Cuniberti, F. Ortmann. 'Absorption Tails of Donor:C60 Blends Provide Insight into Thermally Activated Charge-Transfer Processes and Polaron Relaxation'. *J. Am. Chem. Soc.* 139(4), 1699 (2017).

[41] J.-L. Bredas, J. E. Norton, J. Cornil, V. Coropceanu. 'Molecular Understanding of Organic Solar Cells: The Challenges'. *Acc. Chem. Res.* 42(11), 1691 (2009).

[42] C. Deibel, T. Strobel, V. Dyakonov. 'Role of the charge transfer state in organic donor-acceptor solar cells'. *Adv. Mater.* 22(37), 4097 (2010).

[43] K. Vandewal, K. Tvingstedt, A. Gadisa, O. Inganäs, J. V. Manca. 'Relating the open-circuit voltage to interface molecular properties of donor:acceptor bulk heterojunction solar cells'. *Phys. Rev. B* 81(12), 125204 (2010).

[44] K. Vandewal. 'Interfacial Charge Transfer States in Condensed Phase Systems'. *Annu. Rev. Phys. Chem.* 67(1), 113 (2016).

[45] K. Vandewal, S. Albrecht, E. T. Hoke, K. R. Graham, J. Widmer, J. D. Douglas, M. Schubert, W. R. Mateker, J. T. Bloking, G. F. Burkhard, A. Sellinger, J. M. J. Fréchet, A. Amassian, M. K. Riede, M. D. McGehee, D. Neher, A. Salleo. 'Efficient charge generation by relaxed charge-transfer states at organic interfaces'. *Nat. Mater.* 13(1), 63 (2014).

[46] J. Benduhn, F. Piersimoni, G. Londi, A. Kirch, J. Widmer, C. Koerner, D. Beljonne, D. Neher, D. Spoltore, K. Vandewal. 'Impact of Triplet Excited States on the Open-Circuit Voltage of Organic Solar Cells'. *Adv. Energy Mater.* 8(21), 1800451 (2018).

[47] Y. Song, S. N. Clafton, R. D. Pensack, T. W. Kee, G. D. Scholes. 'Vibrational coherence probes the mechanism of ultrafast electron transfer in polymer-fullerene blends'. *Nat. Commun.* 5, 4933 (2014).

[48] F. Provencher, N. Bérubé, A. W. Parker, G. M. Greetham, M. Towrie, C. Hellmann, M. Côté, N. Stingelin, C. Silva, S. C. Hayes. 'Direct observation of ultrafast long-range charge separation at polymer-fullerene heterojunctions'. *Nat. Commun.* 5, 4288 (2014).

[49] K. Chen, A. J. Barker, M. E. Reish, K. C. Gordon, J. M. Hodgkiss. 'Broadband ultrafast photoluminescence spectroscopy resolves charge photogeneration via delocalized hot excitons in polymer:fullerene photovoltaic blends'. *J. Am. Chem. Soc.* 135(49), 18502 (2013).

[50] S. M. Falke, C. A. Rozzi, D. Brida, M. Maiuri, M. Amato, E. Sommer, A. de Sio, A. Rubio, G. Cerullo, E. Molinari, C. Lienau. 'Coherent ultrafast charge transfer in an organic photovoltaic blend'. *Science* 344(6187), 1001 (2014).

[51] T. Sarkar. *Spectroscopic Characterization of Organic Solar Cells.* Master thesis, Karlsruhe Institute of Technology, Karlsruhe (2015).

[52] J.-L. Bredas. 'Mind the gap!' *Mater. Horiz.* 1(1), 17 (2014).

[53] K. Vandewal, Z. Ma, J. Bergqvist, Z. Tang, E. Wang, P. Henriksson, K. Tvingstedt, M. R. Andersson, F. Zhang, O. Inganäs. 'Quantification of Quantum Efficiency and Energy Losses in Low Bandgap Polymer:Fullerene Solar Cells with High Open-Circuit Voltage'. *Adv. Funct. Mater.* 22(16), 3480 (2012).

[54] G. Ren, C. W. Schlenker, E. Ahmed, S. Subramaniyan, S. Olthof, A. Kahn, D. S. Ginger, S. A. Jenekhe. 'Photoinduced Hole Transfer Becomes Suppressed with Diminished Driving Force in Polymer-Fullerene Solar Cells While Electron Transfer Remains Active'. *Adv. Funct. Mater.* 23(10), 1238 (2013).

[55] E. T. Hoke, K. Vandewal, J. A. Bartelt, W. R. Mateker, J. D. Douglas, R. Noriega, K. R. Graham, J. M. J. Fréchet, A. Salleo, M. D. McGehee. 'Recombination in Polymer: Fullerene Solar Cells with Open-Circuit Voltages Approaching and Exceeding 1.0 V'. *Adv. Energy Mater.* 3(2), 220 (2013).

[56] K. Vandewal, K. Tvingstedt, O. Inganäs. 'Charge Transfer States in Organic Donor–Acceptor Solar Cells'. In 'Quantum Efficiency in Complex Systems, Part II - From Molecular Aggregates to Organic Solar Cells', *Semiconductors and Semimetals*, volume 85, 261–295. Elsevier (2011). ISBN 9780123910608.

[57] R. A. Marcus. 'Relation between charge transfer absorption and fluorescence spectra and the inverted region'. *J. Phys. Chem.* 93(8), 3078 (1989).

[58] K. Tvingstedt, K. Vandewal, A. Gadisa, F. Zhang, J. Manca, O. Inganäs. 'Electroluminescence from charge transfer states in polymer solar cells'. *J. Am. Chem. Soc.* 131(33), 11819 (2009).

[59] T. M. Burke, S. Sweetnam, K. Vandewal, M. D. McGehee. 'Beyond Langevin Recombination: How Equilibrium Between Free Carriers and Charge Transfer States Determines the Open-Circuit Voltage of Organic Solar Cells'. *Adv. Energy Mater.* 5(11), 1500123 (2015).

[60] P. Langevin. 'Recombinaison et mobilites des ions dans les gaz'. *Ann. Chim. Phys.* 1903(28), 433 (1903).

[61] G. Juška, N. Nekrašas, V. Valentinavičius, P. Meredith, A. Pivrikas. 'Extraction of photogenerated charge carriers by linearly increasing voltage in the case of Langevin recombination'. *Phys. Rev. B* 84(15), 155202 (2011).

[62] T. M. Clarke, J. Peet, A. Nattestad, N. Drolet, G. Dennler, C. Lungenschmied, M. Leclerc, A. J. Mozer. 'Charge carrier mobility, bimolecular recombination and trapping in polycarbazole copolymer:fullerene (PCDTBT:PCBM) bulk heterojunction solar cells'. *Org. Electron.* 13(11), 2639 (2012).

[63] C. Deibel, A. Wadsworth, V. Dyakonov. 'Origin of reduced polaron recombination in organic semiconductor devices'. *Phys. Rev. B* 80(7), 433 (2009).

[64] R. Österbacka, A. Pivrikas, G. Juška, A. Poškus, H. Aarnio, G. Sliaužys, K. Genevičius, K. Arlauskas, N. S. Sariciftci. 'Effect of 2-D Delocalization on Charge Transport and Recombination in Bulk-Heterojunction Solar Cells'. *IEEE J. Sel. Top. Quantum Electron.* 16(6), 1738 (2010).

[65] J. Szmytkowski. 'Analysis of the image force effects on the recombination at the donor–acceptor interface in organic bulk heterojunction solar cells'. *Chem. Phys. Lett.* 470(1), 123 (2009).

[66] A. Pivrikas, G. Juška, A. J. Mozer, M. Scharber, K. Arlauskas, N. S. Sariciftci, H. Stubb, R. Österbacka. 'Bimolecular recombination coefficient as a sensitive testing parameter for low-mobility solar-cell materials'. *Phys. Rev. Lett.* 94(17), 176806 (2005).

[67] D. H. K. Murthy, A. Melianas, Z. Tang, G. Juška, K. Arlauskas, F. Zhang, L. D. A. Siebbeles, O. Inganäs, T. J. Savenije. 'Origin of Reduced Bimolecular Recombination in Blends of Conjugated Polymers and Fullerenes'. *Adv. Funct. Mater.* 23(34), 4262 (2013).

[68] J. Benduhn, K. Tvingstedt, F. Piersimoni, S. Ullbrich, Y. Fan, M. Tropiano, K. A. McGarry, O. Zeika, M. K. Riede, C. J. Douglas, S. Barlow, S. R. Marder, D. Neher, D. Spoltore, K. Vandewal. 'Intrinsic non-radiative voltage losses in fullerene-based organic solar cells'. *Nat. Energy* 2(6), 17053 (2017).

[69] H. Bässler. 'Charge Transport in Disordered Organic Photoconductors: A Monte Carlo Simulation Study'. *Phys. Status Solidi B* 175(1), 15 (1993).

[70] N. Karl. 'Charge carrier transport in organic semiconductors'. *Synth. Met.* 133-134, 649 (2003).

[71] I. G. Scheblykin, A. Yartsev, T. Pullerits, V. Gulbinas, V. Sundstrom. 'Excited state and charge photogeneration dynamics in conjugated polymers'. *J. Phys. Chem. B* 111(23), 6303 (2007).

[72] P. E. Shaw, A. Ruseckas, I. D. W. Samuel. 'Exciton Diffusion Measurements in Poly(3-hexylthiophene)'. *Adv. Mater.* 20(18), 3516 (2008).

[73] I. A. Howard, R. Mauer, M. Meister, F. Laquai. 'Effect of morphology on ultrafast free carrier generation in polythiophene:fullerene organic solar cells'. *J. Am. Chem. Soc.* 132(42), 14866 (2010).

[74] J. E. Kroeze, T. J. Savenije, M. J. W. Vermeulen, J. M. Warman. 'Contactless Determination of the Photoconductivity Action Spectrum, Exciton Diffusion Length, and Charge Separation Efficiency in Polythiophene-Sensitized TiO_2 Bilayers'. *J. Phys. Chem. B* 107(31), 7696 (2003).

[75] C. Goh, S. R. Scully, M. D. McGehee. 'Effects of molecular interface modification in hybrid organic-inorganic photovoltaic cells'. *J. Appl. Phys.* 101(11), 114503 (2007).

[76] L. Luer. 'Oxygen-induced quenching of photoexcited states in polythiophene films'. *Org. Electron.* 5(1-3), 83 (2004).

[77] G. Yu, J. Gao, J. C. Hummelen, F. Wudl, A. J. Heeger. 'Polymer Photovoltaic Cells: Enhanced Efficiencies via a Network of Internal Donor-Acceptor Heterojunctions'. *Science* 270(5243), 1789 (1995).

[78] G. Yu, A. J. Heeger. 'Charge separation and photovoltaic conversion in polymer composites with internal donor/acceptor heterojunctions'. *J. Appl. Phys.* 78(7), 4510 (1995).

[79] J. J. M. Halls, C. A. Walsh, N. C. Greenham, E. A. Marseglia, R. H. Friend, S. C. Moratti, A. B. Holmes. 'Efficient photodiodes from interpenetrating polymer networks'. *Nature* 376(6540), 498 (1995).

[80] G. Lakhwani, A. Rao, R. H. Friend. 'Bimolecular recombination in organic photovoltaics'. *Annu. Rev. Phys. Chem.* 65, 557 (2014).

[81] J. R. Vig. 'UV/ozone cleaning of surfaces'. *J. Vac. Sci. Technol. A* 3(3), 1027 (1985).

[82] W. J. Dong, G. H. Jung, S. Y. Kim, J.-L. Lee. 'Effect of ultraviolet-Ozone on ITO/P3HT interface for PEDOT:PSS-free polymer solar cells'. *Sol. Energy Mater. Sol. Cells* 109, 240 (2013).

[83] C. Zhang, T. H. Nguyen, J. Sun, R. Li, S. Black, C. E. Bonner, S.-S. Sun. 'Design, Synthesis, Characterization, and Modeling of a Series of S , S - Dioxothienylenevinylene-Based Conjugated Polymers with Evolving Frontier Orbitals'. *Macromolecules* 42(3), 663 (2009).

[84] C. G. Shuttle, B. O'Regan, A. M. Ballantyne, J. Nelson, Bradley, D. D. C., J. de Mello, J. R. Durrant. 'Experimental determination of the rate law for charge carrier decay in a polythiophene: Fullerene solar cell'. *Appl. Phys. Lett.* 92(9), 93311 (2008).

[85] J. Kniepert, M. Schubert, J. C. Blakesley, D. Neher. 'Photogeneration and Recombination in P3HT/PCBM Solar Cells Probed by Time-Delayed Collection Field Experiments'. *J. Phys. Chem. Lett.* 2(7), 700 (2011).

[86] I. Lange, J. Kniepert, P. Pingel, I. Dumsch, S. Allard, S. Janietz, U. Scherf, D. Neher. 'Correlation between the Open Circuit Voltage and the Energetics of Organic Bulk Heterojunction Solar Cells'. *J. Phys. Chem. Lett.* 4(22), 3865 (2013).

[87] S. Albrecht, J. R. Tumbleston, S. Janietz, I. Dumsch, S. Allard, U. Scherf, H. Ade, D. Neher. 'Quantifying Charge Extraction in Organic Solar Cells: The Case of Fluorinated PCPDTBT'. *J. Phys. Chem. Lett.* 5(7), 1131 (2014).

[88] J. Kniepert, I. Lange, J. Heidbrink, J. Kurpiers, T. J. K. Brenner, L. J. A. Koster, D. Neher. 'Effect of Solvent Additive on Generation, Recombination, and Extraction in PTB7:PCBM Solar Cells: A Conclusive Experimental and Numerical Simulation Study'. *J. Phys. Chem. C* 119(15), 8310 (2015).

[89] E. Collado-Fregoso, S. N. Hood, S. Shoaee, B. C. Schroeder, I. McCulloch, I. Kassal, D. Neher, J. R. Durrant. 'Intercalated vs Nonintercalated Morphologies in Donor-Acceptor Bulk Heterojunction Solar Cells: PBTTT:Fullerene Charge Generation and Recombination Revisited'. *J. Phys. Chem. Lett.* 8(17), 4061 (2017).

[90] J. Kurpiers, T. Ferron, S. Roland, M. Jakoby, T. Thiede, F. Jaiser, S. Albrecht, S. Janietz, B. A. Collins, I. A. Howard, D. Neher. 'Probing the pathways of free

charge generation in organic bulk heterojunction solar cells'. *Nat. Commun.* 9(1), 2038 (2018).

[91] O. Alqahtani, M. Babics, J. Gorenflot, V. Savikhin, T. Ferron, A. H. Balawi, A. Paulke, Z. Kan, M. Pope, A. J. Clulow, J. Wolf, P. L. Burn, I. R. Gentle, D. Neher, M. F. Toney, F. Laquai, P. M. Beaujuge, B. A. Collins. 'Mixed Domains Enhance Charge Generation and Extraction in Bulk-Heterojunction Solar Cells with Small-Molecule Donors'. *Adv. Energy Mater.* 8(19), 1702941 (2018).

[92] J. Kniepert, I. Lange, N. J. van der Kaap, L. J. A. Koster, D. Neher. 'A Conclusive View on Charge Generation, Recombination, and Extraction in As-Prepared and Annealed P3HT:PCBM Blends: Combined Experimental and Simulation Work'. *Adv. Energy Mater.* 4(7), 1301401 (2014).

[93] W. Tress. *Device Physics of Organic Solar Cells.* Phd thesis, Technical University of Darmstadt (2012).

[94] G. A. Buxton, N. Clarke. 'Computer simulation of polymer solar cells'. *Modelling Simul. Mater. Sci. Eng.* 15(2), 13 (2007).

[95] F. F. Stelzl. *2-dimensionales Donator/Akzeptor-Modell für organische Solarzellen und experimentelle Untersuchungen mittels Nanoelektroden.* Phd thesis, Albert Ludwig University of Freiburg (2013).

[96] M. Fischer. *Untersuchung organischer Solarzellen mit numerischen Simulationen und CELIV.* Bachelor thesis, Albert Ludwig University of Freiburg (2013).

[97] A. Wagenpfahl, D. Rauh, M. Binder, C. Deibel, V. Dyakonov. 'S-shaped current-voltage characteristics of organic solar devices'. *Phys. Rev. B* 82(11), 115306 (2010).

[98] S. Lacic, O. Inganäs. 'Modeling electrical transport in blend heterojunction organic solar cells'. *J. Appl. Phys.* 97(12), 124901 (2005).

[99] A. Spies, M. List, T. Sarkar, U. Würfel. 'On the Impact of Contact Selectivity and Charge Transport on the Open-Circuit Voltage of Organic Solar Cells'. *Adv. Energy Mater.* 7(5), 1601750 (2017).

[100] C. Jacoboni. *Theory of Electron Transport in Semiconductors: A Pathway from Elementary Physics to Nonequilibrium Green Functions*, *Springer Series in Solid-State Sciences*, volume 165. Springer-Verlag, Berlin and Heidelberg (2010). ISBN 978-3-642-10586-9.

[101] O. Höhn. *Winkelselektive Photonische Strukturen für eine Optimierte Strahlungsbilanz in Solarzellen.* Phd thesis, Albert Ludwig University of Freiburg (2015).

[102] F. M. J. Bödicker. *Modellierung des strahlenden Emissionsverhaltens in einer photonischen Solarzelle.* Bachelor thesis, Technical University of Darmstadt (2012).

[103] L. Li. 'Formulation and comparison of two recursive matrix algorithms for modeling layered diffraction gratings'. *J. Opt. Soc. Am. A* 13(5), 1024 (1996).

[104] D. M. Whittaker, I. S. Culshaw. 'Scattering-matrix treatment of patterned multilayer photonic structures'. *Phys. Rev. B* 60(4), 2610 (1999).

[105] S. Cho, K.-D. Kim, J. Heo, J. Y. Lee, G. Cha, B. Y. Seo, Y. D. Kim, Y. S. Kim, S.-y. Choi, D. C. Lim. 'Role of additional PCBM layer between ZnO and photoactive layers in inverted bulk-heterojunction solar cells'. *Sci. Rep.* 4, 4306 (2014).

[106] M. Neukom, S. Züfle, S. Jenatsch, B. Ruhstaller. 'Opto-electronic characterization of third-generation solar cells'. *Sci. Technol. Adv. Mater.* 19(1), 291 (2018).

[107] A. Pivrikas, N. S. Sariciftci, G. Juška, R. Österbacka. 'A review of charge transport and recombination in polymer/fullerene organic solar cells'. *Prog. Photovolt: Res. Appl.* 15(8), 677 (2007).

[108] J. Reinhardt, M. Grein, C. Bühler, M. Schubert, U. Würfel. 'Identifying the Impact of Surface Recombination at Electrodes in Organic Solar Cells by Means of Electroluminescence and Modeling'. *Adv. Energy Mater.* 4(11), 1400081 (2014).

[109] J. Reinhardt, P. Apilo, B. Zimmermann, S. Rousu, U. Würfel. 'Determining the photocurrent of individual cells within an organic solar module by LBIC and the filtering approach - experiments and simulations'. *Sol. Energy Mater. Sol. Cells* 134, 157 (2015).

[110] U. Würfel, D. Neher, A. Spies, S. Albrecht. 'Impact of charge transport on current-voltage characteristics and power-conversion efficiency of organic solar cells'. *Nat. Commun.* 6, 6951 (2015).

[111] U. Würfel, M. Seßler, M. Unmüssig, N. Hofmann, M. List, E. Mankel, T. Mayer, G. Reiter, J.-L. Bubendorff, L. Simon, M. Kohlstädt. 'How Molecules with Dipole Moments Enhance the Selectivity of Electrodes in Organic Solar Cells - A Combined Experimental and Theoretical Approach'. *Adv. Energy Mater.* 6(19), 1600594 (2016).

[112] A. Spies, J. Reinhardt, M. List, B. Zimmermann, U. Würfel. 'Impact of Charge Carrier Mobility and Electrode Selectivity on the Performance of Organic Solar Cells'. In K. Leo (editor), 'Elementary Processes in Organic Photovoltaics', 401–418. Springer International Publishing, Cham (2017). ISBN 978-3-319-28338-8.

[113] D. Rauh, C. Deibel, V. Dyakonov. 'Charge Density Dependent Nongeminate Recombination in Organic Bulk Heterojunction Solar Cells'. *Adv. Funct. Mater.* 22(16), 3371 (2012).

[114] D. S. Hecht, L. Hu, G. Irvin. 'Emerging Transparent Electrodes Based on Thin Films of Carbon Nanotubes, Graphene, and Metallic Nanostructures'. *Adv. Mater.* 23(13), 1482 (2011).

[115] Z. Wang, C. Zhang, D. Chen, S. Tang, J. Zhang, L. Sun, T. Heng, Y. Hao. 'ITO-Free Semitransparent Organic Solar Cells Based on Silver Thin Film Electrodes'. *Int. J. Photoenergy* 2014, Article ID 209206 (2014).

[116] M. Glatthaar, M. Niggemann, B. Zimmermann, P. Lewer, M. Riede, A. Hinsch, J. Luther. 'Organic solar cells using inverted layer sequence'. *Thin Solid Films* 491(1-2), 298 (2005).

[117] M. Hösel, D. Angmo, R. R. Søndergaard, G. A. Dos Reis Benatto, J. E. Carlé, M. Jørgensen, F. C. Krebs. 'High-Volume Processed, ITO-Free Superstrates and Substrates for Roll-to-Roll Development of Organic Electronics'. *Adv. Sci.* 1(1), 1400002 (2014).

[118] W. Tress, K. Leo, M. Riede. 'Optimum mobility, contact properties, and open-circuit voltage of organic solar cells: A drift-diffusion simulation study'. *Phys. Rev. B* 85(15), 155201 (2012).

[119] C. Deibel, A. Wagenpfahl, V. Dyakonov. 'Influence of charge carrier mobility on the performance of organic solar cells'. *Phys. Status Solidi RRL* 2(4), 175 (2008).

[120] T. Kirchartz, B. E. Pieters, K. Taretto, U. Rau. 'Mobility dependent efficiencies of organic bulk heterojunction solar cells: Surface recombination and charge transfer state distribution'. *Phys. Rev. B* 80(3), 35334 (2009).

[121] O. J. Sandberg, M. Nyman, R. Österbacka. 'Effect of Contacts in Organic Bulk Heterojunction Solar Cells'. *Phys. Rev. Applied* 1(2), 24003 (2014).

[122] S. Wheeler, F. Deledalle, N. Tokmoldin, T. Kirchartz, J. Nelson, J. R. Durrant. 'Influence of Surface Recombination on Charge-Carrier Kinetics in Organic Bulk Heterojunction Solar Cells with Nickel Oxide Interlayers'. *Phys. Rev. Applied* 4(2), 24020 (2015).

[123] V. D. Mihailetchi, H. X. Xie, B. de Boer, L. J. A. Koster, P. W. M. Blom. 'Charge Transport and Photocurrent Generation in Poly(3-hexylthiophene): Methanofullerene Bulk-Heterojunction Solar Cells'. *Adv. Funct. Mater.* 16(5), 699 (2006).

[124] A. Armin, G. Juska, M. Ullah, M. Velusamy, P. L. Burn, P. Meredith, A. Pivrikas. 'Balanced Carrier Mobilities: Not a Necessary Condition for High-Efficiency Thin Organic Solar Cells as Determined by MIS-CELIV'. *Adv. Energy Mater.* 4(4), 1300954 (2014).

[125] M. Stolterfoht, A. Armin, B. Philippa, R. D. White, P. L. Burn, P. Meredith, G. Juska, A. Pivrikas. 'Photocarrier drift distance in organic solar cells and photodetectors'. *Sci. Rep.* 5, 9949 (2015).

[126] K. Vandewal, K. Tvingstedt, A. Gadisa, O. Inganäs, J. V. Manca. 'On the origin of the open-circuit voltage of polymer-fullerene solar cells'. *Nat. Mater.* 8(11), 904 (2009).

[127] P. Yu, A. Migan-Dubois, J. Alvarez, A. Darga, V. Vissac, D. Mencaraglia, Y. Zhou, M. Krueger. 'Study of traps in P3HT: PCBM based organic solar cells using fractional thermally stimulated current (FTSC) technique'. *J. Non-Cryst. Solids* 358(17), 2537 (2012).

[128] K. Tvingstedt, C. Deibel. 'Temperature Dependence of Ideality Factors in Organic Solar Cells and the Relation to Radiative Efficiency'. *Adv. Energy Mater.* 6(9), 1502230 (2016).

[129] K. Tvingstedt, K. Vandewal, F. Zhang, O. Inganäs. 'On the Dissociation Efficiency of Charge Transfer Excitons and Frenkel Excitons in Organic Solar Cells: A Luminescence Quenching Study'. *J. Phys. Chem. C* 114(49), 21824 (2010).

[130] S. van Reenen, M. V. Vitorino, S. C. J. Meskers, R. A. J. Janssen, M. Kemerink. 'Photoluminescence quenching in films of conjugated polymers by electrochemical doping'. *Phys. Rev. B* 89(20), 205206 (2014).

[131] Z. Liang, B. A. Gregg. 'Compensating Poly(3-hexylthiophene) Reveals Its Doping Density and Its Strong Exciton Quenching by Free Carriers'. *Adv. Mater.* 24(24), 3258 (2012).

[132] W. J. Grzegorczyk, T. J. Savenije, T. E. Dykstra, J. Piris, J. M. Schins, L. D. Siebbeles. 'Temperature-Independent Charge Carrier Photogeneration in P3HT−PCBM Blends with Different Morphology'. *J. Phys. Chem. C* 114(11), 5182 (2010).

[133] T. Kirchartz, F. Deledalle, P. S. Tuladhar, J. R. Durrant, J. Nelson. 'On the Differences between Dark and Light Ideality Factor in Polymer:Fullerene Solar Cells'. *J. Phys. Chem. Lett.* 4(14), 2371 (2013).

[134] M. A. Green, Y. Hishikawa, E. D. Dunlop, D. H. Levi, J. Hohl-Ebinger, A. W. Ho-Baillie. 'Solar cell efficiency tables (version 51)'. *Prog. Photovoltaics* 26(1), 3 (2018).

[135] M. A. Green, Y. Hishikawa, E. D. Dunlop, D. H. Levi, J. Hohl-Ebinger, A. W. Ho-Baillie. 'Solar cell efficiency tables (version 52)'. *Prog. Photovoltaics* 26(7), 427 (2018).

[136] The National Renewable Energy Laboratory. 'NREL Best Research-Cell Efficiencies' (2018). URL `https://www.nrel.gov/pv/assets/pdfs/pv-efficiency-chart.20181221.pdf` (accessed: 12/21/2018).

[137] C. L. M. Hofmann, B. Herter, S. Fischer, J. Gutmann, J. C. Goldschmidt. 'Upconversion in a Bragg structure: Photonic effects of a modified local density of states and irradiance on luminescence and upconversion quantum yield'. *Opt. Express* 24(13), 14895 (2016).

[138] J. D. Jackson. *Classical electrodynamics*. Wiley, Hoboken, NY, 3. ed., repr. 2013, student ed. edition (2013=2009). ISBN 978-81-265-1094-8.

[139] Y. Kim, S. A. Choulis, J. Nelson, Bradley, Donal D. C., S. Cook, J. R. Durrant. 'Device annealing effect in organic solar cells with blends of regioregular poly(3-hexylthiophene) and soluble fullerene'. *Appl. Phys. Lett.* 86(6), 63502 (2005).

[140] S. van Bavel, E. Sourty, G. de With, K. Frolic, J. Loos. 'Relation between Photoactive Layer Thickness, 3D Morphology, and Device Performance in P3HT/PCBM Bulk-Heterojunction Solar Cells'. *Macromolecules* 42(19), 7396 (2009).

[141] J. Zhao, Y. Li, G. Yang, K. Jiang, H. Lin, H. Ade, W. Ma, H. Yan. 'Efficient organic solar cells processed from hydrocarbon solvents'. *Nat. Energy* 1(2), 15027 (2016).

[142] J. Mooney, P. Kambhampati. 'Get the Basics Right: Jacobian Conversion of Wavelength and Energy Scales for Quantitative Analysis of Emission Spectra'. *J. Phys. Chem. Lett.* 4(19), 3316 (2013).

[143] A. R. Molla, A. Tarafder, S. Mukherjee, B. Karmakar. 'Transparent Nd^{3+}-doped bismuth titanate glass-ceramic nanocomposites: Fabrication and properties'. *Opt. Mater. Express* 4(4), 843 (2014).

[144] L. Lajaunie, F. Boucher, R. Dessapt, P. Moreau. 'Strong anisotropic influence of local-field effects on the dielectric response of α -MoO_3'. *Phys. Rev. B* 88(11), 115141 (2013).

[145] M. R. Querry. *Report No. D-A158-623: Optical Constants*. Defense Technical Information Center, Fort Belvoir (1985). URL `http://www.dtic.mil/docs/citations/ADA158623` (accessed: 11/06/2018).

[146] K. M. McPeak, S. V. Jayanti, S. J. P. Kress, S. Meyer, S. Iotti, A. Rossinelli, D. J. Norris. 'Plasmonic Films Can Easily Be Better: Rules and Recipes'. *ACS Photonics* 2(3), 326 (2015).

Danksagung

Ich möchte allen Menschen von ganzem Herzen danken, die zum Gelingen dieser Arbeit beigetragen haben. Mein besonderer Dank gilt:

Prof. Dr. Eicke Weber für die Annahme und Betreuung dieser Arbeit.

Dr. Uli Würfel für die hervorragende wissenschftliche Betreuung und aufschlussreichen Diskussionen über die Physik der Solarzelle.

Annika Spies für die enge Zusammenarbeit, für die unzähligen, fruchtbaren Diskussionen, für ihre Ratschläge und Hilfe bei allen fachlichen und privaten Problemen. Ohne dich wäre diese Arbeit nicht möglich gewesen!

Dr. Birger Zimmermann, Dr. Markus Kohlstädt, Clemens Veit, Sarah Röttinger, Hans-Frieder Schleiermacher für sämtliche Hilfe, Ratschläge, Diskussionen und gemeinsame Stunden während und neben der Arbeitszeit.

Meinen Bachelor-, Masteranden und Hilfswissenschaftlern Tanmoy Sarkar, Jan Herterich, Jared Faißt, Patrick Reiser und Chieh Luo für ihren Einsatz und ihren Beitrag den sie zum Gelingen dieser Arbeit geleistet haben.

Sämtlichen Mitarbeitern der OPV Arbeitsgruppe am FMF. Danke für die tolle Zeit!

Florian Bödicker und Dr. Oliver Höhn für die Bereitstellung der Software und die Unterstützung bei optischen Simulationen.

Der Dr. Ruth Heerdt-Stiftung für die finanzielle Unterstützung in Form eines Promotionsstipendiums.

All meinen Freunden in Freiburg und meiner alten Heimat am Bodensee. Danke für eure

Freundschaft und Unterstützung über all die Jahre und für die tolle Zeit die ich mit euch verbringen durfte. Ihr seid ein wichtiger Teil von mir.

Meiner Familie. Dank an meine Großeltern, für eure liebevolle Führsorge. Meine wärmste Dankbarkeit an meine Mutter und meinen Vater. Danke, dass ihr immer an mich geglaubt und mich ermutigt habt, mich durch die Miseren des Lebens geführt habt, mir geholfen habt die Farben der Welt zu verstehen und dafür, dass ihr meinen gewählten Weg und meine getroffenen Entscheidungen immer unterstützt habt.

Danke für Alles !!

The research and development of organic solar cells is driven by the desire for cheap and sustainable renewable energy sources. While promising progress in cell efficiency has been achieved in recent years, there are still open questions about device physics and fundamental limitations of the performance of this arising technology.

This work investigates the recombination and energetics of photogenerated charge carriers and the resulting open circuit voltage in polymer based organic solar cells by charge extraction and temperature dependent measurements. The applicability and limitations of transient characterization techniques commonly used in the field of organic photovoltaics are elaborated. In addition, recombination at electrode interfaces and the impact of thin film optics on luminescence spectra are studied and described in detail leading to a more comprehensive understanding of device physics governing the characterization of organic solar cells.

UNI FREIBURG

Dr. Ruth Heerdt-Stiftung
zur Förderung der Grundlagenforschung im Bereich alternativer Energien

ISBN 978-3-8396-1468-6